Università degli Studi di Milano
Scuola di Dottorato in Chimica Industriale
XXV Ciclo

PhD Thesis

Gold Nanoconjugates: Preparation, Characterisation and Biological Applications

Svetlana Avvakumova
R08783

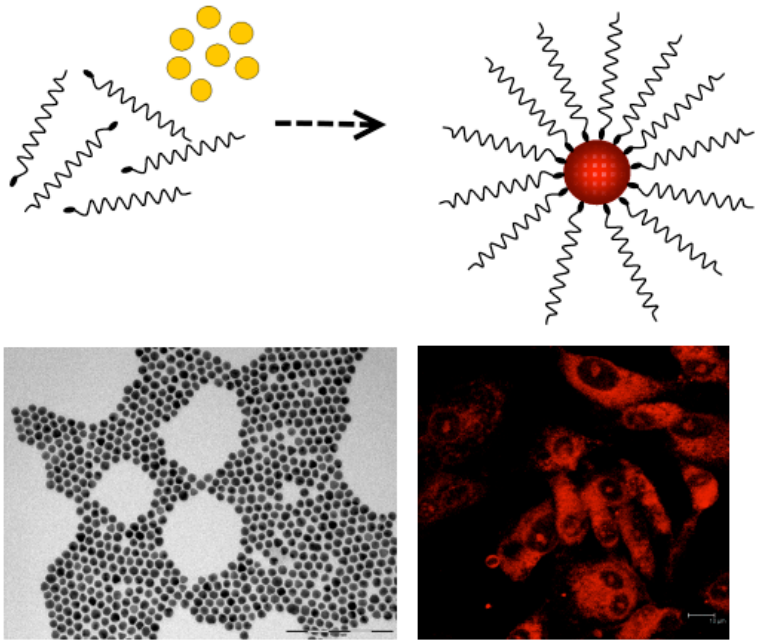

Supervisor: Prof Francesca Porta, Dr Giorgio Scarì

Coordinator: Prof. Dominique Robertò

2011 – 2012

Gold Nanoconjugates: Preparation, Characterisation and Biological Applications

Svetlana Avvakumova

Submitted for the degree of Doctor of Philosophy

at the Università degli Studi di Milano

Scuola di Dottorato in Chimica Industriale

Università degli Studi di Milano

2011 – 2012

Gold Nanoconjugates: Preparation, Characterisation and Biological Applications

PhD Thesis

by

Svetlana Avvakumova

Università degli Studi di Milano
Dipartimento di Chimica
Via Golgi 19
20133 Milano, Italy

Approved by:

Prof. Dominique Robertò
Università degli Studi di Milano
Coordinator

Advisory Committee

Prof. Claudia Bianchi
Università degli Studi di Milano

Prof. **Norberto Masciocchi**
Università dell'Insubria

Prof. Giuseppina Cerrato
Università degli Studi di Torino

Date approved: January, 2012

Table of Contents

Abbreviations

5’-AMP	Adenosine 5’-monophosphate
8-Br-Gua	8-bromoguanosine
5’-CMP	Cytidine 5’-monophosphate
5’-GMP	Guanosine 5’-monophosphate
5’-TMP	Thymidine 5’-monophosphate
Ade	Adenine
Ado	Adenosine
ATR-FTIR	Attenuated Total Reflection Fourier Transform Infrared
BSA	Bovine Serum Albumin
C	Cytosine
CPPs	Cell penetrating peptides
DCC	N,N'-Dicyclohexylcarbodiimide
DMF	Dimethylfomamide
DNA	Deoxyribonucleic acid
dT	Thymidine
EDC	1-Ethyl-3-(3-dimethylaminopropyl) carbidiimide-HCl
EDT	1,2-Ethanedithiol
EtOAc	Ethylacetate
EtOH	Ethanol
Fmoc	9-Fluorenylmethoxycarbonyl
Fmoc/tBu	Fluorenylmethoxycarbonyl/tert-butyl
FTIR	Fourier Transform Infrared
GC	Gly-Cys dipeptide
GK	Gly-Lys dipeptide
GNP	Gold Nanoparticle
GSH	Glutathione
GSSG	Glutathione disulfide
Gua	Guanosine
Guo	Guanine
HBTU/HOBt/DPEA	Coupling reagent on a Fmoc-Gly-Wang resin
HeLa	Immortal cell line derived from HPV18
HMPA	Hexamethylphosphoramide
HOBt	N-Hydroxybenzotriazole
HPLC	High Performance Liquid Chromatography

HPTS	8-Hydroxy-1,3,6-pyrebetrisolfonic acid
Ino	Inosine
M1G	1-methylguanosine
MBA	p-Mercaptobemzoic acid
MEM	Modified Eagle's Medium
MPCs	Monolayer Protected Clusters
MPEG	Methoxy polyethylene glycol
MRI	Magnetic Resonance Imaging
NIR	Near Infrared
NLS	Nuclear Localisation Signal
NMR	Nuclear Magnetic Resonance
NP	Nanoparticle
PBS	Phosphate Buffer Saline
PEG	Poly(ethylene glycol)
PFA	Paraformaldehyde
PL	Photoluminescence
PS	Polystyrene
PSA	Poly(sodium acrylate)
PVA	Polyvinyl alcohol
PyBOP	Benzotriazol-1-yl-oxytripyrrolidinophosphonium hexafluorophosphate
QD	Quantum Dot
rC	Cytidine
RNA	Ribonucleic acid
SAM	Self Assembled Monolayer
SDBS	Spectral Database System for Organic Compounds
SPR	Surface Plasmon Resonance
Sulfo-NHS	N-Hydroxy Sulfosuccinimid
TEA	Triethylamine
TEM	Transmission Electron Microscopy
TFA	Trifluoroacetic acid
T	Thymine
TLC	Thin layer chromatography
TOAB	Tetraoctyl ammonium bromide
Trt	Trityl
UA	Uranyl Acetate

Acknowledgements

There are many people I would like to thank for their support and encouragement, without whom this PhD thesis would not have been possible. My gratitude goes first and foremost to my parents, Yuri and Natalia, who have listened to my ideas, offered suggestions, and always gave me their time, energy, love and encouragement. Special thanks to my partner Paolo for his support and understanding all these years long, to my italian parents from Telese and Rezzato and, to my dear russian friends Marina and Anna, who always believed in me.

I wish to express my deepest gratitude to my supervisor, Prof. Francesca Porta for having teached me not only chemistry but also something about life, for her support and abity to “fight” and obtain the goals.

I’m grateful to Dr. Giorgio Scari for giving an opportunity to learn about biology, and his sence of humour which made our long microscopy experiments less boring.

I would like to express my sincerest thanks to Prof. Mathias Brust for The University of Liverpool who has always been an inspiration for me and for the opportunity he gave me to belong to his group, even if for a brief period of time, and learn a lot of new things about nanochemistry. My dear friends Dr. Zeljka Krpetic Dr. Alison Beckett who opened my mind to new interesting ideas.

I would like to extend my gratitude to the following people who helped me during my PhD thesis: Pasquale Illiano for supporting me every Tuesday with endless NMR samples; Dr. Vladimiro Dal Santo, Dr. Matteo Guidotti, and Prof. Giovanna Speranza for useful discussions, collaboration and generous suggestions. Thanks to Dr. Pierangelo Francescato and Dr. Umberto Fascio for their helpfulness. A special thank to Prof. Franco Cozzi and Prof. Dominique Robertò for their bureaucratic help without which I would not have been able to complete my studies.

And, finally, an enormous thank to Prof. Laura Prati and all the guys from her Lab for their support and funny moments I will always remember!

Chapter I

Gold nanoparticles

1. Introduction

Nanoparticle research has greatly expanded over the past several decades. A significant factor in this increase is development of numerous potential biological applications of nanoparticles, ranging from imaging [1-3] to biochemical sensing [4, 5], tumor targeting [6] and drug delivery [7-9]. The combination of inorganic and biochemical building blocks let to a wide variety of novel hybrid systems with unexpected properties. Functional groups found in biological systems provide a wide range of potential interactions with nanoparticle surface, which can easily interfere with biomolecule structure and function. While there is a huge part of work detailing the use of nanoparticles in biological settings, there are few studies exploring their affects on biomolecular structure and function. Thus, effective use of bio-nano systems requires also a detailed understanding of biomolecule-nanoparticle interactions on their interface.

The modification of peptides, proteins and other complex molecules with specific anchoring groups facilitates the binding to nanoparticles *via* a site-specific linkage, introducing chemical functionalities that can provide recognition or affinity interactions between the biomolecules and antibodies or cell receptors. This approach has been widely used to design nanoparticle conjugates to be used in different applications.

In this PhD thesis we focus our attention on the synthesis of gold nanoparticles modified with different organic molecules with biological activity. The manuscript is organized as follows. Chapter I contains some general data on gold nanoparticle properties, synthesis approaches and their application in order to familiarize the reader with the topic. Materials and methods, used in present work,

are briefly described in Chapter II. While Chapter III is dedicated to the studies of gold nanoparticles modified with nucleic acid components, such as nucleobases, nucleosides and nucleotides. Besides the synthesis details, and nanoparticle characterisation, a thorough study on the binding between the nanoparticles and the compounds, carried out by NMR and FTIR methods, is reported. Novel results are obtained on the binding sites and conformational changes occurred under interaction with gold nanoparticle surface. Moreover, preliminary results on biological studies of the nanoconjugates in U87 cancer cells are shown. The following Chapter IV contains the results on the study of gold nanoparticles modified with an RGD-peptide, designed for the targeting of integrin receptors in U87 cancer cells. The mechanism of the nanoconjugates uptake into the cells is studied by confocal and TEM microscopy, showing some interesting novel results. Finally, Chapter V is dedicated to the design and synthesis of gold nanoparticles functionalized by Halo Tag specific ligands. Different synthesis approaches described and the properties of final conjugates are compared in order to find out the best synthesis conditions. The biological studies using microinjection method are in progress in order to evaluate the activity of the nanoconjugates and study their behaviour in cancer cells.

2. Gold nanoparticles: general aspects

Metal nanoparticles have a long history in terms of preparation, characterization, and application. Understanding the properties of noble metal nanoparticles and exploring their application potential are two major driving forces behind the synthesis of a large variety of nanomaterials. Many properties of nanoparticles arise from their large surface-area-to-volume ratio and the spatial confinement of electrons, phonons, and electric fields in and around the particles. These may cause deviations from the usual bulk atomic arrangements, such as higher reactivity; different elastic, tensile, and magnetic properties; increased conductivity; or increased tendency to reflect and refract light [10].

The SI prefix “nano” means a billionth (10^{-9}) part of a meter, or about one hundred thousandth the thickness of a sheet of paper. The nanoscale, defined by the US National Nanotechnology Initiative, is a range from 1 to 100 nm, including particles which are naturally occurring, such as particles in smoke, volcanic ash, sea spray, and from anthropogenic sources. In terms of biology, the nanoscale is the size range of important cellular components, such as DNA (double-stranded DNA is about 2.5 nm in diameter), proteins (hemoglobin is about 5 nm in diameter), cell walls, cell membranes, and compartments [11].

The ‘‘soluble’’ gold, which we now call colloid gold, was developed around the 5^{th} or 4^{th} century B.C. and has been used technologically due to its optical properties, in particular for staining glass [12]. The modern era of gold nanoparticles synthesis began over 150 years ago with the work of Michael Faraday, who was possibly the first to observe that colloidal gold solutions have properties that differ from bulk gold [13].

Gold nanoparticles (AuNPs) possess distinct physical and chemical attributes that make them excellent tools for biological and medical applications. First, AuNPs can be synthesized in a straightforward manner and can be made highly stable. Second, they possess unique optoelectronic properties. Third, they provide high surface-to-volume ratio with excellent biocompatibility, using appropriate ligands. Finally, AuNPs offer a suitable platform for multifunctionalization with a wide range of organic or biological ligands for the selective binding and detection of small molecules and biological targets [14].

3. Optical properties of gold nanoparticles

AuNPs, like any noble metal NPs, feature surface plasmon resonance band (SPR). The SPR is the result from the collective oscillation of the conduction electrons across the particle due to the resonant excitation by the incoming photons. For AuNPs, the resonance condition is satisfied at visible wavelengths, therefore attributing for its intense colour [15]. The SPR band intensity and wavelength depends on the factors affecting the electron charge density on the particle surface, such as particle size, shape, structure, composition and the dielectric constant of the surrounding medium, as theoretically described by Mie theory [16]. The SPR band of AuNPs with size smaller than 10 nm is largely damped due to the phase changes resulting from the increased rate of electron-surface collisions compared to larger particles. Increasing particle size red-shifts the SPR wavelength and also increases the intensity [17]. The particles shape also determines the position of SPR: with a change from spheres to rods, the SPR band is split into two bands with a strong one in NIR region, corresponding to electron oscillations along the long axis, referred to longitudinal band, and a weak one in the visible region at a wavelength similar to that of gold nanospheres, referred to transverse band [18].

Besides the shape factor for optical tuning in NIR region, structure variations can result in similar phenomena. For instance, the SPR band of gold nanoshells, composed of silica core and gold shell, strongly depends on the shell-to-core ratio, but remaining independent of the particle size, core and shell material and even surrounding medium [19]. While gold nanocages of about 50 nm edge width with few nanometers walls and holes show the SPR band around 800 nm, which can be tuned to NIR region, by controlling the amount of reagents [20].

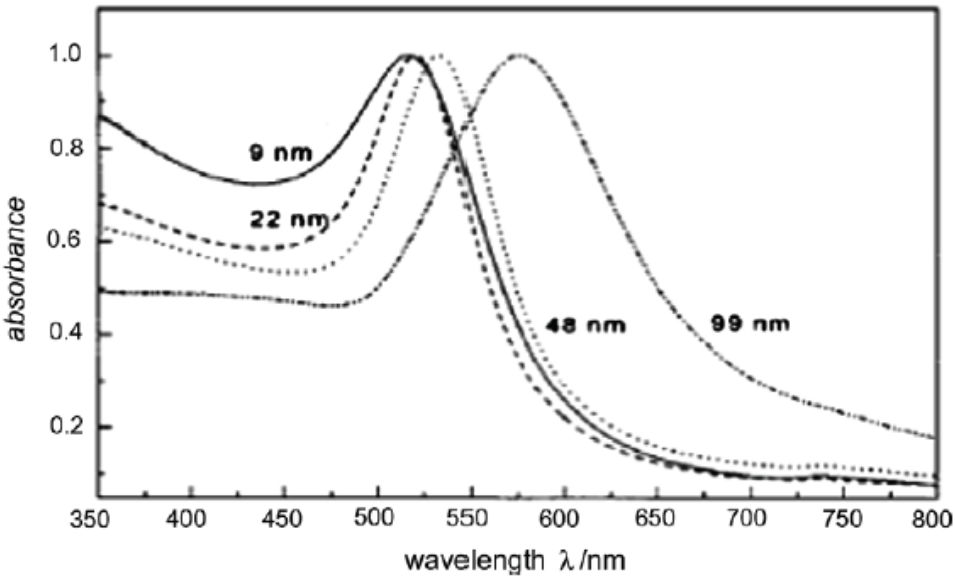

Figure 1. UV-vis spectra of gold nanoparticles in different sizes.

Another parameter affecting the SPR band is the medium surrounding the particle. The fact that the position and intensity of the plasmonic band changes with structural rearrangements in ligand shell is being taken into consideration by the scientists when using ligand exchange and bioconjugation techniques to functionalize the nanoparticles. It is probably the most simple and useful approach to understand if exchange reaction took place [21]. Moreover, the SPR band can be highly indicative of nanoparticle stability: their aggregation can be monitored *via* colour change or variation in the SPR band position and shape. Due to their optical properties, AuNPs have been finding a plenty of applications, from biosensors [22-24] to photothermal therapy [25, 26].

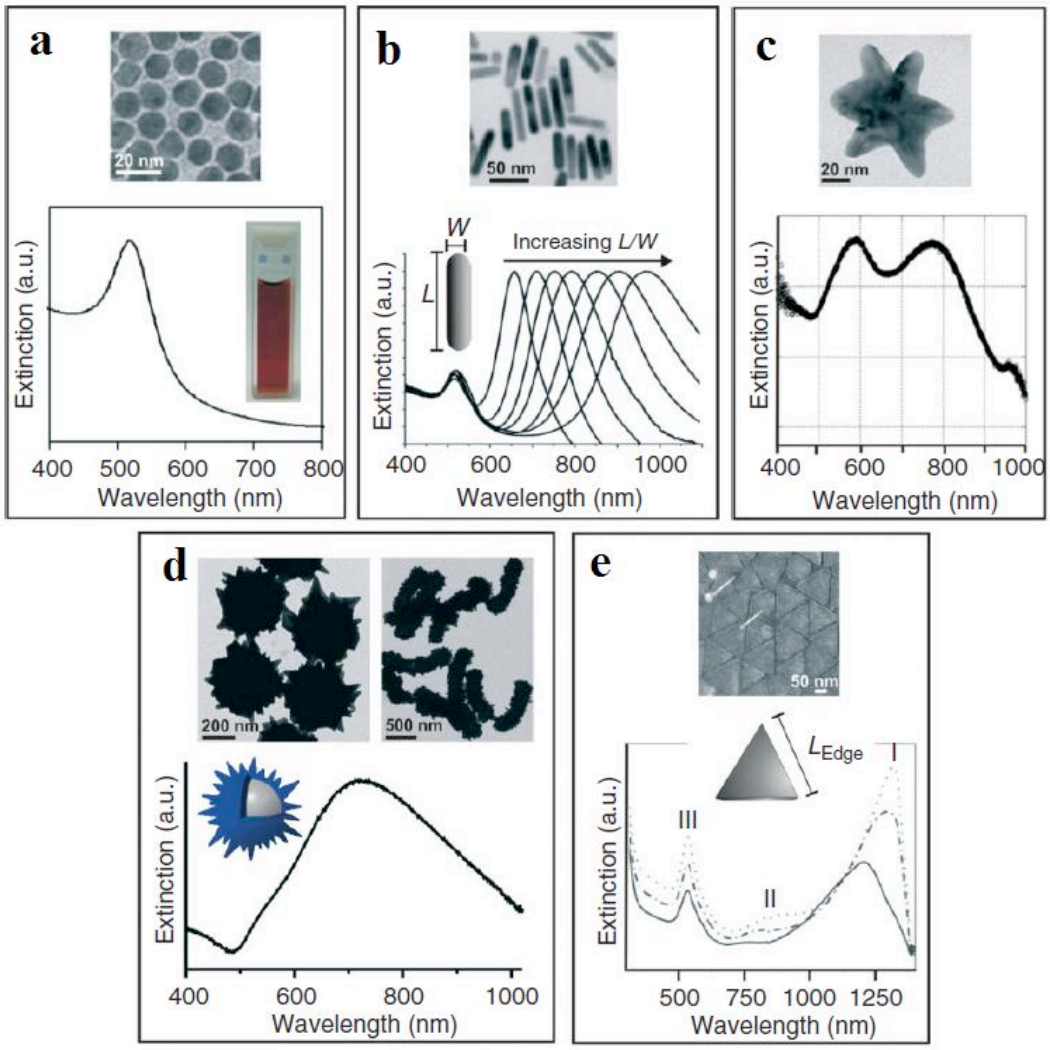

Figure 2. TEM images and extinction spectra of: a) 13 nm gold nanospheres; b) gold nanorods with different aspect ratios; c) gold nanostars; d) spiky gold nanoshells with spherical and rod cores; e) gold nanoprisms with different edge lengths.

4. Colloidal stability of gold nanoparticles

Particle size, surface composition, and density directly affect how a particle behaves in suspension. When particle size gets to about 100 nm, Brownian motion causes water molecules to collide with particles with high enough force-to-mass ratios to prevent them from settling under gravity, and a true colloidal suspension occurs [27]. The forces acting on particles in a colloidal solution mainly can be explained by the Derjaguin, Landau, Verwey, and Overbeek (DLVO) theory, which describes the attractive van der Waals forces and repulsive electrostatic forces affecting the nanoparticle stability (Derjaguin and Landau, 1941; Verwey and Overbeek, 1948). Classical DLVO theory models particles as infinitely flat solid surfaces with uniform surface charge densities. Furthermore, surface potential (i.e. zeta potential) is constant and uniform, and no chemical reactions occur between the solvent and the particles (i.e. solvent influences the solution dielectric constant only) [28-30]. This theory proposes that the nanoparticles are in an interactive regime where strong attractive forces between them can be prevented by an energy barrier resulting from electrostatic and/or steric repulsive forces.

Nanoparticle stabilization includes the following kinds: electrostatic, steric and electrosteric. Electrostatic stabilization (Figure 3, A) bases on the electrical double layer repulsion between the particles. The generation of electrostatic repulsion between charged conjugates is the most common strategy to keep NPs separated in aqueous medium and, subsequently, stable under physiological conditions [31]. For this purpose, AuNPs can be modified by different capping ligands, such as citrate [32], peptides [33, 34], short polyethylene glycol molecules containing polar groups [35] and small charged molecules [36]. A characteristic feature of electrostatic

repulsion is its high sensitivity to the bulk ionic strength; the force of electrostatic repulsion diminishes significantly at high salt concentrations, when the electric double layer is highly suppressed. This explains why citrate-capped AuNPs are stabilized in water but undergo aggregation at elevated salt concentrations (e.g., 50 mM NaCl) [37].

Steric stabilization (Figure 3, B) is achieved by the coordination of sterically bulky organic molecules that act as protective shields on the metallic surface [38-40]. In this way, nanocores are separated from each other and agglomeration is prevented. Macromolecules grafted on colloid surfaces in a “good solvent”— that is, a solvent in which steric stabilization diminishes with decreasing solubility—impart a polymeric barrier that prevents colloids from coming too close, and van der Waals attractive forces can dominate. Essentially, the penetration of polymer chains on colloids when they approach each other results in a loss of polymer configurational entropy, which disfavours the aggregation process. Steric stabilization is much less sensitive towards ionic strength than electrostatic stabilization. Rather, the molecular weight of the macromolecule and surface graft density are more important factors. In general, thicker polymer layers and higher graft densities lead to more effective steric stabilization [41]. Polymers and proteins, like BSA (bovine serum albumin), are large enough to sterically stabilize nanoparticles [42].

Electrosteric stabilization has become one of the most useful and effective method for keeping the nanoparticles stable in aqueous solution, recently (Figure 3, C). DNA (negatively charged polymer) modified AuNPs represent an excellent example of such systems. DNA-modified AuNPs with high DNA graft density remain stabilized even at very high salt concentrations (e.g., 300 mM $MgCl_2$).

Steric factors are expected to play a major role in stabilizing AuNPs at salt concentrations in which the electrostatic repulsion is significantly diminished [41]. Peptides containing charged amino acid residues and PEG molecules with polar side groups such as $–NH_2$ and –COOH, possess an excellent stabilization ability, keeping the particles from aggregation by electrosteric forces [43-45].

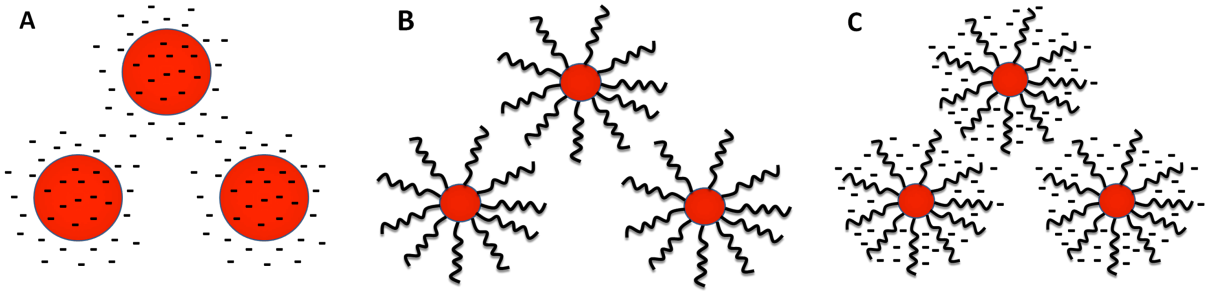

Figure 3. Schematic representation of colloidal stabilization through: A) small charged molecules on the AuNP surface (electrostatic stabilization), B) surface grafted polymers (steric stabilization), and C) surface grafted charged polymers (electrosteric stabilization).

5. Synthesis of gold nanoparticles

The generation of stable colloidal solution with particles of controlled size and shape requires a real synthetic strategy as well as a perfect knowledge of the intimate relationship existing between particle surface and stabilizing agent. The growth of gold nanoparticles persists as long as the crystallization sites are not blocked by the capping agent and as long as the gold (III) salt is available in the reaction medium. Stabilizing molecule should display a higher affinity for the particle surface than the solvent molecules, exhibit a high solubility in the reaction medium and induce mutual repulsions between particles to prevent the aggregation. Therefore, a prerequisite for stabilizing molecules is to possess at least one atom or a functional group exhibiting lone pair electrons that can ensure its binding to the gold surface [46] (Figure 4).

The range of capping agents used to stabilize and functionalize nanoparticles varies from unconventional ones, such as plants extracts (*Aloe* [47], *Cinnamomum camphora* [48] etc.), microorganisms and bacteria, to a more usual kinds, such as small organic molecules (amines [49], amino acids [50]). Polymers such as polypeptides [51-53], PEG with reactive functional groups [54-58] and proteins [59-61] are superior compared with small organic molecules, as they can form a shell around the gold particles and can provide an excellent robustness against agglomeration in various extreme conditions.

The choice of the synthesis procedure is dependent on the needed particle size. Here, the most common methods to obtain spherical gold nanoparticles are reported.

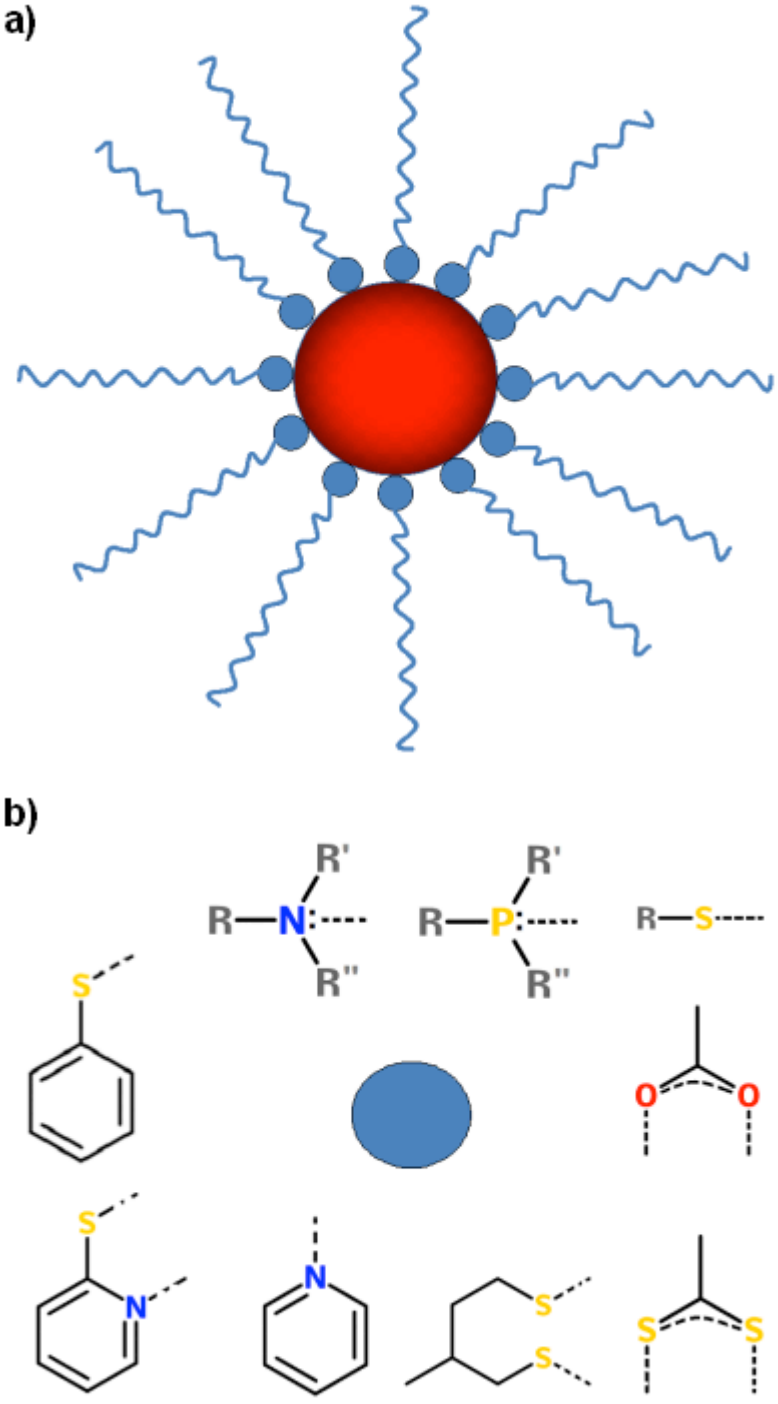

Figure 4. a) Schematic representation of a nanoparticle stabilized by a stabilizing agent; b) A series of functional end-groups commonly used for capping agents.

5.1. Turkevich-Frens method

The method pioneered by J. Turkevich et al. in 1951 [62, 63] and refined by G. Frens in 1970s [64], is one of the most frequently applied methods. Generally, it is used to produce modestly monodisperse nanoparticles of around 10–20 nm in diameter operating in the aqueous phase. The method involves the reaction of boiling chloroauric acid solution with small amounts of warm sodium citrate solution. Citrate ions act as both a reducing agent and a capping agent leading to the formation of nanoparticles.

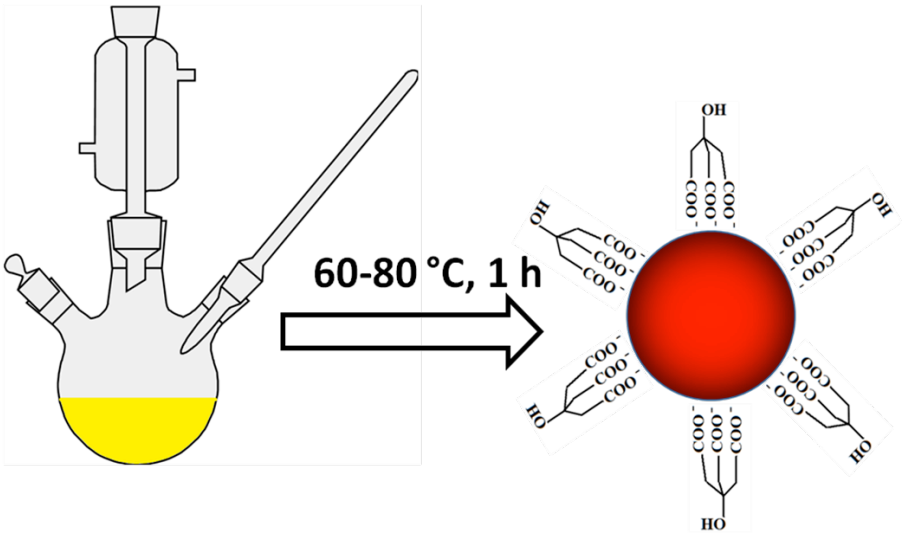

Figure 5. A schematic representation of citrate-stabilized gold nanoparticles by Turkevich-Frens method.

5.2. Brust method

Discovered by Brust and Schiffrin in early 1990s, this method can be used to produce AuNPs in organic solvents that are normally not miscible with water [65, 66]. It involves the reaction in toluene of a chloroauric acid solution with tetraoctylammonium bromide (TOAB) solution and sodium borohydride as a stabilizing and a reducing agent, respectively. The sizes of as-prepared AuNPs are around 5–6 nm. Notably, the TOAB does not bind to the gold nanoparticles particularly strongly, so particle colloid tends to aggregate gradually over the course of approximately two weeks. To prevent this, a stronger binding agent such a thiol can be added, which binds to the gold surface covalently, leading to a stable particle colloidal solution .

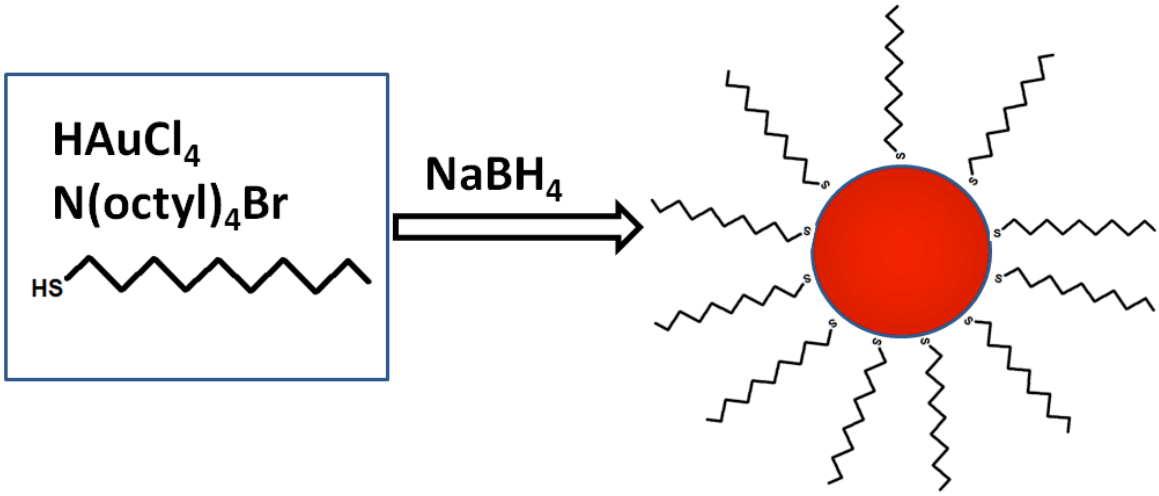

Figure 6. A schematic representation of thiol-stabilized gold nanoparticles by Brust-Schiffrin method.

5.3. Sodium borohydride reduction method

This “one-pot” method involves the reduction of a gold salt ($NaAuCl_4$) by sodium borohydride in presence of stabilizing agents of different kinds, such as simple small or large organic molecules [67, 68], peptides [69] and even proteins [70]. Sodium borohydride is a strong reducing agent capable of producing small AuNPs at room temperature. The particle size is regulated by the amount of stabilizing agent involved in the reaction and normally varies between 4 and 25 nm. The synthesis can be also performed in an organic phase, such as methanol, working with the stabilizing molecules that are not soluble in water.

6. Biomolecule-functionalized gold nanoparticles

Biological molecules have been immobilized on gold nanoparticles by a variety of techniques, including physical adsorption, electrostatic interaction, specific recognition and covalent coupling. Here, we discuss the most important approaches to obtain the gold bioconjugates.

6.1. Functionalization by electrostatic adsorption

The biomolecules ranging from low-molecular-weight organic substrates to large protein/enzyme molecules can interact electrostatically with the anionic ligands such as carboxylic acids (citrate, tartrate, lipoic acid) stabilizing the nanoparticles. For example, setting up the pH of AuNPs prepared by citrate reduction slightly above the isoelectric point of the citrate ligand, allows effective binding between the positively charged amino acid side chains of the peptides and proteins and the negatively charged citrate groups on the nanoparticles [71, 72].

6.2. Functionalization by chemisorption of thiol-derivatized biomolecules

Strong chemisorptions of biomolecules on AuNPs can originate from the binding of thiol groups, for example, from cysteine residues in peptides and proteins [73-75]. DNA molecules functionalized with a steroid-disulfide derivative can readily bind to AuNPs and demonstrate higher adsorption stability because two sulphur atoms of the disulfide anchor group are involved in the attachment process [76, 77]. Enhanced binding of nucleic acids to metal nanoparticles may be accomplished by the use of oligonucleotides that include several adenosyl phosphothiolate residues at

their ends, thus enabling multi-point attachment to the NPs [78].

6.3. Functionalization by specific interactions

The AuNPs can be functionalized with groups such as low-molecular bifunctional linkers that have anchor groups for attachment to nanoparticle surface and functional groups for further covalent coupling to the target biomolecules. Anchor groups such as thiols, disulfides, or phosphane ligands are often used for the binding of the bifunctional linkers to AuNPs, being able to readily substitute weakly adsorbed molecules stabilizing the nanoparticles, or may be incorporated in the nanoparticle synthesis, resulting in a particle surface providing functional groups for further reactions [79-82]. A wide variety of terminal functional groups is available in different bifunctional linkers: amino, active ester, and maleimide groups are used for the covalent coupling of biological compounds by means of carbodiimide-mediated esterification and amidation, or reaction with thiol groups. Biotin-streptavidin interaction is another potential tool to be applied for AuNPs: the binding affinity between the two molecules is very high (($K_a \sim 10^{13}$ M^{-1}) and is considered one of the strongest receptor−ligand interactions found in nature. This high binding affinity, the symmetry of the biotin-binding pockets which are positioned in pairs at opposite faces of the protein, and the ease of functionalization of diverse biomolecules (e.g., antibodies, peptides, and nucleotides) with biotin make the streptavidin−biotin system extremely useful in a wide range of biotechnological applications [83]. Thus, applying this approach to the AuNPs and modifying the gold surface with streptavidin, plenty of biotin-containing biomolecules can be conjugated [84].

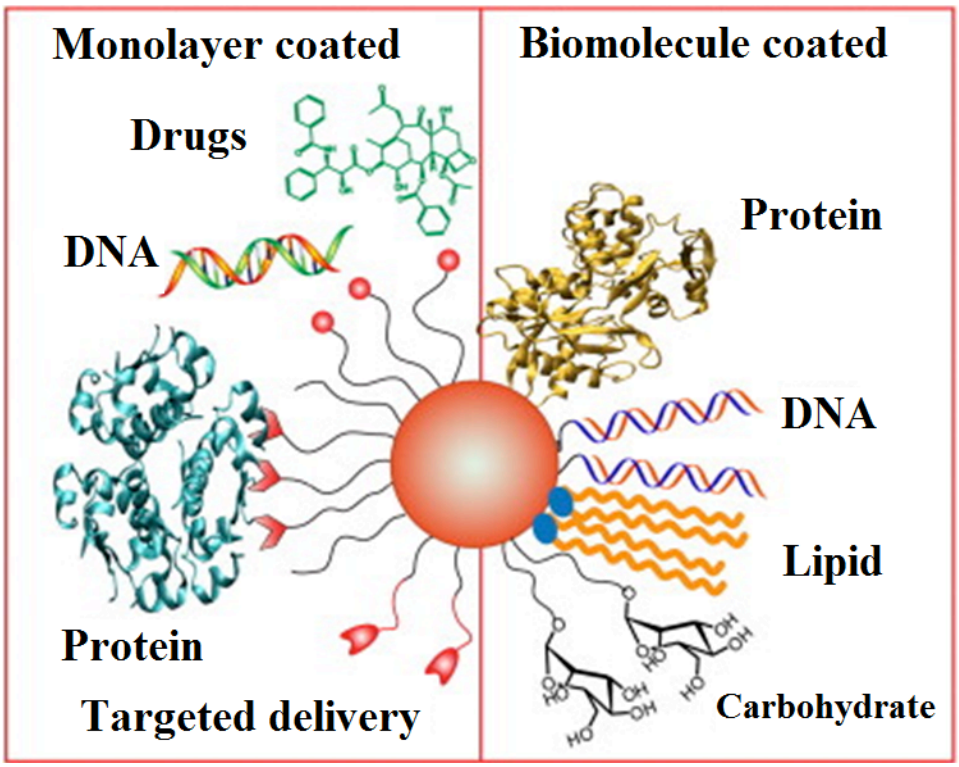

Figure 7. Functionalization of gold nanoparticles: specific interactions and biomolecules monolayer on the particle surface.

7. Application of gold nanoparticles

7.1. Gold nanoparticles as drug delivery systems

AuNPs are found to be attractive platforms for the delivery of increasingly potent, selective, and multifunctional anti-cancer drug conjugates [85, 86]. Drug delivery systems (DDSs) can improve several crucial properties of ‘‘free’’ drugs, such as solubility, in vivo stability, pharmacokinetics, and biodistribution, enhancing their efficacy. Moreover, nanoparticles can provide effective carriers for biomolecules such as DNA, RNA, or proteins, protecting these materials from degradation and transporting them across the cell-membrane barrier. Thiol-PEGylated AuNPs functionalized by tumor therapeutic agents such as paclitaxel [86, 87], anthracycline [88], doxorubicin [89-94] were proved to be efficiently delivered into cancer cells. For successful delivery, carriers must: (a) form condensed complexes with biomolecules, (b) facilitate penetration of the cell membrane after complexation, and (c) unload their payloads inside of cells. Two approaches to serve this purpose are ‘‘passive’’ and ‘‘active’’ targeting. Passive targeting relies on the homing of the carriers to infected tissues. On the other hand, active targeting relies on specific recognition of the ligands that are displayed on delivery vehicles by cell surface receptors. The ligand used for active targeting can be a small molecule, or a peptide or protein [95]. A key goal of delivery systems is to discharge their payloads specifically at the diseased tissue. The release could be triggered by internal (e.g. glutathione (GSH), or pH or external (e.g. light) stimuli. Significantly the internal stimuli operate in a biologically control manner, whereas the external stimuli provide spatio-temporal control over the release [96].

7.2. Gold nanoparticles for photothermal cancer therapy

AuNPs can resonantly absorb and scatter incident light upon excitation of their surface plasmon oscillations typically in the visible range, with their absorption cross sections orders of magnitude larger than those of strongly absorbing organic molecules. In addition, photon energies that are absorbed by AuNPs can be efficiently converted into heat on a picosecond time scale, as a result of electron-phonon and phonon-phonon processes. Thus, AuNPs can be a highly potent photothermal therapeutic agent, by exploiting their strong absorptions and efficient heat conversions [97-100].

Photothermal therapy using spherical AuNPs can be achieved with pulsed or cw (continuous wave) visible lasers due to the SPR absorption in the visible region and thus such treatment is suitable for shallow cancer (e.g. skin cancer). The first thorough study using pulsed laser and gold nanospheres was performed in 2003 by Lin and co-workers for selective and highly localized photothermolysis of targeted lymphocyte cells [101]. Lymphocytes incubated with AnNPs conjugated to antibodies were exposed to nanosecond laser pulses and showed cell death with 100 laser pulses. Adjacent cells just a few micrometers away without nanoparticles remained viable. Their numerical calculations showed that the peak temperature lasting for nanoseconds under a single pulse exceeds 2000 K with a heat fluid layer of 15 nm. The cell death is attributed mainly to the cavitation damage induced by the generated micro-scale bubbles around the nanoparticles. So far, the use of spherical AuNPs in such an application has not been made, first of all because of their limited tissue penetration, which confines their applicability mostly to melanoma. However, the AuNPs of different forms, such as core-shell nanoparticles with ferromagnetic

properties [102], nanorods [103], nanocages [104], nanostars [105] and even popcorn-shaped gold nanoparticles [106] are being tried to be used as photothermal therapy agents using different cancer cell lines.

7.3. Cancer imaging

As I have already mentioned in a previous section, the scattering properties of gold colloids depend on the size, shape and structure of the nanoparticles. Typically, particles of 30–100 nm diameters scatter intensely and can be easily detected by a commercial microscope under dark-field illumination conditions. In fact, 40 nm AuNPs can be easily detected by eye down to a particle concentration of 10^{-14} M. Likewise, the scattering from a 60 nm AuNPs is 10^5 stronger than the emission of a fluorescein molecule [107]. The high scattering cross-sections of AuNPs together with their superior photostability (as compared to organic dyes) make them extremely promising for cellular imaging.

Standard clinical imaging modalities such as X-ray based computer tomography (CT), magnetic resonance imaging, and ultrasound are able to provide basic information regarding tumor location, size and spread. However, these methods are not efficient in detecting tumors and metastases smaller than 0.5 cm and they can barely distinguish between benign and cancerous tumors [108].

Present CT contrast agents based on iodine containing molecules are effective in absorbing X-rays, however, they have a number of limitations: nonspecific targeting, because of their inability to be conjugated to most biological components or cancer markers; they allow only very short imaging times due to rapid clearance by the kidneys.

On the other hand, gold induces a strong X-ray attenuation, having unique physical, chemical, and biological properties, which make them an ideal candidate for CT contrast agents [109, 110].In addition, AuNPs provide a high degree of flexibility in terms of functional groups for coating and targeting and have also proved to be nontoxic and biocompatible *in vivo*.

The feasibility of AuNPs for cancer imaging has been demonstrated in recent years. In the earlier attempts by Sokolov *et al*, the scattered light is collected in a reflection mode under single laser wavelength excitation using a confocal microscope or simply a laser pen [111]. An improvement of the cancer imaging based on the scattering properties of AuNPs was made by El-Sayed *et al.* using dark field microscopy in 2005 [112]. In this case, the nanoparticles are excited by the white light from a halogen lamp which is also the same lamp used for bright field imaging. As the nanoparticles scatter light most strongly at the wavelength of the SPR maximum, the nanoparticles appears in brilliant colour that depends on the size and shape of the particles [15]. Bischof *et al.* demonstrated the use of confocal Raman microscopy to measure the localization of AuNPs with nanoscale resolution. Raman laser interaction with AuNPs inside cells shown unique spectroscopic features corresponding to the different intracellular localizations of AuNPs, proving to be a potential technique for cancer cells imaging [113].

7.4. Cellular targeting

The targeted delivery of nanoparticles to solid tumors is a key task in the development of cancer nanomedicine for *in vivo* molecular imaging and targeted therapy. “Passive” and “active” targeting are two approaches used for tumor targeting. Active targeting relies on specific recognition of the ligands that are displayed on nanoparticles by cell surface receptors, often followed by receptor-mediate endocytosis and nanoparticle internalization [114]. Biomolecules of interest may include one or more of the following: peptides, proteins and antibodies; enzymes, oligonucleotides and aptamers; drugs or other biologically active small molecules; reporter molecules or contrast agents, e.g., radiolabels or fluorescent dyes. On the other hand, in the passive mode, nanoparticles without targeting ligands are accumulated and retained in the tumor interstitial space mainly through the enhanced permeability and retention effect [115, 116]. In both mechanisms, a common feature is that nanoparticles in the blood stream must first move across the tumor blood vessels (usually leaky vasculatures) and extravasate into the tumor interstitium or the perivascular region [117]. Albericio *et al.* functionalized AuNPs with both a targeting peptide and a drug peptide ligand with the aim to improve not only the selectivity of the conjugates *via* a higher capacity to enter the cells, but also their antitumor activity over the free drug via increase of its local concentration [118]. Nam *et al.* used cyclic RGD-PEGylated AuNPs with directly labeled radioactive iodine as molecular imaging probes for tumor sites, taking advantage that radioactive iodine has a sensitivity of 10^{-10}-10^{-11} M for *in vivo* imaging, and finding out that the probes can target tumor sites *via* integrin receptor recognition only after 10 min from intravenous injection. Interestingly, TEM and radio-TLC analysis of urine samples

suggested the ability of these nanoparticles to go through renal filtration and be excreted from the body [119]. El-Sayed and co-workers in their recent paper report on the prostate cancer targeting: AuNPs conjugated with antiandrogen chemotherapeutics target membrane androgen receptor and androgen-sensing G protein-coupled receptor, involved in prostate cancer growth and progression [120]. Eck *et al.* applied antibody-conjugated AuNPs as contrast agent for X-ray computer tomography with the aim of tumor targeting: a heterobifunctional PEG ligand was used for stabilization, while an anti-mouse CD4 monoclonal antibody was coupled to the PEG molecules using a NHS/EDC coupling reactions for CD4-receptor recognition [121]. Finally, DNA- and RNA-conjugated AuNPs were found to be taken up by HeLa cells in serum-free culture by a process involving receptor-mediated endocytosis primarily mediated by scavenger receptors, a class of pattern-recognition receptors [122]. Here we have nominated only most important examples of AuNPs application in biology and nanomedicine: this field is continuosly being developing and, hopefully, soon will bring to *in vivo tests* on humans.

8. References

1. W. Chen, D. P. Cormode, Z. A. Fayad, and W. J. M. Mulder. *Wiley Int. Rev.: Nanomedicine and Nanobiotechnology*, 2011, **3** (2), 146–161.
2. A. Jakhmola, N. Anton, and T. F. Vandamme. *Advanced Healthcare Materials*, 2012, **1** (4), 413–431.
3. P. A. Jarzyna, A. Gianella, T. Skajaa, G. Knudsen, L. H. Deddens, D. P. Cormode, Z. A. Fayad, and W. J. M. Mulder. *Wiley Int. Rev.: Nanomedicine and Nanobiotechnology*, 2010, **2** (2), 138–150.
4. G. Peng, U. Tisch, O. Adams, M. Hakim, N. Shehada, Y. Y. Broza, S. Billan, R. Abdah-Bortnyak, A. Kuten, and H. Haick. *Nature Nanotechnology*, 2009, **4**, 669-673.
5. R.-M. Kong, X.-B. Zhang, Z. Chen, and W. Tan. *Small*, 2011, **7** (17), 2428–2436; L. M. Bellan, D. Wu, and R. S. Langer. *Wiley Int. Rev.: Nanomedicine and Nanobiotechnology*, 2011, **3** (3), 229–246.
6. J. B. Haun, N. K. Devaraj, A. Hilderbrand, H. Lee, and R. Weissleder. *Nature Nanotechnology*, 2010, **5**, 660-665.
7. A. Nasrolahi Shirazi, D. Mandal, R. K. Tiwari, L. Guo, W. Lu, and K. Parang*. Mol. Pharmaceutics*, Article ASAP, **DOI:** 10.1021/mp300448k.
8. J. Song, J. Zhou, and H. Duan. *J. Am. Chem. Soc.*, 2012, **134** (32), 13458–13469.
9. J.-M. Shen, X.-M. Guan, X.-Y. Liu, J.-F. Lan, T. Cheng, and H.-X. Zhang. *Bioconjugate Chem.*, 2012, **23** (5), 1010–1021.
10. T. K. Sau, A. L. Rogach, F. Jäckel, T. A. Klar, and J. Feldmann. *Advanced Materials*, 2010, **22** (16), 1805–1825.

11. Characterization of nanoparticles Intended for Drug Delivery, Edited by S. E. McNeil, Humana Press, Springer Science+Business Media, LLC 2011.
12. R. A. Sperling, P. R. Gil, F. Zhang, M. Zanella, and W. J. Parak. *Chem. Soc. Rev*., 2008, **37**, 1896–1908.
13. D. A. Giljohann, D. S. Seferos, W. L. Daniel, M. D. Massich, P. C. Patel, and C. A. Mirkin. *Angewandte Chemie, International Edition*, 2010, **49** (19), 3280-3294.
14. K. Saha, S. S. Agasti, C. Kim, X. Li, and V. M. Rotello. *Chemical Reviews,* 2012, **112** (5), 2739-2779.
15. X. Huang, and M. A. El-Sayed. *Journal of Advanced Research*, 2010, **1** (1), 13–28.
16. a) L. M. Liz-Marzán. *Langmuir*, 2006, **22** (1), 32–41; b) J. Lv, L. Jiang, C. Li, X. Liu, M. Yuan, J. Xu, W. Zhou, Y. Song, H. Liu, Y. Li, and D. Zhu. *Langmuir*, 2008, **24** (15), 8297–8302.
17. P. K. Jain, and M. A. El-Sayed. *J. Phys. Chem. C*, 2007, **111** (47), 17451–17454.
18. C. Noguez. *J. Phys. Chem. C*, 2007, **111** (10), 3806–3819.
19. P. K. Jain, M. A. El-Sayed. *Nano Lett*, 2007, **7** (9), 2854–2858.
20. J. Chen, B. Wiley,Z. Y. Li, D. Campbell, F. Saeki, H. Cang, L. Au, J. Lee, X. Li, Y. Xia. *Adv Mater*, 2005, **17** (18), 2255–2261.
21. Ž. Krpetić, S. Saleemi, I. A. Prior, V. Sée, R. Qureshi, and M. Brust. *ACS Nano*, 2011, **5** (6), 5195–5201.
22. G. J. Nusz, A. C. Curry, S. M. Marinakos, A. Wax, and A. Chilkoti. *ACS Nano*, 2009, **3** (4), 795–806.
23. S. K. Dondapati, T. K. Sau, C. Hrelescu, T. A. Klar, F. D. Stefani, and J. Feldmann. *ACS Nano*, 2010, **4** (11), 6318–6322.

24. D. Aili, P. Gryko, B. Sepulveda, J. A. G. Dick, N. Kirby, R. Heenan, L. Baltzer, B. Liedberg, M. P. Ryan, and M. M. Stevens. *Nano Lett.*, **2011**, 11 (12), 5564–5573.

25. S. Wang, K.-J. Chen, T.-H. Wu, H. Wang, W.-Y. Lin, M. Ohashi, P.-Y. Chiou, H.-R. Tseng. *Angew. Chem. Int. Ed.* 2010, **49** (22), 3777–3781.

26. H. Ke, J. Wang, Z. Dai, Y. Jin, E. Qu, Z. Xing, C. Guo, X. Yue, J. Liu. *Angew. Chem. Int. Ed.* 2011, **50** (13), 3017–3021.

27. G. T. Hermanson, Bioconjugate techniques, Second edition, Academic press, 2008.

28. R. J. Hunter, Zeta Potential in Colloid Science, Academic Press, New York, 1981.

29. P. C. Hiemenz, Principles of Colloid and Surface Chemistry, Marcel Dekker, New York, 1977.

30. J. T. G. Overbeek, *J. Colloid Interf. Sci.* 1977, **58**, 408-422.

31. I. Ojea-Jiménez, and V. Puntes. *J. Am. Chem. Soc.*, 2009, **131** (37), 13320–13327.

32. J. L.Plaza, P. M. Mendes, S. Diegoli, Y. Chen, J. A. Preece, and R. E. Palmer. *J. of Nanoscience and Nanotechnology*, 2005, **5** (11), 1826-1831(6).

33. R. Lévy, N. T. K. Thanh, R. C. Doty, I. Hussain, R. J. Nichols, D. J. Schiffrin, M. Brust, and D. G. Fernig. *J. Am. Chem. Soc.*, 2004, **126** (32), 10076–10084.

34. D. Aili, K. Enander, J. Rydberg, I. Nesterenko, F. Björefors, L. Baltzer, and B. Liedberg. *J. Am. Chem. Soc.*, 2008, **130** (17), 5780–5788.

35. A. S. Karakoti, S. Das, S. Thevuthasan, and S. Seal. *Angew. Chem. Int. Ed.* 2011, **50** (9), 1980-1994.

36. S. Avvakumova, G. Scari, and F. Porta. *RSC Adv.*, 2012, **2**, 3658-3661.

37. I. Capek. *Adv Colloid Interface Sci.* 2011, **163** (2), 123-143.

38. D. H. Napper. Polymeric Stabilization of Colloidal Dispersions, Academic Press, New York, 1983.

39. W. B. Russel, D. A. Saville, and W. R. Schowalter. Colloidal Dispersions, Cambridge University Press, Cambridge, 1991.

40. P. Somasundaran, B. Markovic, S. Krishnakumar, and X. Yu. Handbook of Surface and Colloid Chemistry, ed. K.S. Birdi, CRC Press, Boca Raton, FL, 1997.

41. W. Zhao, M. A. Brook, Y. Li. *ChemBioChem,* 2008, **9** (15) 2363–2371.

42. E. D. Kaufman, J. Belyea, M. C. Johnson, Z. M. Nicholson, J. L. Ricks, P. K. Shah, M. Bayless, T. Pettersson, Z. Feldotö, E. Blomberg, P. Claesson, and S. Franzen. *Langmuir*, 2007, **23** (11), 6053–6062.

43. X. Qian, X.-H. Peng, D. O Ansari, Q. Yin-Goen, G. Z Chen, D. M Shin, L. Yang, A. N Young, M. D Wang, anf S. Nie. *Nature Biotechnology,* 2008. **26**, 83-90.

44. J. M. Slocik, J. S. Zabinski Jr., D. M. Phillips, R. R. Naik. *Small*, 2008, **4** (5), 548–551.

45. C. M. Goodman, C. D. McCusker, T. Yilmaz, and V. M. Rotello. *Bioconjugate Chem.*, 2004, **15** (4), 897–900.

46. F. Dumur, A. Guerlin, E. Dumas, D. Bertin, D. Gigmes, and C. R. Mayer. *Gold Bulletin,* 2011, **44** (2), 119-137.

47. Ž. Krpetić, G. Scarì, E. Caneva, G. Speranza, and F. Porta. *Langmuir*, 2009, **25** (13), 7217–7221.

48. J. Huang, Q. Li, D. Sun, Y. Lu, Y. Su, X. Yang, H. Wang, Y. Wang, W. Shao, N. He, J. Hong, and C. Chen. *Nanotechnology*, 2007, **18,** 105104 (11pp).

49. F. Porta, Ž. Krpetić, L. Prati, A. Gasassi, and G. Scarì. *Langmuir*, 2008, **24** (14), 7061–7064.

50. P. S. Ghosh, C.-K. Kim, G. Han, N. S. Forbes, and V. M. Rotello. *ACS Nano*, 2008, **2** (11), 2213–2218.

51. Ž. Krpetić, P. Nativo, F. Porta, and M. Brust. *Bioconjugate Chem.*, 2009, **20** (3), 619–624.

52. Z. Wang, R. Lévy, D. G. Fernig, and M. Brust. *Bioconjugate Chem.*, 2005, **16** (3), 497–500.

53. C. P. Shaw, D. A. Middleton, M. Volk, and R. Lévy. *ACS Nano*, 2012, **6** (2), 1416–1426.

54. Ž. Krpetić, S. Saleemi, I. A. Prior, V. Sée, R. Qureshi, and M. Brust. *ACS Nano*, 2011, **5** (6), 5195–5201.

55. T. Liu, and B. Thierry. *Langmuir*, Articles ASAP, **DOI:** 10.1021/la301390u

56. N. B. Shah, G. M. Vercellotti, J. G. White, A. Fegan, C. R. Wagner, and J. C. Bischof. *Mol. Pharmaceutics*, 2012, **9** (8), 2146–2155.

57. J. Zhu, C. Waengler, R. B. Lennox, and R. Schirrmacher. *Langmuir*, 2012, **28** (13), 5508–5512.

58. J. Gao, X. Huang, H. Liu, F. Zan, and J. Ren. *Langmuir*, 2012, **28** (9), 4464–4471.

59. D.-H. Tsai, F. W. DelRio, A. M. Keene, K. M. Tyner, R. I. MacCuspie, T. J. Cho, M. R. Zachariah, and V. A. Hackley. *Langmuir*, 2011, **27** (6), 2464–2477.

60. A. M. W. Reed, and S. J. Metallo. *Langmuir*, 2010, **26** (24), 18945–18950.

61. I.-H. Lee, H.-K. Kwon, S. An, D. Kim, S. Kim, M. K. Yu, J.-H. Lee, T.-S. Lee, S.-H. Im, S. Jon. *Angew. Chem. Int. Ed.* 2012, **124** (35), 8930-8935.

62. J. Turkevich, P. Cooper Stevenson, and J. Hillier. *Discuss. Faraday Soc.*, 1951, **11**, 55-75.

63. J. Turkevich, P. C. Stevenson, and J. Hillier. *J. Phys. Chem.*, 1953, **57** (7), 670–673.

64. G. Frens. *Nature Physical Science,* 1973, **241**, 20-22.

65. M. Brust, M. Walker, D. Bethell, D. J. Schiffrin, and R. Whyman. *J. Chem. Soc., Chem. Commun.*, 1994, 801-802.

66. A. G. Kanaras, F. S. Kamounah, K. Schaumburg, C. J. Kiely, and M. Brust. *Chem. Commun.*, 2002, 2294-2295.

67. K. B. Male, J. Li, C. Chi Bun, S.-C. Ng, and J. H. T. Luong. *J. Phys. Chem. C*, 2008, **112** (2), 443–451.

68. S. R. Isaacs, E. C. Cutler, J.-S. Park, T. R. Lee, and Y.-S. Shon. *Langmuir*, 2005, **21** (13), 5689–5692.

69. G. Scarì, F. Porta, U. Fascio, S. Avvakumova, V. Dal Santo, M. De Simone, M. Saviano, M. Leone, A. Del Gatto, C. Pedone and L. Zaccaro. *Bioconjugate Chem.*, 2012, **23** (3), 340–349.

70. M. Colombo, S. Mazzucchelli, V. Collico, S. Avvakumova, L. Pandolfi, F. Corsi, F. Porta and D. Prosperi. *Ang. Chem. Int. Ed.*, 2012, **37** (51), 9272–9275.

71. S. H. Brewer, W. R. Glomm, M. C. Johnson, M. K. Knag, and S. Franzen. *Langmuir*, 2005, **21** (20), 9303–9307.

72. W. R. Glomm, Ø. Halskau, Jr., A.-M. D. Hanneseth, and S. Volden. *J. Phys. Chem. B*, 2007, **111** (51), 14329–14345.

73. Q. Qian, J. Deng, D. Wang, L. Yang, P. Yu, and L. Mao. *Anal. Chem.*, Article ASAP, **DOI:**10.1021/ac3024608

74. R. P. Brinãs, A. Sundgren, P. Sahoo, S. Morey, K. Rittenhouse-Olson, G. E. Wilding, W. Deng, and J. J. Barchi. *Bioconjugate Chem.*, 2012, **23** (8), 1513–

1523.

75. L. J. Cruz, F. Rueda, B. Cordobilla, L. Simón, L. Hosta, F. Albericio, and J. Carles Domingo. *Mol. Pharmaceutics*, 2011, ***8*** (1), 104–116.

76. P. Sandström, M. Boncheva, and B. Åkerman. *Langmuir*, 2003, **19** (18), 7537–7543.

77. N. Bhatt, P. J. Huang, N. Dave, and J. Liu. *Langmuir*, 2011, **27** (10), 6132-6127.

78. R. L. Letsinger, R. Elghanian, G. Viswanadham, and C. A. Mirkin. *Bioconjugate Chem.*, 2000, **11** (2), 289–291.

79. L. Castaneda, J. Valle, N. Yang, S. Pluskat, and K. Slowinska. *Biomacromolecules*, 2008, **9** (12), 3383–3388.

80. D. Bartczak, and A. G. Kanaras. *Langmuir*, 2011, **27** (16), 10119–10123.

81. X.-Q. Zhang, X. Xu, R. Lam, D. Giljohann, D. Ho, and C. A. Mirkin. *ACS Nano*, 2011, **5** (9), 6962–6970.

82. L. Maus, O. Dick, H. Bading, J. P. Spatz, and R. Fiammengo. *ACS Nano*, 2010, **4** (11), 6617–6628.

83. V. H. Pérez-Luna, M. J. O'Brien, K. A. Opperman, P. D. Hampton, G. P. López, L. A. Klumb, and P. S. Stayton. *J. Am. Chem. Soc.*, 1999, **121** (27), 6469–6478.

84. M. S. Wang, and S. M. Reed. Electrophoresis, 2012, **33** (2), 348–351.

85. G. E. Craig, S. D. Brown, D. A. Lamprou, D. Graham, and N. J. Wheate. *Inorg. Chem.*, 2012, **51** (6), 3490–3497.

86. J. D. Gibson, B. P. Khanal, and E. R. Zubarev. *J. Am. Chem. Soc.*, 2007, **129** (37), 11653–11661.

87. X.-Q. Zhang, X. Xu, R. Lam, D. Giljohann, D. Ho, and C. A. Mirkin. *ACS Nano*, 2011, **5** (9), 6962–6970.

88. J. You, G. Zhang, and C. Li, *ACS Nano*, 2010, **4**, 1033-1041.

89. B. Asadishad, M. Vossoughi, and I. Alemzadeh. *Ind. Eng. Chem. Res.*, 2010, **49** (4), 1958–1963.

90. F. Wang, Y.-C. Wang, S. Dou, M.-H. Xiong, T.-M. Sun, and J. Wang. *ACS Nano*, 2011, **5** (5), 3679–3692.

91. H. Park, J. Yang, J. Lee, S. Haam, I.-H. Choi, and K.-H. Yoo. *ACS Nano*, 2009, **3** (10), 2919–2926.

92. X. Zhang, H. Chibli, R. Mielke, and J. Nadeau. *Bioconjugate Chem.*, 2011, **22** (2), 235–243.

93. C. M. Alexander, J. C. Dabrowiak, and M. M. Maye. *Bioconjugate Chem.*, 2012, **23** (10), 2061–2070.

94. Y.-L. Luo, Y.-S. Shiao, and Y.-F. Huang. *ACS Nano*, **2011**, 5 (10), 7796–7804.

95. M. De, P. S. Ghosh, V. M. Rotello. *Advanced Materials,* 2008*,* **20** (22), 4225–4241.

96. P. Ghosh, G. Han, M. De, C. K. Kim, and V. M. Rotello. *Adv. Drug Deliv. Rev.,* 2008*,* **60** (11), 1307–1315.

97. J. Nam, N. Won, H. Jin, H. Chung, and S. Kim. *J. Am. Chem. Soc.*, 2009, **131** (38), 13639–13645.

98. B. N. Khlebtsov, E. V. Panfilova, G. S. Terentyuk, I. L. Maksimova, A. V. Ivanov, and N. G. Khlebtsov. *Langmuir*, 2012, **28** (24), 8994–9002.

99. Y. Haba, C. Kojima, A. Harada, T. Ura, H. Horinaka, and K. Kono. *Langmuir*, 2007, **23** (10), 5243–5246.

100. S. Ibrahimkutty, J. Kim, M. Cammarata, F. Ewald, J. Choi, H. Ihee, and A. Plech. *ACS Nano*, 2011, **5** (5), 3788–3794.

101. C. M. Pitsillides, E. K. Joe, X. Wei, R. R. Anderson, and C. P. Lin. *Biophys J.*, 2003, **84** (6), 4023–4032.

102. J. Ren, S. Shen, Z. Pang, X. Lu, C. Deng, and X. Jiang. *Chem. Commun.*, 2011,**47**, 11692-11694.

103. J. Wang, G. Zhu, M. You, E. Song, M. I. Shukoor, K. Zhang, M. B. Altman, Y. Chen, Z. Zhu, C. Z. Huang, and W. Tan. *ACS Nano*, **2012**, 6 (6), 5070–5077.

104. J. Chen, C. Glaus, R. Laforest, Q. Zhang, M. Yang, M. Gidding, M. J. Welch, and Y. Xia. *Small*, 2010, **6** (7), 811–817.

105. L.-C. Cheng, J.-H. Huang, H. M. Chen, T.-C. Lai, K.-Y. Yang, R.-S. Liu, M. Hsiao, C.-H. Chen, L.-J. Her, and D. P. Tsai. *J. Mater. Chem.*, 2012, **22**, 2244-2253.

106. S. A. Khan, A. K. Singh, D. Senapati, Z. Fan, and P. C. Ray. *J. Mater. Chem.*, 2011, **21**, 17705-17709.

107. T. Lan, C. Q. Dong, X. Y. Huang, and J. C. Ren. *Analyst,* 2011, **136**, 4247−4253.

108. R. Popovtzer, A. Agrawal, N. A. Kotov, A. Popovtzer, J. Balter, T. E. Carey, and R. Kopelman. *Nano Lett.*, 2008, **8** (12), 4593–4596.

109. D. Kim, S. Park, J. H. Lee, Y. Y. Jeong, and S. Jon. *J. Am. Chem. Soc.*, 2007, **129** (24), 7661–7665.

110. R. Guo, H. Wang, C. Peng, M. Shen, M. Pan, X. Cao, G. Zhang, and X. Shi. *J. Phys. Chem. C*, 2010, **114** (1), 50–56.

111. S. Mallidi, T. Larson, J. Tam, P. P. Joshi, A. Karpiouk, K. Sokolov, and S. Emelianov. *Nano Lett.*, 2009, **9** (8), 2825–2831.

112. I. H. El-Sayed, X. Huang, and M. A. El-Sayed. *Nano Lett.*, 2005, **5** (5), 829–834.

113. N. B. Shah, J. Dong, and J. C. Bischof. *Mol. Pharmaceutics*, 2011, **8** (1), 176–184.

114. M. K. Yu, J. Park, and S. Jon. *Theranostics,* 2012, **2** (1), 3-44.

115. A. K. Iyer, G. Khaled, J. Fang, and H. Maeda. *Drug Discovery Today,* 2006, **11** (17–18), 812–818.

116. H. Maeda, J. Wu, T. Sawa, Y. Matsumura, K. Hori. *Journal of Controlled Release,* 2000, **65** (1–2), 271–284.

117. X. Huang, X. Peng, Y. Wang, Y. Wang, D. M. Shin, M. A. El-Sayed, and S. Nie. *ACS Nano*, 2010, **4** (10), 5887–5896.

118. L. Hosta-Rigau, I. Olmedo, J. Arbiol, L. J. Cruz, M. J. Kogan,and F. Albericio. *Bioconjugate Chem.*, 2010, **21** (6), 1070–1078.

119. Y.-H. Kim, J. Jeon, S. H. Hong, W.-K. Rhim, Y.-S. Lee, H. Youn, J.-K. Chung, M. C. Lee, D. S. Lee, K. W. Kang, and J.-M. Nam. *Small,* 2011, 7 (14), 2052-2060.

120. E. C Dreaden, B. E Gryder, L. A Austin, B. A Tene Defo, S. C Hayden, M. Pi, L. D Quarles, A. K Oyelere, and M. A. El-Sayed. *Bioconjug. Chem.* 2012, **23**(8), 1507-1512.

121. W. Eck, A. I. Nicholson, H. Zentgraf, W. Semmler, and S. Bartling. *Nano Lett.*, 2010, **10** (7), 2318–2322.

122. P. C. Patel, D. A. Giljohann, W. L. Daniel, D. Zheng, A. E. Prigodich, and C. A. Mirkin. *Bioconjugate Chem.*, 2010, **21** (12), 2250–2256.

Chapter II

Materials and Methods

1. Characterization challenges

A rational characterization strategy for bioconjugated nanoparticles contains three elements: physicochemical characterization, *in vitro* assays, and *in vivo* studies. Each of these is essential to a comprehensive understanding of nanoparticle safety and efficacy. However, physicochemical characterization plays a key role in the interpretation of *in vitro* or *in vivo* biological data. While testing *in vitro* physiological models can give an initial estimate of formulation efficacy and toxicity. The approaches traditionally used for small molecules to ascertain their physicochemical properties, can be perfectly applied for nanoconjugates. Techniques like nuclear magnetic resonance (NMR), mass spectrometry, ultraviolet-visible (UV-vis) spectroscopy, infrared spectroscopy (IR) can be run in a high-throughput fashion to analyze the molecule-nanoparticle interactions. The nanoconjugates properties, such as composition, purity, stability, influence biological activity, and may depend on parameters such as particle size, size distribution, surface area, surface charge, surface functionality, shape, and aggregation state. Additionally, since many nanoparticle concepts are multifunctional (with targeting, imaging, and therapeutic components), the stability and distribution of these components can have dramatic effects on nanoparticle biological activity as well.

Physicochemical characterization of properties such as size, surface area, surface chemistry, and aggregation state can provide the basis for better understanding of structure–activity relationships. Determination of nanoparticle size in solution by dynamic light scattering (DLS), surface charge through zeta potential

measurements, core diameter by transmission electron microscopy (TEM) are some of the up-to-date methods widely used for characterization of nanoconjugates.

Another important and challenging area of nanoparticle characterization is measurement under physiological conditions that resembles or mimics the physical state *in vivo*. Many properties of nanoparticles are environment and condition dependent; for example, the particle's hydrodynamic size at physiological pH and ionic strength may differ from the size in water. Surface charge may also depend on the pH and ionic strength of the suspending solution. While *in vitro* characterization is performed to elucidate mechanisms and biocompatibility of nanomaterials, making use of numerous immortalized cell lines.

2. Core size and shape

2.1. Transmission electron microscopy

Transmission electron microscopy (TEM) remains the first choice for the investigation of size, dispersion and shape of NPs. TEM gives a photograph of the gold core, and by measuring each particle's diameter the histogram of size distribution is obtained. Thus, the information about the dispersity of the sample can be calculated.

In present work, TEM micrographs of AuNPs were obtained using an EFTEM Leo 912 AB instrument at an accelerating voltage of 100 kV. The samples were prepared by evaporating a drop of nanoparticles onto carbon-coated copper grid and allowing it to dry on the air. The histograms of the particle size distribution and the average particle diameter were obtained by measuring about 150-200 particles by using Measure IT Olympus Software.

2.2. Analytical centrifugation

Particle size, size distribution and extent of aggregation were analyzed by analytical centrifugation on a CPS disc centrifuge DC24000 (CPS Instruments Inc.). The CPS Disc Centrifuge separates particles by size using centrifugal sedimentation in a liquid medium. The sedimentation is stabilized by a slight density gradient within the liquid. The particles sediment within an optically clear, rotating disc. Approaching the outside edge of the disc, they scatter a portion of a light beam that passes through the disc. The change in light intensity is continuously recorded, and converted by the operating software into a particle size distribution.

As a gradient fluid, 8–24 wt% sucrose solution in Milli-Q water was used and filled successively in nine steps into the disc, starting with the dilution of highest density. For analysis, the disc rotation speed was set to 24 000 rpm. Calibration was performed using polyvinylchloride (PVC) particles (0.377 μm) as calibration standard (Analytik Ltd.). The colloids were sonicated before injection into the disc centrifuge.

2.3. Dynamic Light Scattering

Dynamic Light Scattering (DLS) is one of few techniques capable of determining the size of nanoparticles in solution, providing an accurate measure of nanoparticle hydrodynamic size. In DLS, the nanoparticle solution is illuminated by a monochromatic laser and its scattering intensity is recorded with a photon detector at a fixed or variable scattering angle with time. Generally, nanoparticle samples contain a distribution of sizes as a result of imperfections in synthesis and due to natural conformational variations in the large number of atoms involved. A metric for size variability is the polydispersity index (PI) equivalent to the relative variance of the distribution.

DLS measurements were performed, using a 90 Plus Particle Size Analyzer from Brookhaven Instrument Corporation (Holtsville, NY) operating at 15 mW of a solid-state laser (λ = 661 nm), using a scattering angle of 90°. A disposable cuvette with 1 cm optical path length was used for the measurements. The cuvettes were cleaned with Milli-Q water and stored dry. The samples were prepared by dilution with Milli-Q water or 10mM NaCl in order to obtain the final concentration of AuNPs close to 100 μg/mL, followed by filtration with a 0.45 μm cellulose acetate syringe filter before loading into the cuvette in order to remove large interfering

particulate matter. Each sample was allowed to equilibrate for 4 min prior to starting measurement. Three to ten independent measurements of 60 s duration were performed, at 25°C. The calculations of hydrodynamic diameter were performed using Mie theory, considering absolute viscosity and refractive index values of the medium to be 0.911 cP and 1.334, respectively.

2.4. UV-vis spectroscopy

If a routinely sizing of nanoparticles is needed, UV-vis spectroscopy can be a useful tool in fast and real-time monitoring of AuNPs size, providing information about AuNPs aggregation and concentration [1]. Surface plasmon resonance originates an extinction spectrum which depends on the size, shape, and aggregation of AuNPs. The position of the plasmon resonance is affected by multiple factors, like environment dielectric properties [2-4], physical or chemical interactions on particles surface [5], surface charge [6], interparticles distance [7, 8], and aggregation [9].

In present work, UV-visible spectra were recorded on a JASCO V530 spectrometer using 1 cm path length quartz cuvettes and a solution obtained by diluting three times the original sols with Milli-Q water. Haiss and co-workers, analyzing the optical properties of spherical AuNPs of 3-120 nm diameters in aqueous solutions, proposed a method to calculate the particle diameter from UV-vis spectra, considering an analytical relation between the extinction efficiency and diameter, which allow the determination of the particle concentration [10]. Using a ratio of the absorbance of AuNPs at the surface plasma resonance peak (A_{SPR}) to the absorbance at 450 nm (A_{450}), the particle diameter and corresponding extinction coefficient can be detected.

Subsequently, the particle concentration can be calculated by dividing the value of A_{450} to the corresponding extinction coefficient (see Tables A5.1-3 in Appendix).

2.5. Zeta-potential measurements

In an ionic solution, nanoparticles with a net charge will have two surrounding layers: a layer of ions of opposite charge strongly bound to their surface, and a diffuse outer layer of loosely associated ions. These two layers are collectively called the electrical double layer. As the particle moves, a distinction is created between ions in the diffuse layer that move with the nanoparticle and ions that remain with the bulk dispersant. The electrostatic potential at this “slipping plane” boundary is called the zeta potential and is related to the surface charge of the nanoparticle. In zeta potential measurements, an electrical field is applied across the sample and the electrophoretic mobility of nanoparticles is measured by laser doppler velocimetry [11]. Nanoparticles with a zeta potential between −10 and +10 mV are considered approximately neutral, while nanoparticles with zeta potentials greater than +30 mV or less than −30 mV are considered strongly cationic and anionic, respectively [12].

The zeta-potential was determined at 25°C using a 90 Plus Particle Size Analyzer from Brookhaven Instrument Corporation (Holtsville, NY) equipped with an AQ-809 electrode, operating at applied voltage of 120 V. The samples for measurements were prepared by dilution the concentrated nanoparticle sols in 10 mM NaCl solution up to 0.01 mg/mL final concentration, with pH value of 7. A minimum of three runs and ten sub runs per sample were performed to establish measurement repeatability.

The Zeta-potential was automatically calculated from electrophoretic mobility based on the Smoluchowski theory. A viscosity of 0.891 cP, a dielectric constant of 78.6, and Henry function of 1.5 were used for the calculations.

$$u_e = \frac{\varepsilon_{rs}\varepsilon_0\zeta}{\eta}$$

Helmholtz-Smoluchowski equation,

where U_e- electrophoretic mobility, ε_{rs}- relative permittivity of the electrolyte solution, ε_0 –electric permittivity in vacuum, η-dynamic viscosity of the liquid, ζ-zeta-potential [12].

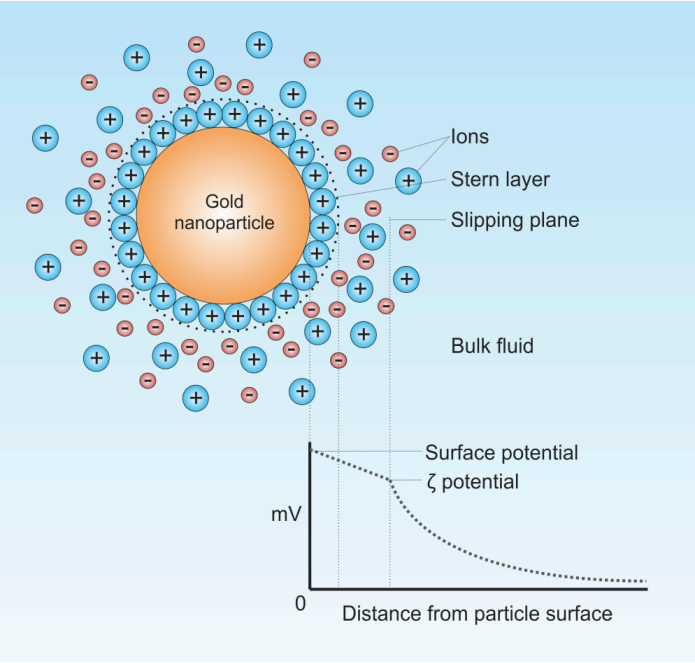

Figure 1. Electrical double layer on gold nanoparticle surface.

3. Characterization of organic shell

The organic shell of AuNPs can be investigated by a variety of techniques, as nuclear magnetic resonance (NMR) and infrared (IR) spectroscopies, and thermogravimetric analysis (TGA). The data obtained with most of these measurements represent average parameters because the materials examined are typically polydispersed samples.

3.1. ATR-FTIR spectroscopy

FTIR spectroscopy is widely used for characterizing the secondary structure of proteins and peptides. Recently, FTIR spectroscopy has been used for studying the interactions between nanoparticles and organic molecules: both the binding sites and conformational changes [13-16].

ATR-FTIR analysis was performed on a Biorad FTS-40 spectrometer equipped with a Specac Golden Gate ATR platform with a diamond crystal. The spectra of free ligands were recorded in the solid state, while the AuNPs were analyzed throughout the formation of a colloidal thin film structured on the ATR crystal surface.

3.2. NMR spectroscopy

NMR spectroscopy is another potential tool in studying the interactions between ligand shell and nanoparticle surface: shielding and/or deshielding of the proton resonances indicates an interaction or a conformational rearrangement in organic molecule bound to the gold surface. It is possible that a strong NMR signal broadening is observed in the spectra of gold nanoparticles.

This is the combined result of several factors: (1) the solid-like appearance of gold nanoparticles-the groups closest to the gold surface are more densely packed and thereby experience fast spin relaxation from dipolar interaction, similar to solid-state samples; (2) the distribution of chemical shifts-the site where the molecules are connected to the gold core has specific influence on the chemical shift of the neighboring groups, thereby causing a substantial broadening of the resonance for the groups closest to the site [17].

In present study, since the total amount of organic molecules on the particle surface is very low comparing to free organic substance, the samples for NMR analysis were prepared scaling up the molar amounts of every reagent in order to obtain a highly concentrated sol, for a better spectra resolution. The resulting sols were lyophilized, and redispersed in a H_2O/D_2O (90:10) mixture in case of peptides coated nanoparticles and in D_2O in case of nucleic acid components, prior to analysis.

NMR spectra were collected at 25 °C using both Bruker Avance 400 MHz and a Varian UNITY INOVA 600 MHz spectrometer equipped with a cold probe. Proton resonances of free peptides were assigned using a standard protocol based on the comparison of 2D [1H, 1H] TOCSY [18] (mixing time: 70 ms) and 2D [1H, 1H] ROESY [19] (mixing times: 150 and 200 ms) experiments. 2D experiments for resonance assignments were generally recorded with 16 scans, 128-256 FIDs in t1, 1024 or 2048 data points in t2.

NMR spectra of Au-peptides NPs were recorded with 1024 scans for 1D and 256 scans for 2D experiments, respectively.

Water signal was suppressed by means of either the WATERGATE PFG18 or the DPFGSE (Double Pulsed Field Gradient Selective Echo) techniques. Proton resonances were referenced to the water signal at 4.75 ppm. The spectra were processed with the Varian software VNMRJ 1.1D and analyzed with NEASY as implemented in CARA.

3.3. TGA analysis

Although it is an extremely valuable technique for surface characterization of nanoparticles, it is not commonly applied in the literature. The information one can retrieve from TGA measurements is bipartite. First of all, TGA allows us to determine the bonding strength of the ligand to the nanoparticles' surface and its thermal stability. Typically, ligands that are bound more strongly desorb at higher temperatures. Second, TGA provides direct information about the quantity of organic components on the AuNP, by measuring the total mass loss under gradual heating of dry nanoparticles. The advantage of this technique is that it can be applied to any kind of hybrid organic-inorganic nanostructures, even when dealing with a very small amount of the organic material present on the nanoparticle surface. The ligand coverage can be calculated using the following equation

$$N = \frac{\omega N_A \rho \frac{4}{3}\pi R^3 \times 10^{-23}}{MM},$$

where N is the number of ligands on each particle, R is the mean radius of the AuNPs, ρ is the density of the nanoparticles (19.30 g/cm3), N_A is Avogadro's number, MM is the molar mass of the ligand molecules (g/mol) and ω is the mass loss in percent (%) [20.]

TGA analyses were performed on Perkin-Elmer 7 HT thermo-balance. AuNPs were prepared scaling up the amounts of reagents in order to obtain about 10^{-3} mmol of organic molecules in the resulting sols. The sols were lyophilized and subsequently washed several times with mQ water and centrifuged at 2000 rpm for 5 min. The resulting dark brown powders were used for TGA measurements. The samples were maintained at 120 °C, under isothermal conditions for 1 h to remove any residual water and then ramped at 5 °C/min to 900 °C.

4. Biological experiments

U87 human glioblastoma and HeLa cervical cancer cell lines were used for biological experiments.

4.1. Cell culture

The U87 cells were cultured in 3 cm Petri dishes at 37 °C in a humidified atmosphere of 5% CO_2 in Dulbecco's Modified Eagle Medium (DMEM) cell culture media, supplemented with 10% heat-inactivated fetal calf serum, 1% penicillin-streptomycin, and 2×10^{-3} M L-glutamine. Cells were typically grown to 80% confluence before splitting and re-seeding at 40–50% confluence the day before an uptake experiment. The uptake experiments were carried out at approximately 80% confluence.

HeLa cells were cultured in 3 cm culture Petri dishes at 37 °C in a humidified atmosphere of 5% CO_2 in Dulbecco's Modified Eagle Medium (DMEM) cell culture media containing 10% heat-inactivated fetal bovine serum, 1% penicillin-streptomycin, and 1% non-essential amino acid solution. Passages 5–25 were used for the experiments; cells were typically grown to 80% confluence before splitting and re-seeding at 40–50% confluence the day before an uptake experiment. The uptake experiments were carried out at approximately 80% confluence.

4.2. TEM on the cells

TEM can visualize internal subcellular structures from thin sliced cells. Since many biological molecules may not have a rigid structure or density capable of scattering high velocity electrons, the electrons simply pass through the molecules and are therefore not visible in the resulting images.

Embedding in epoxy resin can be used to render some biological molecules sufficiently structured to scatter electrons and be visible in TEM micrographs. TEM allows detection of nanoparticles in biological materials (tissue specimens or cell culture samples) and visualization of fine cellular structures (details of subcellular organelles such as mitochondria, endoplasmic reticula, Golgi, centrioles, microtubules, endosomes, and ribosomes).

Figure 1 shows a schematic illustration of TEM samples preparation. To prepare the samples for epoxy resin embedding, immediately after incubation, the cells were fixed by addition of 4% para-formaldehyde/2.5% glutaraldehyde in 0.1 M phosphate buffer pH 7.4 (0.7 mL) for 1 h. Then the cells were rinsed with PBS buffer, postfixed using 1% aqueous solution of OsO_4 (0.5 mL) for 1 h. Subsequently, the cells were washed with Milli-Q H_2O, 30% ethanol solution, and stained with 0.5% uranyl acetate (0.5 mL, in 30% ethanol) for 1h (*Caution, extremely toxic!)*. Cells were then gradually dehydrated using a series of ethanol solutions (30, 60, 70, 80, and 100%) and embedded in epoxy resin. The resin was polymerized at 60 °C for 48h. Ultrathin sections (70–100 nm) were cut using a diamond knife on a Leica Ultramicrotome and mounted on Formvar-coated copper grids (200 mesh). The sections were then post stained with 5% uranyl acetate in 50% ethanol and 2% aqueous lead citrate solution and imaged with an FEI Tecnai Spirit TEM at 100 kV using AnalySIS software (Soft Imaging Systems).

4.3. Confocal microscopy

Confocal microscopy is one of the most important cellular analysis techniques and has been used with considerable success in the real-time observation of cells. Normally, molecular fluorescent probes are employed to label the cells to be

observed [21]. However, AuNPs can be a promising tool as contrast agent for cellular labeling due to their optical properties [22].

Confocal microscopy studies on the cells were performed by a Leica TCS-NT instrument using reflected-light optics at a magnification of 63× (1.53 NA Plan-Apochromat). The samples were illuminated with a 488 nm Argon/Krypton laser, using an intensity of AOTF filter by 10%. A neutral filter RT 30/70 was used as beam splitter and placed at a 45° angle in the path of beam.

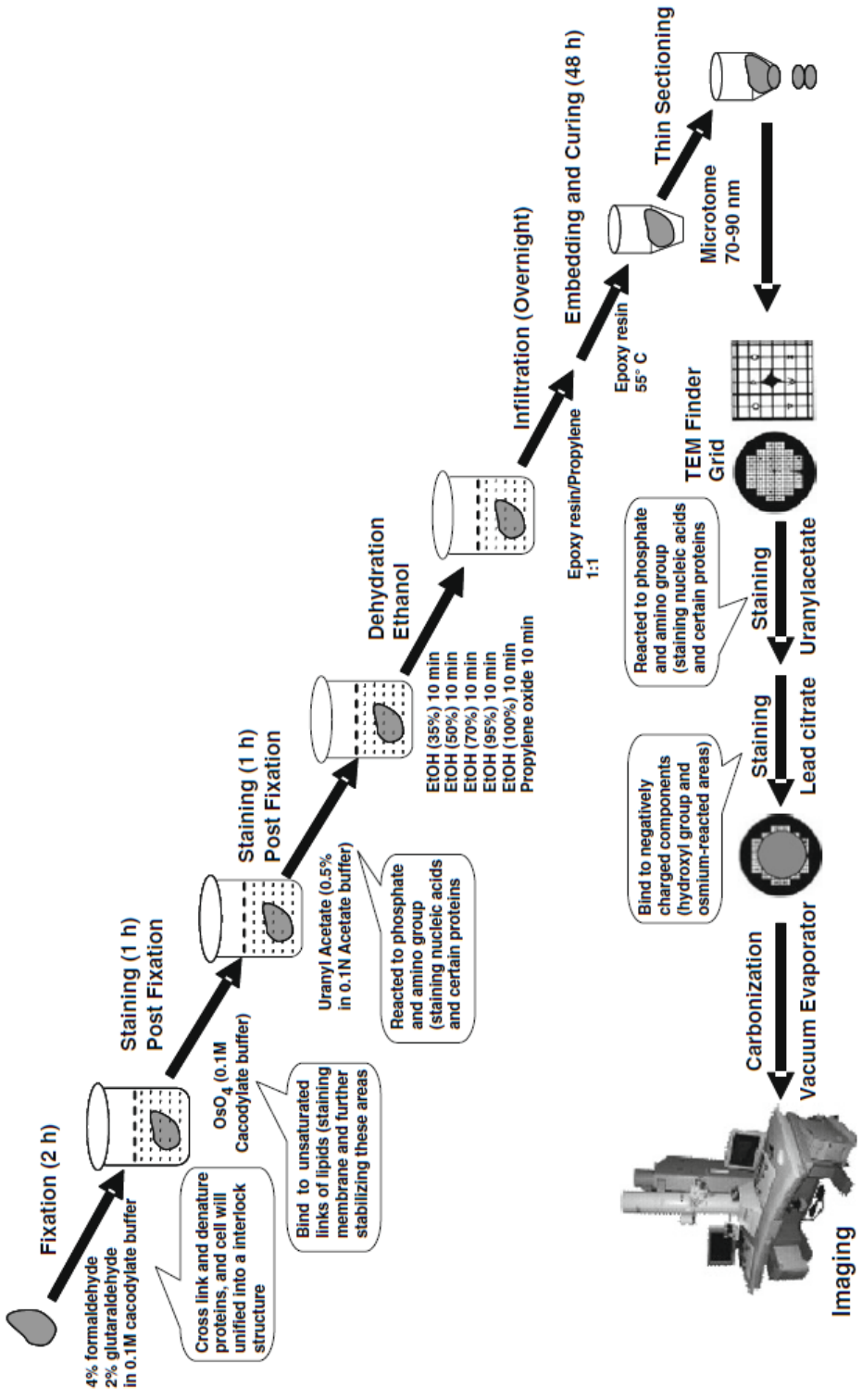

Figure 1. Schematic illustration of TEM cell sample preparation procedure.

5. References

1. V. Amendola, and M. Meneghetti. *J. Phys. Chem. C*, 2009, **113** (11), 4277–4285.
2. P. K. Jain, K. S. Lee, I. H. El-Sayed, and M. A. El-Sayed. *J. Phys.Chem. B,* 2006, **110**, 7238–7248.
3. K. S. Lee, and M. A. El-Sayed. *J. Phys. Chem. B,* 2006, **110**, 19220–19225.
4. K. L. Kelly, E. Coronado, L. L. Zhao, and G. C. Schatz. *J. Phys. Chem. B,* 2003, **107**, 668–677.
5. H. Hovel, S. Fritz, A. Hilger, U. Kreibig, and M. Vollmer. *Phys. Rev. B,* 1993, **48**, 18178–18188.
6. B. K. Juluri, Y. B. Zheng, D. Ahmed, L. Jensen, and T. J. Huang. *J. Phys. Chem. C,* 2008, **112**, 7309–7317.
7. P. K. Jain, and M. A. El-Sayed. *Nano Lett.* 2007, **7**, 2854–2858.
8. T. Klar, M. Perner, S. Grosse, G. von Plessen, W. Spirkl, and J. Feldmann. *Phys. Rev. Lett.* 1998, **80**, 4249–4252.
9. T. J. Norman Jr, C. D. Grant, D. Magana, J. Z. Zhang, J. Liu, D. Cao, F. Bridges, and A. Van Buuren. *J. Phys. Chem. B,* 2002, **106**, 7005–7012.
10. W. Haiss, N. T. K. Thanh, J. Aveyard, and D. G. Fernig. *Anal. Chem*. 2007, **79**, 4215-4221.
11. Characterization of nanoparticles intended for drug delivery. Edited by Scott E. McNeil, Humana Press, New York, USA, 2011.
12. A.V. Delgado, F. Gonzalez-Caballero, R. J. Hunter, L. K. Koopal, and J. Lyklema. *Pure Appl. Chem.* 2005, **77** (10), 1753–1805.
13. I. Ojea-Jiménez, L. García-Fernández, J. Lorenzo, and V. F. Puntes. *ACS Nano*, 2012, **6** (9), 7692–7702.

14. S. Goy-López, J. Juárez, M. Alatorre-Meda, E. Casals, V. F. Puntes, P. Taboada, and V. Mosquera. *Langmuir*, 2012, **28** (24), 9113–9126.

15. C. P. Shaw, D. A. Middleton, M. Volk, and R. Lévy. *ACS Nano*, 2012, **6** (2), 1416–1426.

16. D.-H. Tsai, M. Davila-Morris, F. W. DelRio, S. Guha, M. R. Zachariah, and V. A. Hackley. *Langmuir*, 2011, **27** (15), 9302–9313.

17. A. Badia, L. Demers, L. Dickinson, F. G. Morin, R. B. Lennox, and L. Reven. *J. Am. Chem. Soc.*, 1997, **119** (45), 11104–11105.

18. C. Griesinger, G. Otting, K. Wüthrich, and R. R. Ernst. *J. Am. Chem. Soc.* 1988, **110**, 7870-7872.

19. A. Bax, and D. G. Davis. *J. Magn. Reson.*1985, **63**, 207-213.

20. R. De Palma, S. Peeters, M. J. Van Bael, H. Van den Rul, K. Bonroy, W. Laureyn, J. Mullens, G. Borghs, and G. Maes. *Chem Mater.,* 2007, **19**, 1821-1831.

21. R. Shukla, V. Bansal, M. Chaudhary, A. Basu, R. R. Bhonde, and M. Sastry. *Langmuir*, 2005, **21** (23), 10644–10654.

22. P. A. Jarzyna, A. Gianella, T. Skajaa, G. Knudsen, L. H. Deddens, D. P. Cormode, Z. A. Fayad, and W. J. M. Mulder. *Wiley Interdiscip. Rev. Nanomed. Nanobiotechnol.* 2010, **2** (2), 138-50.

Chapter III

AuNPs modified by nucleic acid components: synthesis, spectroscopic study and potential application in biology

1. Introduction

The interaction of DNA with metal nanoparticles has found diverse applications in the recent advancements of nanobiotechnology [1-12]. Of particular interest is the DNA-gold interaction which forms the basis of several diagnostics applications involving DNA detection employing such techniques as surface plasmon resonance spectroscopy (SERS), electrochemical, colorimetric detection, etc [13-17]. DNA molecule adsorbed on gold films, gold electrodes, or DNA coated with gold nanoparticles have been reported to have applications in the field of electronics, sensors, drug delivery, chips, imaging, etc [18, 19].

The nucleobases are nitrogenous ring compounds consisting of either purine or pyrimidine derivatives. A purine is a fused-ring compound containig one 6-membered ring attached to a 5-membered ring, whereas a pyrimidine consists of a single 6-membered ring structure (Figure 1). Adenine, guanine, thymine, and cytosine are the four main base constituents found in DNA. Nucleic acid sugar residues are attached to the associated base units in an N-glycosidic bond, involving N-1 nitrogen of pyrimidine bases or the N-9 nitrogen of purines directly linked to the C-1 carbon of the monosaccharide derivative to give a nucleoside (Figure 2). In DNA, the sugar group consists of a β-D-2-deoxyribose unit. A nucleotide consists of a base and a sugar plus a phosphate group. In each nucleotide monomer of DNA, a phosphate group is attached to the C-5 hydroxyl of each sugar residue in an ester (anhydride) linkage.

With the development of DNA microarray techniques there has been particular interest in understanding the nature of the interaction of the DNA molecules with the

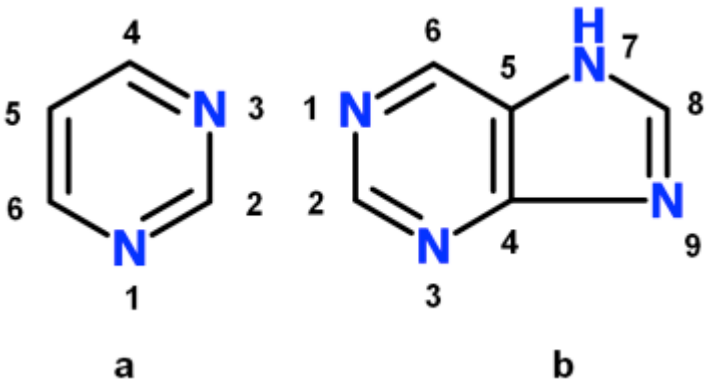

Figure 1. The pyrimidine (a) and purine (b) ring structures common to nucleic acids.

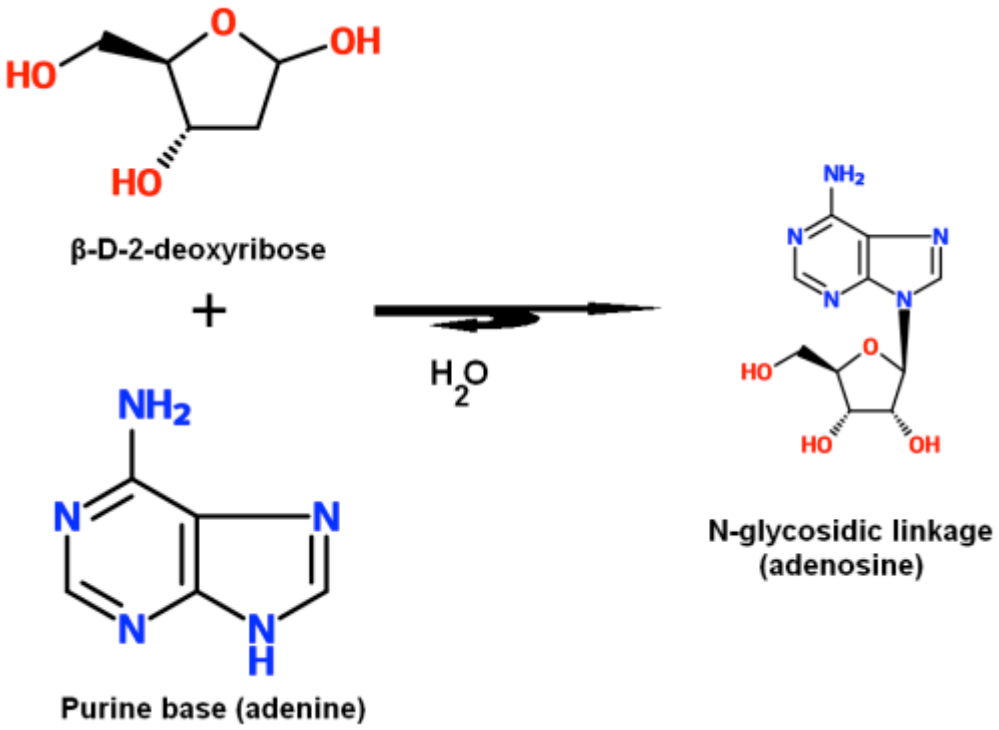

Figure 2. The formation of an *N*-glycosidic bond links the base unit of nucleic acids to the associated ribose derivative.

gold surface. To build a model of the complex DNA-gold interactions, one should first understand the interactions involving every single DNA fragment (adenine, guanine, thymine and cytosine) and AuNPs. The strength of the interactions appears to be very sequence-dependent [20-23].

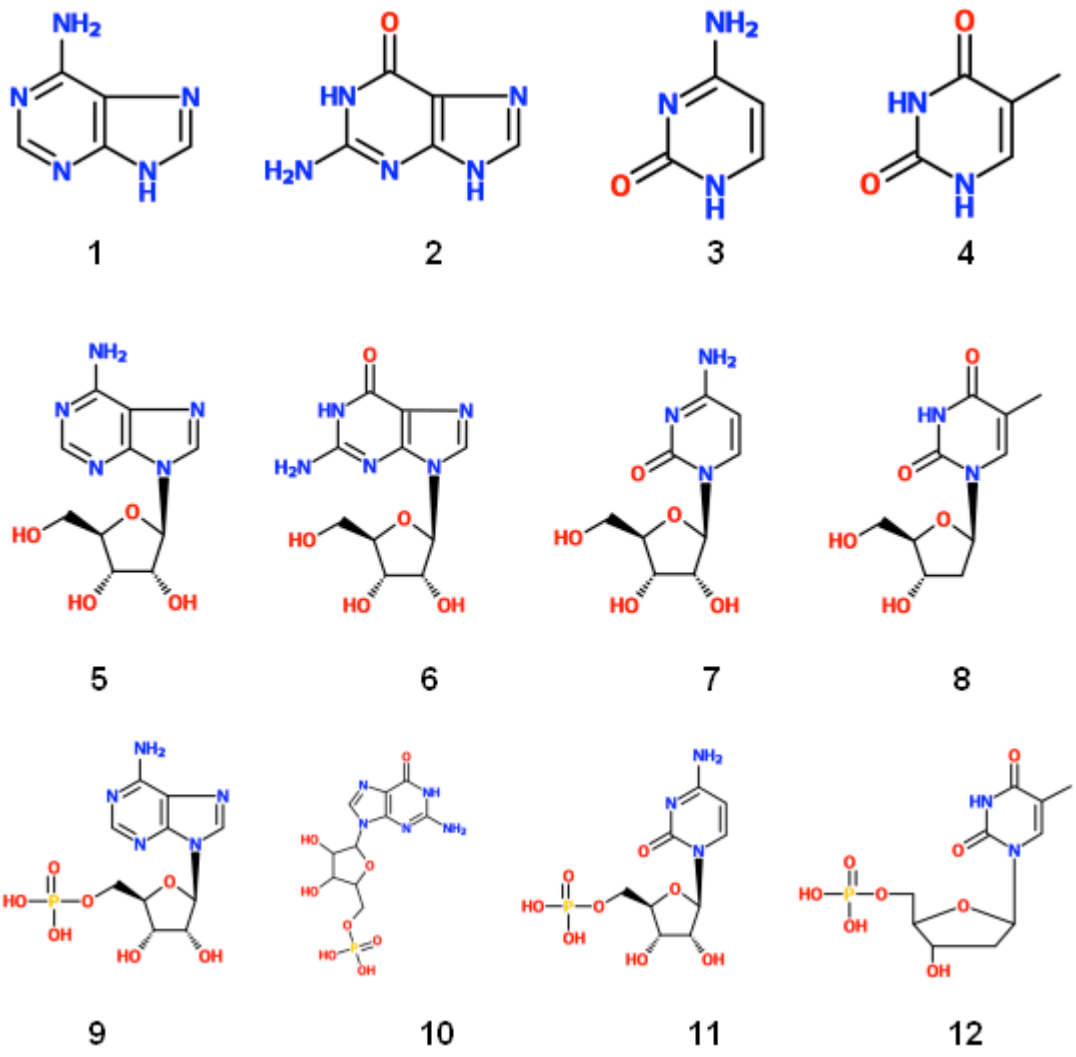

Figure 3a. Structural formula of nucleobases, nucleosides and nucleotides: adenine (1), guanine (2), cytosine (3). thymine (4), adenosine (5), guanosine (6), cytidine (7), thymidine (8), adenosine 5`-monophosphate (9), guanosine 5`-monophosphate (10), cytidine 5`-monophosphate (11) and thymidine 5`-monophosphate (12).

Demers *et al.* have studied the interaction of nucleic acid bases and nucleosides with gold surfaces using the temperature-programmed desorption and reflection absorption Fourier transform infrared spectroscopic techniques. They have found that desorption from the gold surface takes place at lower temperature for pyrimidine bases (thymine and cytosine) than for purine bases (guanine and adenine) (Figure 3a). Consequently, the measured desorption was revealed in the order thymine<cytosine<adenine<guanine. Kryachko and Remacle [24, 25] have investigated the interaction of small gold clusters with nucleic acid bases and base pairs at the density functional theory level. In these experiments, the interaction energies of small gold clusters with different sites of bases, proton affinity, and deprotonating affinity were evaluated, and, thus, the most probable site for binding with gold was determined. They have found that gold interacts with oxygen and nitrogen centres and revealed the presence of NH---Au hydrogen bonding.

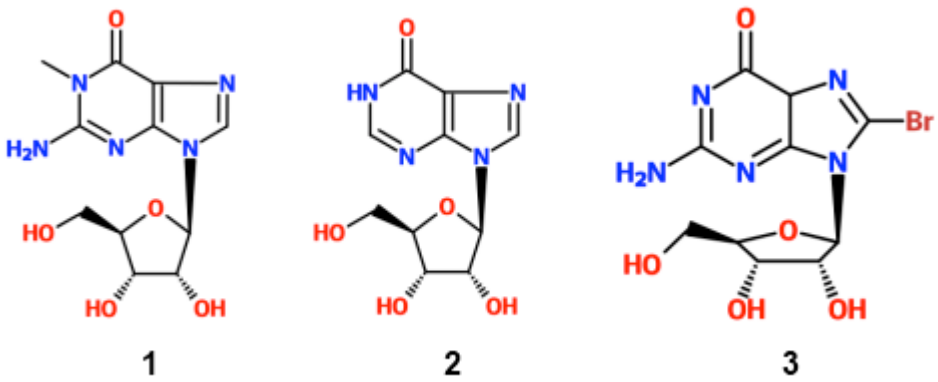

Figure 3b. Structural formula of 1-methylguanosine (1), inosine (2) and 8-bromoguanosine (3):

2. Synthesis of AuNPs

2.1. Synthesis of nucleobase capped AuNPs

The solutions were prepared freshly for each synthesis, except for sodium tetrachloroaurate (III), which was prepared as a 34.1 mM stock solution. Being nucleobases insoluble in water at room temperature, the stock solutions were prepared by dissolving in the 0.01 M NaOH, following by dilution with water up to necessary concentration. All the glass vessels and stirrers were washed with *aqua regia* (Caution! Extremely corrosive), and the solutions were filtered through 0.22 μm cellulose filter prior to use in order to avoid undesirable nucleation.

The molar ratios between the reagents are reported in Table 1. In a typical reaction, to 5 mL of Milli-Q water, an aqueous solution of $NaAuCl_4$ ($2 \cdot 10^{-3}$ mmol; 34.1 mM) was added. Under vigorous stirring, an aqueous solution of adenine ($6 \cdot 10^{-6}$ mmol, 3.95 mM), guanine ($8 \cdot 10^{-6}$ mmol, 0.909 mM), cytosine ($1.8 \cdot 10^{-5}$ mmol, 5.09 mM) or thymine ($8 \cdot 10^{-6}$ mmol, 4.48 mM) was added. After 5 minutes, an aqueous solution of $NaBH_4$ was added (4 μmol; 0.1M) and red sols were immediately formed. The obtained colloidal solutions were left under stirring several hours to complete the reaction. The particles were purified by dialysis overnight (Sigma-Aldrich Dialysis tubing cellulose membrane, cut off 12.400 MW) or by repeated centrifugation.

2.2. Synthesis of nucleoside capped AuNPs

The molar ratios between the reagents are reported in Table 2. In a tipical reaction, to 5 mL of Milli-Q water, an aqueous solution of $NaAuCl_4$ ($2 \cdot 10^{-3}$ mmol; 34.1 mM) was added. Under vigorous stirring, an aqueous solution of adenosine ($9 \cdot 10^{-6}$ mmol, 2.53 mM), guanosine ($1 \cdot 10^{-5}$ mmol, 0.42 mM), cytidine ($1 \cdot 10^{-5}$ mmol, 2.77

mM), or thymidine ($1.4 \cdot 10^{-5}$ mmol, 2.3 mM **)** was added. After 5 minutes, an aqueous solution of $NaBH_4$ was added (4 μmol; 0.1M) and red sols were immediately formed. The obtained colloidal solutions were left under stirring several hours to complete the reaction. The particles were purified by dialysis overnight or by repeated centrifugation.

Table 1. Molar ratios between Au (III), nucleobases and sodium borohydride used for the synthesis of AuNPs.

Stabilising agent	**Au (III): nucleobase: $NaBH_4$**
Adenine	1:0.001:1
Guanine	1:0.006:2
Cytosine	1:0.003:2
Thymine	1:0.002:2

Table 2. Molar ratios between Au (III), nucleosides and sodium borohydride used for the synthesis of AuNPs.

Stabilising agent	**Au (III): nucleoside: $NaBH_4$**
Adenosine	1:0.003:2
Guanosine	1:0.005:2
Cytidine	1:0.005:2
Thymidine	1:0.007:2

2.3. Synthesis of nucleotide capped AuNPs

The molar ratios between the reagents are reported in Table 3. In a typical reaction, to 5 mL of Milli-Q water, an aqueous solution of $NaAuCl_4$ ($2 \cdot 10^{-3}$ mmol; 34.1 mM) was added. Under vigorous stirring, an aqueous solution of adenosine 5`-monophosphate ($6 \cdot 10^{-6}$ mmol, 1.1 mM), guanosine 5`-monophosphate ($6 \cdot 10^{-4}$ mmol, 1.18 mM), cytidine 5`-monophosphate ($1.25 \cdot 10^{-6}$ mmol, 0.925 mM), or thymidine 5`-monophosphate **(**$2 \cdot 10^{-5}$ mmol, 1.3 mM**)** was added. After 5 minutes, an aqueous solution of $NaBH_4$ was added (4 μmol; 0.1M) and red sols were immediately formed. The obtained colloidal solutions were left under stirring several hours to complete the reaction. The particles were purified by dialysis overnight or by repeated centrifugation.

2.4. Synthesis of AuNPs capped by guanosine derivatives

1-methylguanosine and 8-bromoguanosine were synthesized as reported in ref. 25. The molar ratios between the reagents are reported in Table 4. In a tipical reaction, to 5 mL of Milli-Q water, an aqueous solution of $NaAuCl_4$ ($2 \cdot 10^{-3}$ mmol; 34.1 mM) was added. Under vigorous stirring, an aqueous solution of 1-methylguanosine ($1 \cdot 10^{-5}$ mmol, 0.272 mM), 8-bromoguanosine ($2 \cdot 10^{-5}$ mmol, 0.263 mM) or inosine ($1 \cdot 10^{-5}$ mmol, 0.69 mM) was added. After 5 minutes, an aqueous solution of $NaBH_4$ was added (4 μmol; 0.1M) and red sols were immediately formed. The obtained colloidal solutions were left under stirring for several hours to complete the reaction. The particles were purified by dialysis overnight.

Table 3. Molar ratios between Au (III), nucleotides and sodium borohydride used for the synthesis of AuNPs.

Stabilising agent	Au (III): nucleoside: $NaBH_4$
Adenosine 5`-monophosphate	1:0.003:2
Guanosine 5`-monophosphate	1:0.3:2
Cytidine 5`-monophosphate	1:0.08:2
Thymidine 5`-monophosphate	1:0.01:2

Table 4. Molar ratios between Au (III), guanosine derivatives and sodium borohydride used for the synthesis of AuNPs.

Stabilizing agent	Au (III): ligand: $NaBH_4$
Au-8-bromoguanosine	1:0.01:2
Au-Inosine	1:0.005:2
Au- 1-methylguanosine	1:0.005:2

3. Results and discussion

We prepared small water-soluble AuNPs following “one-pot” approach, where a gold salt aqueous solution was reduced by sodium borohydride in the presence of purine and pyrimidine derivatives as capping ligands (Figure 2, 3). The molar ratios between the ligands, gold salt and sodium borohydride were varied in the preliminary experiments in order to find out the reaction conditions at which the resulting AuNPs possess a number of characteristics we were interested in, such as particle size and stability. These experiments were based on changing the molar amount of organic ligand to be added to the gold precursor, and following the reaction progress by UV-vis spectroscopy. Both shape and position of SPR band, along with the colour of resulting colloidal dispersions were an indication of stability and certain particle size. Relying on these facts, we selected the ratios reported in Table 1-4 which were used in further experiments.

Besides UV-vis spectroscopy used for preliminary studies of AuNPs stability, we employed Dynamic Light Scattering and Z-potential measurements in order to evaluate the particle electro-kinetic characteristics. The morphology was studied by TEM microscopy and the ligand shell interaction with gold was characterized by ATR-FTIR, ^{1}H- and ^{31}P NMR spectroscopy.

As a result of gold nanoparticles formation, the characteristic SPR bands with the wavelengths varying between 516 and 531 nm, depending on the ligand used, were observed. The UV-vis spectra of functionalized AuNPs were constantly run from the moment of reducing agent addition until the absorbance of SPR band stopped growing. This indicated the completion of AuNPs formation.

The UV-vis spectra related to every kind of particles are reported in Figures 4-6, whereas SPR band values are reported in Table 5.

Table 5. Comparison of SPR band values of AuNPs stabilized by nucleobases, nucleosides, nucleotides, and guanosine derivatives.

Au-ligand	Plasmon band, nm
Au-adenine	529
Au-adenosine	525
Au-adenosine 5`-monophosphate	531
Au-guanine	524
Au-guanosine	525
Au-guanosine 5`-monophosphate	525
Au-thymine	517
Au-thymidine	516
Au-thymidine 5`-monophosphate	517
Au-cytosine	529
Au-cytidine	527
Au-cytidine 5`-monophosphate	523
Au-8-bromoguanosine	519
Au-inosine	519
Au- 1-methylguanosine	519

TEM results indicate the diameter of the particles to vary from 6 to 35 nm: the largest nanoparticles of 35 nm were obtained using adenosine 5`-monophosphate as capping agent, while the smallest ones of 6 nm were produced both with guanosine 5`-monophosphate and cytidine and corresponding nucleotide, which indicates a dependence of the size from the ligand nature and its amount per nanoparticles.

The shape of the nanoparticles was found nearly spherical, except for several cases when the nanoparticles had an ovate shape. TEM images and diagrams of mean particle diameter distributions are reported in Figure 7-9. Small nanoparticle agglomerates were detected in several TEM images, while the nanoparticles capped by guanosine derivatives were found to form chain-like structures likely due to charge loss (Figure 8, a-c).

One pot synthesis does allow obtaining the nanoparticles of quite small sizes, because of the reducing agent used to reduce gold ions to Au (0). Sodium borohydride is considered a strong reducing agent, able to quickly reduce metal ions to metal nanoparticles [26-28].

Dynamic Light Scattering studies supports TEM results, showing the presence of fractions with larger mean diameters (34-95 nm), arising from the formation of small particle agglomerates (Table 6). Despite the presence of agglomerates, they do not bring about any nanoparticle aggregation.

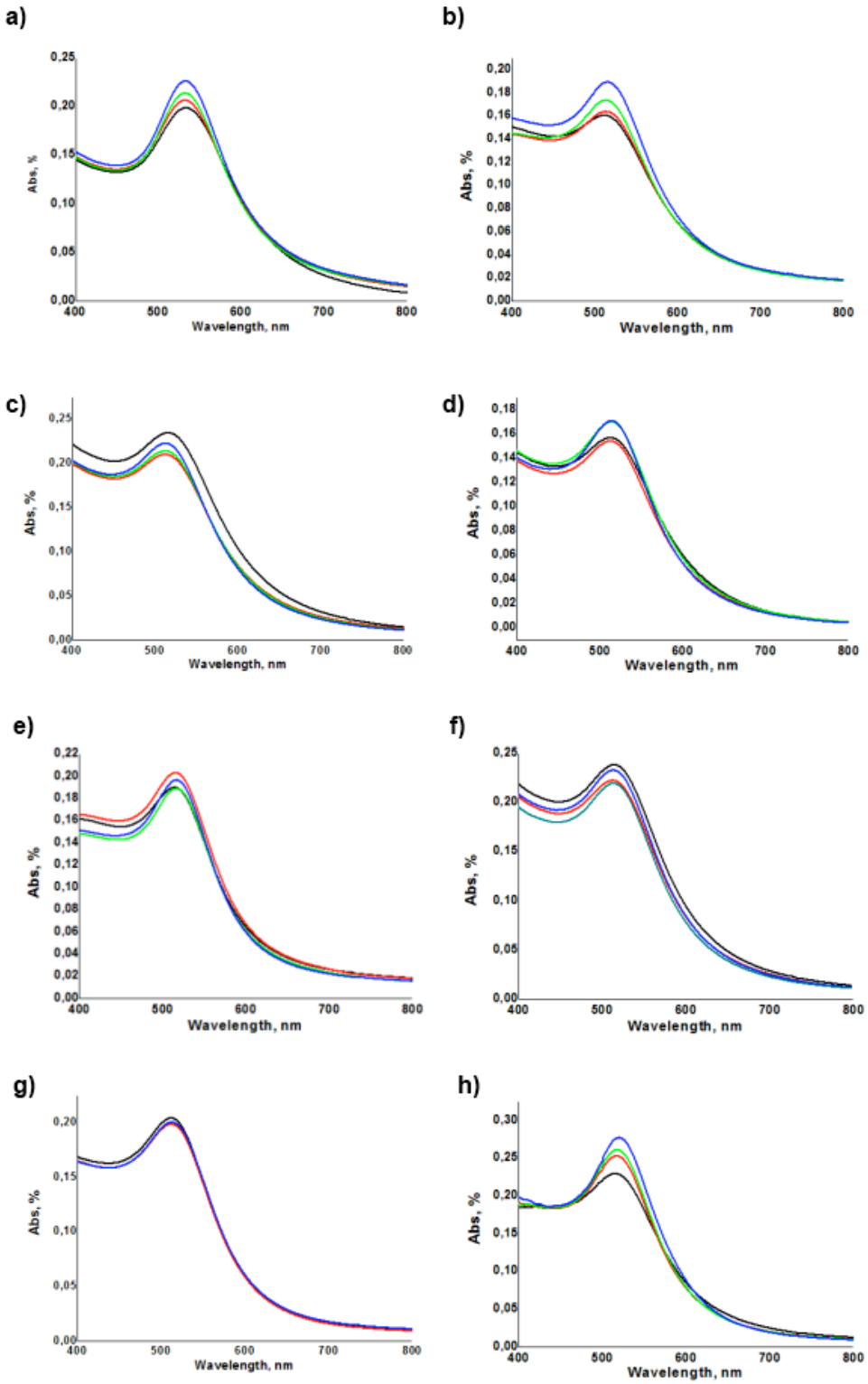

Figure 4. UV-vis spectra of a) adenine, b) guanine, c) cytosine, d) thymine, e) adenosine, f) guanosine, g) cytidine and h) thymidine: SPR band values were recorded every 15 min until their absorbance value was constant.

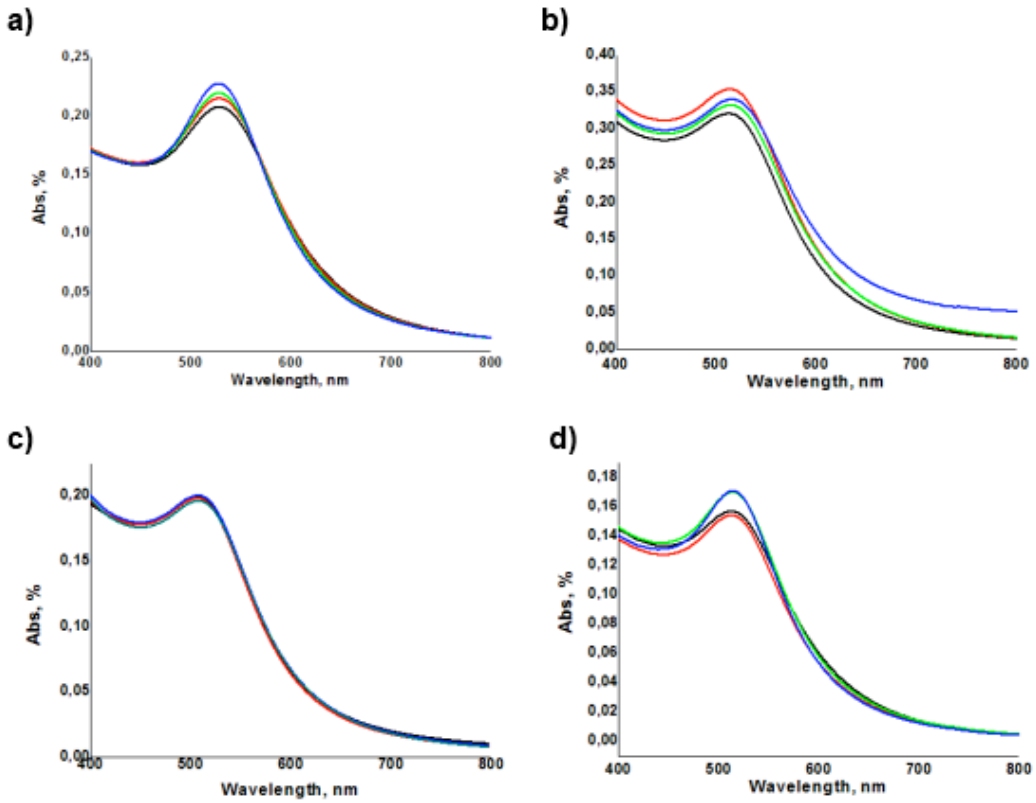

Figure 5. UV-vis spectra of a) adenosine 5`-monophosphate, b) guanosine 5`-monophosphate, c) cytidine 5`-monophosphate and d) thymidine 5`-monophosphate: SPR band values were recorded every 15 min until their absorbance value was constant.

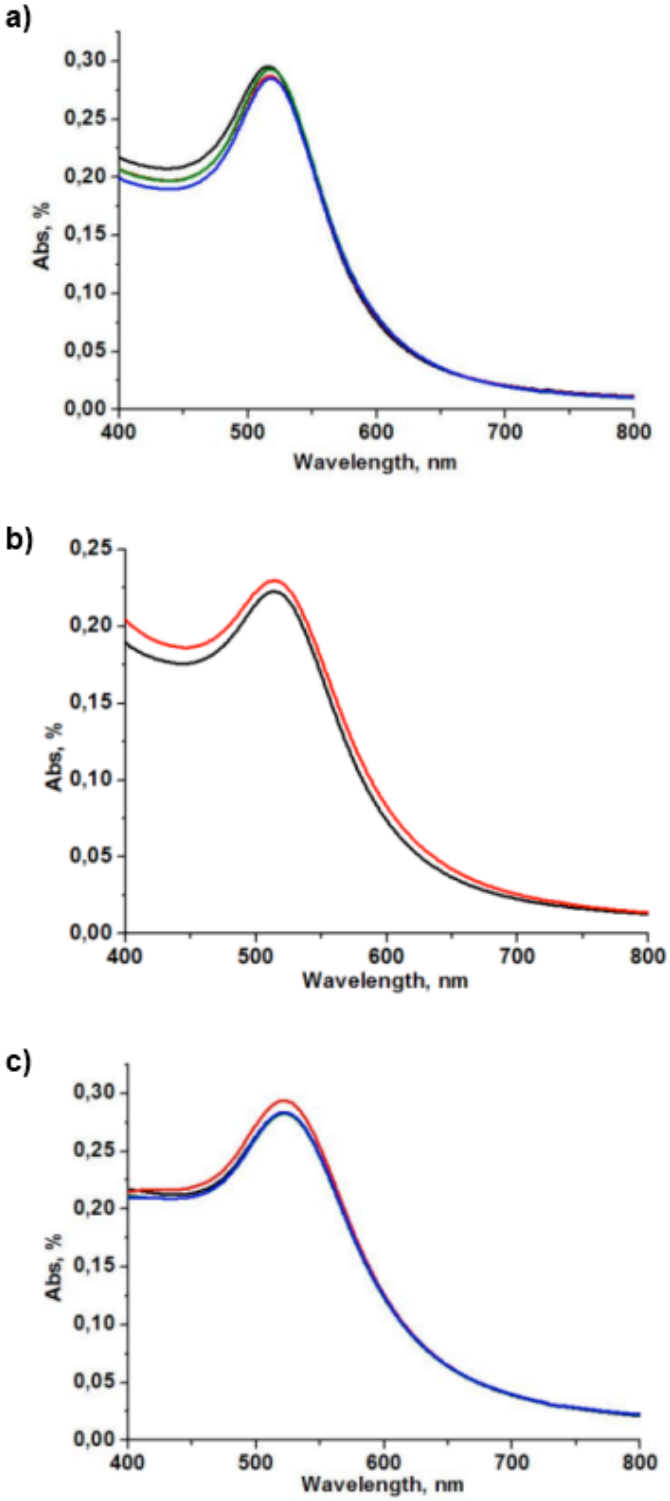

Figure 6. UV-vis spectra of a) 1-methylguanosine, b) inosine and c) 8-bromoguanosinee: SPR band values were recorded every 30 min until their absorbance value was constant.

Table 6. Hydrodynamic diameter obtained by Dynamic Light Scattering and core diameter of nanoparticles obtained by TEM.

Au-ligand	Diameter (DLS), nm	Diameter (TEM), nm
Au-adenine	18	12
Au-adenosine	19 (90)	16
Au-adenosine 5`-monophosphate	39	35
Au-guanine	19 (95)	16
Au-guanosine	16 (64)	16
Au-guanosine 5`-monophosphate	24	6
Au-thymine	13	11
Au-thymidine	32	16
Au-thymidine 5`-monophosphate	12 (83)	10
Au-cytosine	15 (84)	15
Au-cytidine	15 (54)	6
Au-cytidine 5`-monophosphate	9 (34)	6
Au-8-bromoguanosine	27	13
Au-inosine	28	10
Au- 1-methylguanosine	23	13

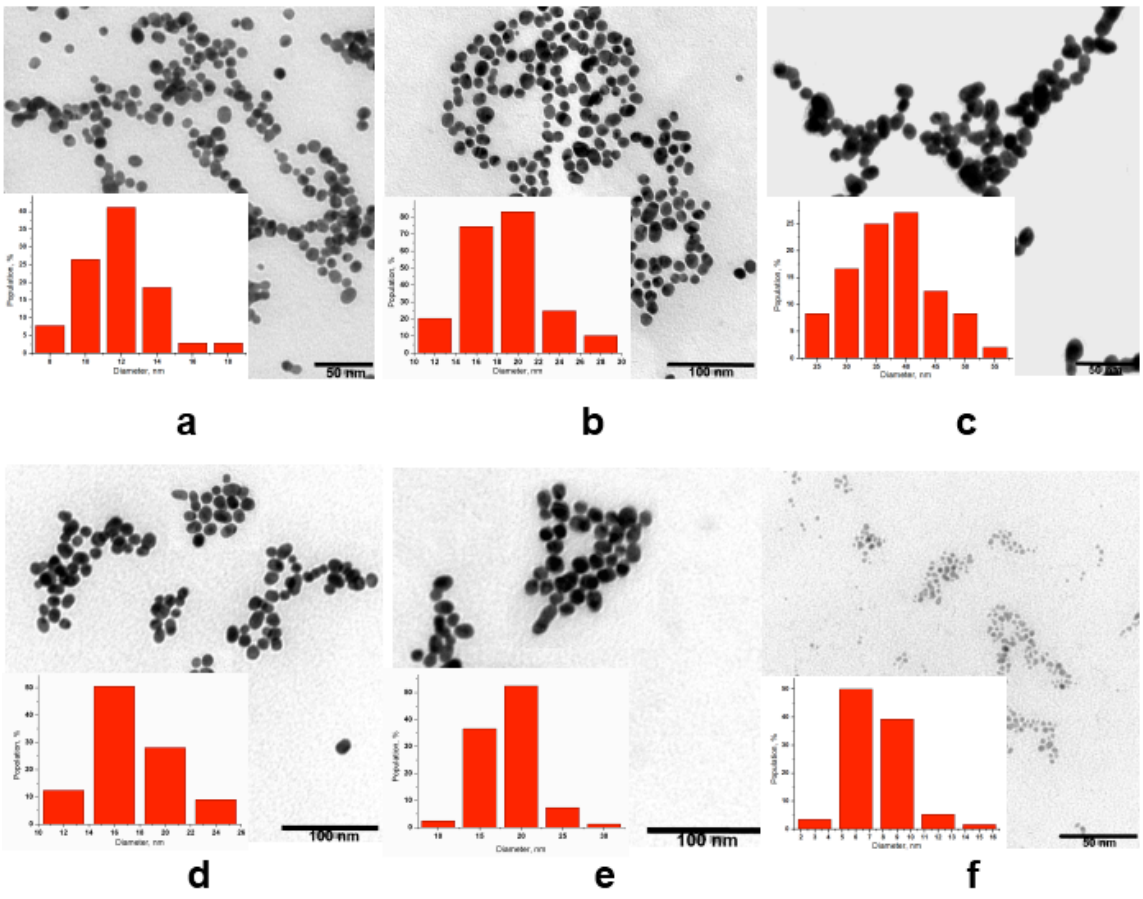

Figure 7. TEM images and diameter distributions of: a) Au-adenine, b) Au-adenosine, c) Au-adenosine 5`-monophosphate, d) Au-guanine, e) Au-guanosine and f) Au-guanosine 5`-monophosphate NPs.

To evaluate the particle charge and stability, we employed zeta-potential approach. Zeta potential measurements can be a convenient tool which allows chemical reactions to be quickly monitored on particles with minimal sample preparation [29]. Zeta-potential, being easily calculated from measured particle mobility, can be used to derive information concerning the particle surface charge, and, hence, chemical composition. The values obtained for each kind of particle, are reported in Table 7. For comparison, we report the zeta-potential value of “bare” nanoparticles, *i.e.* those without any specific ligand surrounding the nanoparticle.

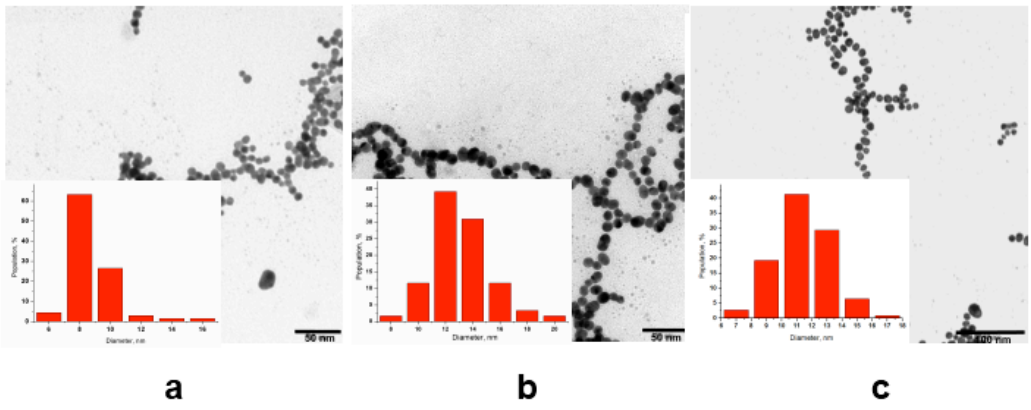

Figure 8a. TEM images and diameter distributions of: a) Au-1-methylguanosine, b) Au-8-bromoguanosine and c) Au-inosine NPs.

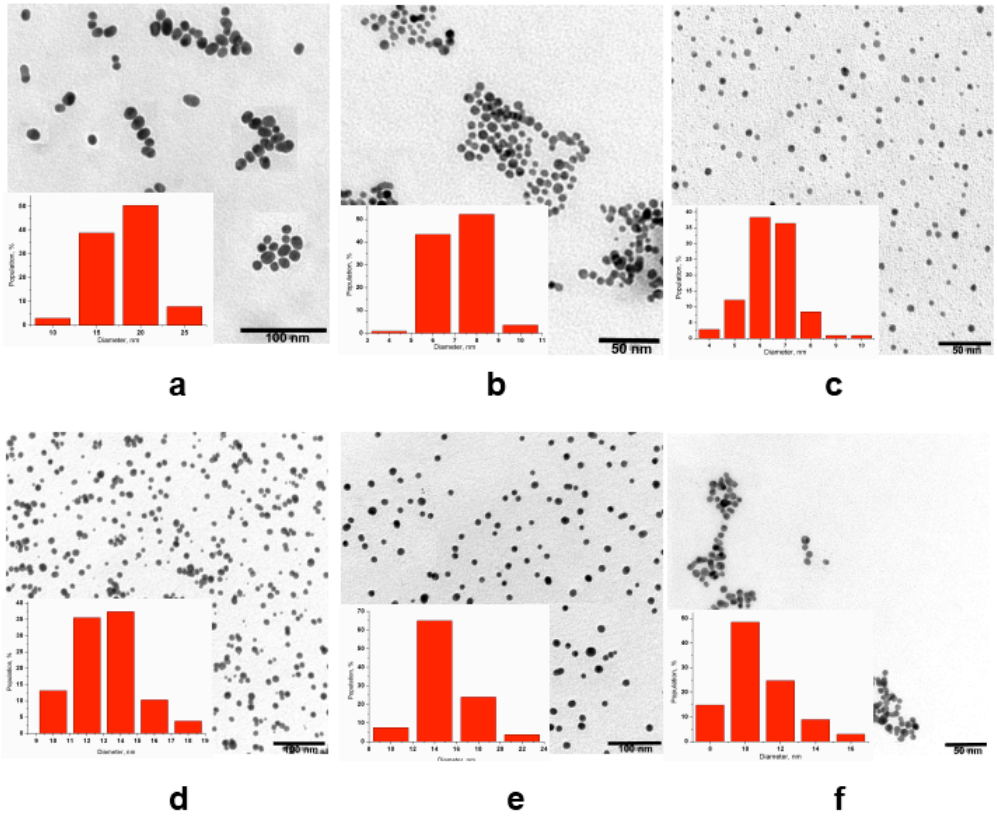

Figure 8b. TEM images and diameter distributions of: a) Au-cytosine, b) Au-cytidine, c) Au-cytidine 5`-monophosphate, d) Au-thymine, e) Au-thymidine and f) Au-thymidine 5`-monophosphate NPs.

The “bare” nanoparticles were prepared by using the same amounts of gold salt and reducing agent used in a typical reaction, leaving out the ligand. Since the “bare” nanoparticles tend to quickly aggregate due to the absence of a stabilizing shell, the zeta-potential measurement was performed using a freshly formed sol. As-prepared “bare” AuNPs shows a positive zeta-potential value of +11.04 mV. On the other hand, all the capped particles are negatively charged showing negative zeta-potential values. Notably, the particles capped by nucleobases and nucleosides show similar zeta-potential values around -20-23 mV, indicating that sugar does not greatly contribute to the particle charge. On the other hand, the particles capped by nucleotides show very negative values close to -50 mV, indicating a contribution of the phosphate moiety in the stabilization of the AuNPs. The only exception is Au-adenosine 5`-monophosphate NPs, which show a zeta-potential close to the zero, that, probably, is explained by the charge loss during the measurements.

The electro-kinetic characteristics of some nucleosides and nucleotides have been studied elsewhere [30, 31]. Brook *et al.* have discovered that, under given reaction conditions, the AuNPs capped by adenosine phosphates are stable and possess negative zeta-potentials, while AuNPs functionalized by nucleosides (e.g. adenosine or inosine) undergo aggregation caused by surface charge loss. In our case the adenosine 5`-monophosphate capped AuNPs seem to undergo a charge loss under electric field applied, having the zeta potential close to the zero. While inosine-AuNPs do show a charge loss under electron beam effect (Figure 8, c). The zeta-potential values of the AuNPs capped by “thymine-family” molecules followed the order Au–thymine< Au–thymidine< Au-thymidine 5`-monophosphate increasing along with the AuNPs hydrodynamic diameter.

The rise in the zeta-potential value can be associated with the formation of small nanoparticle arrangements, causing a light scattering increase and a mobility bias by the largest particles in the poly-dispersed sample [32]. Nevertheless, it is well known that the interpretation of the f-potential values of ‘‘uncapped’’ particles, with sizes in the 5–100 nm range, represents a delicate challenge.

Table 7. Zeta potential values of the nanoparticles.

Au-ligand	**Zeta-potential, mV**
“Bare” Au NPs	+11.04
Au-adenine	-25.29
Au-adenosine	-26.51
Au-adenosine 5`-monophosphate	-0.59
Au-guanine	-25.55
Au-guanosine	-21.56
Au-guanosine 5`-monophosphate	-47.56
Au-thymine	-40.63
Au-thymidine	-49.17
Au-thymidine 5`-monophosphate	-51.71
Au-cytosine	-21.47
Au-cytidine	-21.19
Au-cytidine 5`-monophosphate	-51.39
Au-8-bromoguanosine	-16.78
Au-inosine	-22.07
Au- 1-methylguanosine	-20.25

Therefore, the ligand-coated NPs provide further complexity, because the hydrodynamic size and surface-charge shielding depend on the ligand conformation [33].

In order to understand in which form (neutral or protonated) the molecules exist in the solution under given conditions, we measured pH values during the reaction progress: the pH of the starting solutions, before adding sodium borohydride, was quite acidic (pH 2.5-2.7), while the pH of the formed sols was close to 3.5-3.7 (likely due to traces of $HAuCl_4$ present in the $NaAuCl_4$ solution). Afterwards, we calculated the values of concentration fractions (α) as function of pH, using the acidity constant logarithms, *pKa*. From these, one can readily calculate an approximate ionization state of the species at any pH value in aqueous solution [34]. The summary of *pKa* and α values at pH 3.5 is reported in Table 8.

Concentration fraction α were calculated from the following equations: considering for the molecules with three different *pKa* values known:

$[H_3B^+]$ – mono-protonated form,

$[H_2B^+]$ – neutral form,

$[HB^+]$ – mono-deprotonated form,

[B] – fully deprotonated form

$$C = [H3B+] + [H2B+] + [HB+] + [B]$$

$$Ka1 = \frac{[H+] \cdot [H2B+]}{[H3B+]}$$

$$Ka2 = \frac{[HB+] \cdot [H+]}{[H2B+]}$$

$$Ka3 = \frac{[B] \cdot [H+]}{[HB+]}$$

$$\propto (B) = \frac{Ka1 \cdot Ka2 \cdot Ka3}{Ka1 \cdot Ka2 \cdot Ka3 + Ka1 \cdot Ka2 \cdot [H+] + Ka1 \cdot [H+]2 + [H+]3}$$

$$\propto (HB+) = \frac{Ka1 \cdot Ka2 \cdot [H+]}{Ka1 \cdot Ka2 \cdot Ka3 + Ka1 \cdot Ka2 \cdot [H+] + Ka1 \cdot [H+]2 + [H+]3}$$

$$\propto (H2B+) = \frac{Ka1 \cdot [H+]2}{Ka1 \cdot Ka2 \cdot Ka3 + Ka1 \cdot Ka2 \cdot [H+] + Ka1 \cdot [H+]2 + [H+]3}$$

$$\propto (H3B+) = \frac{[H+]3}{Ka1 \cdot Ka2 \cdot Ka3 + Ka1 \cdot Ka2 \cdot [H+] + Ka1 \cdot [H+]2 + [H+]3}$$

While for the molecules with two different *pKa* values known:

$[H_2B^+]$ – mono-protonated form,

$[HB^+]$ - neutral form,

[B] – mono-deprotonated form.

$$C = [H2B+] + [HB+] + [B]$$

$$Ka1 = \frac{[H+] \cdot [HB+]}{[H2B+]}$$

$$Ka2 = \frac{[H+] \cdot [B]}{[HB+]}$$

$$\propto (B) = \frac{Ka1 \cdot Ka2}{Ka1 \cdot Ka2 + Ka1 \cdot [H+] + [H+]2}$$

$$\propto (HB+) = \frac{Ka1 \cdot [H+]}{Ka1 \cdot Ka2 + Ka1 \cdot [H+] + [H+]2}$$

$$\propto (H2B+) = \frac{[H+]2}{Ka1 \cdot Ka2 + Ka1 \cdot [H+] + [H+]2}$$

The patterns of concentration fraction values (α) as function of pH are reported in Appendix. Table 8 reports the *pKa* values and corresponding protonation/deprotonation sites of each molecule, along with the percentage of protonated and neutral form existing at given conditions. The majority of the molecules exist both in mono-protonated and neutral state. Only adenosine 5'-monophosphate exists in bi- and triprotonated state: both at N1, N3, N7 atoms and N1, N7 atoms, respectively. On the other hand, thymine, thymidine and corresponding nucleotide are mostly nonprotonated (neutral) at given conditions. The same is for guanosine derivatives, which exist mostly in neutral form.

The protonation state of the molecules influences directly their spectroscopic characteristics and the way they interact with gold surface. Besides this, the variety of existing tautomeric forms of nucleic acid bases is believed to affect their spectroscopic data, such as infrared and NMR spectral line shapes. Moreover, tautomers of nucleic acid bases are believed to be involved in many different biochemical processes, including point mutations [35]. Their presence in biomolecules can alter cell functions and contribute to carcinogenic behaviour. In biological systems, nucleic acid bases are dominantly present in the stable canonical form. The adenine bases have been shown to exist in 14 different tautomeric forms by shifting one or two protons to a different nitrogen atom [35]. A recent

Table 8. *pKa* values and estimated protonation states at pH 3.5.

Ligand	Protonatio/deprotonation site	pKa	Concentration fraction α, %
Adenine	N1	4.15	78% Ade N(1)H+
	N9	9.80	22% Ade
Adenosine	N1	3.3	50% Ado N(1)H+
	N9	12.5	50% Ado
Adenosine 5'-monophosphate	N1	1.75	41% 5'-AMP N1(H)+ N3(H)+ N7(H)+
	N3	3.74	59% 5'-AMP N1(H)+ N7(H)+
Guanine	N7	3.3	40% Guo (N7)H+
	N1	9.2	60% Guo
	N9	12.3	
Guanosine	N7	2.2	4% Gua (N7)H+
	N1	9.5	96 % Gua
Guanosine 5'-monophosphate	N7	2.4	6% 5'-GMP (N7)H+
	N1	9.4	94 % 5'-GMP
Cytosine	N3	4.45	89% Cyt N3(H)+
	N1	12.2	11% Cyt

Cytidine	N3	4.22	78% dCyt N3(H)+
	N1	12.5	22% dCyt
Cytidine 5'-monophosphate	N3	4.5	90.9% 5'-CMP N3(H)+ 9.9 % 5'-CMP
Thymine	O4	0.9	100% Thy
	N3	9.8	
	N1	13	
Thymidine	N3	9.69	100% dThy
Thymidine 5'-monophosphate	O4	1.6	1% 5'-TMP (O4)+
	N3	10	99% 5'-TMP
Inosine	N7	1.2	1% Ino (N7)H+
	N1	8.7	99% Ino
M^1G	N7	2.44	6% M^1G N(7)H+
	NH2	13.22	94% M1G
8-Br-Gua	N7	1.55	1% 8-Br-Gua N(7)H+
	N1	13.00	99% 8-Br-Gua

theoretical study performed by Hobza *et al.* shows that the adenine tautomers may also exist in water [36]. Guanine also has several tautomeric forms, the stability of which is significantly influenced by the reaction medium. The reported IR studies reveal that both *keto*- and *enol*- guanine tautomers are present in equal proportions in solution, although the *keto*-N(9)-H form dominates in polar solvents [37].

Some structural investigations of the ligand shell surrounding gold nanoparticle have been already performed by infrared techniques to characterize the ligand-gold interactions. In particular, Mirkin and co-workers have used the temperature-programmed desorption method to study the interactions of DNA bases and nucleosides with a gold thin film, deposited on a flat support. The scientists have shown that nucleobases bind to the gold surface in a highly complex manner, with each base behaving differently.

However, a common behaviour has been found: none of the four nucleobases adsorb on gold in an orientation where the plane of the ring is perfectly parallel to the gold surface. Instead, all four molecules appear to be oriented with the molecular plane at an angle with respect to the gold surface [38]. Pergolese *et al.* have studied the adsorption of guanine, guanosine and 2′-deoxyguanosine on gold colloidal particles by SERS spectroscopy, suggesting that the molecules are tilted respect to the gold surface and the sugar moiety is not involved in the interaction [39]. Finally, Kryachko *et al.* have discovered that the bonding between DNA bases and $Au_{3,4}$ clusters occurs via Au-N or Au-O bonds. Moreover, a novel type of nonconventional N-H---Au hydrogen bonding formed between nucleic acid bases and gold clusters has been identified [24].

Besides infrared studies, ^{1}H and ^{31}P NMR spectroscopies have been widely used to study metal complexes with nucleobases or other nucleic acid components. Here, we apply this coordinative metallorganic approach to explain the interaction of the compounds under investigation with gold surface, comparing ^{1}H NMR spectra of free molecules, with ^{1}H NMR spectra of capped AuNPs [40, 41]. Since spectra resolution highly depends on the concentration of the molecule under investigation, in order to scale up the amount of the ligands in the nanoparticle suspension, very concentrated colloidal solutions were synthesized, freeze-dried and re-dispersed in D_2O just before the analyses.

In theory, the gold core can interact with the ligands in many ways: *via* phosphate oxygen atoms, sugar oxygen atoms, and (N, C, O) atoms of the heterocyclic base; or combinations thereof [40]. Here we discuss the binding of nucleobases, nucleosides and nucleotides to the gold nanoparticle surface.

The discussion is organized as follows: first, we concern guanine, corresponding nucleoside and nucleotide, along with guanine derivatives, comparing the NMR and FTIR results on the binding sites between these molecules and gold surface. Then, we consider adenine “family”, followed by thymine and cytosine compounds.

3.1. Spectroscopic study of the binding between nucleobases, nucleoside and nucleotides and AuNPs

3.1.1. Guanine and its derivatives.

Guanine N(7) atom possesses a high basicity and a favourable electrostatic potential to be the target for the metal coordination. A large dipole moment of guanine and its orientation does allow the coordination of any positively charged metal entity to this site [40].

A comparison of ^{1}H and ^{31}P chemical shifts of the free guanine, guanosine, guanosine 5'-monophosphate, 1-methylguanosine, 8-bromoguanosine and inosine, and corresponding capped AuNPs, is reported in Table 9 (an expanded version of the Table 9 is reported in Appendix). At pH 3.5, H8 signal of free **guanine** moves downfield as the N7 atom protonation causes an electron density to be withdrawn from H8, in accordance with *α* data. The proton resonances of all the purine derivatives, except for guanine, are not much affected

Table 9. ^{1}H and ^{31}P chemical shift values of the free ligands at pH 3.5 and after interaction with AuNPs.

	Mult	Δ	Mult	Δ
	Ino		**Au-Ino**	
H2	s	8.24	s	8.42-8.19
H8	s	8.12	s	
H1'	d	6.00	d	6.20-6.07
H2'	Burried under H_2O signal			
H3'	dd	4.36	dd	4.41
H4'	dd	4.20	dd	4.25

H5’	dd dd	3.85 3.77	dd dd	3.96 3.81
	Gua		**Au-Gua**	
H8	s	7.98	s	8.28
	Guo		**Au-Guo**	
H8	s	7.96	s	7.90
H1’	d	5.86	d	5.59
H2’	Burried under H_2O signal			
H3’	dd	4.35	dd	4.40|
H4’	q	4.17	q	4.01
H5’	dd	3.82 3.76	dd	3.82 3.65
	5’-GMP		**Au-5`-GMP**	
H8	s	8.09	s	8.58
H1’	d	5.85	d	5.86
H2’	Burried under H_2O signal			
H3’	dd	4.42	dd	4.42
H4’	q	4.25	q	4.32
H5’	dd	3.96	dd	4.11
P	s	2.87	s	0.34
	M^1G		**Au-M^1G**	
H8	s	7.92	s	7.99
H1’	d	5.85	d	5.88
H2’	Burried under H_2O signal			
H3’	dd	4.35	dd	4.39
H4’	q	4.17	q	4.24
H5’	d d	3.82 3.76	d d	3.84 3.82
CH3	s	3.41	s	3.46
	8-Br-Gua		**Au-8-Br-Gua**	
H1`	s	5.81	s	---
H2`	dd	4.91	dd	---
H3`	dd	4.28	dd	4.15
H4`	q	4.17	q	3.95
H5`	d d	3.82 3.75	d d	3.73 3.68

Abbreviations: Ino-inosine, Gua-guanine, Guo-guanosine, 5'-GMP-guanosine 5'-monophosphate, 8-Br-Guo-8-bromoguanosine, M1G-1-methylguanosine

---

by acidic pH and do not change considerably. On the contrary, the phosphate moiety suffers by the acidic medium and the value of ^{31}P chemical shift of **5'-GMP** did change from 3.96 to 2.87 ppm with pH moving from physiological to 3.5. The change can be attributed to the mono protonation of oxygen anion (*pKa*~6.3) [42]. Analysing ^{1}H NMR spectrum of **Au-guanine** NPs, we observed the H8 signal (8.28 ppm), shifted downfield more than that of free neutral molecule (7.65 ppm, δ = 0.63 ppm) and even more than that of free guanine in acidic conditions (7.98 ppm, δ = 0.3 ppm) (Figure 9).

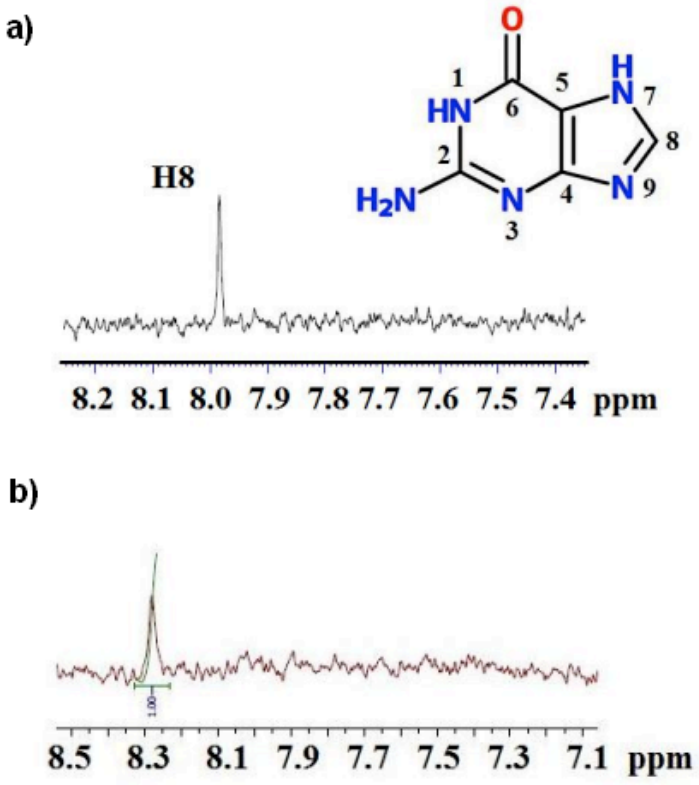

Figure 9. a) ^{1}H NMR spectra of free guanine in D_2O+CD_3COOD in the 8.2-7.4 ppm region, b) ^{1}H NMR spectra of Au-guanine NPs in the 8.5-7.1 ppm region.

The change is attributable to the electron density variation of the ring system, as a result of the gold interaction with the N7 lone pair of not-protonated guanine. The effect appears stronger than the deshielding effect observed upon protonation, suggesting an interaction of the basic guanine with a partially positive site on AuNPs (*i.e.* Au(+I) centres on gold surface). The protonated guanine species, if present, does not seem to interact with the particle, considering the presence of only one H8 signal in the ^{1}H NMR spectrum of Au-guanine NPs.

In ^{1}H NMR spectrum of **Au-guanosine** NPs, H8 proton at 7.96 ppm is slightly upfield shifted (δ = 0.06 ppm, respect to acidic condition), indicating an interaction of N7 atom with Au less strong than in **Au-guanine** NPs. On the contrary, the H1'-H5' sugar proton signals are broadened, with H1` and H4` signals being significantly upfield (δ H1`= 0.27 ppm; δ H4`= 0.16 ppm) compared with the values of **guanosine** at the same pH (Figure 10). The variations of ribose suggest eventual changes in its conformation upon interaction with Au.

^{1}H NMR spectrum of **Au-guanosine 5'-monophosphate NPs** (Figure 11), shows a downfield shift of the H8 signal at 8.09 ppm (δ = 0.49 ppm, with respect to the acidic condition). The H1'-H4' signals of ribose are broadened and slightly downfield, and only the H5' signal undergoes a really significant change (δ = 0.15 ppm), likely, due to its proximity to the phosphate group. Indeed, ^{31}P NMR revealed a δ P value drastically upfield (from 2.87 to 0.34 ppm) upon formation of AuNPs, indicating a strong interaction with Au (Figure 12). The interactions of **5'-GMP** and metal centres throughout purine N7 atom and oxygen atom(s) of the phosphate group has been already reported elsewhere in metal coordination complexes [40].

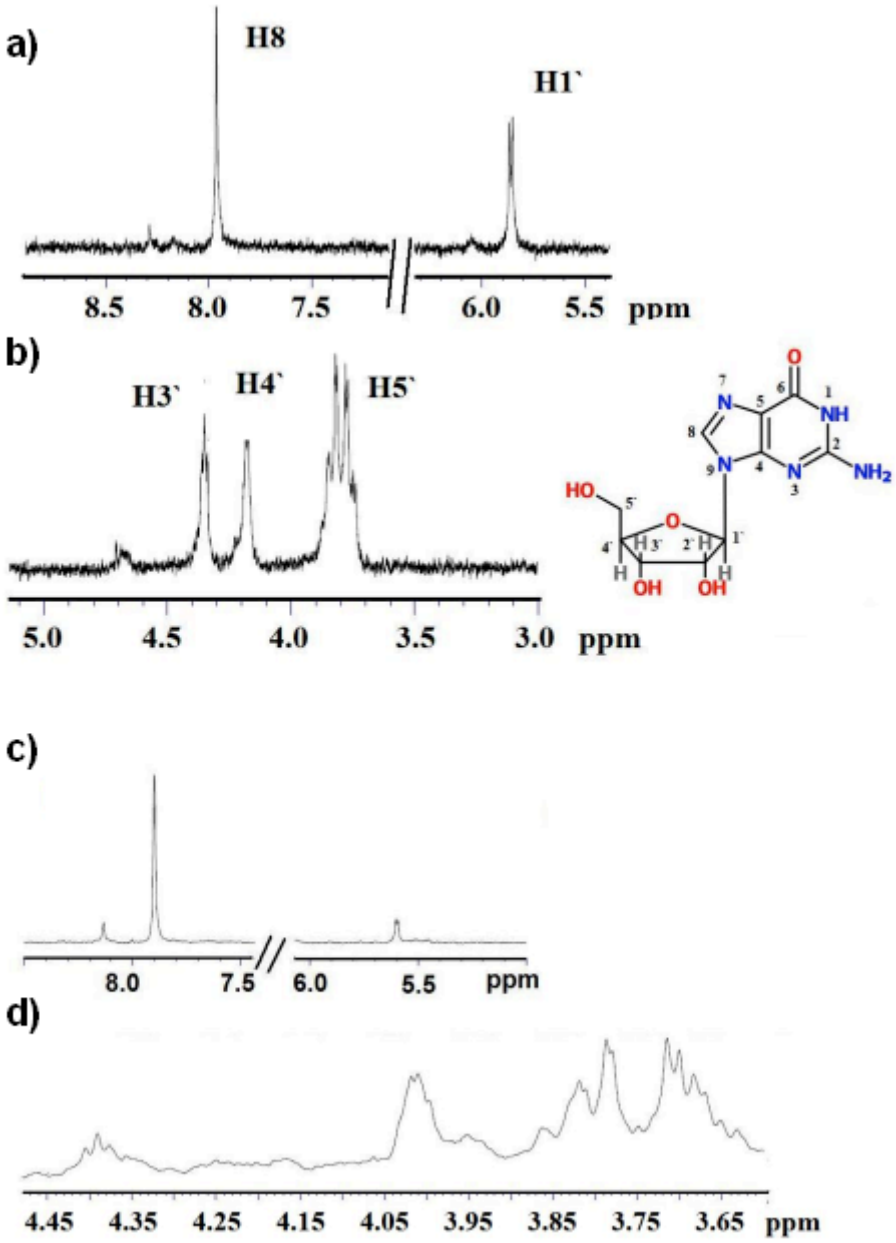

Figure 10. ^{1}H NMR spectra of free guanosine in D_2O+CD_3COOD: a) in the 8.5-5.5 ppm region; b) in the 5.0-3.0 ppm region; ^{1}H NMR spectra of Au-guanosine NPs in c) 8.5-5.0 ppm region; d) 4.45-3.65 ppm region.

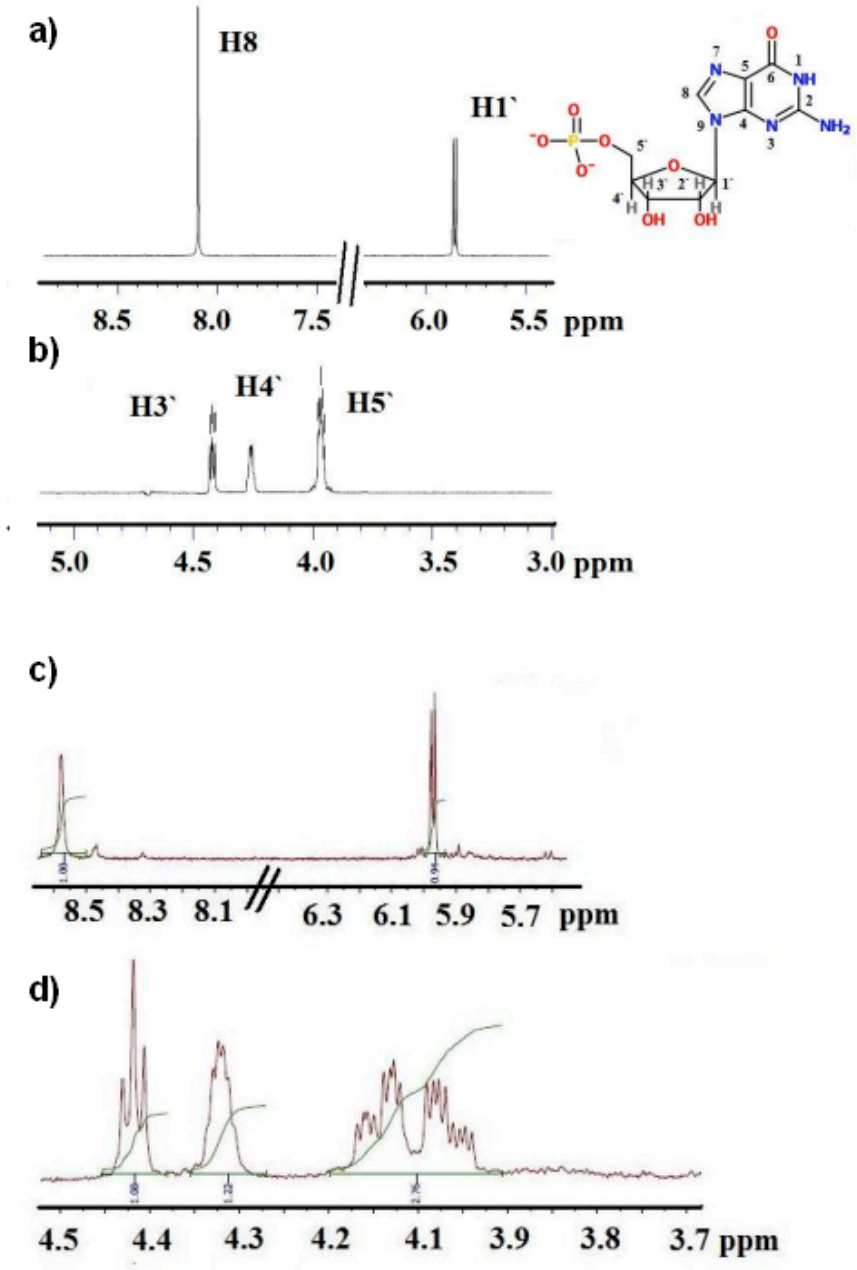

Figure 11. ^{1}H NMR spectra of free guanosine 5`-monophosphate in $D_2O$+$CD_3COOD$: a) in the 8.5-5.5 ppm region; b) in the 5.0-3.0 ppm region; $^{1}$H NMR spectra of Au-guanosine 5`-monophosphate NPs: c) in the 8.5-5.5 ppm region; d) in the 4.5-3.7 ppm region.

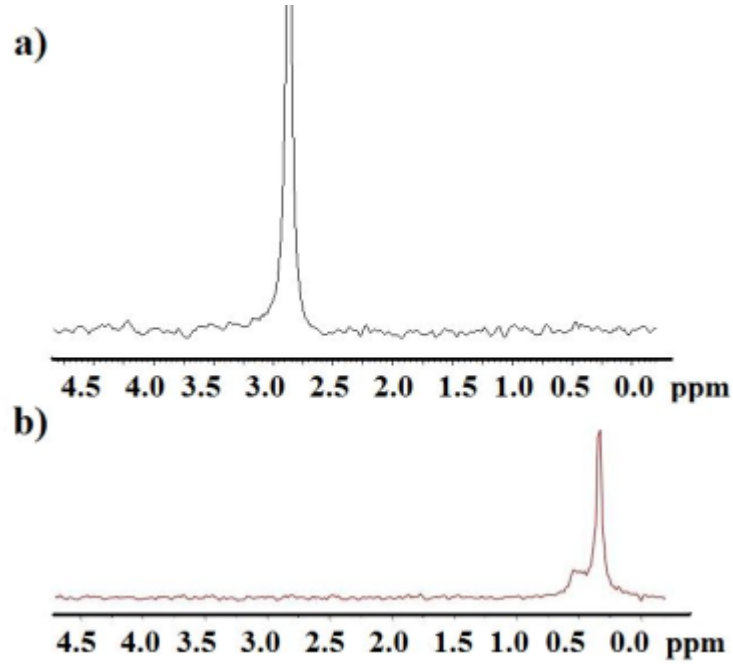

Figure 12. ^{31}P NMR spectra of a) free guanosine 5-monophosphate; b) Au-guanosine 5`-monophosphate NPs.

Figure 13 shows ^{1}H NMR spectra of **Au-1-methylguanosine** NPs. Only little changes and broadening of ribose signals are revealed under interaction with AuNPs. The presence of methyl substituent in N1 does not provide information on the coordination of **M^{1}G** to AuNPs, but NMR data suggest that ribose conformation is not affected by the presence of gold. On the contrary, interesting information can be obtained from ^{1}H NMR spectrum of **Au-8-bromoguanosine** NPs, in which strongly upfield shifted signals of H3'-H5'protons have been observed (δ = 0.1-0.28 ppm). The H1'and H2' signals even disappear from the usual region (Figure 14). Taking into account that substituted nucleosides (nucleotides) exist mainly as *syn* conformations, the torsional angle of the glycosidic bond in **8-Br-Guo** can induce different ribose conformations to fulfil the interaction with Au surface.

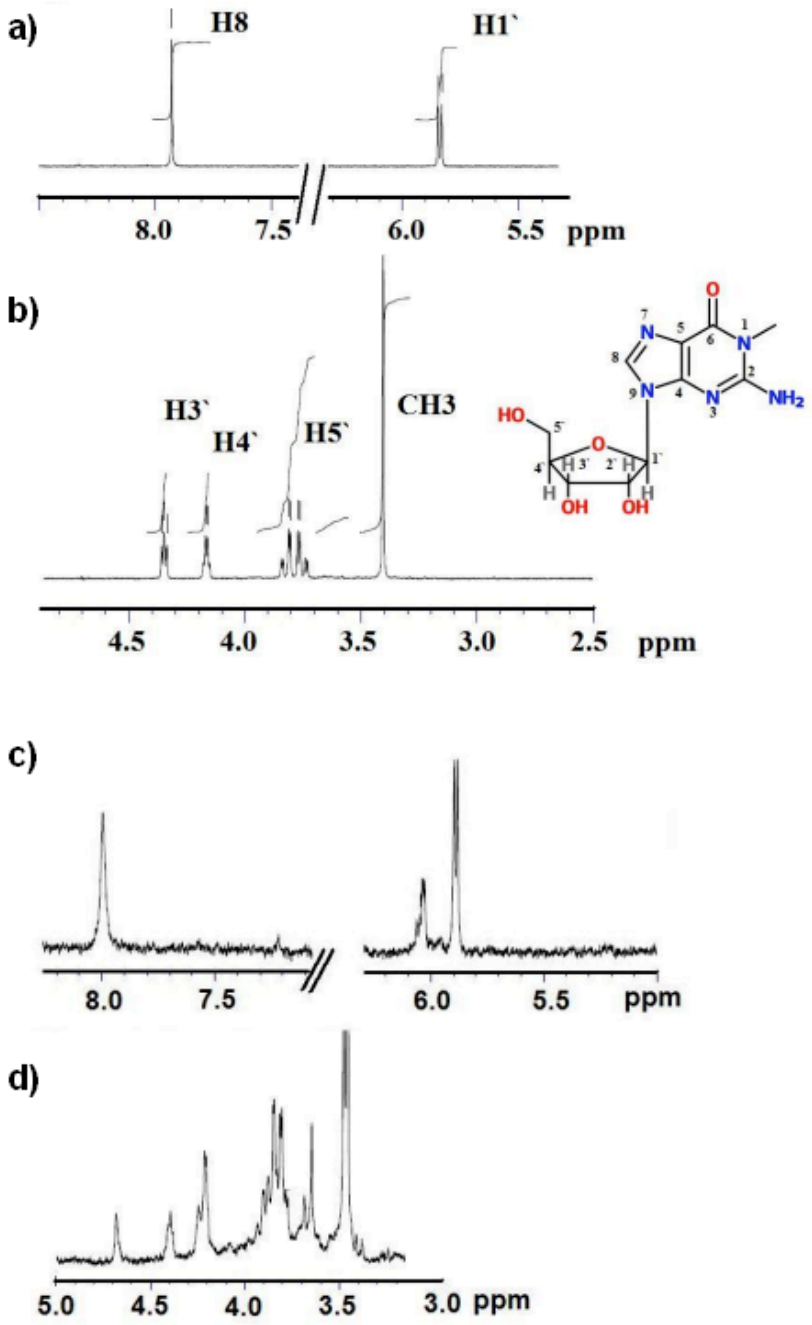

Figure 13. ^{1}H NMR spectra of free 1-methylguanosine in D_2O+CD_3COOD: a) in the 8.5-5.5 ppm region; b) in the 5.0-2.5 ppm region; ^{1}H NMR spectra of Au-1-methylguanosine NPs: c) in the 8.0-5.5 ppm region; d) in the 5.0-3.0 ppm region.

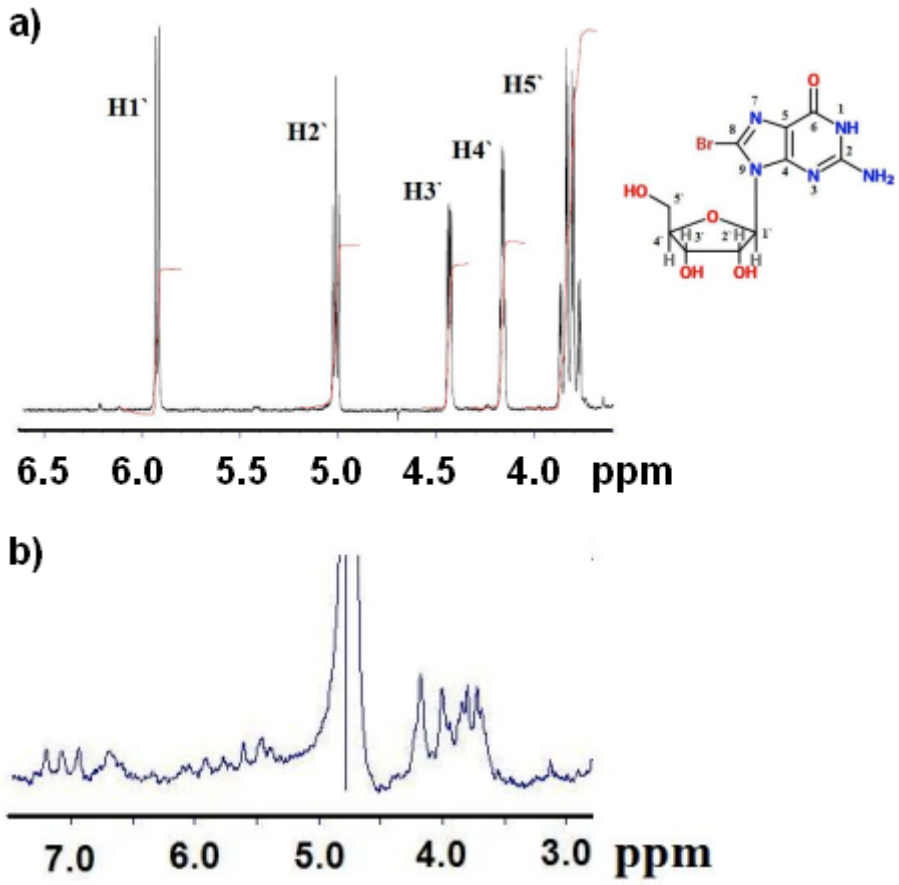

Figure 14. a) ^{1}H NMR spectrum of free 8-bromoguanosine in D_2O+CD_3COOD in the 6.5-4.0 region; b) ^{1}H NMR spectrum of Au-8-bromoguanosine NPs in the 7.0-3.0 ppm region.

Finally, Figure 15 shows ^{1}H NMR spectrum of **Au-inosine** NPs. It is clearly seen that a large number of signals appeared in the 8.4-8.2 ppm region making it more complicated, probably because of oligomer species formation, and/or side products. In the case of inosine, the electron density on aromatic rings does not allow its (or its oligomers') simple and univocal coordination to Au surface, being N1 and N7 both prone to a binding with gold.

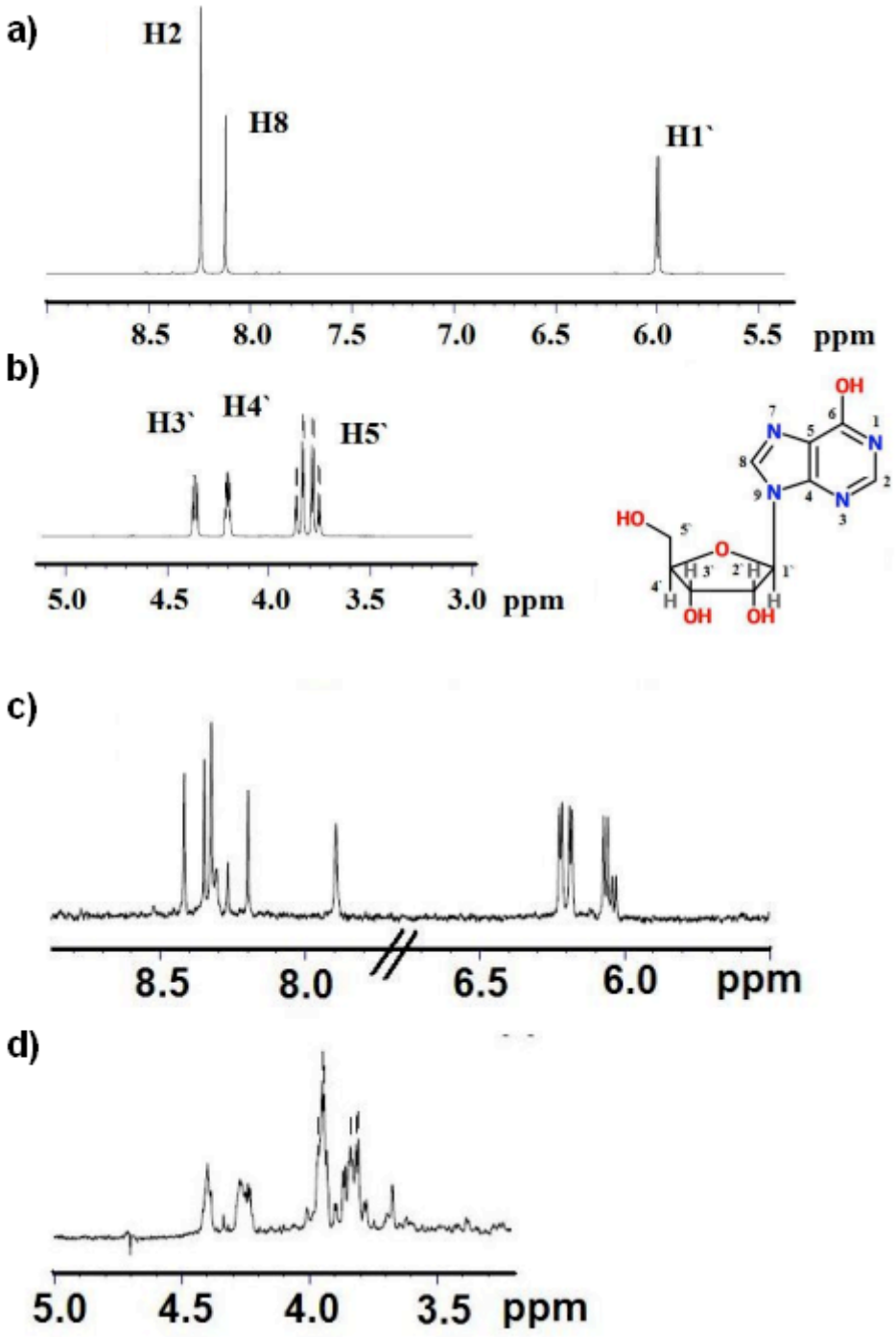

Figure 15. ^{1}H NMR spectra of free inosine in D_2O+CD_3COOD: a) in the 8.5-5.5 ppm region; b) in the 5.0-3.0 ppm region; ^{1}H NMR spectra of Au-inosine NPs: c) in the 8.5-5.5 ppm region; d) in the 5.0-3.5 ppm region.

To summarize, we have established that guanine N7 atom is involved in the interaction with gold surface, while ribose moiety seems free from the binding, undergoing some conformational rearrangements (Scheme 1).

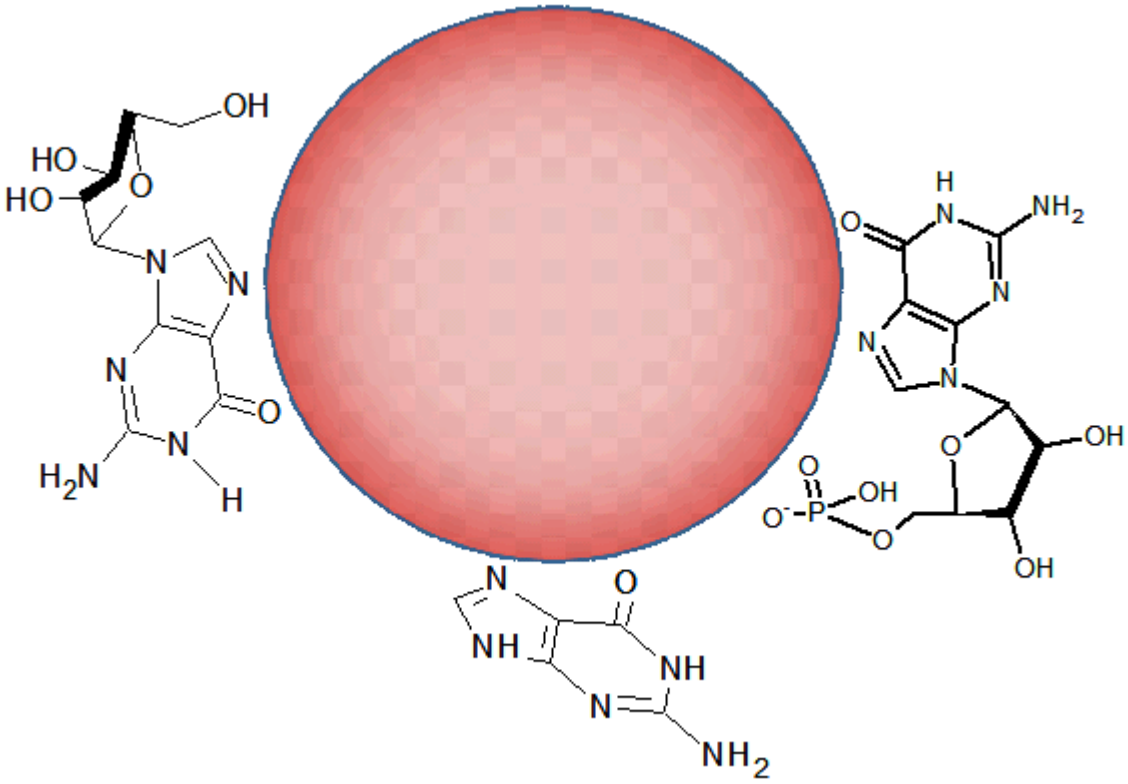

Scheme 1. A representation of the binding sites between guanine, guanosine and guanosine 5`-monophosphate and gold nanoparticles.

To have a clear view of the changes of the ribose puckering taking place under interaction with gold, as well as to understand if other groups are involved in the interaction, we performed ATR-FTIR analysis. In this context, bands of amino- and carbonyl stretching vibrations are of great interest, as well as ring breathing vibrations of guanine moiety, that are useful to diagnose the ribose conformation [43]. Further, the spectra of free compounds are reported with a black line, while those of

capped AuNPs are shown with a red line. The tables of the most important data for each spectrum, and the attributed vibration values are reported in Appendix. Moreover, being a few individual bands strongly overlapped, for their better resolution we used the second derivative spectra, having a maximum at the same position as the original band, but smaller bandwidth [44].

In the spectrum of **Au-guanine** NPs (Figure 16), a strong band at 3202 cm^{-1}, attributed to the stretching modes of the N2-H_2 group, is redshifted of 119 cm^{-1}, suggesting its vertical orientation towards Au. The C6=O stretching decreased in intensity and shifted at lower frequencies with respect to the free molecule, indicating an elongation of C6=O bond, therefore its interaction *via* the oxygen lone pair or double bond. The drastic weakness of C=O stretching vibration should suggest a nearly parallel disposition of guanine with respect to Au surface, while the enhanced out of plane C-H bending indicates that an edge-on orientation does not take place, suggesting its tilting towards gold. In addition, analyzing the second derivative spectrum of **Au-guanine**, broad and intense peak, comprising v (N7-C8) and v (C5-N7) appears after interaction with Au (Figure A3.1, Appendix) [44, 45]. Correlating NMR and FTIR data, guanine interacts with gold *via* its N7 lone pair and C=O double bond, being arranged in a bent position towards Au surface, stabilizing the particles.

Mirkin *et al.* have performed a temperature-programmed study supported by infrared-reflection absorption spectroscopy using a flat gold support with an adsorbed guanine monolayer. It has been found that guanine adsorbs onto a single site represented by two peaks. From the study, the strong C=O stretching peak observed at 1745 cm^{-1} peak suggests the molecular plane of guanine to be nonparallel with the

metal surface, thus, ruling out the possibility of a flat “belly-down” conformation, that go in accordance with our findings.

The spectrum of **Au-guanosine** appears to be significantly different from that of free molecule, because of the nanoparticle-induced changes in the structure of guanosine (Figure 17). Notably, the N2-H_2 stretching vibrations almost disappear, while a very weak band at 2923 cm^{-1} is detectable, tentatively attributed to a hydrogen bond between Au and a H-N group of guanosine. A strongly shifted and split band arises from the carbonyl group, confirming its participation in the interaction with $Au^{\delta+}$ gold sites. On the other hand, a sharp and intense signal, attributed to N-H bending, changes of 71-95 cm^{-1} compared to free molecule, due to the redistribution of electronic density in the aromatic part, involving the perturbations of N1-H and NH_2 bonds, which can originate H-bindings with negatively charged gold centres. Interestingly, both the ribose C-C and guanine ring breathing vibration bands undergo a significant change, being shifted at lower wavenumbers upon interaction with Au, suggesting the changes in the ribose conformation: a C3’-*endo-anti versus* O4’ *-endo-anti* [43], according to the literature data [45] (Scheme 2, panel A). Guanosine binding to different gold surfaces has been discussed elsewhere, giving rise to different suggestions. Having performed SERS analysis, Jang has found that the coordination of guanosine to the gold surface is realized *via* the N1 atom and the oxygen of the C6=O group of the pyrimidine ring [46]. The geometrical configuration proposed indicates that the pyrimidine ring adopts preferably a perpendicular position on the gold surface through the nitrogen N1 atom. Another study performed by Pergolese *et al.* evidenced that guanosine adsorbs on gold nanoparticles through the guanine moiety being parallel to the gold surface, and expressing the oxygen of the

carbonylic group and the N7 atom as molecular sites involved in the interaction with the gold surface [45].

The FTIR spectrum of AuNPs capped by corresponding nucleotide (Figure 18) shows the guanine moiety of **guanosine 5'-monophosphate** involved in the interaction with gold in a similar way: a middle-intensity C(6)=O stretching band splits into two shoulders and shifts of 32 cm^{-1}. Moreover, the shift of 16 cm^{-1} of the phosphate band is e related to its different spatial disposition after interaction with Au, being in a mono-anionic form, i.e. HO-P(=O)(-O-R)($-O^-$) (R = nucleoside). A sharp band at 3334 cm^{-1}, assigned to v(OH) of the ribose, suggests its proximity to the gold surface, while its puckering

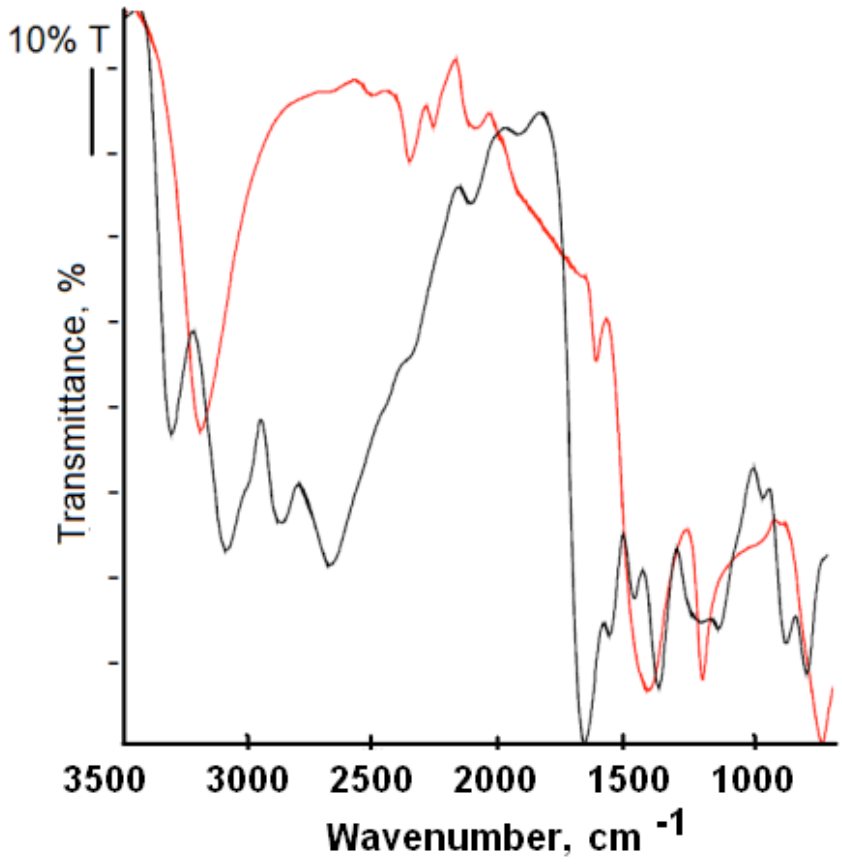

Figure 16. FTIR spectra of guanine (black line) and Au-guanine NPs (red line).

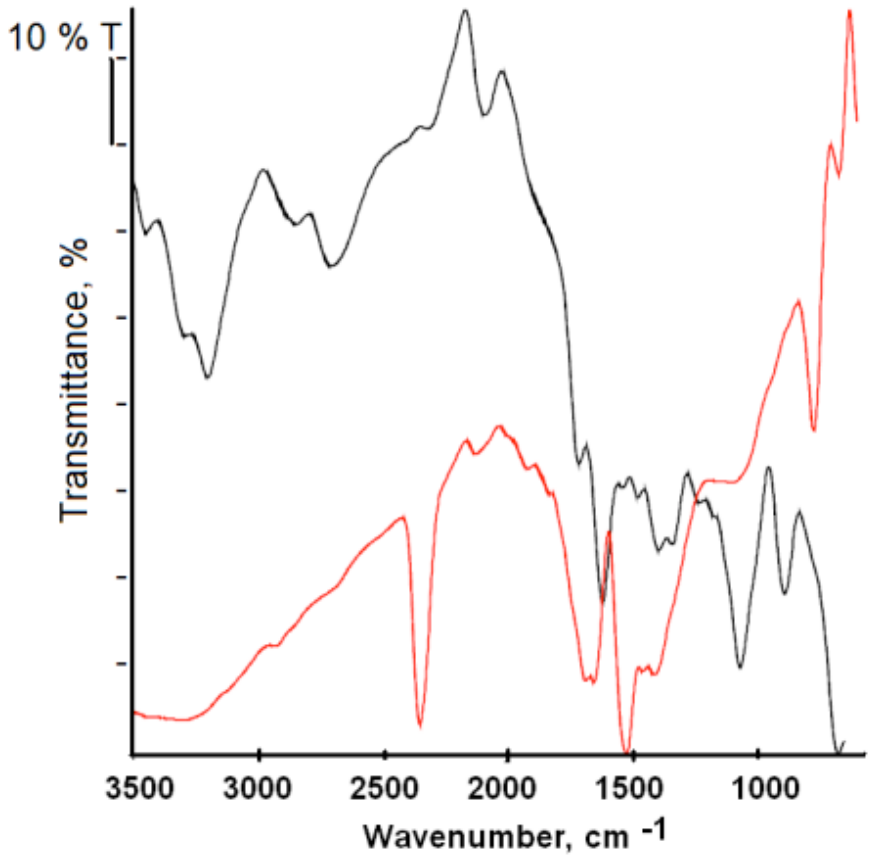

Figure 17. FTIR spectra of guanosine (black line) and Au-guanosine NPs (red line).

changes assuming a C1' *exo-anti* conformation [47] (Scheme 2, panel B), allowing an easy approach of phosphate group. The ^{31}P NMR spectrum is in agreement with FTIR results (Figure 12).

FTIR spectrum of **Au-1-methylguanosine** NPs (Figure 19) shows new vibrations with respect to the free compound**.** We observed a sharp band at 3214 cm^{-1}, arising from NH_2 stretching, and a redistribution of intensities of the components in the 1700–1540 cm^{-1} region: C=O stretching band becomes less intense and shifts of 42 cm^{-1}, while the NH_2 bending band takes part of a broad and intense peak, that includes also a two-shoulder band of N7-C8 and C5-N7 vibrations.

These evidences indicate the **M[1]G** to interact with Au *via* C=O double bond, besides the N7 lone pair (NMR evidence), and suggest that the plane of the molecule is slightly bent towards the gold surface, supporting the general tendency of interaction of these molecules with AuNPs. The ribose (C-O) stretching modes decrease in intensity, becoming hardly detectable, at the same time being well distinguishable in the second derivate spectrum. Interestingly, the band of guanine ring breathing remains centred at 670 cm^{-1}, indicating the conservation of ribose C3'- *endo-anti* conformation in good agreement with NMR data [47].

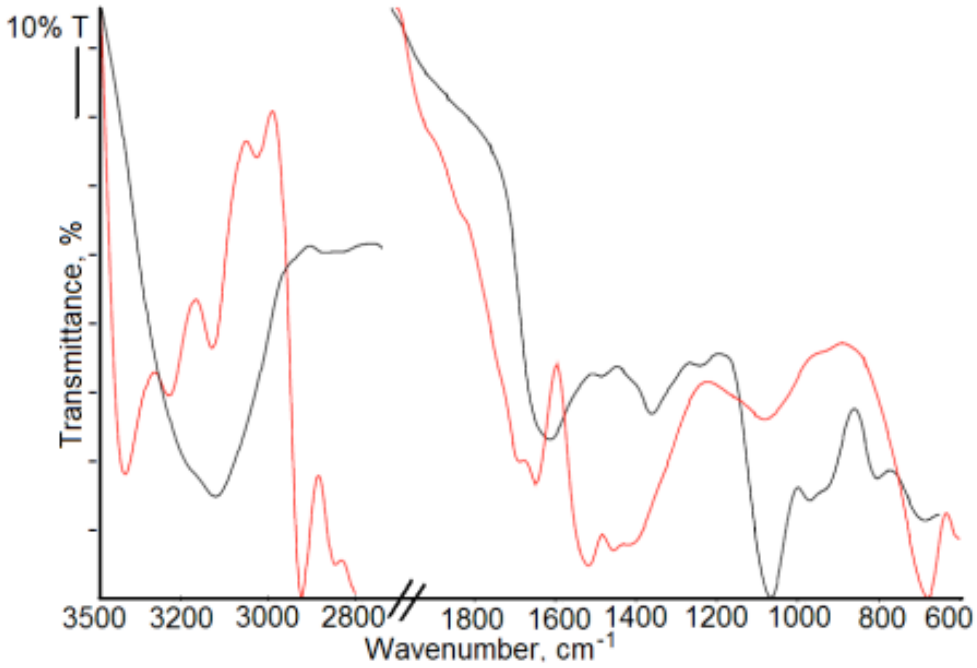

Figure 18. FTIR spectra of guanosine 5'-monophosphate (black line) and Au-guanosine 5'-monophosphate NPs (red line).

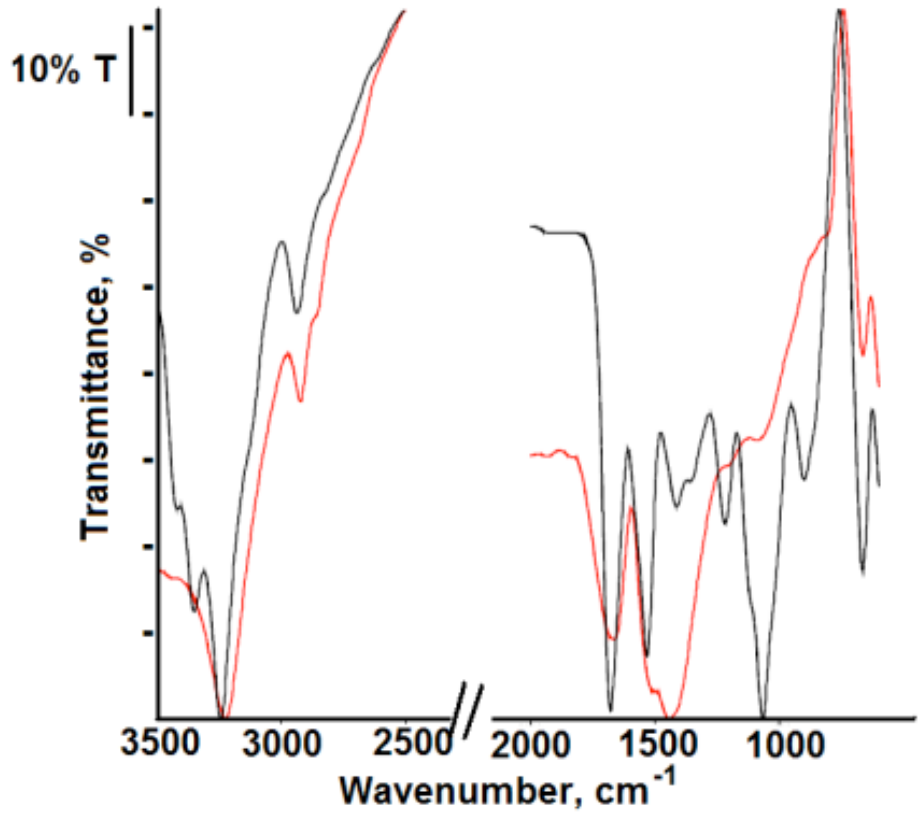

Figure 19. FTIR spectra of 1-methylguanosine (black line) and Au-M^{1}G NPs (red line).

FTIR spectrum of **Au-inosine** NPs shows large differences of the signals in comparison with the free inosine (Figure 20): a new weak band at 3425 cm^{-1} was assigned to OH stretching of ribose moiety, whereas N1-H stretching band is shifted of 80 cm^{-1} at lower frequencies. The C6=O band is split into two components of low intensity, while N1-H bending and N7-C8 ring stretching bands are stuck together forming an intense band. It probably means that inosine has nearly an edge-on disposition on the gold surface, being also able to get involved in C=O interaction and a hydrogen bond with N1-H. Considering ribose vibrations, we observed a sharp band at 1204 cm^{-1}, slightly shifted in comparison with inosine**,** and C-C ribose ring vibrations decreased in intensity.

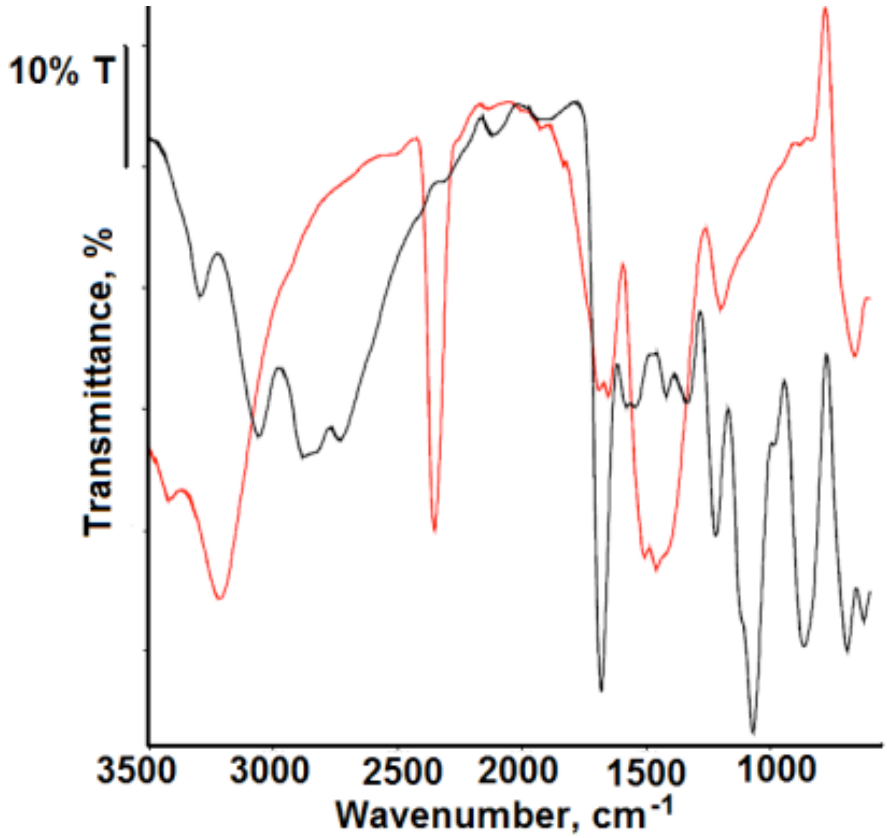

Figure 20. FTIR spectra of inosine (black line) and Au-inosine NPs (red line).

The position of ring breathing bands does mean a C3',C4' *exo-syn* conformation of ribose moiety becoming a C3'-*endo*- *anti* when bound to the gold [47]. The correlation of NMR and FTIR data of Au-inosine NPs suggests a different behaviour in D_2O (^1H NMR) and in the solid state (ATR-FTIR). In solution, the ligand shell is probably not stable with oligomer species being detached and free in D_2O; while in the solid phase the interactions between inosine and gold can be detected, suggesting its edge-on disposition on the gold surface, involving an electronic donation of C6=O oxygen lone pair coupled with an hydrogen bond of N1-H.

Finally, the stretching vibrations of N1-H and NH_2 of free 8-bromoguanosine become a large shapeless band in **Au-8-Br-Gua** NPs (Figure 21), composed of

several signals whereas the CH stretching decreases in intensity and shifts. Moreover, a strong peak appears in the 1700-1500 cm^{-1} region, including both C=O stretching and bending vibrations of N1-H and NH_2. In particular, a two-shoulder band at 1696-1636 cm^{-1} attributed to ν(CO) and NH bending band at 1518 cm^{-1} are both shifted to lower wavenumbers (see the second derivative spectrum for a better examination). The ribose vibrations give rise to a new large band composed of two shoulders at 1079 and 1032 cm^{-1}, and C-C ribose vibrations at 819 and 731 cm^{-1}. Notably, the C2'-*endo*-*syn* ribose conformation in free 8-bromoguanosine changes to C3'-*endo*-*syn* [47]. Thus, the correlation of NMR and FTIR data indicates the 8-bromoguanosine coordination to the gold particles *via* N7 lone pair is not favoured by the steric hindrance of Br substituent. The AuNPs are therefore stabilised by the electronic interactions of C=O double bond and NH_2. Due to the Br atom, the ribose puckering assumes a C3'-*endo*-*syn* conformation, the same observed in the free ligand (Scheme 2, panel D).

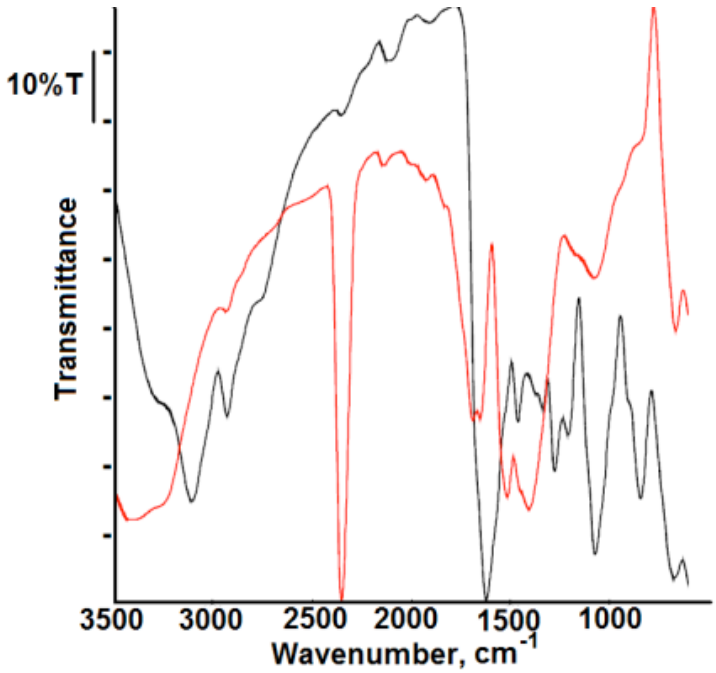

Figure 21. FTIR spectra of 8-bromoguanosine (black line) and Au-8-Br-Guo NPs (red line).

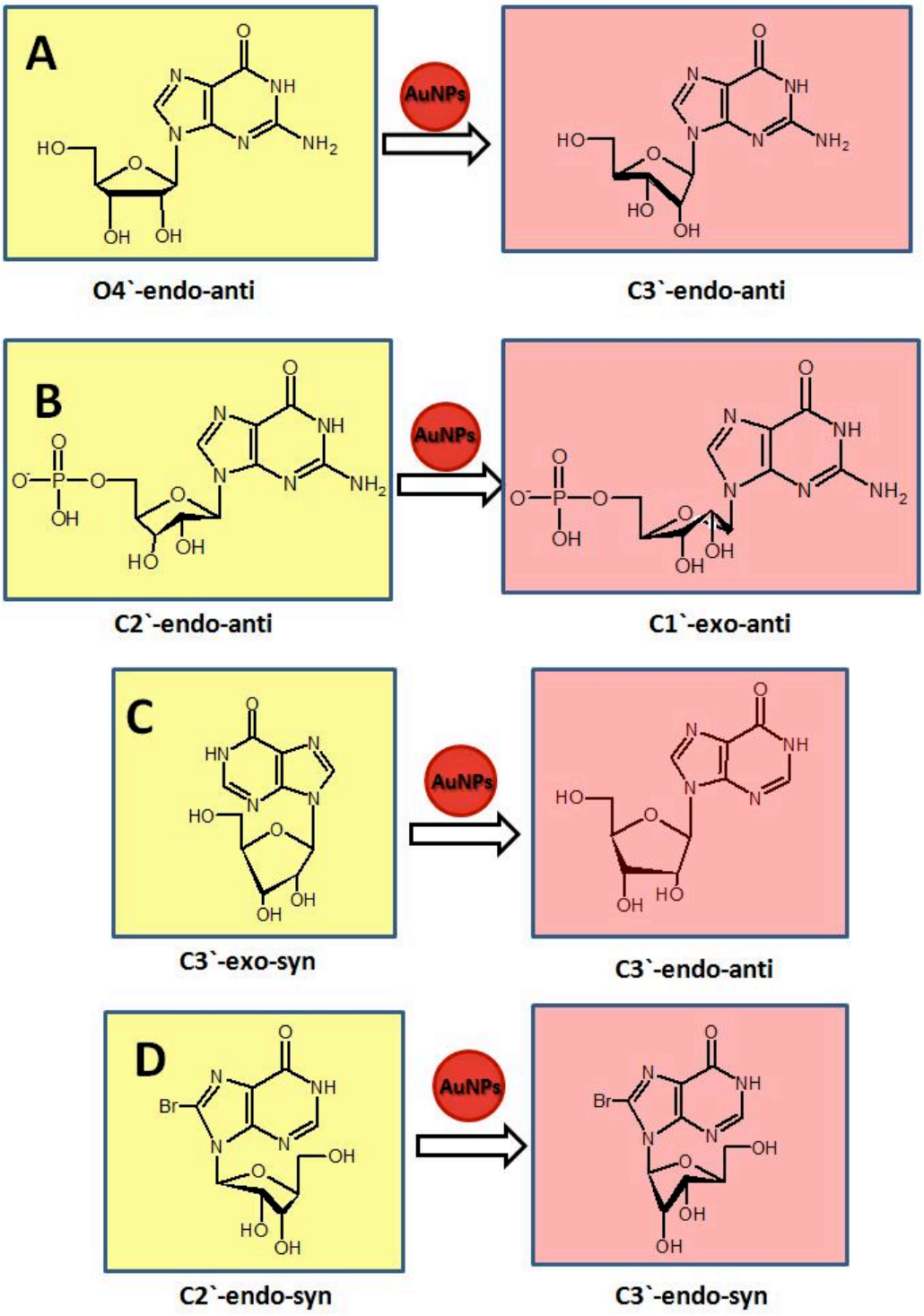

Scheme 2. An illustration of the conformational changes of the ribose moiety after binding to the AuNPs: A) guanosine, B) guanosine 5`-monophosphate, C) inosine, D) 8-bromoguanosine.

Table 3. Ribose puckering and ring breathing bands before and after interaction with gold nanoparticles.

Guo	**Au-Guo**
C3`-endo-anti 686 cm^{-1}	*O4`-endo-anti* 665 cm^{-1}
5`-GMP	**Au-5`-GMP**
C2`-endo-anti 699 cm^{-1}	*C1`-exo-anti* 674 cm^{-1}
M^1G	**Au-M^1G**
C3`-endo-anti 668 cm^{-1}	*C3`-endo-anti* 670 cm^{-1}
Ino	**Au-Ino**
C3`-exo-syn 692; 629 cm^{-1}	*C3`-endo-anti* 662 cm^{-1}
8-Br-Guo	**Au-8-Br-Guo**
C2`-endo-syn 681 cm^{-1}	*C3`-endo-syn* 667 cm^{-1}

Based on the above interpretation of NMR and FTIR results, we can conclude that most of “guanine family” compounds interact with the particles *via* N7 atom and C=O group, in their neutral form, as the H8 signal is shifts in ^{1}H NMR and the C=O band significantly changes in ATR-FTIR spectra, in comparison with free compounds. On the other hand, 8-bromoguanosine differs in its binding, while inosine gives more than one product in the colloidal system. Moreover, guanosine and 8-bromoguanosine derivatives showed to be able to form weak hydrogen bonds between N1-H group and gold surface, having observed changes of stretching and

bending NH bands after interaction with gold. Kryachko and Remakle have found that guanine moiety interacts with gold clusters throughout an Au-O6 anchor bond along with nonconventional hydrogen bonds with N1-H center. The formation of the anchor bond “catalyzes” through charge redistribution the gold atoms to serve as a nonconventional proton acceptor and to form, *via* its lone pair 5*d* orbital, a nonconventional hydrogen bond with the conventional proton donor of guanine moiety [24].

The substitution on C8 atom leads to a different constrain depending on bulky substituent, and different pathways of reaction can be possible for the building up of Au-purine NPs, as demonstrated for Au-8-bromoguanosine NPs. Novel results on the conformational changes of ribose puckering highlight that it can occur when purine derivatives interact with AuNPs. The need of conformational changes is strictly related to the electronic properties of guanine ring after contact with gold surface throughout N7 and C=O. Moreover, the phosphate group of guanosine nucleotide is strongly involved in a polar interaction with gold surface, being monoprotonated, HO(O)PO-R)(O^-) due to the pH of colloids.

3.1.2. Thymine, thymidine and thymidine 5`-monophosphate

Having *pKa* of N3 atom deprotonation ~ 10, all the three compounds exist in neutral (unprotonated) form at giving reaction conditions (pH 3.5) (Figures A3.10-12, Appendix). It has been already mentioned that thymine can spontaneously form platinum-nucleobase complexes, with bridging donor atom to be originated from pyrimidine entity (e.g. N3 and O4 atoms). Thymidine adsorption on Au(111) surface studied by photoemission spectroscopy revealed that the thymine moiety is lying nearly parallel to the Au(111) surface. Surface-enhanced Raman spectroscopy (SERS) study of Jang [46] shows that thymidine binds to the gold surface *via* the oxygen of the C4=O group of the pyrimidine ring. While Mirkin *et al.* have found from TPD-MS studies that thymine desorption occurs at the lowest temperature comparing with other nucleobases, giving rise to a single peak, suggesting the weakness of the bond between gold surface and thymine, and the binding *via* a single-site [38].

NMR studies were carried out using the samples prepared by concentrating gold nanoparticles suspensions scaling up the amounts of all the components. ^{1}H NMR spectra of thymine and **Au-thymine** NPs in D_2O are reported in Figure 22. The signals at 7.31 and 1.79 ppm were assigned to H6 and CH_3 of free thymine. The chemical shift has not changed significantly, but the peaks are broadened in the spectra of capped AuNPs, indicating a very weak interaction, that is in accordance with Mirkin`s observations. The same behavior is observed from the spectra of thymidine and **Au-thymidine** NPs (Figure 23). This may indicate both the weakness of the interaction between thymine ring, and uninvolvement of the ribose moiety in the binding.

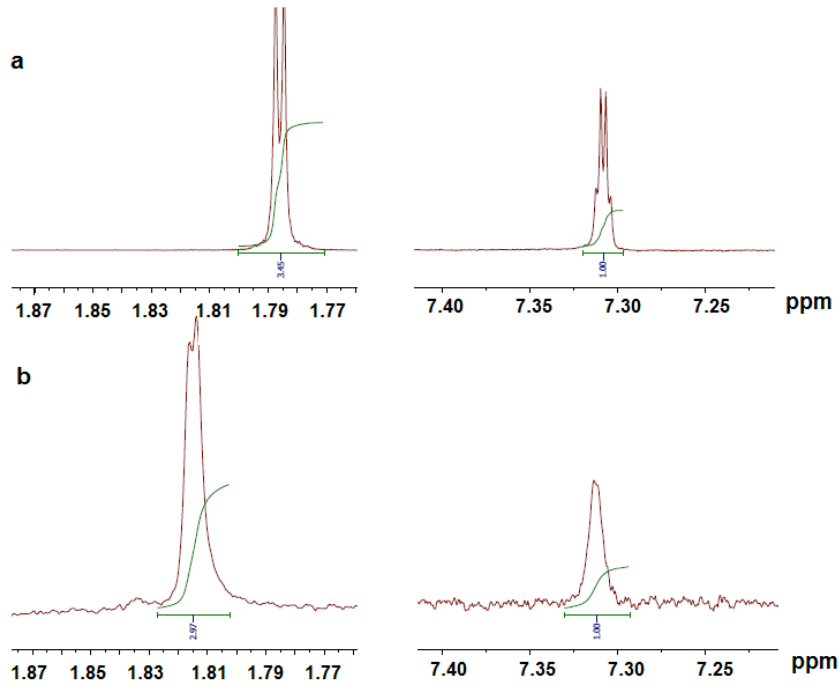

Figure 22. ^{1}H NMR spectra of thymine (a) and Au-thymine NPs (b) in D_2O in the range from 1.9 to 1.75 ppm and from 7.4 to 7.2 ppm.

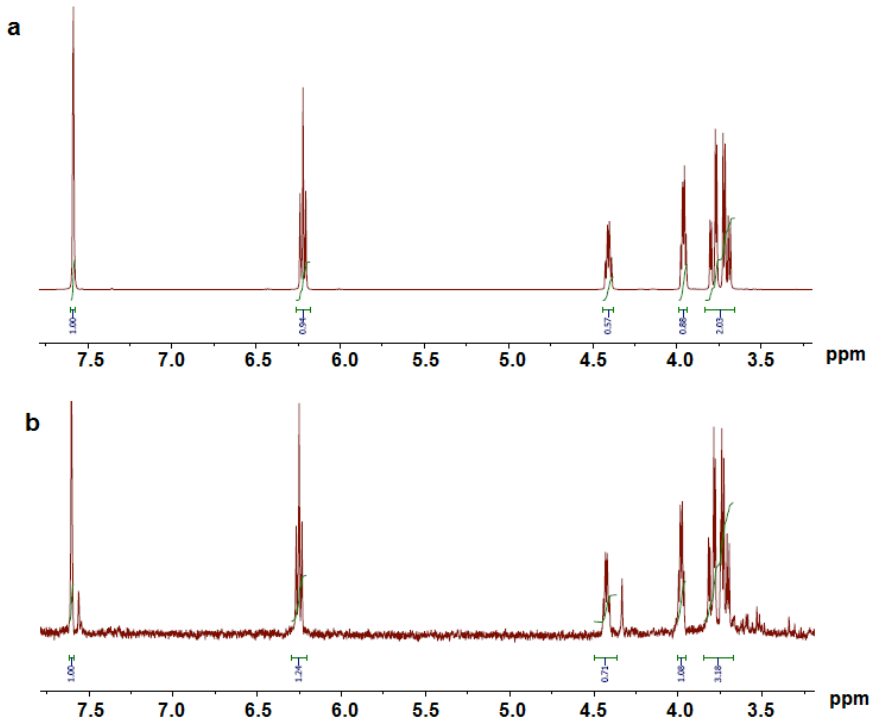

Figure 23. ^{1}H NMR spectra of thymidine (a) and Au-thymidine NPs (b) in the 7.5 to 3.5 ppm range.

On the other hand, the spectrum of **Au-thymidine 5`-monophosphate** NPs is considerably different from that of free compound (Figure 24-26). The signals corresponding to the thymine ring have not notably changed the position, while the H4`- H5` ribose signals drastically change upon interaction with gold (see Appendix). ^{31}P NMR spectra reveal an important shift of the phosphorous signal from 3.79 to 0.27 ppm after interaction with AuNPs (Figure 27). These findings indicate that phosphate moiety and neighboring oxygen atoms are strongly affected by the proximity of the gold surface.

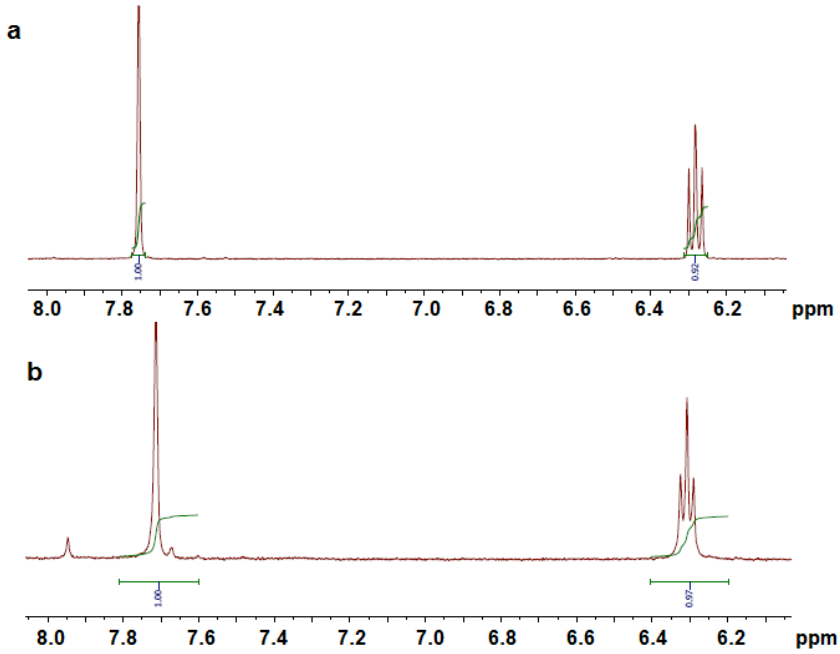

Figure 24. ^{1}H NMR spectra of thymidine 5'-monophosphate (a) and Au-thymidine 5'-monophosphate NPs (b) in D_2O in the 8 to 6.2 ppm range.

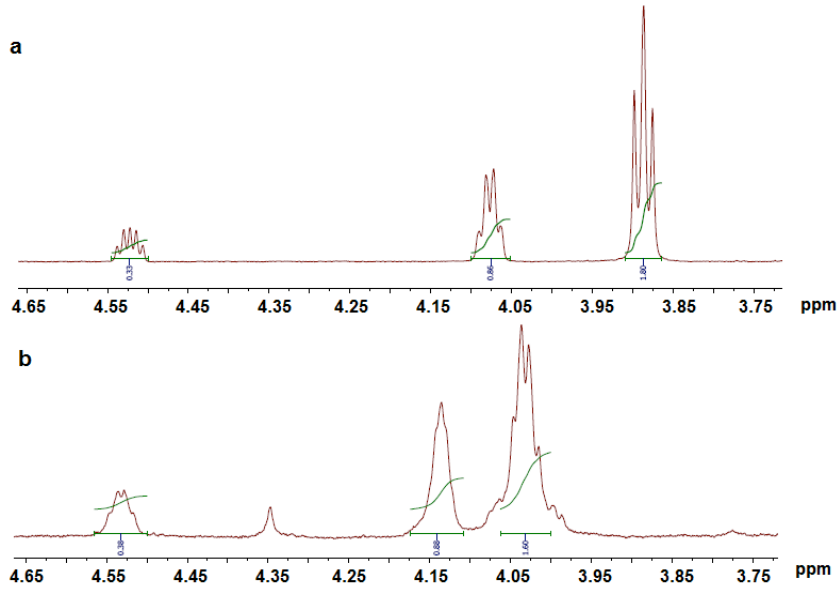

Figure 25. ^{1}H NMR spectra of thymidine 5'-monophosphate (a) and Au-thymidine 5'-monophosphate NPs (b) in D_2O in the 4.7 to 3.7 ppm range.

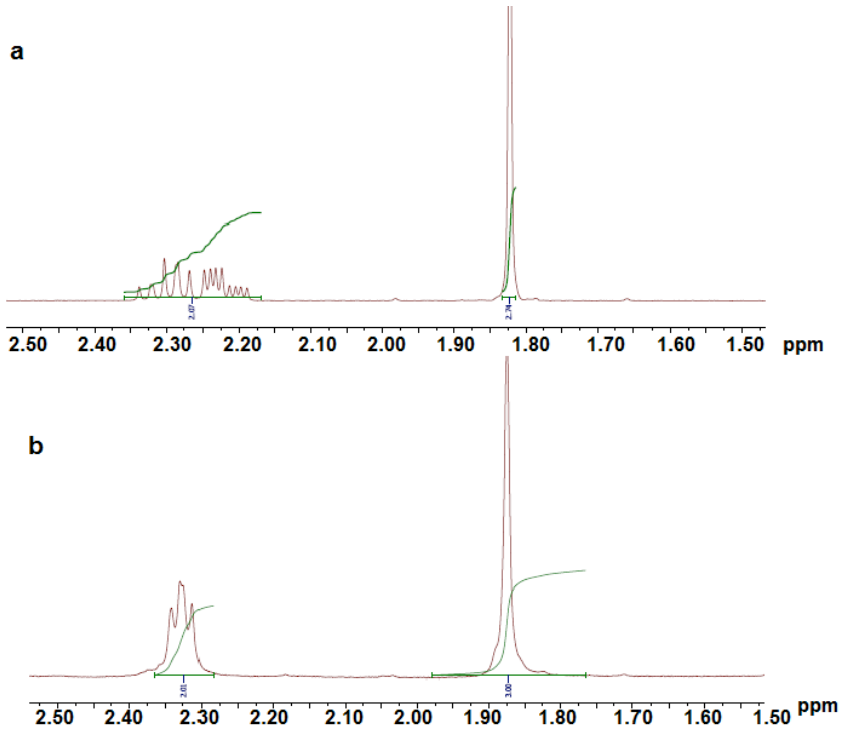

Figure 26. ^{1}H NMR spectra of thymidine 5'-monophosphate (a) and Au-thymidine 5'-monophosphate NPs (b) in D_2O in the 2.5 to 1.5 ppm range.

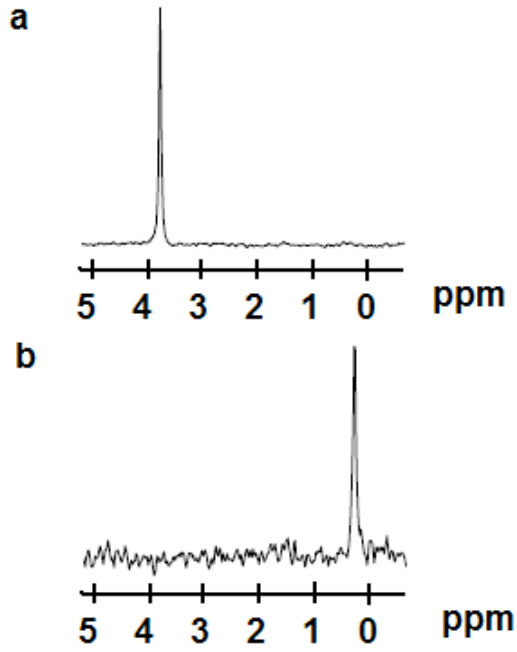

Figure 27. ^{31}P NMR spectra of thymidine 5'-monophosphate (a) and Au-thymidine 5'-monophosphate NPs (b) in D_2O in the 5 to 0 ppm range.

Due to the weakness of the changes observed for the hydrogen signals of thymine ring, we performed more detailed FTIR study in order to better analyze the binding sites. The plots in Figure 28 reveal that when **thymine** binds to gold, the infrared spectra change significantly compared to the isotropic spectrum of the compound in the crystalline state. Sharp characteristic bands of NH and C=O varies both in intensity and wavenumber after interaction. A weak band, found at 3201 cm^{-1} in free thymine and assigned to the stretching of amino group, shifts of 16 cm^{-1} to longer wavenumbers and enhances in intensity, while CH and CH_3 stretching bands become almost undetectable in the Au-thymine spectrum. A sharp and intense stretching band, attributed to C2=O and C4=O, shifts from 1736 to 1697 cm^{-1} under binding, most likely because of interactions with the gold nanoparticles. The band of NH bending (1431 cm^{-1}) gives rise to two different bands at 1512 and 1415 cm^{-1} with

a major intensity. It has been proved by Kryachko, that thymine can create nonconventional N–H---Au hydrogen bonds, similar to weak conventional H–bonds, that is in accordance with our data [24, 25]. Finally, the out-of-plane δ(C-H) provide a shifted very strong band at 726 cm^{-1}. These observations suggest that thymine is affected by the proximity to the metal surface, interacting *via* the carbonyl oxygen, involving also amino N3-H group. Mirkin *et al.* suggest that both the C4=O and C2=O groups, along with amino group, are involved in the binding to the gold. A flat "belly-down" orientation would allow thymine to interact simultaneously with gold in this way.

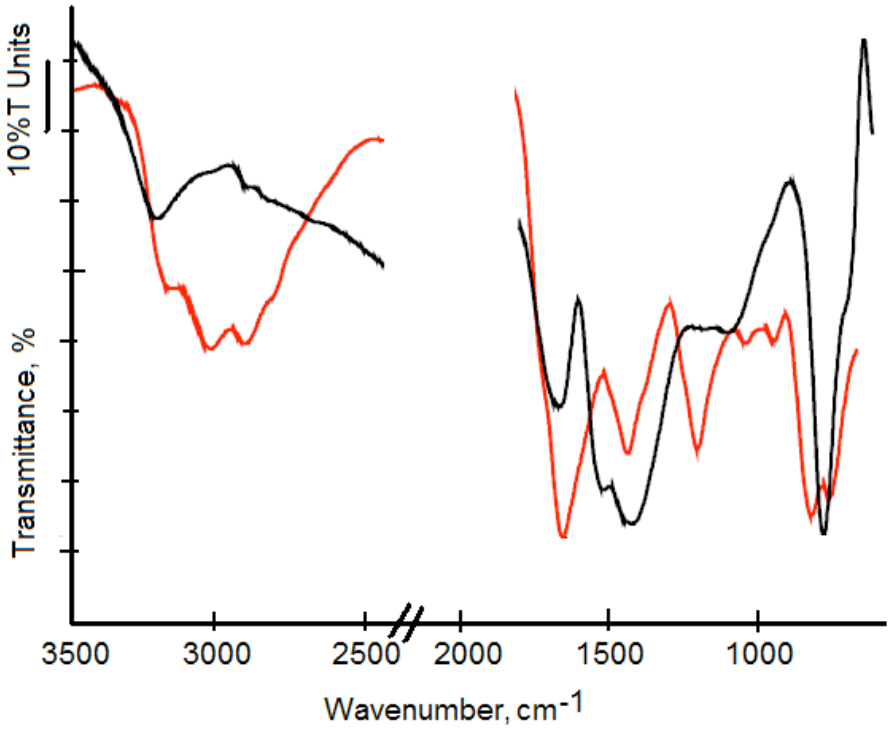

Figure 28. ATR-FTIR spectra of thymine (red line) and Au-thymine NPs (black line).

The spectrum of **thymidine** significantly changes under interaction with gold, as well. The band at 3296 cm^{-1} assigned to the stretching modes of N3-H group, shifts at lower frequencies giving rise to a large equal-intensity band at 3216 cm^{-1}. On the other hand, an intense band at 1664 cm^{-1}, comprising both C=O and C=C stretching vibrations, becomes very weak, while the bands in 1450-1000 cm^{-1} region, comprising ribose ring vibrations, originate a shapeless large set of bands decreased in intensity under interaction with gold.

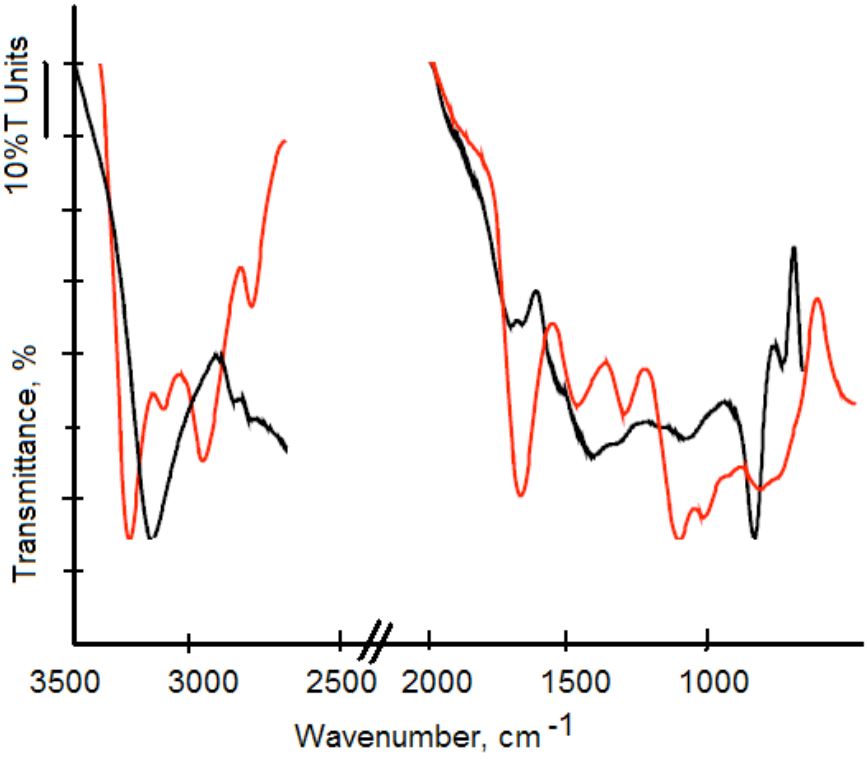

Figure 29. ATR-FTIR spectra of thymidine (red line) and Au-thymidine NPs (black line).

Finally, a weak band, centered at 731 cm^{-1} in free thymidine spectrum and assigned to the out-of-plane C-H bending modes, shifts of 43 cm^{-1} to the higher frequencies upon interaction, significantly increasing in intensity. Basing on these data, thymidine seems to bind to AuNPs in a similar way as corresponding

nucleobase, with the ribose moiety to be affected under interaction.

The spectra of **thymidine 5`-monophosphate** and capped AuNPs are shown in Figure 30. Due to the difficulty to accurately assign the position of the stretching modes of NH, OH and CH groups in the both spectra, caused by the broadness of the bands, we recur to the second derivative spectra. The data of the bands before and after interaction with gold are reported in Table A3.12, Appendix. All the bands of **Au-5`-TMP** NPs seem to be shifted comparing to the free ligand, indicating a perturbation caused by the proximity to the gold.

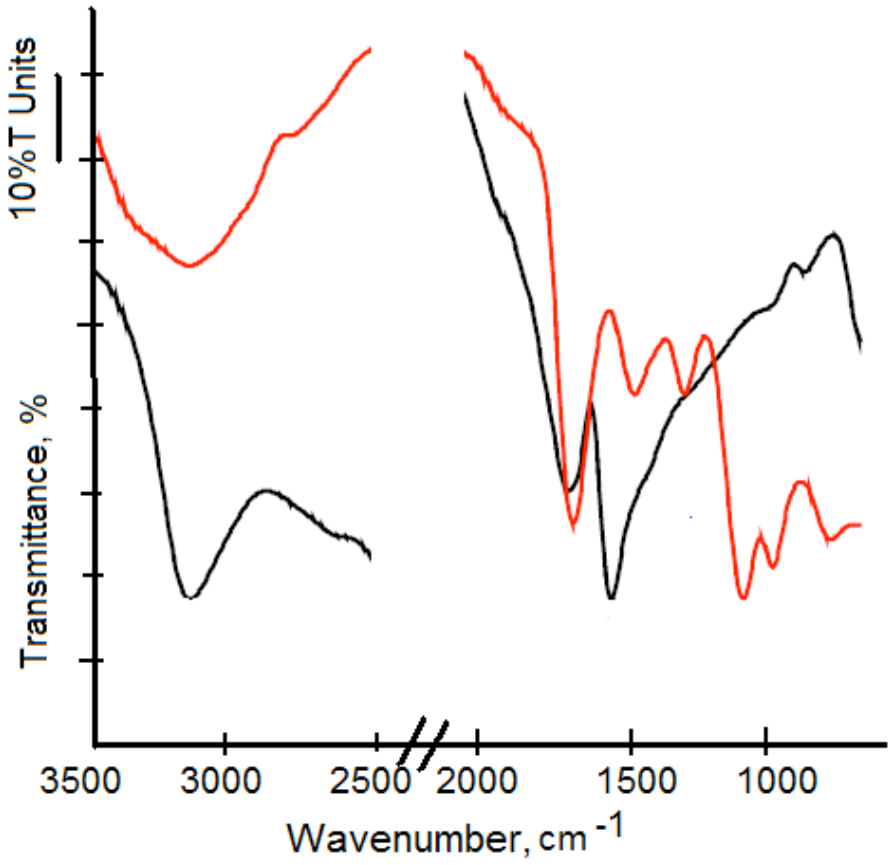

Figure 30. ATR-FTIR spectra of thymidine 5'-monophosphate (red line) and Au-thymidine 5'-monophosphate NPs (black line).

The C=O stretching band is slightly shifted from 1671 to 1688 cm^{-1}, showing an intense band in AuNPs spectrum. Like in other cases, a significant up-shift was observed for the N3-H bending modes (from 1453 to 1522 cm^{-1}), indicating the involvement of the amino group in the interaction. The phosphate R-OPO_3^{2-} bands, normally appearing in the characteristic zone (1150–900 cm^{-1}) [48, 49] for free nucleotides, is hardly recognized in the spectrum of the capped AuNPs, and can be seen only in the second derivative spectrum, suggesting P=O vibrations in a plane close to parallel to the gold surface.

Thus, correlating the data obtained from NMR and FTIR, we can draw the following conclusions: thymine and thymidine weakly bind to the gold surface involving C=O4 and N3-H groups, with the latter able to form non-conventional hydrogen bonds with gold surface. Thymidine 5`-monophosphate seems to show a stronger interaction due to the presence of a phosphate group, which may participate in electrostatic stabilization of AuNPs.

3.1.3. Adenine, adenosine and adenosine 5`-monophosphate

Adenine provides three unprotonated endocyclic nitrogen atoms (N1, N3, N7) at physiological pH, all of which are potential metal binding sites. The basicity order is N1>N7>N3 [40]. While in duplex DNA the N7 site is preferred as a metal binding site, with isolated adenine base a pronounced dichotomy exists for metal binding at N1 and N7. Only in strongly acidic pH, when N1 site is fully protonated, the metal binding is preferentially through N7. Under given reaction conditions (pH 3.5), adenine exists both in neutral form (78%) and protonated at N1 atom (22%) (Table 8).

Figure 31 shows the spectra of adenine at pH 3.5 (a) and **Au-adenine** NPs (b). The both H2 and H8 signals are upfield upon interaction with gold: H2 signal

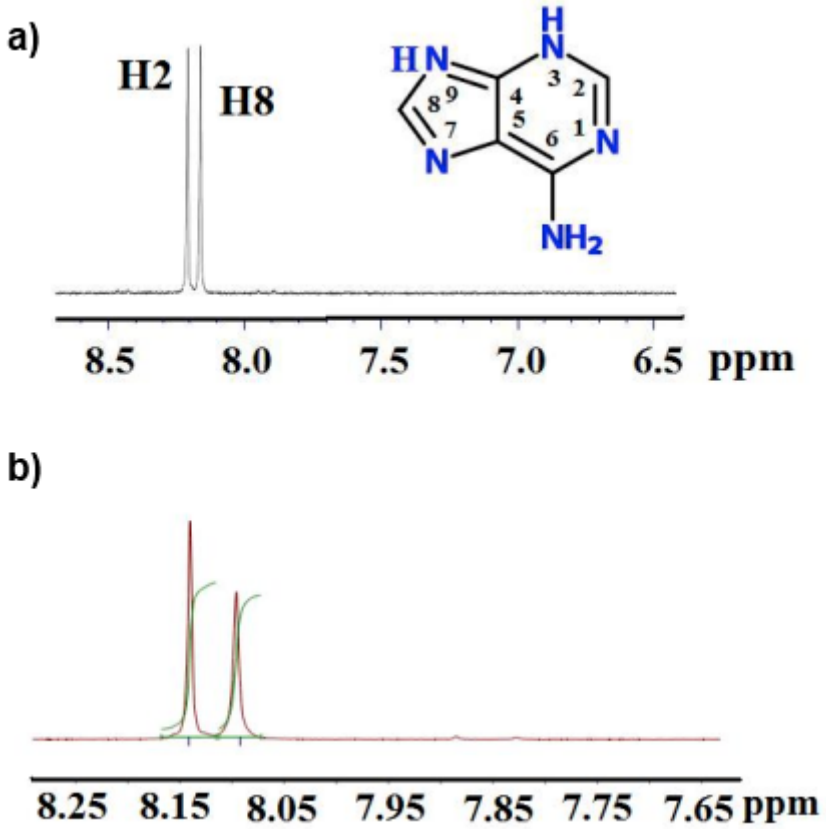

Figure 31.1H NMR spectra of a) adenine and b) Au-adenine NPs.

moves from 8.21 to 8.14 ppm, while H8 signal changes from 8.16 to 8.10 ppm. Since the most part of the species are unprotonated at N7 and N1, the chemical shift of the neighboring hydrogen atoms may indicate the interaction *via* the two nitrogen atoms or the presence of two separate species on the gold surface.

Adenosine does show significant changes in the chemical shift of all the signals after interaction with gold (Figure 32). The H2 and H8 signals shift upfield from 8.28 and 8.17 ppm to 7.94 and 7.68 ppm, respectively. The ribose signals are also affected by the interaction, in particular, the H1` and H3` signals drastically shift

from 6 and 4.23 ppm to 5.55 and 3.95 ppm, respectively. It is clearly seen that adenosine behaves in a similar way with the corresponding nucleobase: both N7 and

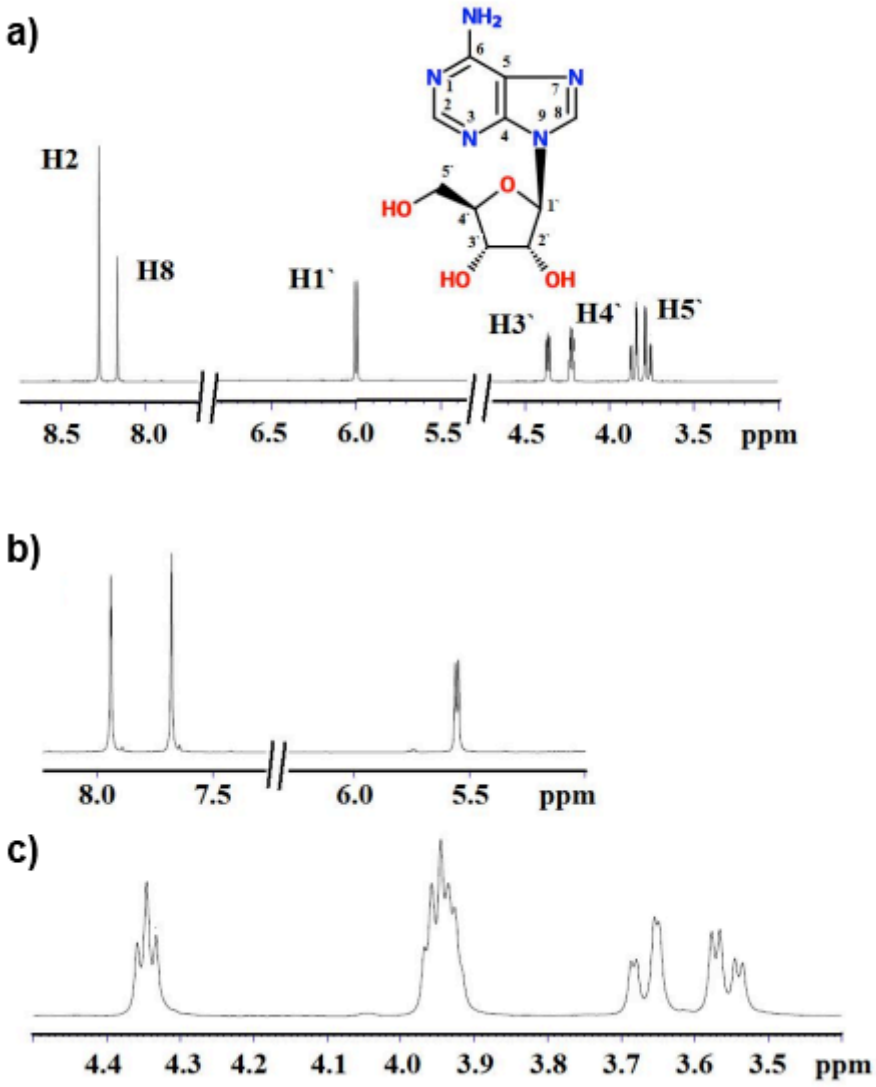

Figure 32.1H NMR spectra of a) adenosine, b) Au-adenosine NPs in 8.5-5.0 ppm region, and c) Au-adenosine NPs in 4.5-3.4 ppm region.

N1 atoms are probably involved in the binding, while the ribose moiety is strongly affected by the interaction.

The spectra of **adenosine 5'-monophosphate** and corresponding AuNPs are reported in Figure 33, 34. It is clearly seen that nanoparticles spectrum changes considerably and becomes more complicated. The H2, H8 and H1' signals give rise to several signals, which may be due to the presence of different species in the sample. Ribose region also changes: all the signals broaden and shift indicating a perturbation of ribose moiety in the proximity with gold surface. Importantly, the phosphorous signal notably changes from 3.60 ppm to 0.23 ppm, pointing to a strong interaction between the phosphate group and gold surface.

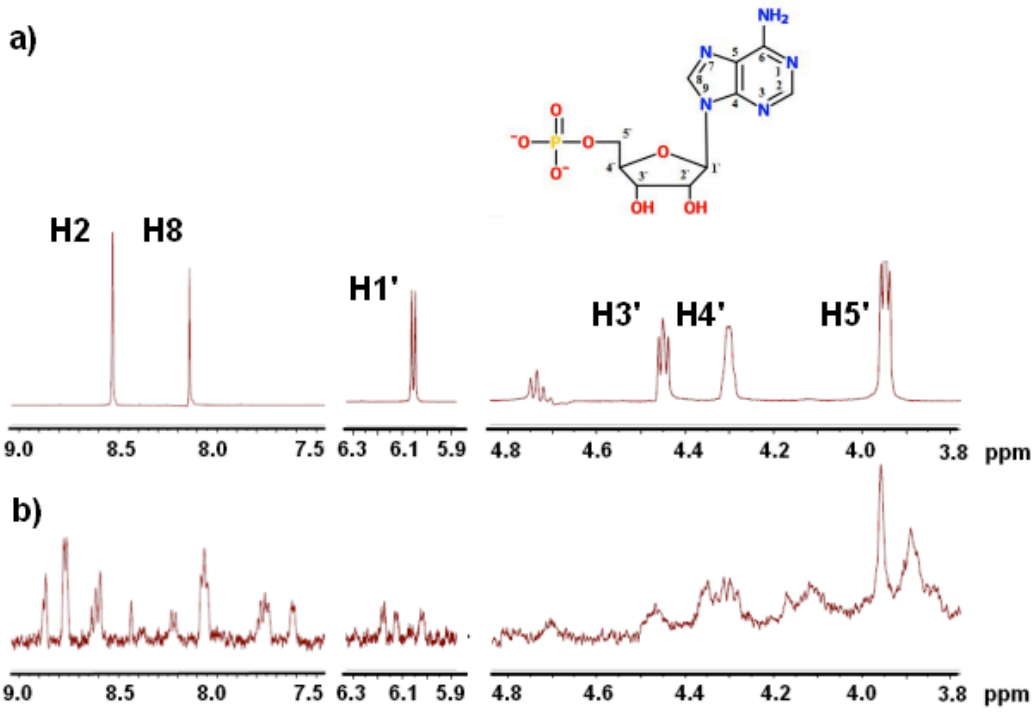

Figure 33.1H NMR spectra of a) adenosine 5'-monophosphate, and b) Au-adenosine 5'-monophosphate NPs in 6- -1 ppm region.

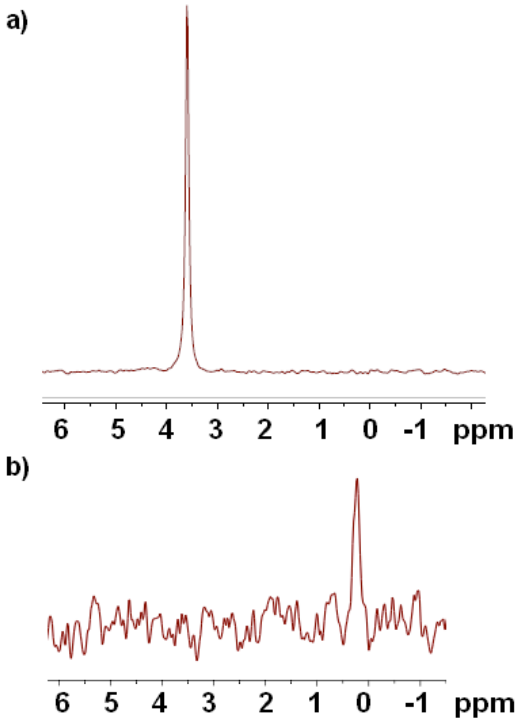

Figure 34. 31P NMR spectra of a) adenosine 5'-monophosphate, and b) Au-adenosine 5'-monophosphate NPs in 6- -1 ppm region.

The FTIR spectra of adenine and **Au-adenine** NPs are reported in Figure 35. The spectrum of solid adenine shows clearly defined bands at 3273, 3092 and 2969 cm^{-1} attributed to the stretching modes of NH_2, C8-H and C2-H groups, respectively. Upon interaction with gold, the only band located at 3202 cm^{-1} is visible, suggesting a flat orientation of the NH_2 onto the gold surface. The δ (NH_2) scissoring, found at 1663 cm^{-1} in solid adenine, significantly changes and splits in two bands at 1697 and 1645 cm^{-1} in Au-adenine NPs, suggesting a possible slightly tilted orientation. The low intensities of the bands corresponding to the ring and located in the 1300-900 cm^{-1} region in Au-adenine spectrum, support its flat orientation. Our findings are in accordance with Mirkin`s *et al.* which suggest that adenine coordinates to the gold

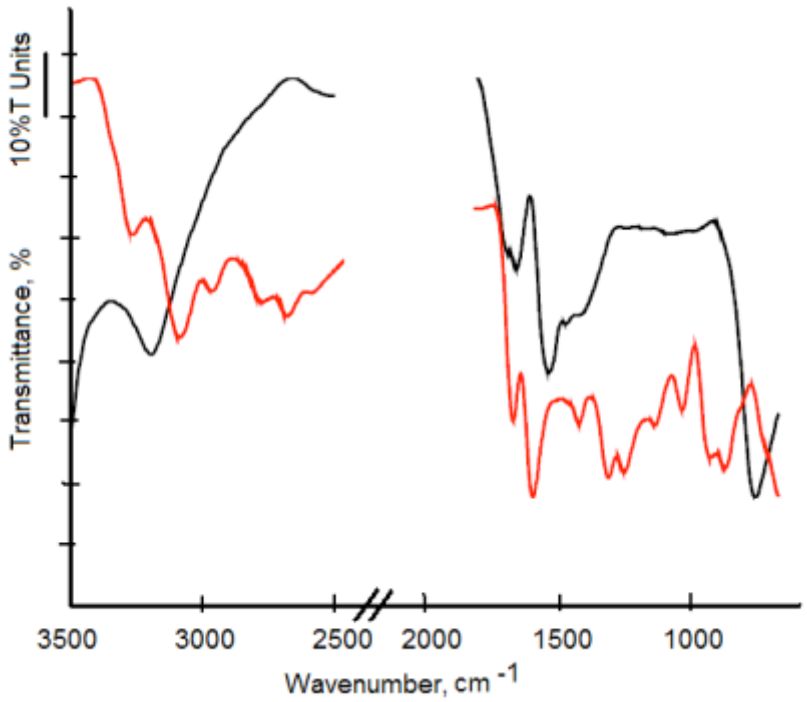

Figure 35. ATR-FTIR spectra of adenine (red line) and Au-adenine NPs (black line).

flat surface through the amino group, thus changing the hybridization of the N10 atom from sp^2 (planar) to sp^3 (pyramidal). This distorted, no planar geometry is compatible with appearance of NH_2 scissoring.

The FTIR spectrum of free **adenosine** is quite similar to that of adenine and shows intense bands at 1644 and 1590 cm^{-1} due to the scissoring modes of NH_2 and NH groups (Figure 36). The stretching NH_2 modes give a band at 3147 cm^{-1} in free adenosine which increases in intensity and shifts a few wavenumbers to 3201 cm^{-1} under interaction with AuNPs. On the other hand, the scissoring band significantly decreases in intensity and is hardly detectable at 1608 cm^{-1} in the AuNPs spectrum. Adenine ring vibrations found in free adenosine in 1470-1300 cm^{-1} region, now shift and take part of a single large sharp band and can be detected in the second derivative spectrum.

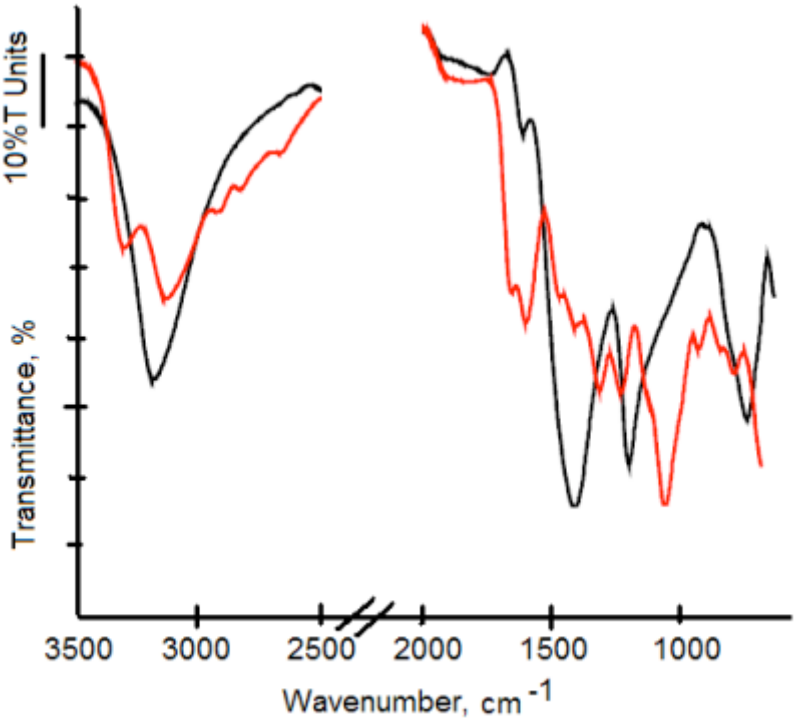

Figure 36. ATR-FTIR spectra of adenosine (red line) and Au-adenosine NPs (black line).

A middle-intensity band at 1209 cm^{-1} assigned to C1`-N9 vibrations in free adenosine, is detected at 1184 cm^{-1} in Au-adenosine spectrum, indicating a nonplanar orientation of the glycosidic bond on the gold surface. Moreover, ribose breathing band is now shifted (from 759 to 708 cm^{-1}) and increased in intensity confirming a nonplanar orientation of the ribose moiety. Thus, the FTIR results are in accordance with the NMR data, indicating a perturbation in the ribose moiety under interaction with AuNPs.

The spectrum of **adenosine 5'-monophosphate** (Figure 37) changes considerably after interaction with gold: all the stretching bands (-OH, -NH, $-NH_2$) clearly seen in the 3400-3100 cm^{-1} region become a large shapeless band; the only band, found at 2924 cm^{-1}, may be a result of a small shift of v (CH) band centered at

2953 cm^{-1} in the spectrum of free compound. The scissoring vibrations of NH_2 group give rise to a band at 1640 cm^{-1} in nucleotide spectrum, slightly shifted to 1645 cm^{-1} under interaction. A set of the middle-intensity bands in the 1490-1240 cm^{-1} region may be assigned to the adenine ring modes, and becomes a large intense band containing several components. The possibility to observe both amino-group and adenine ring modes in the spectrum of AuNPs indicate a tilted disposition of the molecule on the gold surface. Importantly, phosphate moiety symmetrical vibrations band centered at 1074 cm^{-1} in free nucleotide spectrum, gives rise to a less intensive but still clearly observed band with two components, at 1097 and 1028 cm^{-1}, indicating a strong electrostatic interaction with AuNPs.

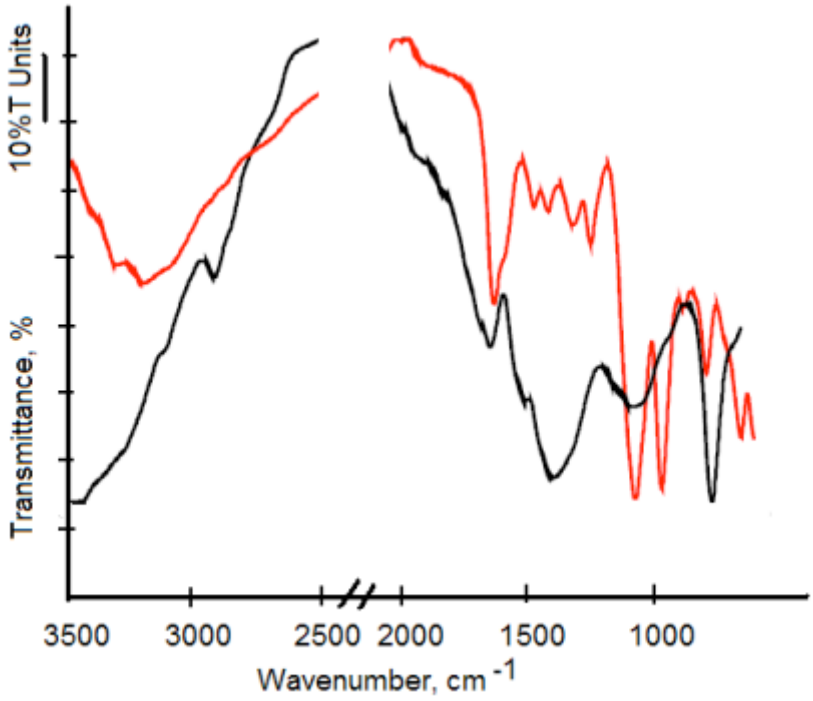

Figure 37. ATR-FTIR spectra of adenosine 5'-monophosphate (red line) and Au-adenosine 5'-monophosphate NPs (black line).

Concluding NMR and FTIR results, adenine, adenosine and adenosine 5'-monophosphate seem to interact with AuNPs *via* NH_2 group of adenine ring, involving N7 lone pair of electrons. The ribose moiety is affected by the interaction, giving rise to a significant changes in NMR spectra, while the phosphate moiety may interact with gold surface electrostatically, providing the particle stabilization.

3.1.4. Cytosine, cytidine and cytidine 5'-monophosphate

Of all endocyclic N atoms of the four nucleobases, N3 of cytosine is the most basic one, hence has the highest *pKa* value and the highest affinity for H^+. Thus, binding to either N3 or O2 is favored. At our reaction conditions, cytosine is protonated at 89% at N3 atom, and only 11 % of cytosine exists in neutral unprotonated form. The change of pH from neutral (pH 7) to acidic does not provoke a great change of H6 and H5 chemical shifts in ^1H NMR spectrum of free cytosine (Table 3, Appendix). On the other hand, the spectrum of **Au-cytosine** NPs becomes more complicated showing a group of new signals in the 8.2-7.4 ppm range (Figure 38). This may be due to the formation of side products soluble in water or the presence of different cytosine species (protonated and unprotonated). The H5 signal considerably shifts, from 5.93 ppm to 5.40 ppm, being affected by the interaction with gold. The binding to N1 blocked cytosine (*e.g.* cytidine and cytidine 5'-monophosphate) can occur in any of the following ways: through N3, O2, NH_2, C5, or in π-fashion through C5 and C6 [40]. Cytidine, like corresponding nucleobase, exists both in protonated form at N3 atom (78%) and in neutral.

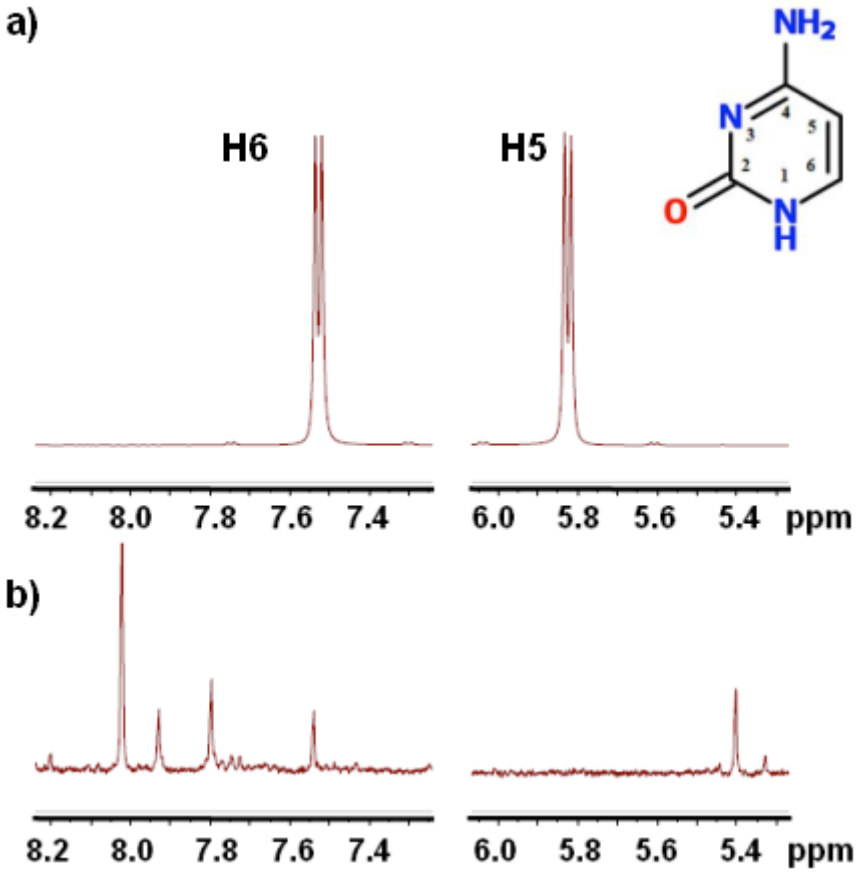

Figure 38.1H NMR spectra of a) cytosine, and b) Au-cytosine NPs in the 8.2-7.4 and 6.0-5.4 ppm region.

Similarly to cytosine, ^{1}H NMR spectrum of **cytidine** is not affected by the acidic conditions, showing a minimal downfield change of the chemical shift values (Figure 39). A similar picture is observed in the spectrum of Au-cytidine NPs: the 8.5-8.0 ppm region shows numerous signals, among which, however, it may be possible to detect the H6 and H5 proton signals. The two resonances shift downfield from 7.79 and 5.99 ppm to 8.13 an 6.25 ppm, respectively. Nevertheless it is hard to track the exact position of the signals, it is clearly seen that ribose resonances are highly affected by the interaction, causing their broadening.

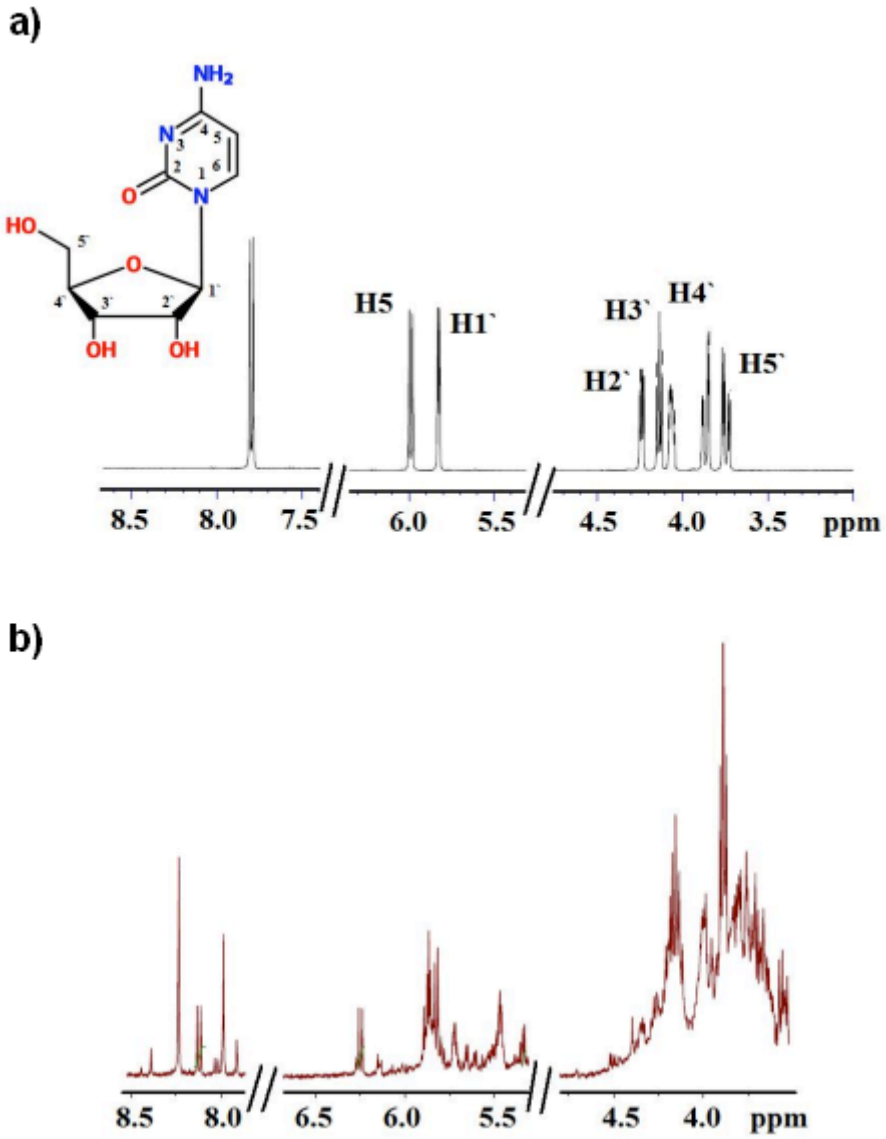

Figure 39.1H NMR spectra of a) cytidine, and b) Au-cytidine NPs.

The spectrum of **Au-cytidine 5'-monophosphate**NPs (Figure 40) seems less complicated and the ring signals can be clearly detected: H6 and H5 resonances notably shift from 7.98 and 6.06 ppm to 8.17 and 6.24 ppm, respectively. The H1' signal is less affected and moves from 5.94 to 5.90 ppm, while the ribose region strongly broadens comparing with free nucleotide.

Finally, the phosphate moiety is perturbed by the interaction, undergoing a considerable shift from 1.85 to 0.25 ppm (Figure 41).

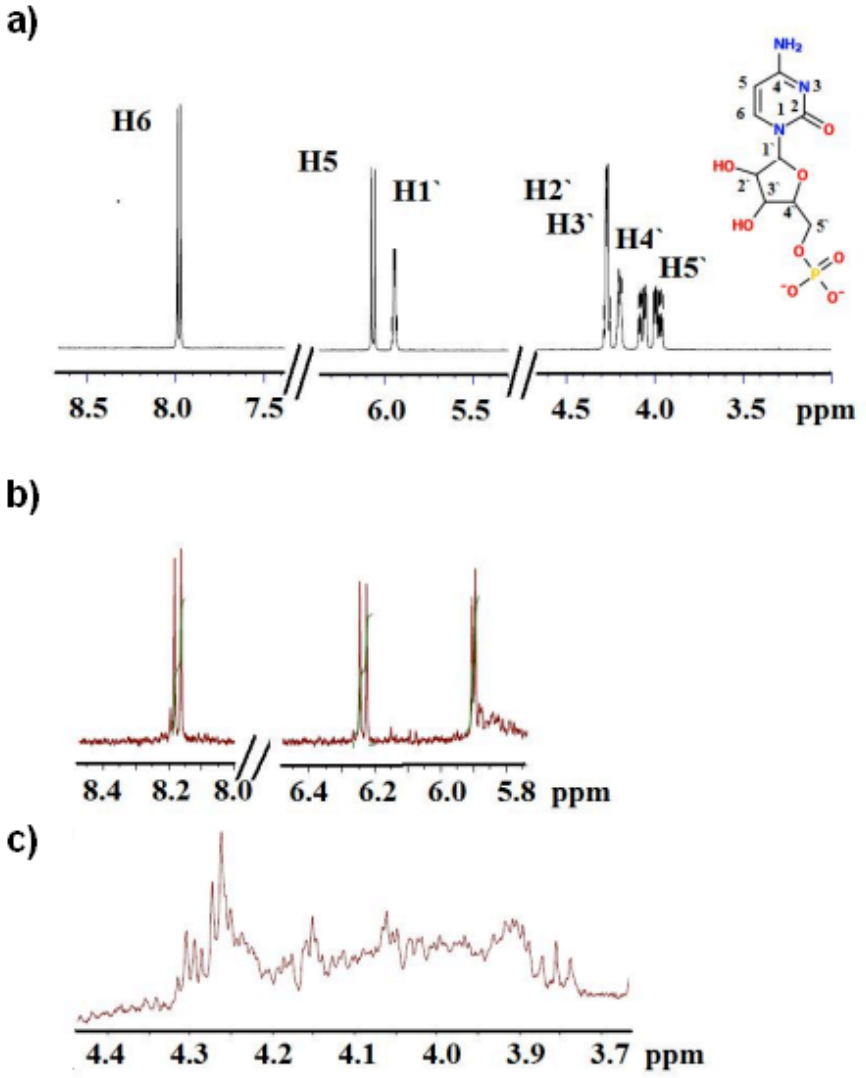

Figure 40.1H NMR spectra of a) cytidine 5'-monophosphate, and b) Au-cytidine 5'-monophosphate NPs.

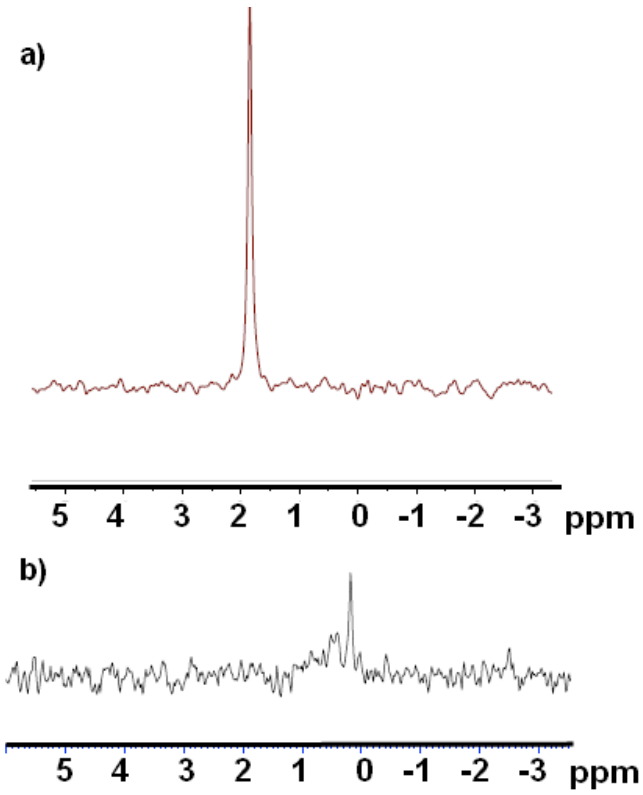

Figure 41. 31P NMR spectra of a) cytidine 5'-monophosphate, and b) Au-cytidine 5'-monophosphate NPs.

The FTIR spectra of cytosine, cytidine and cytidine 5'-monophosphate and AuNPs are reported in Figures 42-44. The spectrum of free **cytosine** (Figure 42) shows two intense bands at 3368 and 3157 cm^{-1} responsible for symmetric and asymmetric stretching vibrations of NH_2. In the Au-cytosine spectrum the only band appears in that region (3215 cm^{-1}) assigned to the same NH_2 vibrations. A middle-intensity band is found at lower frequencies (2927 cm^{-1}) in the AuNPs spectrum, which seems to be a result of a significant blue shift of the v (CH) bands centered at 2927 and 2851 cm^{-1}.

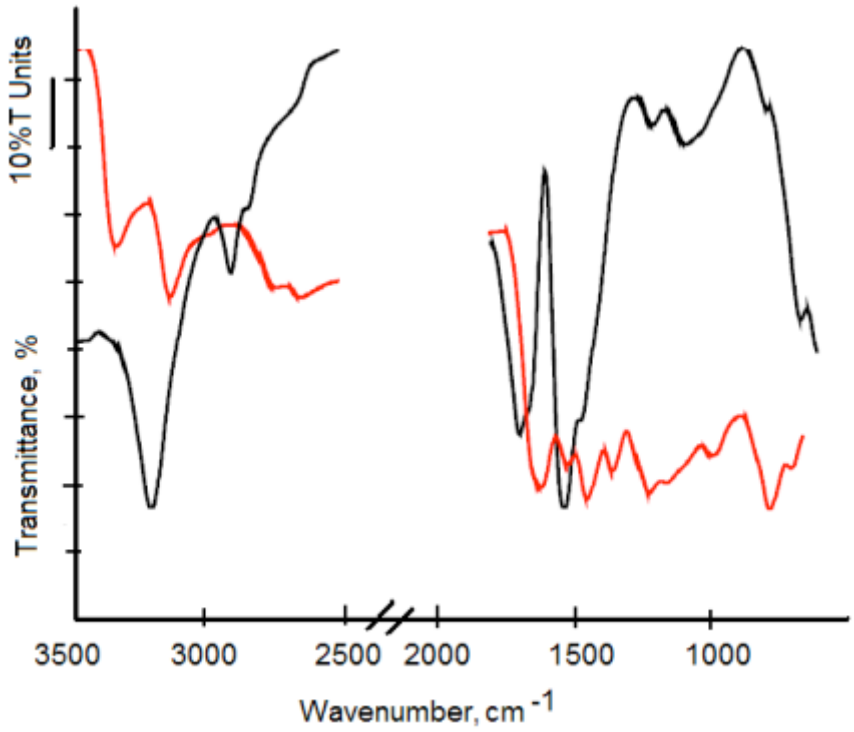

Figure 42. ATR-FTIR spectra of cytosine (red line) and Au-cytosine NPs (black line).

There are significant changes in the 2000-600 cm^{-1} region as well: the v (C=O) band, centrered at 1647 cm^{-1} in free cytosine, gives a band with two components, at 1710 and 1645 cm^{-1}, that may correspond to the δ (NH_2) and v (C=O) modes of bound cytosine. The C-N stretching vibrations, showing two bands at 1520 and 1441 cm^{-1}, shift at 1541 and 1449 cm^{-1}, respectively. Finally, a group of the bands responsible for the ring stretching vibrations found in the 1216-974 cm^{-1} region in free cytosine spectrum, shifts to higher frequencies and decrease in intensity, while a very intense ring breathing band becomes weak and shifts from 773 to 811 cm^{-1} under interaction with gold. Mirkin *et al.* suggest a tilted orientation of cytosine on the gold surface, since the presence of *x*- and *z*-modes in the gold spectrum [38]. A clear observation of the NH_2 and C=O bands in our Au-cytosine spectrum, suggests a non-parallel

orientation of the molecule on the particle surface, which is supported by the presence of ring vibrational bands.

The spectra of free cytidine and **Au-cytidine** NPs show a similar behaviour (Figure 43): OH ribose vibration, along with *sym* and *asym* stretching vibrations of NH_2 group (3443, 3337 and 3220 cm^{-1}) give rise to a large formless band including several components at 3442, 3350 and 3209 cm^{-1}, which can be better observed in the second derivative spectrum (Figure A3.14, Appendix). The band at 1618 cm^{-1} in free cytidine may be due to both C=O hydrogen bonding with other molecules (normally, v (C=O) is found in 1670 cm^{-1} region) or C=C vibrations. The Au-cytidine spectrum shows a band with two shoulders (1696 and 1642 cm^{-1}), probably, due to both NH_2 bending and C=O stretching vibrations. Another band with the components at 1556 and 1518 cm^{-1} is a result of the C-N (C=N) stretching vibrations. All the ring vibrations are broadened but still can be observed in the AuNPs spectrum, indicating a similar to cytosine non-parallel orientation.

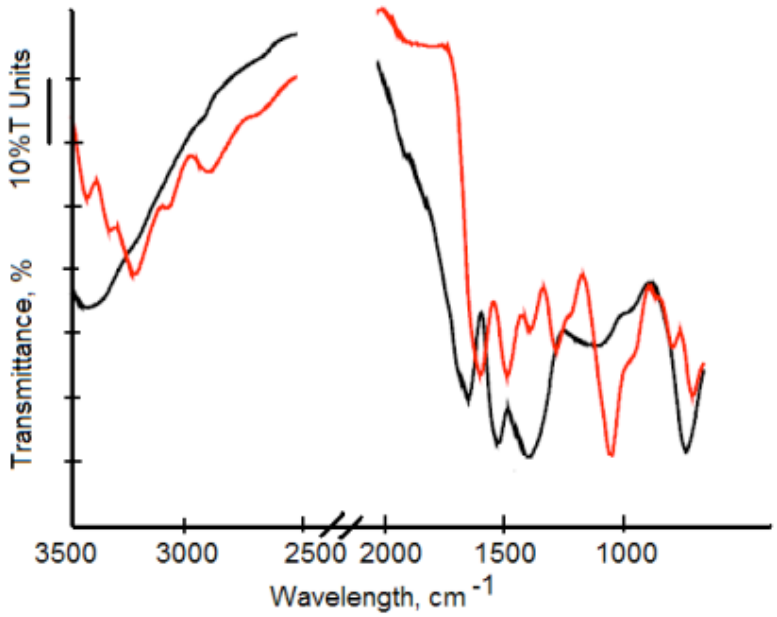

Figure 43. ATR-FTIR spectra of cytidine (red line) and Au-cytidine NPs (black line).

This is supported by the presence of a very strong band at 769 cm^{-1}, at a lower frequency comparing to the free cytidine, assigned to the ring breathing vibrations of cytosine moiety.

It can be clearly seen in the spectrum of **Au-cytidine 5'-monophosphate** NPs, that ribose moiety is highly perturbed by the interaction, showing a broad but intense band at 3415 cm^{-1}, which is not observable in the spectrum of free molecule (Figure 44). On the other hand, the v (C=O) band slightly shifts indicating a weak interaction (or its absence) with gold, while the cytosine ring vibrations give rise to a broad and intense multicomponent band confirming the above discussed non-parallel disposition of the ring. Importantly, the phosphate *sym* vibrations centered at 1066 cm^{-1} in free nucleotide, give a weak band with two components (1094 and 1026 cm^{-1}), suggesting a strong interaction between the phosphate moiety and gold, thus, supporting ^{31}P NMR data.

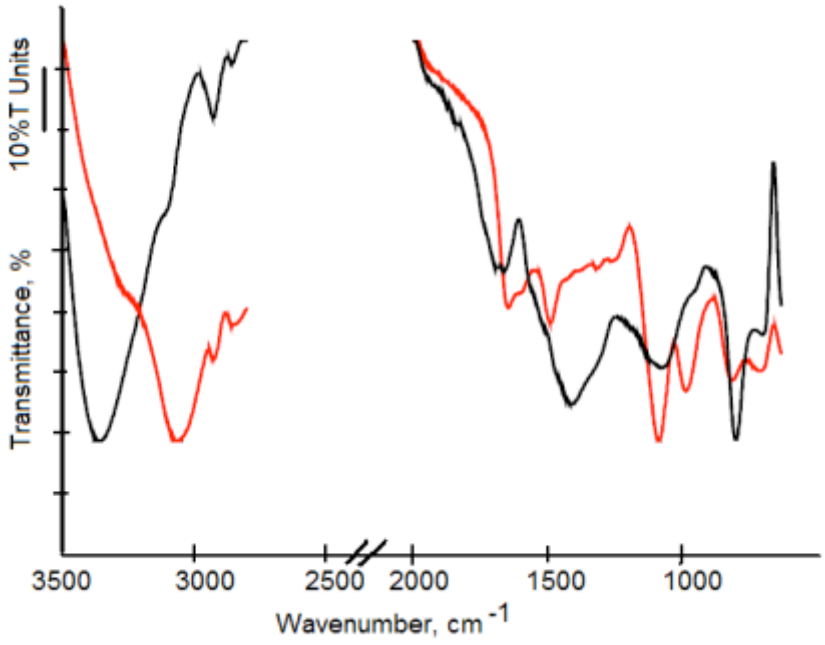

Figure 44. ATR-FTIR spectra of cytidine 5'-monophosphate (red line) and Au-cytidine 5'-monophosphate NPs (black line).

To summarize, “cytosine family” compounds interact with AuNPs involving N3 atom of cytosine moiety, with the ribose moiety to be strongly perturbed under interaction. Likewise other nucleotides, the phosphate group of cytidine 5’-monophosphate is involved in the interaction, showing a large chemical shift in ^{31}P NMR spectrum. Cytosine moiety seems to has a non-parallel orientation onto the gold surface concerning the three molecules.

Based on the above interpretation of NMR and FTIR results, we conclude that guanine, adenine, thymine and cytosine “families” do interact with the gold in rather different ways. The most of “guanine family” compounds interact with the particles *via* N7 atom and C=O group of guanine moiety, in their neutral form. While guanosine and 8-bromoguanosine derivatives showed to be able to form weak hydrogen bonds between N1-H group and gold surface. The substitution on C8 atom leads to a different constrain depending on bulky substituent, and different pathways of reaction can be possible for the building up of Au-purine NPs, as demonstrated for Au-8-bromoguanosine NPs. Novel results on the conformational changes of ribose puckering highlight that it can occur when purine derivatives interact with AuNPs. As for “thymine family”, thymine and thymidine weakly bind to the gold surface involving C=O4 and N3-H groups, with the latter able to form non-conventional hydrogen bonds with gold surface. Concerning “adenine family”, adenine and adenosine seem to interact with AuNPs *via* NH_2 group of adenine ring, involving N7 lone pair of electrons. The ribose moiety is affected by the interaction, while the phosphate moiety interacts with gold surface electrostatically, providing the particle stabilization. Finally, cytosine interacts with AuNPs *via* N3 atom having a non-parallel orientation onto the gold surface.

Cytidine shows the same binding sites along with a strong perturbation of the ribose moiety. Notably, the phosphate group of the four nucleotides is strongly involved in a polar interaction with gold surface, being monoprotonated, HO(O)PO-R)(O^-) due to the pH of colloids. The molecules interact with a different strength with AuNPs, likely due to the varying ability of the bases to coordinate to the substrate as a result of the different types of possible surface binding moieties (e.g., carbonyls and amides; mono- versus polydentate) [21].

3.2. Biological experiments

Besides structural studies on AuNPs modified by nucleobases, nucleosides and nucleotides, we have also performed the cytotoxicity and cellular uptake experiments in order to evaluate their potential application in biology. Cytotoxicity experiments were performed using U-87 human glyoblastoma cell line. Glioblastoma is the highest dedifferentiated form of astrocytic brain tumours, and it is refractory to chemotherapy in most cases [50]. U-87 cells are used as *in vitro* model of human glioblastoma cells to investigate the cytotoxic effect of chemotherapeutic drugs towards cancer cells. The cells were incubated for 1 h with both conjugated AuNPs and Au-citrate NPs for comparison, using 6 nM AuNPs suspensions. The cell mortality was then studied by trypan blue exclusion test by determining the number of viable cells present in the cell suspension [51]. The assay is based on the principle that live cells possess intact cell membrane that exclude certain dyes, such as trypan blue, Eosin, or propidium, whereas dead cells do not. For this purpose, incubated with AuNPs cells, resuspended in PBS, were mixed with trypan blue 0.4% solution and then fixed. The plates with as-treated cells were visually examined to determine the number of cells which took up and exclude dye. Thus, viable cells have a clear cytoplasm whereas a nonviable ones have a blue cytoplasm. A few fields of every sample were analyzed by optical microscopy and cell mortality was calculated using the following equation:

$$\text{Cell mortality, \%} = \frac{\text{total number of nonviable cells}}{\text{total number of cells}} \times 100$$

Figure 45 shows a histogram of cell mortality for different kinds of nanoparticles compared to Au-citrate NPs as a control.

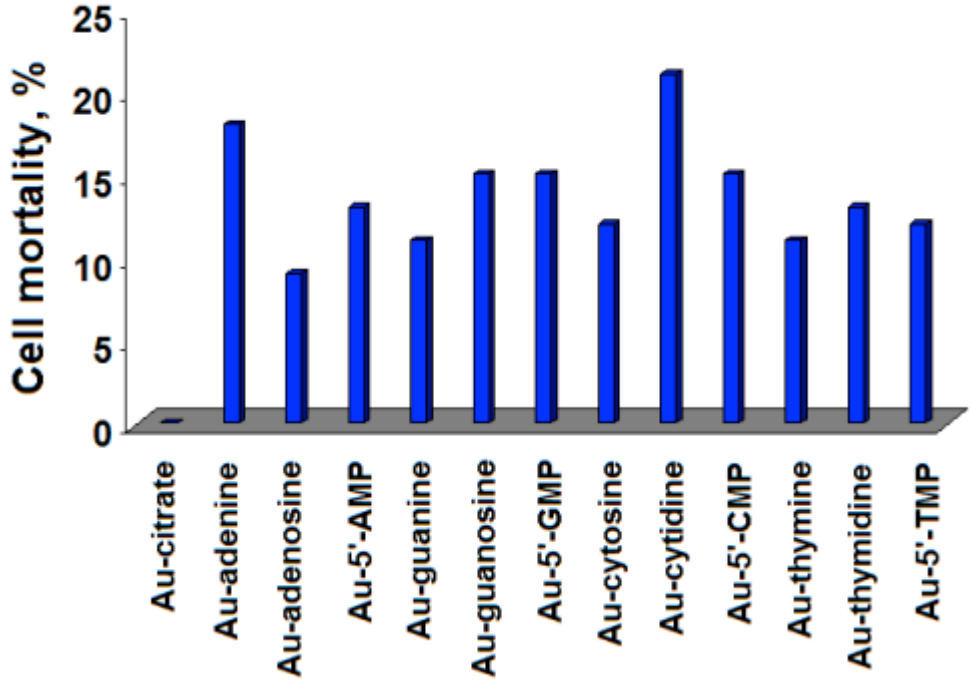

Figure 45. Cytotoxicity of AuNPs modified by nucleobases, nucleosides and nucleotides, compared to Au-citrate NPs. The U87 cells were incubated with 6nM AuNPs for 1 h.

After one hour of incubation, the nanoparticles modified with nucleobases caused 12-18% cell death, while nucleobases and nucleotides conjugates shown 8-23% of cell mortality. It is known that the kind of surface coating may play an important role in the cytotoxicity of AuNPs. Goodman et al. have studied the cytotoxicity of differently charged AuNPs and have found that cationic (ammonium-functionalized) AuNPs are clearly more toxic than the anionic (carboxylate-functionalized) ones [52]. Moreover, Connor et al. have found that the gold-salt ($AuCl_4^-$) is highly toxic for the cells (over 90%) [53]. The light microscopy images of the incubated with trypan blue cells are reported in Figures A4.1-2, Appendix.

The cellular uptake studies of several gold conjugates were performed both by confocal microscopy and TEM. Confocal laser microscopy is one of the most important cellular analysis techniques and has been used with considerable success in the real-time observation of cells [54]. In this technique, molecular fluorescent probes are employed to label the cells to be observed. Ren *et al.* studied AuNPs as a tool for confocal microscopy imaging of cancer cells. They observed that fluorescence of AuNPs possessed an excellent behaviour of antiphotobleaching under strong light illumination. On the basis of this AuNPs property and easy photobleaching of cellular autofluorescence, they developed a new method for imaging the cells using AuNPs as fluorescent probes. After photobleaching of cellular autofluorescence by illumination of strong light for several minutes, they were able to clearly observe AuNPs inside the cells [55]. The results of confocal microscopy studies are reported in Figures 46, 47. To note, the colour of the dots is chosen occasionally and does not represent the real colour of the nanoparticles. It can be clearly seen that all the tasted conjugates were taken up by the cells: the nanoparticles are distributed in different cellular compartments, and some of them even can be found inside the nucleus. Since the cells were post-fixed after incubation with nanoparticles, their form is not perfectly uniform and a few bubbles can be observed.

To further confirm the successful cellular uptake of the gold conjugates, TEM experiments were performed. Owing to electron density and capability of strong emission of secondary electrons, gold nanoparticles have been widely used as specific marker in microscopy both at the low and high resolution level. Since gold nanoparticles bind non-specifically to a very low extent, the technique has found

application in TEM for marking intracellular components on thin sections.

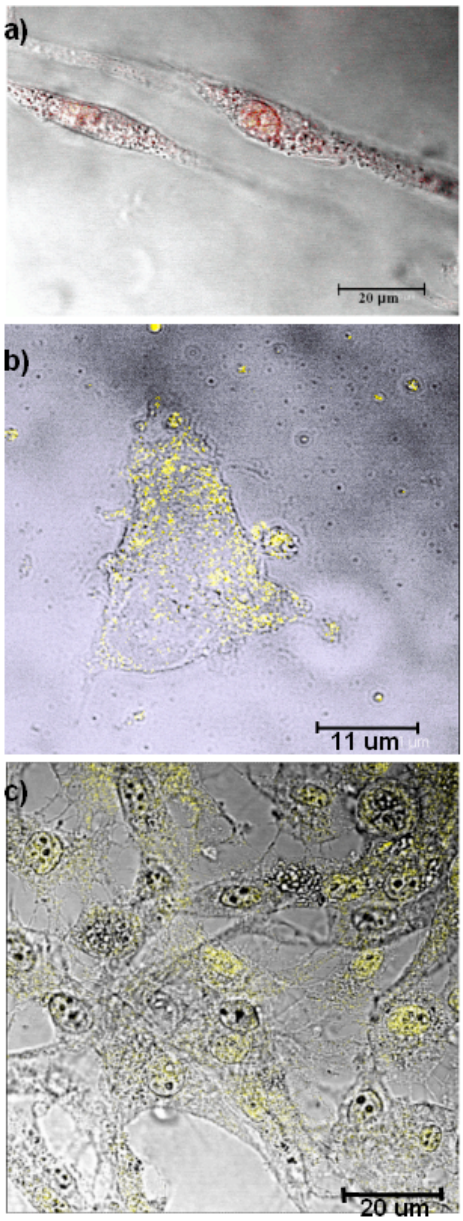

Figure 46. Confocal microscopy images of U87 cells incubated with a) Au-thymine, b) Au-thymidine and c) Au-thymidine 5'-monophosphate NPs.

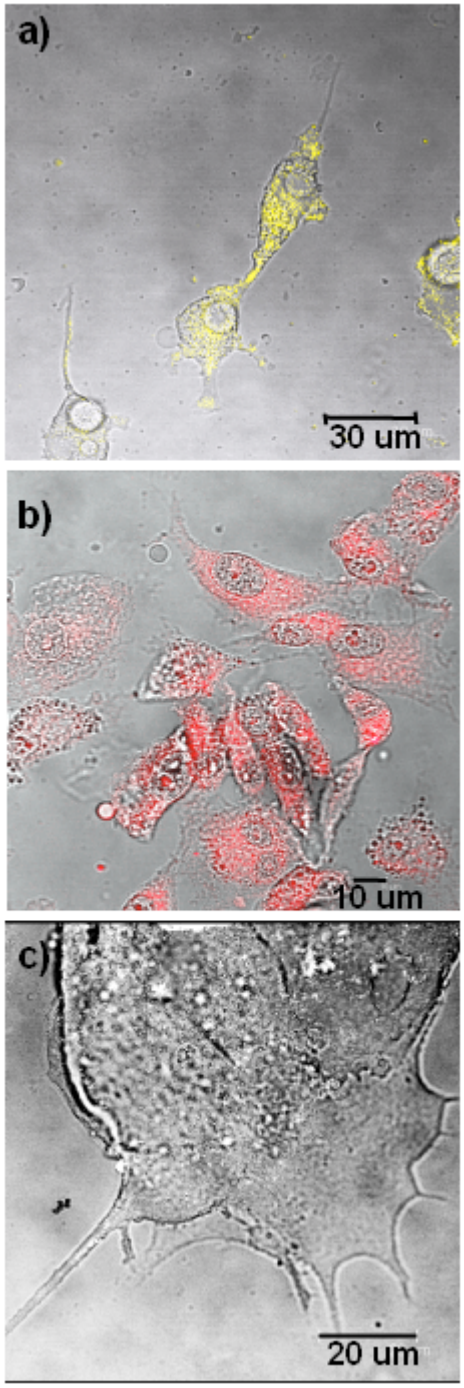

Figure 47. Confocal microscopy images of U87 cells incubated with a) Au-cytosine, b) Au-adenine and c) Au-guanosine NPs.

Here, we focused our attention on the cellular uptake of Au-thymidine 5'-monophosphate NPs. The results of these experiments are shown in Figure 48. After one hour of incubation, the nanoparticles are found approaching cellular membrane (a, b), and clustered together in cellular compartment that appear to be an endosome (b, c).

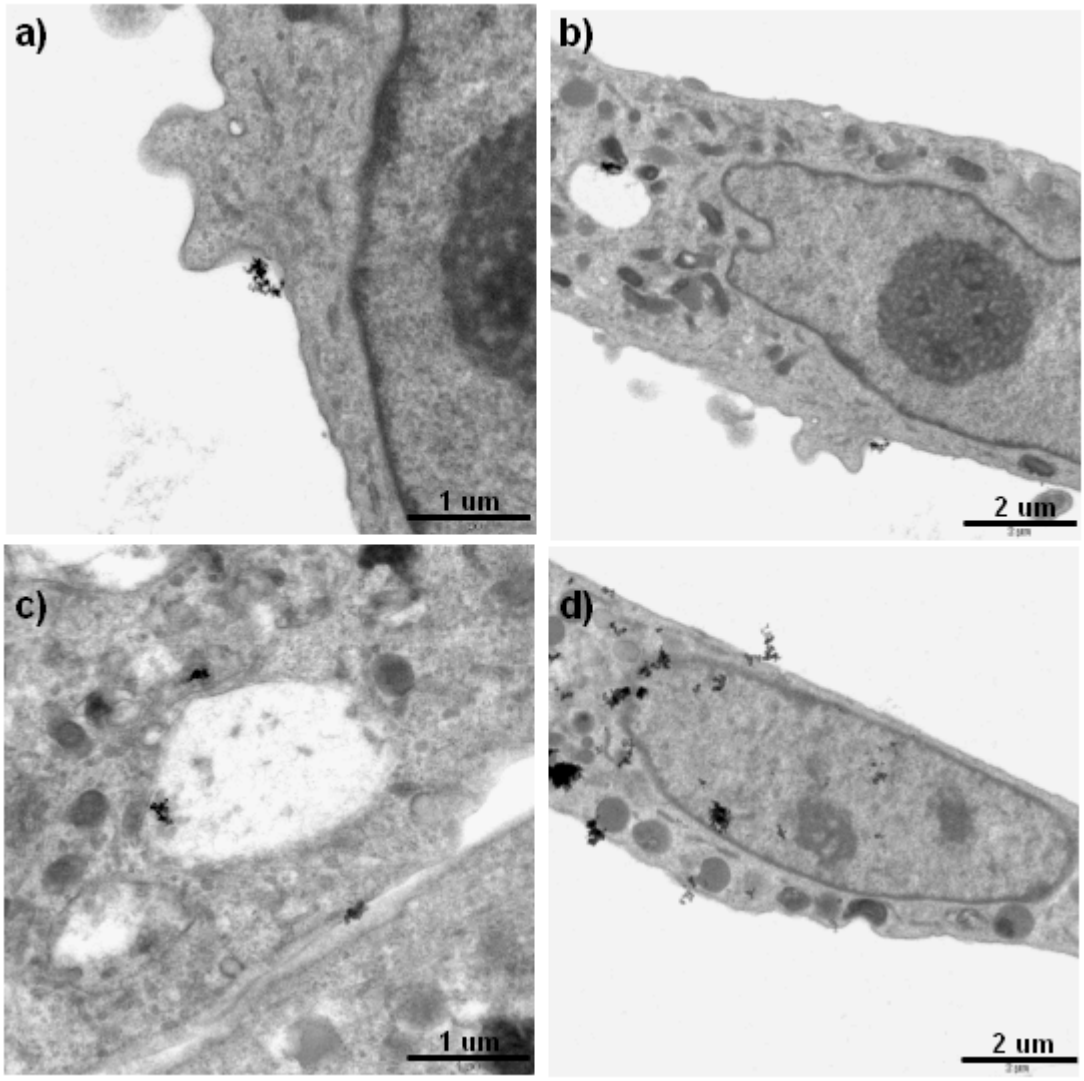

Figure 48. TEM micrographs of U87 cells incubated with Au-thymidine 5'-monophosphate NPs for 1 h: a) AuNPs approaching cellular membrane, b) enclosed into an endosome, c) free into the cytoplasm and endosome, and d) roaming into different cellular compartments.

Moreover, the nanoparticles are observed free in the cytoplasm, which may indicate their ability to escape endosomal pathway. Infact, the nanoparticles are also found roaming into different cellular compartments, and, in particular, crossing nuclear membrane and even into the nucleus. Figure 41d shows the nanoparticles clustered in different parts of the nucleus.

Targeted nuclear delivery is a challenging task, however, as any cell-specific nuclear probe must satisfy the following requirements: it must be small enough to enter cells and cross the nuclear membrane (<100 nm for uptake by receptor-mediated endocytosis and <30 nm for import through nuclear pores, penetrate cellular membranes or bind to cell-specific plasma membrane receptors, bypass or escape endosomal/lysosomal pathways, penetrate nuclear membranes or access importins to pass through the nuclear pore complex, and have low toxicity [56]. The Au-thymidine 5'-monophosphate nanoparticles seem to fulfil these conditions, being small enough (10 nm) to be able to penetrate nuclear membrane, and be probably taken up by the cells *via* passive uptake. This mechanism is still unclear and needs a more detailed study, by variation of cellular uptake conditions and using different cell lines.

4. Concluding remarks

We have synthesized small water-soluble gold nanoparticles using nucleobases (guanine, adenine, cytosine, thymine), nucleosides (guanosine, adenosine, cytidine, thymidine) and nucleotides (corresponding monophosphates) as stabilizing ligands. The nanoconjugates have been fully characterized by TEM, UV-vis, DLS and zeta-potential methods, whereas the binding properties of the molecules towards gold nanoparticles have been studied by ^{1}H, ^{31}P NMR and ATR-FTIR spectroscopy. The nanoconjugates have a 6-35 nm size and are negatively charged, as TEM and zeta-potential studies show. Basing on the previous studies on the binding of nucleobases to the gold, carried out by Mirkin, Pergolese and Kryachko, and our spectroscopic results, we have found out a behaviour of the nucleic acid components when bound to the gold surface. The binding of the molecules is shown to have a complex character involving different atoms of nucleobase ring. The ribose moiety does not seem to be involved in the binding, however, it does change the conformation under interaction with gold, in order to fulfill a better disposition of the binding atoms on the metal surface. Finally, phosphate group of the nucleotides is found to strongly interact with gold surface, likely, electrostatically, as shown by ^{31}P NMR. Novel results have been obtained by FTIR spectroscopy on ribose conformation affected by the interaction with gold. Finally, cytotoxicity experiments carried out using U87 human glioblastoma cancer cell line have shown that as-prepared nanoconjugates possess a low toxicity with a maximum of 23%. Cellular uptake studies of several nanoconjugates have been performed both by confocal microscopy and TEM, revealing the ability of the nanoparticles to be taken up by the cells. Interestingly, thymidine 5'-monophosphate

nanoparticles were also found roaming into different cellular compartments, including cytoplasm and cellular nucleus, as shown by TEM. This let us believe that endosomal escape mechanism takes place. Despite the encouraging results, the biological experiments on the nanoconjugates still need a deeper examination, in order to fully understand the mechanism driving the nanoparticles uptake.

5. References

1. X. Xie, W. Xu, and X. Liu. *Acc. Chem. Res.*, 2012, ***45*** (9), 1511–1520.
2. R. Wan, Y. Mo, L. Feng, S. Chien, D. J. Tollerud, and Q. Zhang. *Chem. Res. Toxicol.*, 2012, **25** (7), 1402–1411.
3. Y. Zhang, Q. Yuan, T. Chen, X. Zhang, Y. Chen, and W. Tan. *Anal. Chem.*, 2012, **84** (4), 1956–1962.
4. C. H Lalander, Y. Zheng, S. Dhuey, S. Cabrini, and U. Bach. *ACS Nano*, 2010, **4** (10), 6153–6161.
5. Z. Wang, J. Zhang, J. M. Ekman, P. J. A. Kenis, and Y. Lu. *Nano Lett.*, 2010, **10** (5), 1886–1891.
6. D. Li, S. Song, and C. Fan. *Acc. Chem. Res.*, 2010, **43** (5), 631–641.
7. D. G. Thompson, A. Enright, K. Faulds, W. E. Smith, and D. Graham. *Anal. Chem.*, 2008, **80** (8), 2805–2810.
8. P. J. Endres, T. Paunesku, S. Vogt, T. J. Meade, and G. E. Woloschak. *J. Am. Chem. Soc.*, 2007, **129** (51), 15760–15761.
9. G. Braun, S. Joon Lee, M. Dante, T.-Q. Nguyen, M. Moskovits, and N. Reich. *J. Am. Chem. Soc.*, 2007, **129** (20), 6378–6379.
10. Y. Chen, W. Cheng. *Wiley Interd. Rev.: Nanomedicine and Nanobiotechnology.* 2012, **4** (6), 587-604.
11. L. Song, V. H.B. Ho, C. Chen, Z. Yang, D. Liu, R. Chen, and D. Zhou. *Adv. Health. Mat.* **DOI**: 10.1002/adhm.201200112.
12. A. Elbakry, E.-C. Wurster, A. Zaky, R. Liebl, E. Schindler, P. Bauer-Kreisel, T. Blunk, R. Rachel, A. Goepferich, M. Breunig. *Small*, **DOI**: 10.1002/smll.201201112.

13. R. P. Johnson, J. A. Richardson, T. Brown, and P. N. Bartlett. *J. Am. Chem. Soc.*, 2012, **134** (34), 14099–14107.

14. S. Zhang, J. Xia, and X. Li. *Anal. Chem.*, 2008, **80** (22), 8382–8388.

15. L. Authier, C. Grossiord, P. Brossier, and B. Limoges. *Anal. Chem.*, 2001, **73** (18), 4450–4456.

16. A. Charrier, N. Candoni, and F. Thibaudau. *J. Phys. Chem. B*, **2006**, **110** (26), 12896–12900.

17. J.-H. Oh, and J.-S. Lee. *Anal. Chem.*, 2011, **83** (19), 7364–7370.

18. C. M. Alexander, J. C. Dabrowiak, and M. M. Maye. *Bioconjugate Chem.*, 2012, **23** (10), 2061–2070.

19. D.-Q. Tang, D.-J. Zhang, D.-Y. Tang, and H. Ai. *Electroanalysis*, 2006, **18** (22), 2194-2201.

20. S. Piana, and A. Bilic. *J. Phys. Chem. B,* 2006**, 110***,* 23467-23471.

21. L. M. Demers, M. Ostblom, H. Zhang, N.-H. Jang, B. Liedberg, and C. A. Mirkin. *J. Am. Chem. Soc.* 2002, **124**, 11248-11249.

22. H. Kimura-Suda, D. Y. Petrovykh, M. J. Tarlov, and L. J. Whitman. *J. Am. Chem. Soc.* 2003, **125**, 9014-9015.

23. J. J. Storhoff, R. Elghanian, C. A. Mirkin, and R. L. Letsinger. *Langmuir,* 2002, **18**, 6666-6670.

24. E. S. Kryachko, F. Remacle. *Nano Lett.* 2005, **5**, 735-739.

25. a) E. S. Kryachko, F. Remacle. *J. Phys. Chem. B,* 2005, **109**, 22746-22757; b) D. Ubiali, C. D. Serra, I. Serra, C. F. Morelli, M. Terreni, A. M. Albertini, P. Manitto, and G. Speranza. *Advanced Synthesis & Catalysis,* 2012, **354** (1), 96-104.

26. S. Eustis, and M. A. El-Sayed. *Chem. Soc. Rev.***,** 2006, **35**, 209-217.

27. M. A. H. Muhammed, F. Aldeek, G. Palui, L. Trapiella-Alfonso, and H.

Mattoussi. *ACS Nano*, 2012, **6** (10), 8950–8961.

28. A. L. Brown, and A. M. Goforth. *Chem. Mater.*, 2012, **24** (9), 1599–1605.
29. F. Thielbeer, K. Donaldson, and M. Bradley. *Bioconjugate Chem.*, 2011, **22** (2), 144–150.
30. W. Zhao, W. Chiuman, J. C. F. Lam, M. A. Brook, and Y. Li. *Chem. Commun*. 2007, **36**, 3729-3731.
31. W. Zhao, F. Gonzaga, Y. Li, and M. A. Brook. *Adv. Mater*. 2007, **19**, 1766-1771.
32. T. L. Doane, C. H. Chuang, R. J. Hill, and C. Burda, *Acc. Chem. Res.,* **DOI**: 10.1021/ar200113c.
33. A. V. Delgado, F. Gonzalez-Caballero, R. J.Hunter, and L.K.Koopal, *J. Colloid Interface Sci.,* 2007, **309**, 194–224.
34. D.A. Skoog, D.M. Weat, and F.J. Holler. *Foundamentals of Analytical Chemistry*, Eds, Edises, 2005.
35. R. K. Singh, J. V. Ortiz, and M. K. Mishra. *Int. J. of Quantum Chem.*, 2010, **110** (10), 1901-1915.
36. M. Hanus, M. Kabelac, J. Rejnek, F. Ryjacek, and P. Hobza. *J. Phys Chem B,* 2004, **108**, 2087-2097.
37. J. Leszczynski. *Advances in Molecular Structure Research*, ed. by M. Hargittai and I. Hargittai. JAI Press*,* Stamford*,* CT 2000, **6**, 209.
38. M. Ostblom, B. Liedberg, L. M. Demers, and C. A. Mirkin. *J. Phys. Chem. B,* 2005**, 109***,* 15150-15160.
39. B. Pergolese, A. Bonifacio, and A. Bigotto. *Phys . Chem. Chem. Phys*. 2005, **7** , 3610–3613.
40. B.Lippert. *Coordination Chemistry Reviews,* 2000, **200–202**, 487–516.
41. D. Yang, S. G. E. Van Boom, J. Reedijk, J. H. Van Boom, and A. H.

Wang. *J. Biochemistry,* 1995, **34**, 12912- 12920.

42. R. B. Martin. *Acc. Chem. Res.* 1985, **18**, 32–38.
43. Y. Nishimura, M. Tsuboi, and T. Sato. *Nucl. Acids Res.* 1984, **12** (17), 6901-6908.
44. C. P. Shaw, D. A. Middleton, M. Volk, R. Lévy. *ACS Nano,* 2012, **6**, 1416–1426.
45. B. Pergolese, A. Bonifacio, A. Bigotto. *Phys . Chem. Chem. Phys*. 2005, **7**, 3610–3613.
46. N. H. Jang. *Bull. Korean Chem. Soc.* 2002, **23**, 1790−1800.
47. T. D. Son, and W.Guschibauer. *Nucl. Acids Res.* 1975, **2** (6), 873-888.
48. C. L. Angell, *J. Chem. Soc*., 1961, 504–515.
49. Haiss, B. Roelfs, S. N. Port, E. Bunge, H. Baumgartel and R. J. Nichols, *J. Electroanal. Chem.,* 1998, **454**, 107–113.
50. M. Rittierodt, and K. Harada. *Experimental and Toxicologic Pathology,* 2003, **55** (1), 39–44.
51. S. A. Altman, L. Randers, and G. Rao. *Biotechnology Progress,* 1993*,* **9** (6), 671–674.
52. C. Goodman, C. McCusker, T. Yilmaz, V. Rotello, Bioconjugate. Chem. 2004, 15, 897–900.
53. E. Connor, J. Mwamuka, A. Gole, C. Murphy, M. Wyatt, Small 2005, 1, 325–327.
54. M. Laurent, G. Johannin, N. Gilbert, L. Lucas, D. Cassio, P. X Petit, and A. Fleury. *Biology of the Cell,* 1994, **80** (2-3), 229–240.
55. H. He, C. Xie, and J. Ren. *Anal. Chem.* 2008**, 80***,* 5951–5957.
56. A. G. Tkachenko, H. Xie, Y. Liu, D. Coleman, J. Ryan, W. R. Glomm, M. K. Shipton, S. Franzen, and D. L. Feldheim. *Bioconjugate Chem.* 2004**, 15***,* 482-490.

Chapter IV

AuNPs functionalized by RGD-containing peptide for integrin targeting

1. Introduction

Tumors produce many angiogenic factors, which are able to activate endothelial cells in established blood vessels and induce endothelial proliferation, migration, and new vessel formation (angiogenesis) through a series of sequential but partially overlapping steps. Angiogenesis is a requirement for tumor growth and metastasis. Without the neovasculature to provide oxygen and nutrients, tumors cannot grow beyond 1-2 mm in size. Once vascularized, the tumors begin to grow rapidly. The angiogenic process depends on vascular endothelial cell migration and invasion and is regulated by cell adhesion receptors.

Integrins are a family of proteins that facilitate cellular adhesion and migration on extracellular matrix proteins in the intercellular spaces and basement membranes, and regulate cellular entry and withdraw from the cell cycle [1]. Integrins are divalent cation-dependent heterodimeric membrane glycoproteins composed of noncovalently associated α- and β-subunits. Eighteen α-subunits and 8 β-subunits can assemble into 24 different heterodimers. Each subunit is composed of an extracellular domain, a single transmembrane region, and a cytoplasmic region (Scheme 1).

Most integrins recognize their respective extracellular matrix proteins through short peptide sequences such as Arg-Gly-Asp (RGD) [2]. Integrin $\alpha_V\beta_3$ is expressed at low levels on epithelial cells and mature endothelial cells, but is overexpressed on the activated endothelial cells of tumor neovasculature, including osteosarcomas, neuroblastomas, glioblastomas, melanomas, lung carcinomas, and breast cancer [3]. The restricted expression of integrin $\alpha_V\beta_3$ during tumor growth, invasion, and

metastasis presents an interesting molecular target for both early detection and treatment of rapidly growing solid tumors. Most integrins can have “on” and “off” states. The extracellular domain of $\alpha_V\beta_3$ integrin is bent or folded, thereby hiding the RGD-binding site and preventing ligand binding. Conversely, RGD-bound $\alpha_V\beta_3$ integrin has an unbent or straighter extracellular domain (Scheme 1). Although integrin cytoplasmic tails are much smaller than their extracellular domains, they can play pivotal roles in integrin signaling events, with separation, twisting, and hinging of the tails all considered mechanisms to allow activation [4].

RGD-containing peptides compete in the binding of proteins to cell surface $\alpha_V\beta_3$, preventing cellular adhesion to the extracellular matrix, thwarting cell metastasis, and inducing apoptosis [5]. Linear and cyclic RGD peptide motifs have been employed as delivery agents for small molecular weight drugs, peptides, and proteins to the tumor endothelial cells [6]. RGD analogues have been also used for tumor imaging and targeting with chemotherapeutic drugs or radionuclides [7]. Radiolabeled RGD peptides were targeted to xenograft tumors expressing the integrins [8].

There is an increasing interest in nanocarriers such as inorganic and polymeric nanoparticles, liposomes, and quantum dots coated with RGD analogues as targeting and imaging agents. Graf *et al.* have synthesized polymeric nanoparticle construct that encapsulates a Pt(IV) complex in the core and is targeted to $\alpha_V\beta_3$ integrin-expressing cells using the cyclic pentapeptide c(RGDfK) [2]. Nam *et al.* studied cyclic RGD-PEGylated AuNPs with directly labeled radioactive iodine as molecular imaging probes, having found their ability to specifically target integrin

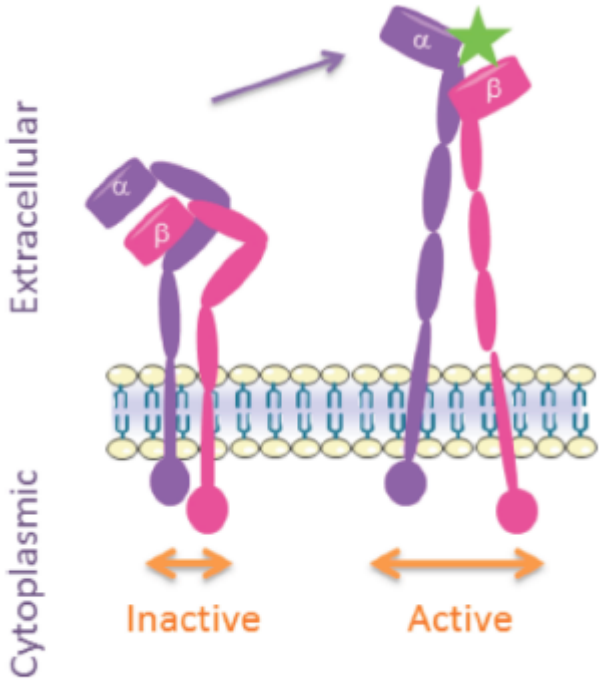

Scheme 1. Structure of $\alpha_V\beta_3$ integrin receptor. An illustration of conformational changes in $\alpha_V\beta_3$ integrin. Upon activation the extracellular domains extend and straighten, exposing the RGD-binding domain (star).

receptors and penetrate the cells *via* receptor-mediated endocytosis with almost no cytotoxicity. The authors pointed out the importance of RGD functionality for efficient and long-term tumor-targeted imaging *in vivo* [9].

Cellular uptake of AuNPs conjugated both with the monocyclic RGDfK and linear RGD peptides into HUVEC cells was compared by Dowling *et al*. The researchers showed *via* MAIL (Multiphoton Absorption Induced Luminescence) imaging the importance both of the nanoparticle size and structure of the RGD analogue: cyclic RGD analogue was found to give a higher signal respect to the

linear control, while 16 nm particles exhibited significantly higher MAIL signal than those incubated with the smaller 4.5 nm AuNPs [10]. ^{99}Tc-labeled AuNPs conjugated with HYNIC-GGC and c(RGDfK(C)) peptides were synthesized as a potential radiopharmaceutical for tumor integrin expression imaging and incubated with cancer cells and their distribution in different mice compartments was studied *in vivo* [11].

2. Peptide design

Figure 1 shows a schematic illustration of both RGD-$(GC)_2$ and $(GC)_2$ peptides. The RGD-$(GC)_2$ peptide is a chimeric molecule of 12 amino acids containing two parts: encompassing an RGD-sequence and a $(GC)_2$-motif for integrin targeting and nanoparticle stabilization, respectively. The RGD-containing part was derived from the c(RGDfK) peptide, an $\alpha_v\beta_3$ antagonist, where the lysine residue was replaced by glutamic acid to allow the conjugation to the $(GC)_2$-motif by its γ-carboxylic group. The $(GC)_2$ portion contains a sequence of glycines and cysteines needed for the binding to the gold surface via Au-S covalent bond and providing nanoparticle stabilization against aggregation, allowing a parallel disposition towards gold surface.

3. Peptide synthesis

The peptides were synthesized by Dr. Laura Zaccaro's group at the Institute of Biostructures and Bioimages (Naples). A standard Fmoc (fluorenylmethyloxycarbonyl) solid-phase strategy was applied, using NovaSyn TGR resin (loading 0.28 mmol/g resin), and all the standard amino acids except for Fmoc-Glu-OAll. The amino acids in 10-fold excess were preactivated with 2-(1H-benzotriazole-1-yl)-1,1,3,3-tetramethyluronium hexafluorophosphate (HBTU) (9.8 equiv)/1-hydroxybenzotriazole (HOBT) (9.8 equiv)/DIPEA (10 equiv) in DMF for 5 min and then added to the resin in the presence of DIPEA (10 equiv) in DMF.

The Cys residues were coupled in 5-fold excess with HBTU (5 equiv)/2,4,6-trimethylpyridine (5 equiv) in DMF/DCM (1:1 v/v) for 90 min without preactivation to prevent racemisation [12]. The Fmoc deprotection step was performed with 30% piperidine in DMF for 10 min. Before the final Fmoc deprotection of the Arg^1 in RGD-$(GC)_2$, a selective deprotection of the Glu residue from the allyl group was carried out by treatment of the peptidyl resins with $PhSiH_3$ (24 equiv)/$Pd(PPh_3)_4$ (0.25 equiv) in DCM twice for 30 min. The cyclisation reaction was carried out on the resin with benzotriazole-1-yl-oxytripyrrolidinophosphonium hexafluorophosphate (PyBop) (1.5 eqiv)/HOBT (1.5 equiv)/DIPEA (2 equiv) in DMF for 3 h and monitored by Kaiser test. The peptides were cleaved off the resin by treatment with a mixture of trifluoroacetic acid/water/ethandithiol/triisopropylsilane (94:2.5:2.5:1 v/v/v/v) for 3 h at room temperature. The resins were filtered and the crude peptides were precipitated with diethyl ether, dissolved in a H_2O/CH_3CN solution and lyophilized. The products were purified by preparative RP-HPLC on a Shimadzu system equipped with a UV-visible detector SPD10A using a Phenomenex Jupiter Proteo column (21.2×250 mm; 4 µm; 90 Å) and a linear gradient of H_2 (0.1% TFA)/CH_3CN (0.1% TFA) from 5 to 70% of CH_3CN (0.1% TFA) in 30 min at flow rate of 20 mL/min. The collected fractions containing the peptides were lyophilized.

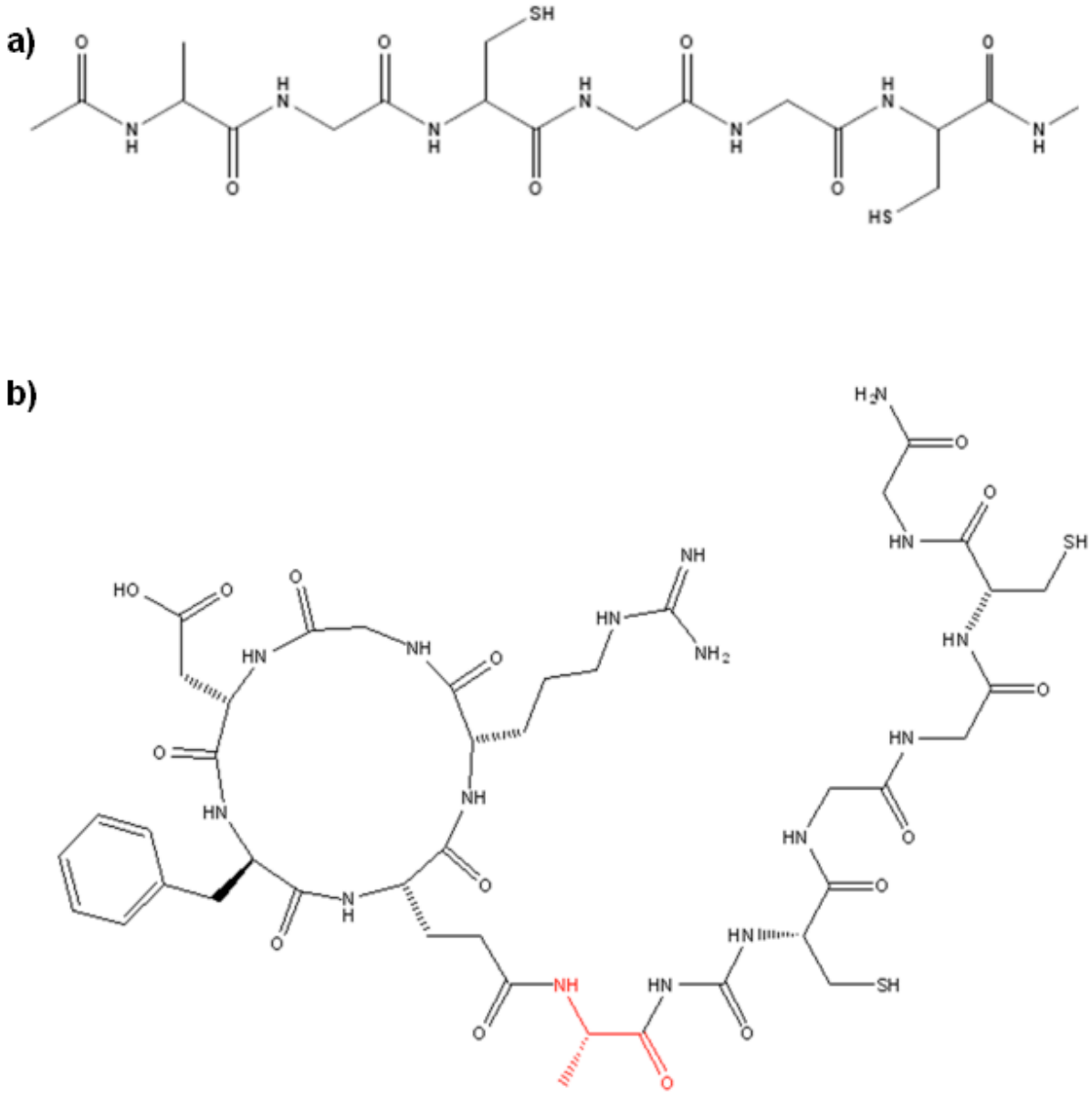

Figure 1. a) $(GC)_2$ peptide; b) RGD-$(GC)_2$ peptide.

The identity and purity of the compounds were assessed by ESI-LC-MS ThermoFinnigan instrument equipped with a diode array detector combined with an electrospray ion source and ion trap mass analyser on Phenomenex C18 column (250× 2 mm; 4µm; 90 Å) at flow rate of 200 µL/min. The peptide yield was 21% and 95% for RGD-$(GC)_2$ and $(GC)_2$, respectively. Figure 2 shows RP-HPLC chromatograms and corresponding mass spectra of $(GC)_2$ and RGD-$(GC)_2$ pure peptides.

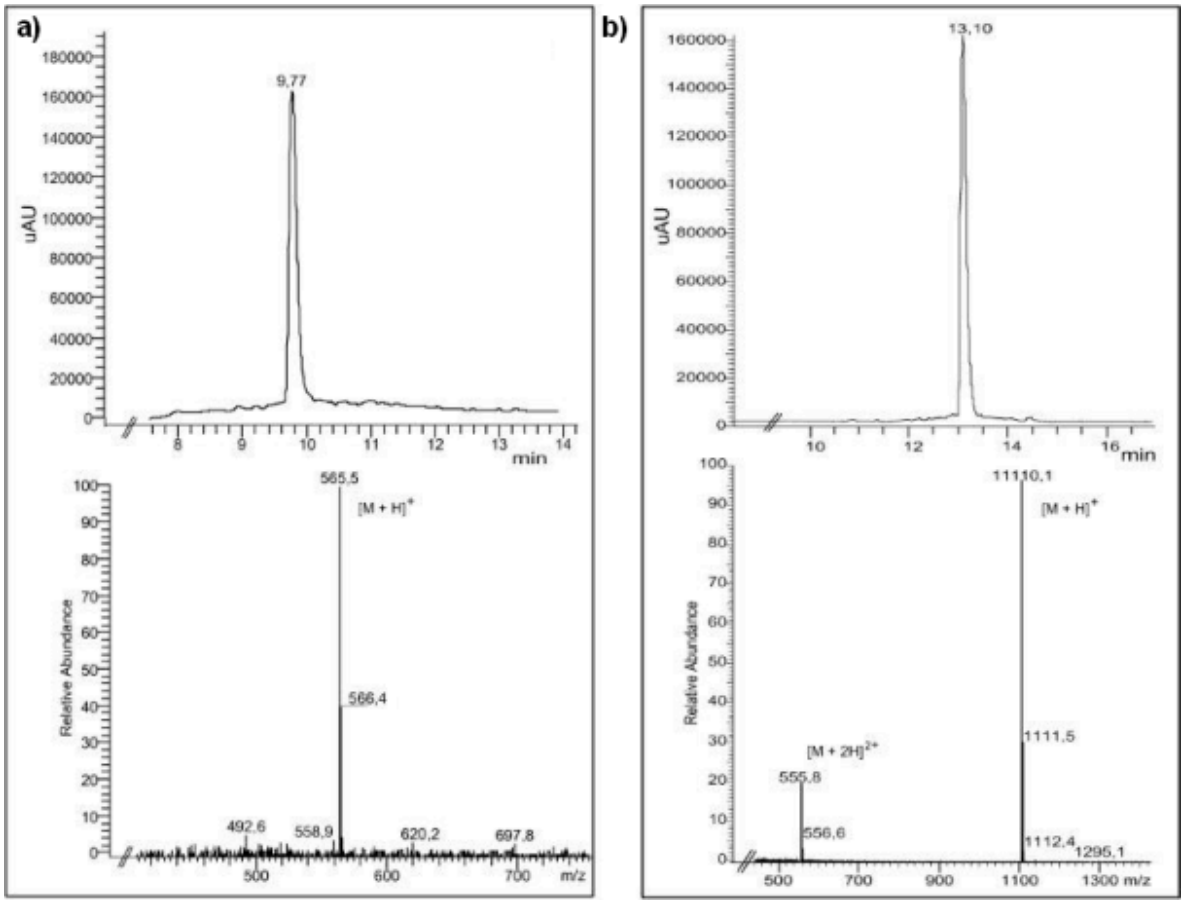

Figure 2. RP-HPLC chromatograms and corresponding mass spectra of (a) $(GC)_2$ and (b) RGD-$(GC)_2$.

4. Synthesis of gold nanoconjugates

4.1. Au-RGD-$(GC)_2$ nanoparticles preparation

In a typical reaction, to 0.06 mmol of $NaAuCl_4$ (50.7 mM) in 60 mL of Milli-Q water $3 \cdot 10^{-5}$ mmol of RGD-$(GC)_2$ aqueous solution (3.95 mM) was added, under stirring. After 10 min, 0.12 mmol of sodiumborohydride aqueous solution (112 mM) was quickly added and left under vigorous stirring for further few hours. The particles were purified by dialysis for 48 h, by using Spectra/Por 6 dialysis tubing, 2K MWCO.

4.2. Au-$(GC)_2$ nanoparticles preparation

In a typical reaction, to 0.03 mmol of $NaAuCl_4$ (34.1 mM) in 40 mL of Milli-Q water $21 \cdot 10^{-5}$ mmol of $(GC)_2$ aqueous solution (0.796 mM) was added, under stirring. After 10 min, 0.06 mmol of sodiumborohydride aqueous solution (100 mM) was quickly added and left under vigorous stirring for further few hours. The particles were purified by dialysis for 48 h, by using Spectra/Por 6 dialysis tubing, 2K MWCO.

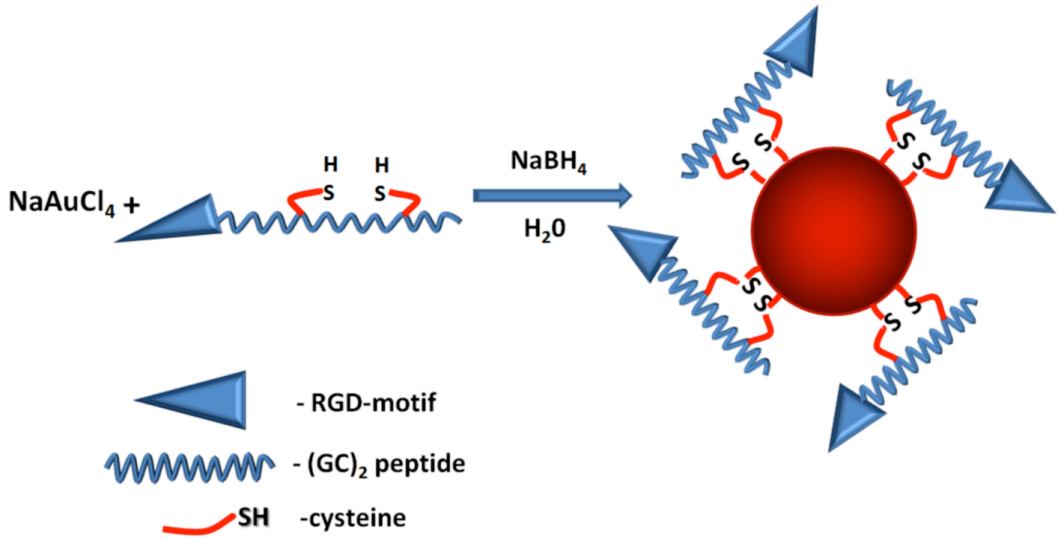

Scheme 2. Au-RGD-$(GC)_2$ nanoparticles preparation.

5. Results and discussion

AuNPs were prepared using “one-pot” sodium borohydride reduction method in the presence of RGD-$(GC)_2$ and $(GC)_2$ peptides to give small nanoparticles of 10.2 nm and 13.9 nm, respectively. The conjugation of AuNPs with peptides was confirmed by ^{1}H NMR and ATR-FTIR spectroscopy, the stability of the conjugates was verified using both UV-vis spectroscopy and Zeta-potential studies, while their morphology analysed by TEM.

In order to match the conditions at which the nanoparticles were the most stable, the molar ratios between Au(III), peptides and sodium borohydride were varied. The reaction termination was detected by the constancy of SPR absorbance value, which, generally, stopped growing after 2 hours. The UV-vis spectra of conjugated AuNPs are reported in Figure 3.

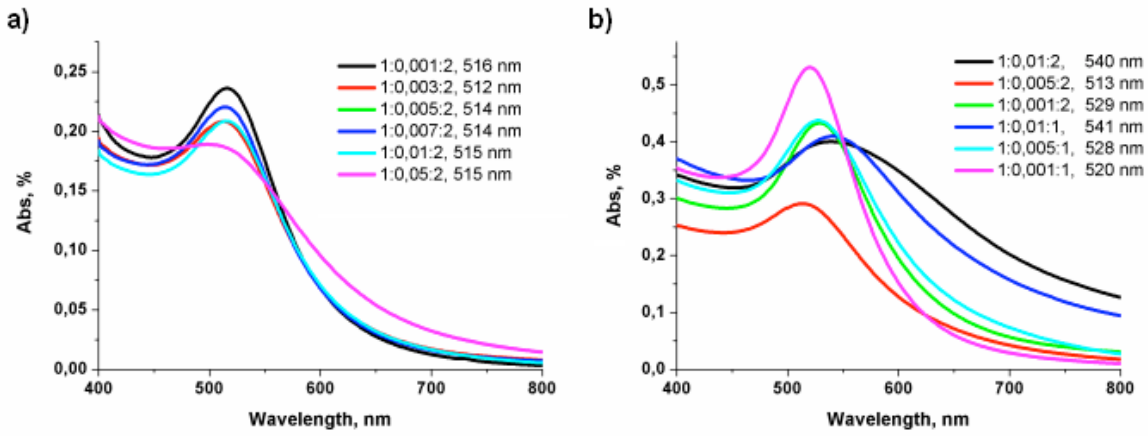

Figure 3. UV-vis spectra of Au-$(GC)_2$ (a) and Au-RGD-$(GC)_2$ (b) NPs prepared using various ratios between $AuCl_4^-$, peptides and sodium borohydride.

Having analyzed the SPR band position and its intensity for every sample, we choose 1:0.005:2 and 1:0.001:2 molar ratios for $(GC)_2$ and (RGD)-$(GC)_2$ peptides, respectively. All further experiments were carried out using the AuNPs prepared by the two conditions. The SPR band of as-prepared Au-$(GC)_2$ NPs was found at 514 nm, while Au-RGD-$(GC)_2$ NPs shown the SPR band at 529 nm.

The as-prepared Au-$(GC)_2$ and Au-RGD-$(GC)_2$ NPs shown a shape close to spherical and mean diameter of 13.9 and 10.2 nm, respectively, as found by TEM analysis (Figure 4 (b, c).

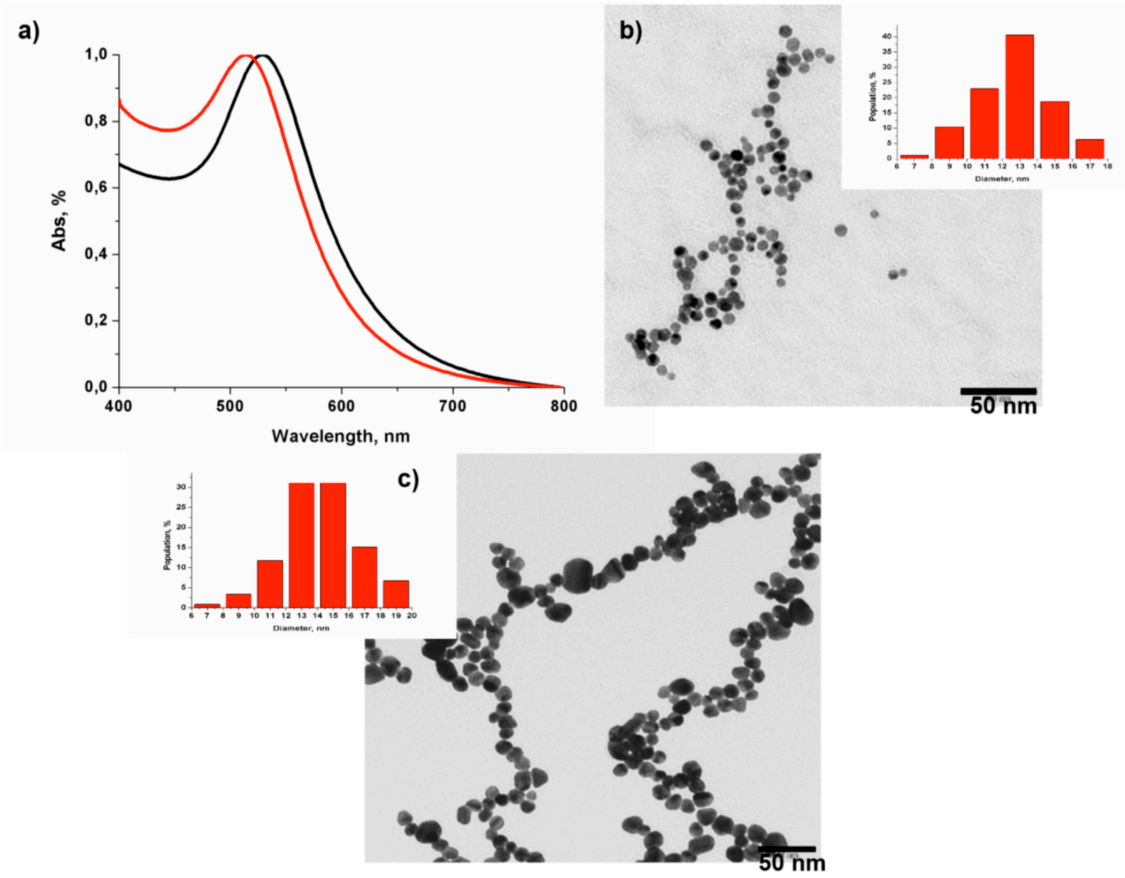

Figure 4. a) UV-vis spectra of: Au-RGD-$(GC)_2$ NPs (black line, 529 nm); Au-$(GC)_2$ NPs (red line, 514 nm); b) TEM micrograph of Au-RGD-$(GC)_2$ NPs (10.2 nm); c) TEM micrograph of Au-$(GC)_2$ NPs (13.9 nm).

Hydrodynamic diameter values, obtained by DLS, revealed the presence of small aggregates, also clearly observed by TEM, giving the fractions close to 45-46 nm for both kinds of conjugates (Figure 5, a and b).

Zeta-potential measurements were run using the original sols diluted with Milli-Q water. The particles were found negatively charged with Zeta-potential values of -27.27 mV and -40.59 mV for Au-RGD-$(GC)_2$ and Au-$(GC)_2$, respectively. The difference between the Zeta-potential values can be due to a different local environment surrounding a single nanoparticle, and can depend on: surface concentration of the peptides on the particle, possible ionic dissociations or zwitterionic forms of the peptides, disposition of the peptide molecules on the particle surface, interactions of the two organic chains with water, and, most importantly, ionic strengths of the solutions [13].

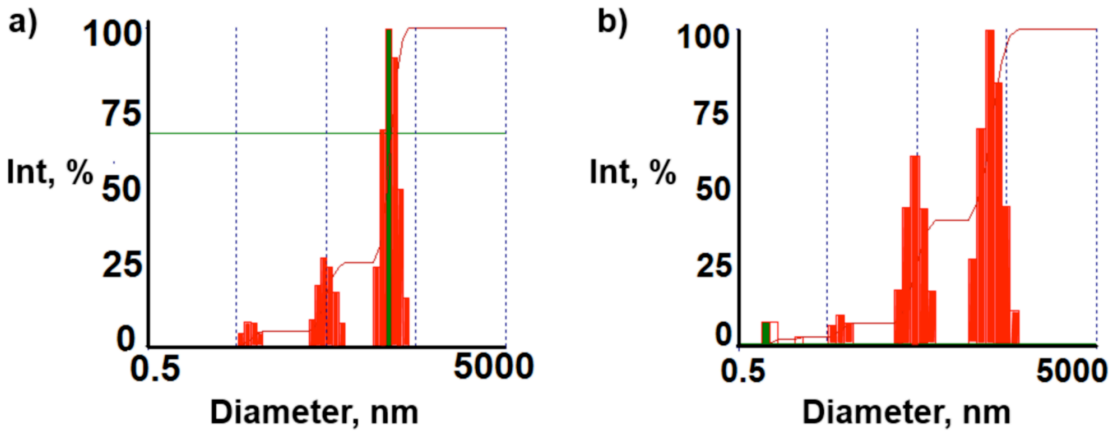

Figure 5. DLS diagrams of particle hydrodynamic diameter distribution: a) Au-RGD-$(GC)_2$ NPs, b) Au-$(GC)_2$ NPs.

In order to have an idea of coverage density on the nanoparticle surface, the number of peptide molecules per particle was determined by TGA analysis. For this purpose, the nanoparticles were lyophilized, purified from residual unbound peptides by repeated washing with Milli-Q water and centrifugation, and, finally, dried. The thermograms of both conjugates show a first weight loss between room temperature and 120°C due to the evaporation of residual and physisorbed water that can be neglected in our calculations (Figure 6). The weight losses of 1.609% and 1.058% were recorded in the 120-450°C heating range, and assigned to the combustion of the peptides bound to the particle surface. The number of peptide molecules residing on each gold particle was calculated, using a simple equation described by De Palma and co-workers [14], giving the numbers of 94 and 298 molecules for RGD-$(GC)_2$ and $(GC)_2$ peptides, respectively.

$$N = \frac{\omega N_A \rho \frac{4}{3} \pi R^3 \times 10^{-23}}{MM},$$

where N is the number of ligands on each particle, R is the mean radius of the AuNPs, ρ is the density of the nanoparticles (19.30 g/cm3), N_A is Avogadro's number, MM is the molar mass of the ligand molecules (g/mol) and ω is the mass loss in percent (%).

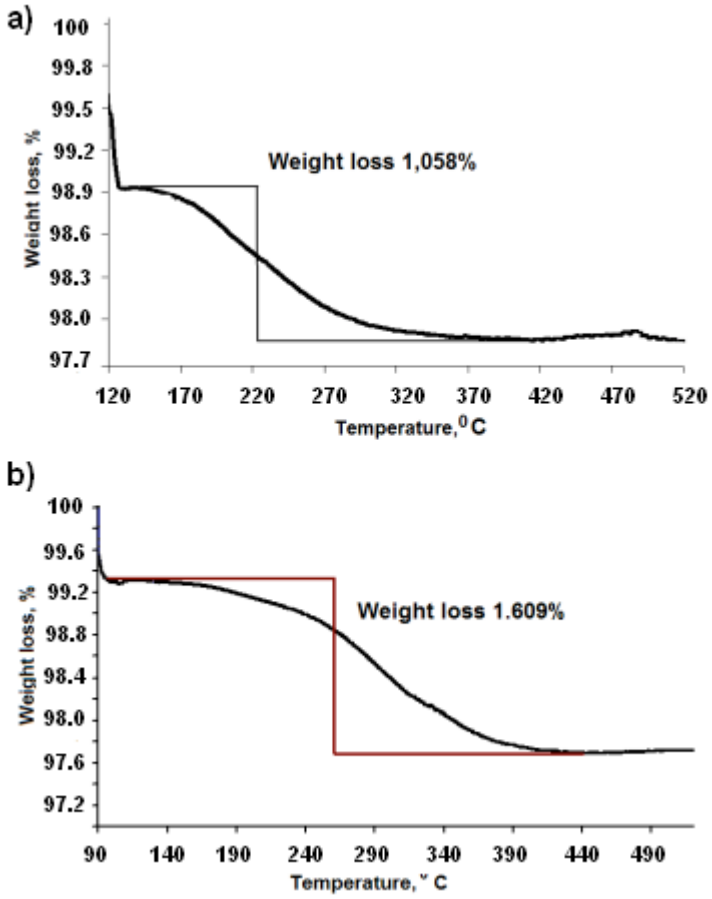

Figure 6. a) TGA curve of Au-RGD-$(GC)_2$ NPs. Main weight loss of about 1.609 % from RGD-$(GC)_2$ peptide occurs from 120 to 450 °C. (b) TGA curve of Au-$(GC)_2$ NPs. Main weight loss of about 1.058 % from $(GC)_2$ peptide occurs from 120 to 450 °C. Residual water is lost at 120 °C.

In order to verify the binding of the peptides to nanoparticle surface and investigate the interactions in the ligand shell of the conjugates, ATR-FTIR and NMR spectroscopy were performed. A comparison between ATR-FTIR spectra of free peptides and gold conjugates are shown in Figures 7, 8. Pure RGD-$(GC)_2$ and $(GC)_2$ peptides (solid line, Figures 7, 8) show similar FTIR spectra.

The only difference is in the amide I and II regions, where $(GC)_2$ shows two peaks located at 1644 and1540 cm^{-1}, while RGD-$(GC)_2$ peaks fall at 1655 and 1534 cm^{-1}. In the N-H stretching region $(GC)_2$ has a sharper band located at 3292 cm^{-1}, whereas RGD-$(GC)_2$ shows a broader two component band with one component at 3301 and a shoulder at 3205 cm^{-1}. The S-H stretching vibration falls around 2550 cm^{-1} for free cysteine, which vibration, unfortunately, was not clearly revealed in any of the recorded FTIR spectra. In pure $(GC)_2$ peptide, a broad feeble band located at 2547 cm^{-1} appears, but in the literature a feeble but sharp band of the S-H vibration is usually reported [15]. The whole spectrum of $(GC)_2$ is strongly affected after interaction with gold surface (Figure 7): amide I and II bands undergo a significant splitting and the band located at 1644 cm^{-1} in the free peptide now shows a main component at 1652 cm^{-1} plus a shoulder at 1620 cm^{-1}, and, in addition, two bands at 1698 and 1687 cm^{-1} appear; the band at 1540 cm^{-1} is split in three components at 1555, 1544 and 1513 cm^{-1}, respectively. The N-H stretching band, which in the free peptide is located at 3264 cm^{-1}, is almost absent when $(GC)_2$ interacts with gold, probably, forbidden by surface selection rules. This result agrees with a flat and parallel disposition of $(GC)_2$ over gold surface.

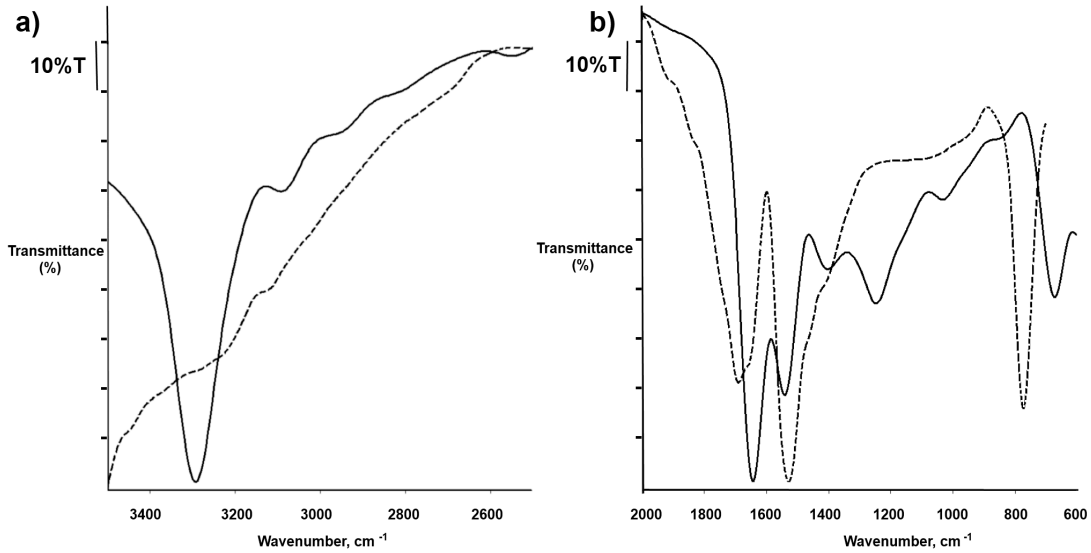

Figure 7. ATR-FTIR spectra of $(GC)_2$ peptide (solid line) and Au-$(GC)_2$ NPs (dashed line) in 3500-2500 cm^{-1} (a) and 2000-600 cm^{-1} region.

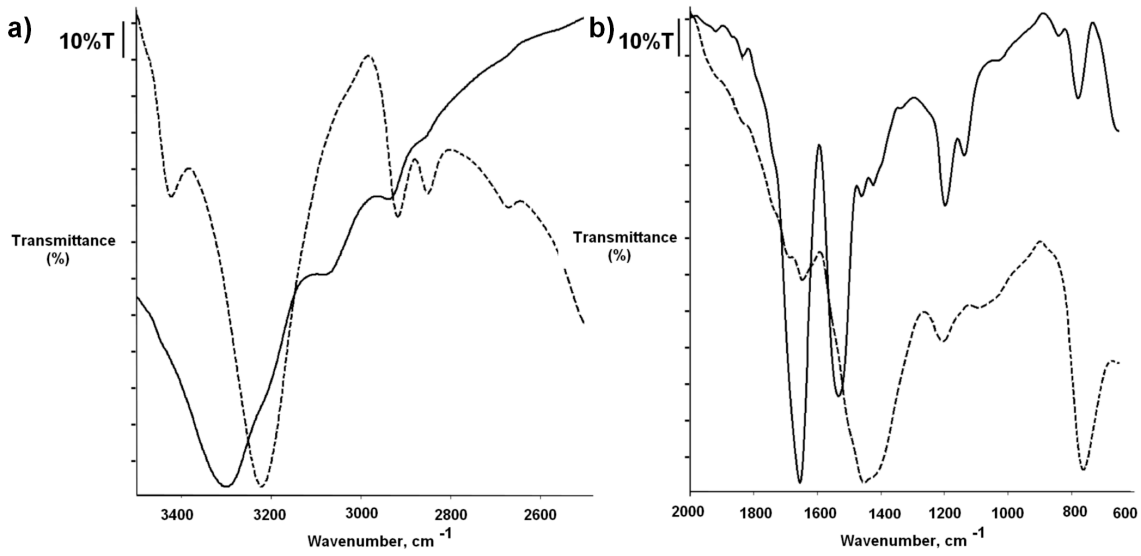

Figure 8. ATR-FTIR spectra of RGD-$(GC)_2$ peptide (solid line) and Au-RGD-$(GC)_2$ NPs (dashed line) in 3500-2500 cm^{-1} (a) and 2000-600 cm^{-1} region.

The changes are also evident in the spectrum of RGD-$(GC)_2$ peptide after conjugation with gold nanoparticles (dashed line, Figure 8): amide I band shows two feeble components at 1686 and 1646 cm^{-1}, while amide II shows a broad band centered at 1455 cm^{-1}. The N-H stretching vibrations are also affected: in the free peptide a strong absorption at 3301 cm^{-1} with 3195 and 3065 cm^{-1} less intense components are present, whereas the only strong band at 3221 cm^{-1} is evident upon interaction. These data suggest that both CO and NH groups of the amide bonds are affected by the interaction of the peptides with gold surface, and that the backbone conformation and the hydrogen bonding pattern of the conjugated peptides undergo significant changes.

FTIR results were correlated with NMR spectroscopy data to further validate the binding of the peptides to the gold nanoparticles and identify key organic residues involved in the interaction. First of all, ^1H NMR spectra of the free peptides were recorded and proton resonance signals were attributed to the most important peptide components.

Due to the fast tumbling of these small peptides, no NOE contacts could be observed in 2D [^1H, ^1H] NOESY experiments [16], thus, we recorded 2D [^1H, ^1H] ROESY spectra [17]. By comparing 2D [^1H, ^1H] TOCSY and 2D [^1H, ^1H] ROESY we were able to identify all the different spin-systems and sequentially assign them (Figure 9). In particular, the presence of strong sequential ROE contacts of the H_{Ni}-$H_{\alpha i-1}$ type allowed us to clearly connect all the residues.

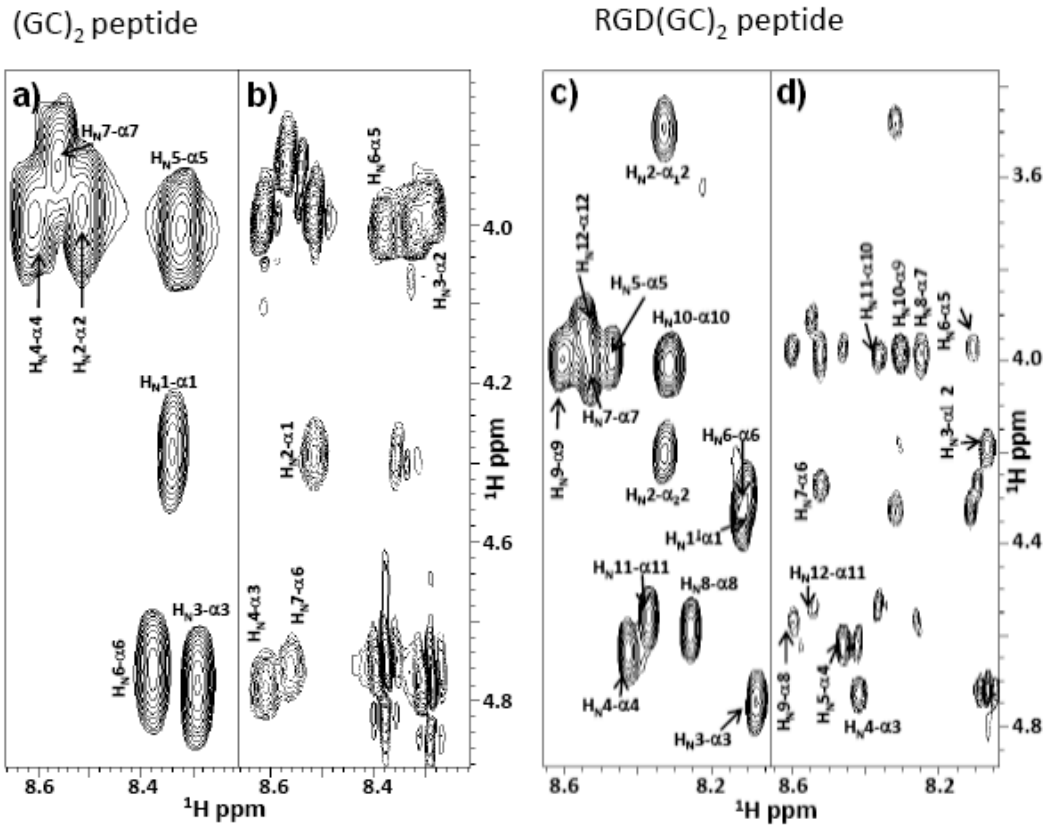

Figure 9. Comparison of 2D [^{1}H, ^{1}H] TOCSY (a,c) and 2D [^{1}H, ^{1}H] ROESY (b,d) spectra of the $(GC)_2$ and RGD-$(GC)_2$ peptides. Intra-residue H_{Ni}-$H\alpha_i$ and sequential H_{Ni}-$H\alpha_{i-1}$ connectivities are indicated.

1D proton spectra of Au-$(GC)_2$ NPs (Figure 10, b) shown an evident change of peptide resonances after interaction with gold, where a large broadening of all the signals was observed. Cysteine residues are highly influenced and their β-CH_2 proton signals either move or totally disappear, with respect to the corresponding peak in the spectrum of the free $(GC)_2$ peptide (Figure 10, a). Similarly, we compared 1D proton and 2D [^{1}H, ^{1}H] TOCSY spectra of the RGD-$(GC)_2$ peptide with those of the

Au-RGD-$(GC)_2$ nanoparticles (Figure 11, 12). In the spectrum of Au-RGD-$(GC)_2$ NPs, the interaction between the peptide with large hydrophobic gold surface causes a severe enlargement of all the NMR lines (Figure 11, lower panel). The line broadening is, in fact, widespread in the 1D proton spectrum in the HN and aromatic region as well as in the side-chain region. It's worth noting that the peak around 2.9 ppm, corresponding to the β-CH_2 groups of the cysteines in the free peptide, vanishes when the peptide is conjugated to the particles (Figure 11, b).

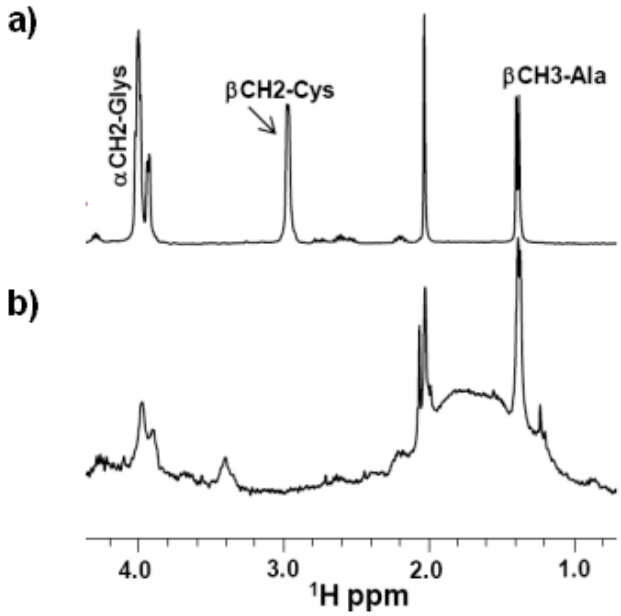

Figure 10. Comparison of 1D proton spectra of the $(GC)_2$ peptide (a) and Au-$(GC)_2$ nanoparticles (b). Spectral regions containing signals from side-chain protons are shown.

This feature has been previously observed for resonances belonging to the protons that are located rather close to the gold surface [18]. The changes can be better seen in the 2D [^{1}H, ^{1}H] TOCSY spectra (Figure 12). Since the large broadening of the resonances causes the loss of many peaks and highly reduces the quality of the 2D spectrum, the use of a cold-probe allows us to partially overcome this problem. In fact, spin systems for Ala, Arg, Asp and Glu are easily recognised in the spectrum of the Au-RGD-$(GC)_2$ NPs (Figure 12, b).

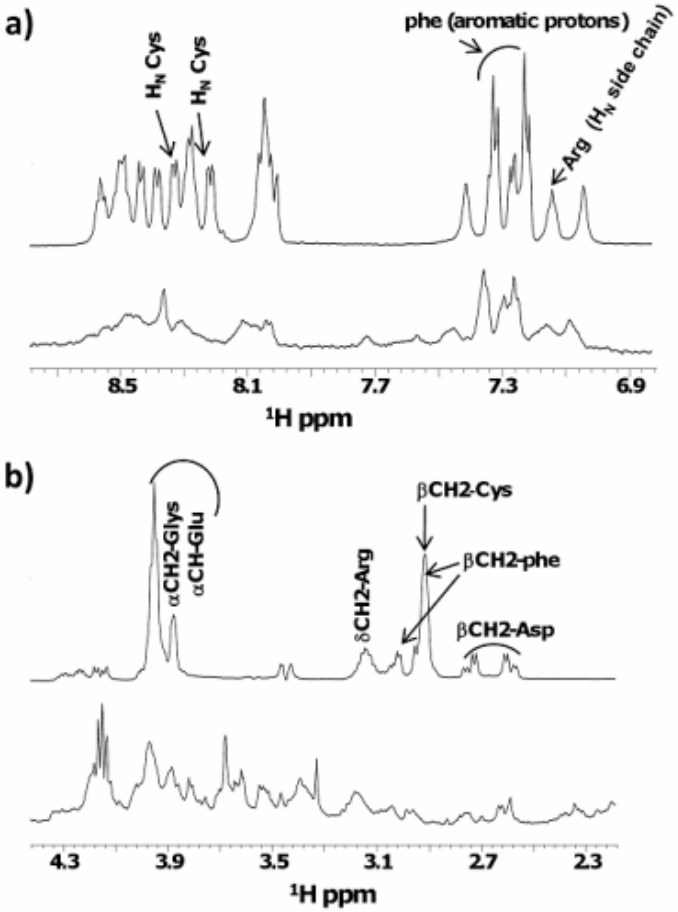

Figure 11. Comparison of 1D proton spectra of the RGD-$(GC)_2$ peptide (a, b, upper panels) and Au-RGD-$(GC)_2$ nanoparticles (a, b, lower panels). An expansion of the H_N and aromatic protons region is reported in (a) while signals from side-chain protons are shown in (b).

Correlations between HN and side chain protons disappear for the two Cys residues. Line broadening comes along with the small chemical shift changes mainly affecting the backbone HN group of the Arg (8.05 ppm in the apo-form and 8.16 ppm in the bound-form) as well as the β-CH_2 protons of the Asp (2.75-2.61 ppm in the apo-form and 2.82-2.64 ppm in the bound-form), thus, indicating that only a small structural rearrangement takes place in the peptide-cyclic portion.

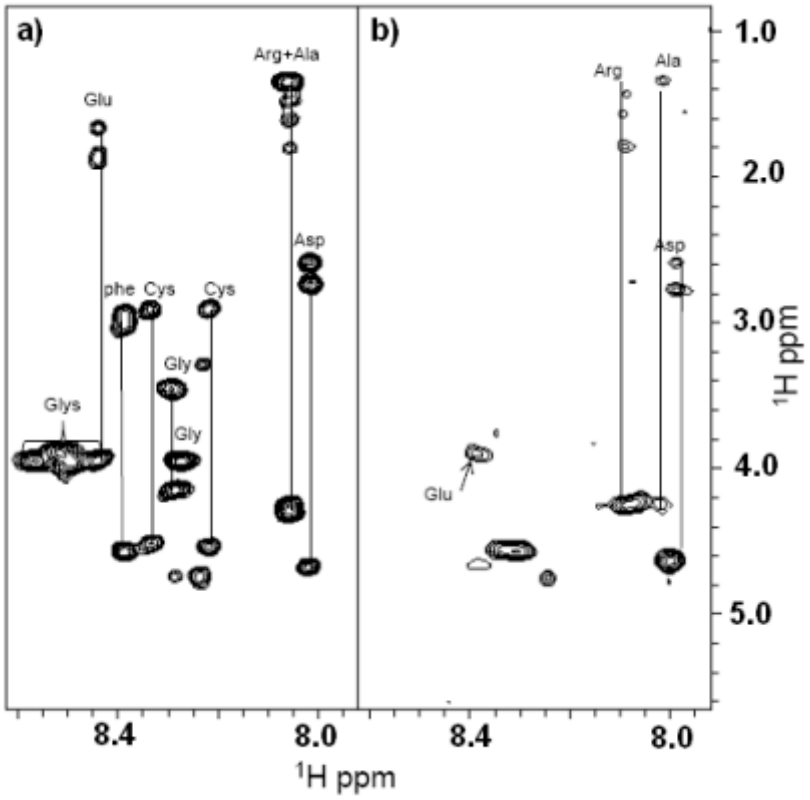

Figure 12. Comparison of 2D [^{1}H, ^{1}H] TOCSY spectra of the RGD-$(GC)_2$ peptide (a) and Au-RGD-$(GC)_2$ nanoparticles (b). The H_N-aliphatic protons correlation region is reported and spin systems assignments indicated.

From the perusal of spectroscopic ATR-FTIR and NMR data a number of conclusions about the conjugation of the peptides to gold particle can be drawn: a strong interaction of the $(GC)_2$ part with gold surface *via* the sulphur atom of cysteine residues results in a strong perturbation of CO and NH groups and disappearance of Cys β-CH_2 proton signal. On the contrary, the rigid RGD ring seems to be almost unaffected upon interaction with gold: from NMR spectra only a minor structural rearrangement of the peptide-cyclic portion can be detected; in the FTIR spectrum, amide I and amide II bands show the patterns different from those found in the Au-$(GC)_2$ spectrum, likely, because of the amide I band to be forbidden by surface selection rules causing its low intensity. Summing-up, the interaction between $(GC)_2$ or RGD-$(GC)_2$ and AuNPs mainly consists in the formation of S-Au bonds between the cysteine residues of $(CG)_2$ part and gold surface, leaving the RGD moiety almost unaffected and free for the interaction with integrin receptor.

For cellular uptake studies, peptide conjugated nanoparticles were added to cultures of U87 cells, a human glioblastoma cell line, and the cellular uptake was compared after different incubation times, using confocal microscopy (Figure 13, a-d). Importantly, the extent of cellular uptake in each case was vastly different: a large amount of Au-RGD-$(GC)_2$ conjugates was found to be present into cellular body even after 5 min of incubation (Figure 13, b), while Au-$(GC)_2$ particles were hardly taken up by the cells even after 30 min of incubation (Figure 13, c). The quantitative extent of cellular uptake was evaluated by measuring the pixel brightness of the confocal images. The cellular areas nearly equal to 780 μm^2, containing conjugated gold nanoparticles, were examinated by using Leica Confocal Software.

The results of the experiments are reported in Table 1, showing a huge difference between the pixels related to the cells treated with RGD-containing nanoparticles and $(GC)_2$ conjugated nanoparticles, respectively.

Table 1. Comparison of Au-RGD-$(GC)_2$ and Au-$(GC)_2$ nanoparticles uptaken by U87 glioblastoma cells. The brightness (pxl) of similar areas (780 μm^2) measured by the images collected by confocal microscopy of Au-RGD-$(GC)_2$ and Au-$(GC)_2$ nanoparticles was calculated by the Leica Confocal Software.

Peptide	Pixel brightness (5 min)	Pixel brightness (30 min)
RGD-$(GC)_2$	0.87	13.3
$(GC)_2$	0.07	0

As expected, the amount of Au-RGD-$(GC)_2$ particles taken up by the cells is growing along with incubation time, giving the pixel brightness of 0.87 and 13.3 after 5 and 30 min of incubation, respectively. On the contrary, the cells incubated with the particles conjugated with peptide lacking RGD-moiety, shown the pixel brightness near to the zero.

In order to better understand the uptake mechanism and discover the fate of the particles into the cellular body, TEM experiments were performed. For this purpose, the cells were incubated with the nanoconjugates for 1 hour. The results of these experiments are shown in Figures 14-15. The nanoparticles functionalized by linear $(GC)_2$ peptide are approaching the cellular membrane after 1 h of incubation, however, are not able to cross it and be taken up by the cells (Figure 14).

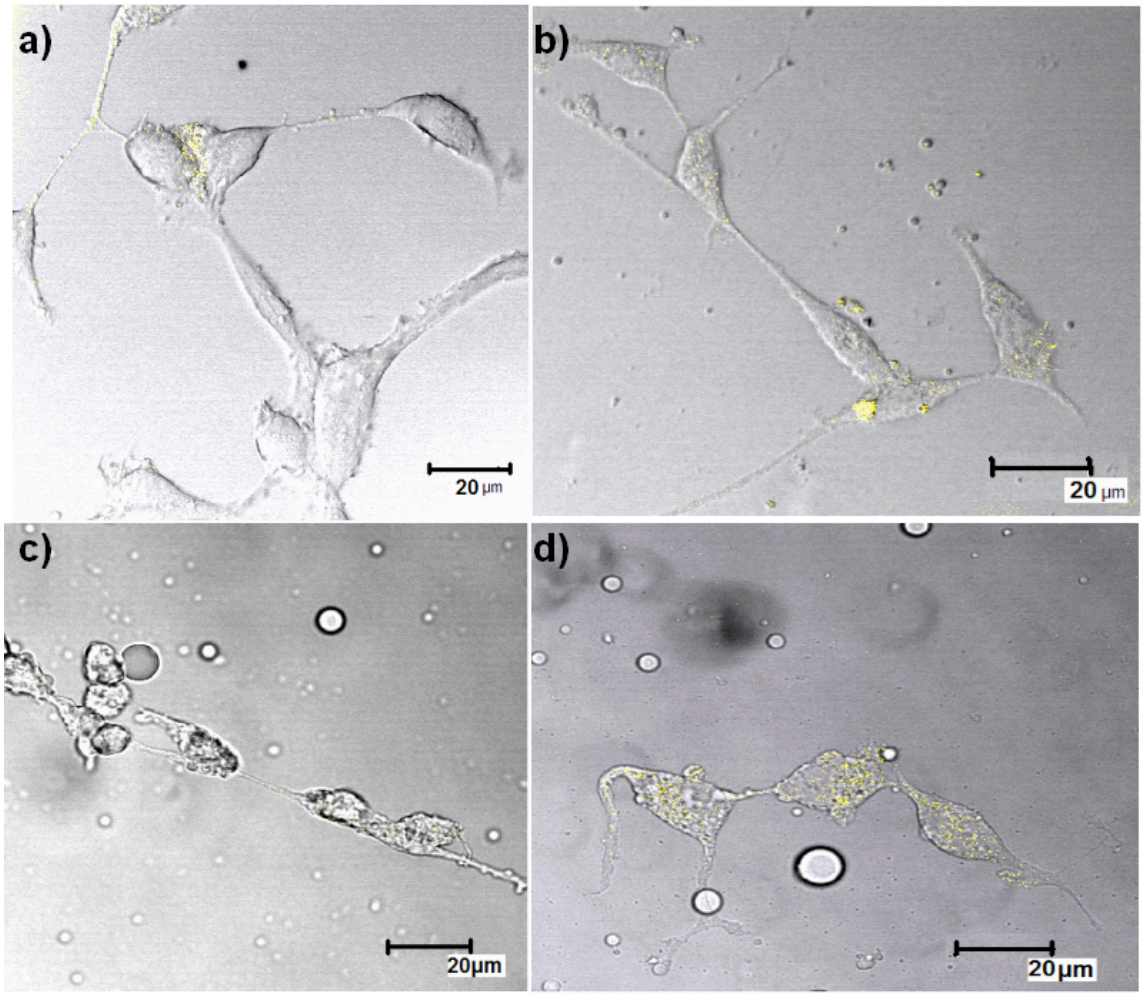

Figure 13. Cellular uptake of conjugated gold nanoparticles into U87 cells recorded by confocal microscopy in the reflection mode: a) Au-$(GC)_2$ after 5 min incubation, b) Au-RGD-$(GC)_2$ after 5 min incubation, c) Au-$(GC)_2$ after 30 min incubation, d) Au-RGD-$(GC)_2$ after 30 min incubation.

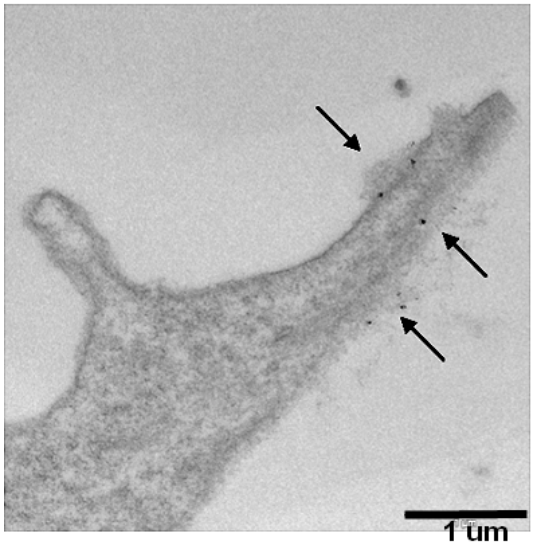

Figure 14. TEM image of Au-$(GC)_2$ nanoparticles incubated with U87 cells for 1 hour. The AuNPs are located outside the cellular membrane (black arrows).

On the contrary, Au-RGD-$(GC)_2$ NPs are found while crossing cellular membrane and enclosed into the endosomes (Figure 15, a, b, e). These findings are in accordance with confocal microscopy results, supporting an internalization mechanism *via* integrin-receptor mediated endocytosis [19]. Of extreme interest is that the RGD-conjugated nanoparticles were also found crossing nuclear pore complex, accumulated inside the nucleus and even into the nucleolus (Figure 15, c and d).

Nuclear delivery is known to be a challenging task, since the nanoparticles, once into the cell, must escape endosomal/lysosomal pathways, possess a nuclear localization sequence, and be small enough (<30 nm) to cross the nuclear membrane *via* nuclear pores [20].

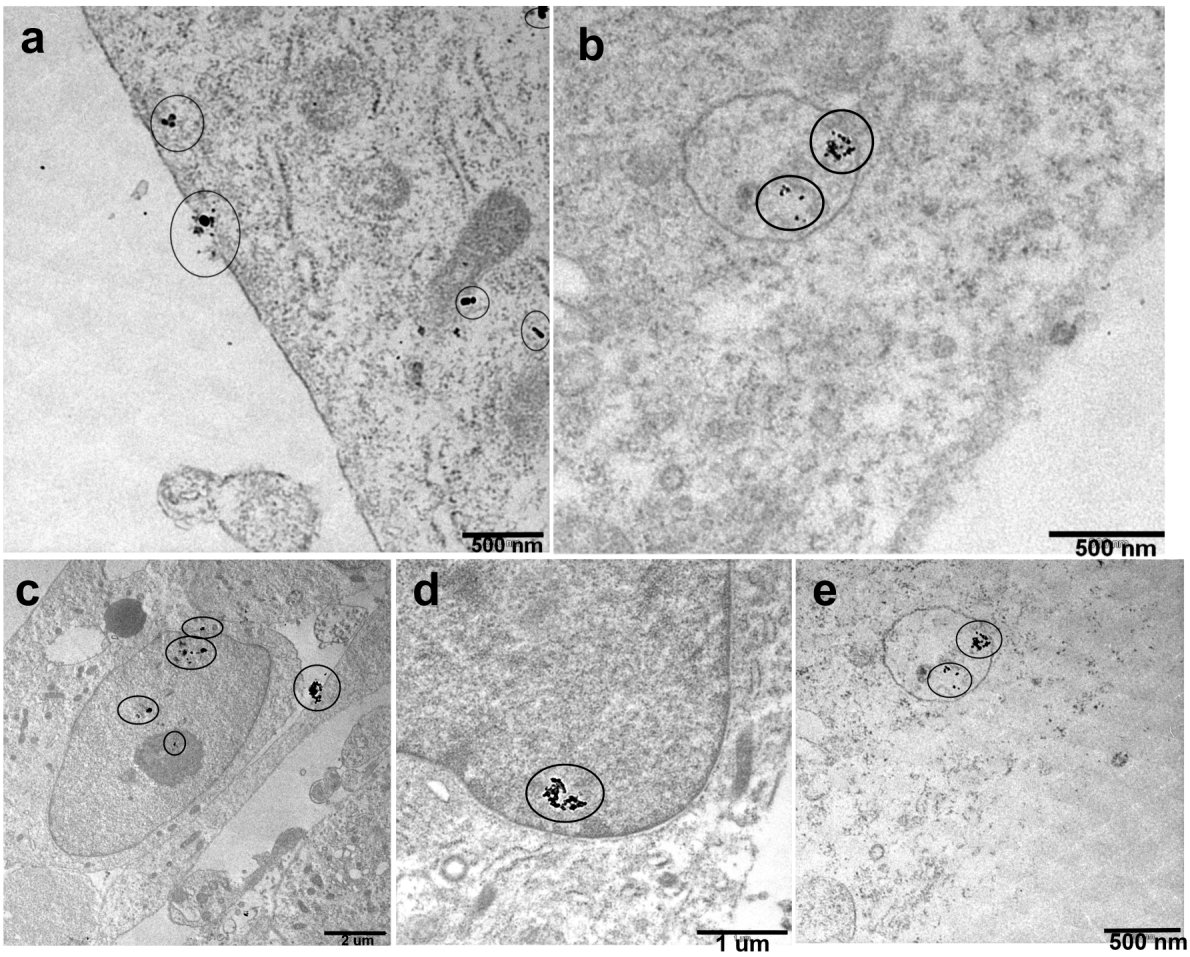

Figure 15. TEM images of internalization of Au-RGD-$(GC)_2$ NPs into the U87 cells after 1 hour of incubation. Particles are found: a) crossing cellular membrane; b), e) enclosed into the endosomes; c), d) crossing nuclear pore complex and into the nucleus and nucleolus.

In fact, the presence of nanoparticles free in the cytoplasm does suggest endosomal escape mechanism to take place, allowing the nanoparticles to get free to be ready to interact with nuclear pore complex (Figure 15, a). Even if RGD-peptide has not ever been recognized as nuclear localization signal (NLS) peptide, it appears to be able to perform this functionality.

Undoubtedly, the internalization mechanism and nanoparticle fate still need to be explored in details, performing more specific experiments, as the ability to direct the “cargo” nanoparticles into the nucleus has been a task of a great interest so far.

6. Concluding remarks

The RGD sequence is currently the basic module for a variety of molecules designed for the preferential binding to $\alpha_V\beta_3$ integrin. The affinity of RGD peptides for their ligands may be affected by steric conformation of the peptide. Indeed, the cyclization is commonly employed to improve the binding properties of RGD peptides, conferring rigidity to the structure. The RGD peptide sequence is normally flanked by other amino acids to build a ring system, offering a possibility to present the RGD sequence in a specific conformation for a selected integrin [21]. Integrins are able to mediate adhesive events during various cancer stages such as malignant transformation, tumor growth and progression, invasion, and metastasis. Among all integrins, $\alpha_V\beta_3$ is probably the most strongly involved in the regulation of angiogenesis. Importantly, $\alpha_V\beta_3$ integrin is widely expressed on blood vessels of human tumors but not on the vessels in normal tissues.

Nanoparticles can be grafted at their surface with a targeting ligand such as an RGD-based sequence. Several advantages are attributable to these nanoconjugates: their size leads to the “passive targeting” of tumors *via* the so-called enhanced permeability and retention effect; because of their size, renal filtration is avoided, leading to prolonged blood circulation times and longer accessibility of the ligand to target receptors within the tissue; RGD-targeted nanoparticles may specifically address drugs to angiogenic endothelial cells or cancer cells by the binding of the RGD peptide to $\alpha_V\beta_3$ overexpressed by these cells, allowing the “active” targeting of the tumors; RGD-targeted nanoparticles can be internalized *via* receptor-mediated

endocytosis, which is not possible with single peptide construct or with nontargeted nanoparticles. Subsequently, intracellular drug cytosolic release occurs, followed by direct killing of endothelial cells. The destruction of the endothelium in solid tumors can result in the death of tumor cells induced by lack of oxygen and nutrients [4].

Inspired by these facts, we designed and synthesized small (10-14 nm) gold nanoparticles covalently conjugated with an RGD-containing peptide. The nanoconjugates were fully characterized by a number of spectroscopic and microscopic methods, leading to the following findings: $(GC)_2$ linear part of the RGD-containing peptide was confirmed to be covalently bound to the gold surface *via* two Cys residues, while RGD-motif was free and ready to integrin receptor recognition. After incubation with U87 glioblastoma cells, the nanoparticles expressing RGD sequence where found taken up by the cells and distributed in different cellular compartments, while Au-$(GC)_2$ nanoparticles were not able to penetrate the cellular membrane. The internalization mechanism was studied by TEM, confirming the receptor-mediated endocytosis pathway followed by an endosomal escape, since the nanoparticles were found also free in the cytosol. Moreover, the nanoparticles were even able to cross nuclear membrane complex and were found into the nucleus and nucleolus. A further, more detailed understanding of the nanoparticle fate inside the cell is needed though. A quantitative analysis of the cellular uptake, carried out by pixel brightness measurements, confirmed the importance of RGD motif and the conservation of the conformation needed for the peptide to be active in integrin-binding.

7. References

1. L. Shuang, *Bioconjugate Chem.,* 2009, **12** (20), 2199-2213.
2. N. Graf, D. R. Bielenberg, N. Kolishetti, C. Muus, J. Banyard, O. C. Farokhzad, and S. J. Lippard, *ACS Nano*, 2012, **5** (6), 4530-4539.
3. R. K. Goswami, K. M. Bajjuri, J. S. Forsyth, S. Das, W. Hassenpflug, Z.-Z. Huang, R. A. Lerner, B. Felding-Habermann, and S. C. Sinha, *Bioconjugate Chem*., 2011, **22**, 1535–1544.
4. F. Danhier, A. Le Breton, and V. Préat. *Mol. Pharmaceutics,* Article ASAP, **DOI:** 10.1021/mp3002733.
5. S. Mukhopadhyay, C. M. Barnes, A. Haskel, S. M. Short, K. R. Barnes, and S. J. Lippard, *Bioconjugate Chem.*, 2008, **19**, 39-49.
6. K. Temming, R. M. Schiffelers, G. Molema, and R. J. Kok, *Drug Resist. Update,* 2005, **8,** 381–402.
7. W. Arap, R. Pasquallini, and E. Ruoslahti, *Science*, 1998, **279**, 377-380.
8. R. Haubner, H.-J. Wester, U. Reuning, R. Senekowitsch-Schmidtke, B. Diefenbach, H. Kessler, G. Stocklin, and M. Schwaiger, *J. Nucl. Med.* 1999, **40**, 1061-1071.
9. Y.-H. Kim, J. Jeon, S. H. Hong, W.-K. Rhim, Y.-S. Lee, H. Youn, J.-K. Chung, M. C. Lee, D. S. Lee, K. W. Kang, and J.-M. Nam, *Small*, 2011, **14** (7), 2052-2060.
10. M. B. Dowling, L. Li, J. Park, G. Kumi, A. Nan, H. Ghandehari, J. T. Fourkas, and P. deShong, *Bioconjugate Chem.,* 2010, **21**, 1968-1977.

11. E. Morales-Avila, G. Ferro-Flores, B. E. Ocampo-Garcia, L.M. De Leon-Rodriguez, C. L. Santos-Cuevas, R. Garcia-Becerra, L. A. Medina, and L. Gomez-Olivan, *Bioconjugate Chem.,* 2011, **22**, 913-922.
12. Y. Han, F. Albericio, and G. Barany, *J Org Chem.,* 1997*,* **62**, 4307-4312.
13. G. Scarì, F. Porta, U. Fascio, S. Avvakumova, V. Dal Santo, M. De Simone, M. Saviano, M. Leone, A. Del Gatto, C. Pedone, and L. Zaccaro. *Bioconjugate Chem.*, 2012, **23** (3), 340–349.
14. R. De Palma, S. Peeters, M. J. Van Bael, H. Van den Rul, K. Bonroy, W. Laureyn, J.Mullens, G. Borghs, and G. Maes, *Chem Mater.,* 2007*,* **19**, 1821-1831.
15. S. Aryal, B. K. C. Remant, N. Dharmaraj, N. Bhattarai, C. H. H. Kim, and Y. Kim, *Spectrochimica Acta A,* 2006*,* **63**, 160–163.
16. A. Kumar, R. R. Ernst, and K. Wuthrich, *Biochem Biophys Res Commun.,* 1980*,* **95**, 1-6.
17. A. Bax, and D. G. Davis, *J. Magn. Reson.,* 1985*,* **63**, 207-213.
18. Z. Krpetic, P. Nativo, F. Porta, and M. Brust, *Bioconjugate Chem.,* 2009*,* **20**, 619-624.
19. R. L. Juliano, R. Alam, V. Dixit, and H. M. Kang, *Nanomedicine and Nanobiotechnology,* 2009*,* **1**, 324-335.
20. J. M. de la Fuente, and C. C. Berry, *Bioconjugate Chem.* 2005**, 16**, 1176-1180.
21. S. Liu. *Mol Pharm.* 2006, **3** (5), 472-487.

Chapter V

Design and synthesis of AuNPs conjugated with Halo Tag specific ligands for cellular targeting

1. Introduction

The specific labeling of proteins is a key to revealing their dynamics and functions in living cells [1]. However, many conventional methods used to generate fluorescently tagged proteins and image them in their native environment are time-consuming and dificult, requiring expertise in protein chemistry, the successful microinjection of labeled products into cells, and specialized techniques [2]. Recently, a new modern approach, called Halo Tag technology, applied for cellular imaging, protein quantification and interaction analysis has been developed. It is designed to provide new options for rapid, side-specific labeling of proteins in living cells and *in vitro,* and based on the efficient formation of a covalent bond between the Halo Tag protein and synthetic ligands (Figure 1). The Halo Tag protein is a catalytically inactive, genetically modified derivative of a hydrolase protein [3]. This 33kDa monomeric protein can be used to generate N- or C-terminal fusions that can be efficiently expressed in a variety of cell types. The Halo Tag ligands are small chemical tags capable of covalently labeling the Halo Tag protein. These contain two crutial components: a common Halo Tag reactive linker that initiates formation of the covalent bond and a functional reporter such as a fluorescent dye or affinity handles such biotin. The rate of the ligand-protein binding is remarkably fast. The stability of the covalent bond easily allows fixed-cell imaging. The covalent bond forms rapidly under physiological conditions, is highly specific and essentially irreversible yielding a stable complex even under denaturing conditions. The flexibility to create labeled Halo Tag fusion proteins with a wide range of optical properties and functions allows

to image and localize labeled Halo Tag protein fusions in live- or fixed-cell populations as well as isolate and analyze Halo Tag protein fusions and protein complexes [3].

Several requirements are needed for specific ligand to be active for interaction with Halo Tag protein: the linker between halide and functional group should be 14 atoms long and contain 6 carbon atoms proximal to the terminal chloride (Figure 2) [4]. Normally, nanoparticle bioconjugates are prepared *via* formation of new chemical bonds between functional groups associated with a nanoparticle and a biomolecule or small molecule of interest. In general, the structure of a nanoparticle bioconjugate affects its function, and the controlled display of biomolecules on NPs is paramount in obtaining conjugates with well-defined and reproducible properties [5].

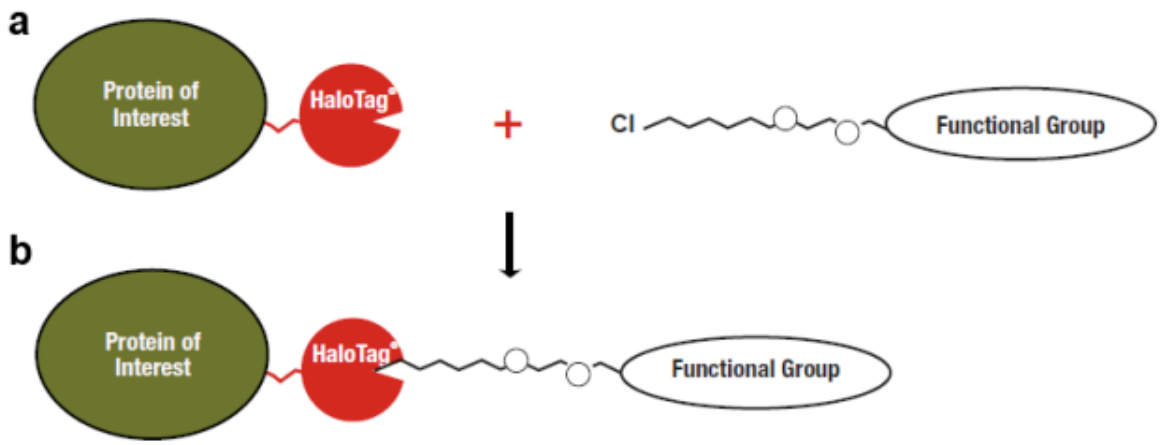

Figure 1. A schematic representation of Halo Tag Technology: a) Halo Tag protein is fused with a protein of interest, and a Halo Tag specific ligand is added; b) Halo Tag ligand is recognized by Halo Tag-containing protein.

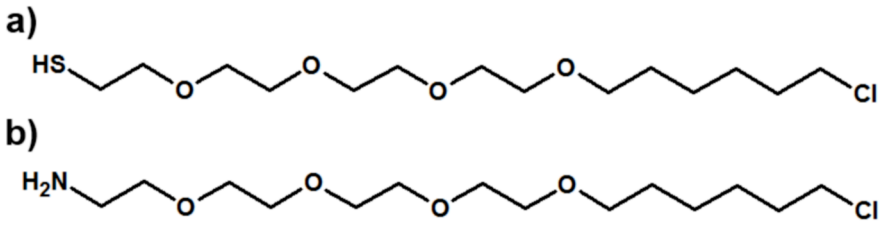

Figure 2. Halo Tag ligand building blocks: a) Halo Tag Thiol (O4); b) Halo Tag Amino (O4).

For creating a continuous passivation layer around AuNPs thiol compounds have been widely used, allowing efficiently improve their stability and dispersity in aqueous solution. This is mainly attributed to the fact that the thiol groups can bind covalently to the surface of AuNPs via an Au−S bond. Currently used thiol compounds mainly include glutathione (GSH), mercaptopropionic acid (MPA), cysteine, cystamine, dihydrolipoic acid (DHLA), thiol-ending polyethylene glycol (PEG-SH) etc [6-17]. As found by Ren *et al.*, PEG-SH-modified AuNPs are most stable in aqueous solution compared to other thiol compounds [18]. Conjugation of appropriately chosen functional molecules is then used to control the interaction of the nanoparticles with a desired target, affording functional AuNPs that specifically interacts with the proteins [19], nucleic acids [20], or other nanoparticles [21]. These few examples clearly show that the ligand shell surrounding the gold core is of paramount importance for its functionality. Conjugation of peptides, proteins and other biologically active molecules to the ligand shell of AuNPs, and not directly to the Au surface through the Au-S bond, is an appealing strategy to preserve their biological activity. For this purpose the AuNPs need to be capped by a mixed ligand

shell displaying some functionalizable groups, and an efficient coupling reaction for attachment of the peptide to these reactive groups is established [22]. We have already had an experience in attaching biologically active thiol-containing peptides and proteins directly to the gold surface, observing a successful preservation of their biological functionality [23, 24].

The goal of this work was to design and synthesize gold nanoparticles conjugated with Halo Tag functional ligands, in order to obtain bioactive conjugates with a number of properties, such as stability in a wide pH range and physiological media, certain size and functionality. These particles should be able to be recognised by Halo Tag protein expressed in different cellular compartments of interest.

From a wide range of available Halo Tag ligands, we have chosen a thiol- and an amino-containing molecules (Figure 2). Different techniques have been used to obtain the conjugates, and their properties have been compared on the basis of the synthesis method used. To stabilize the nanoparticles, a mixture of short PEGs, containing –OH, -COOH and –NHS functional groups, has been used. The choice of a modified PEG provides the functionality to coordinate to the Au surface while providing a well-ordered packing layer near the NP surface. This PEG layer provides a shield between the biological target and AuNP surface, thus reducing nonspecific interactions between the two [25].

The Halo Tag Thiol ligand has been used both for direct conjugation to the gold surface and conjugation *via* a spacer separating the PEG layer and Halo Tag ligand. The spacer allows to expose the active chlorine atom from the particle surface to be coupled to the Halo Tag protein in the cells.

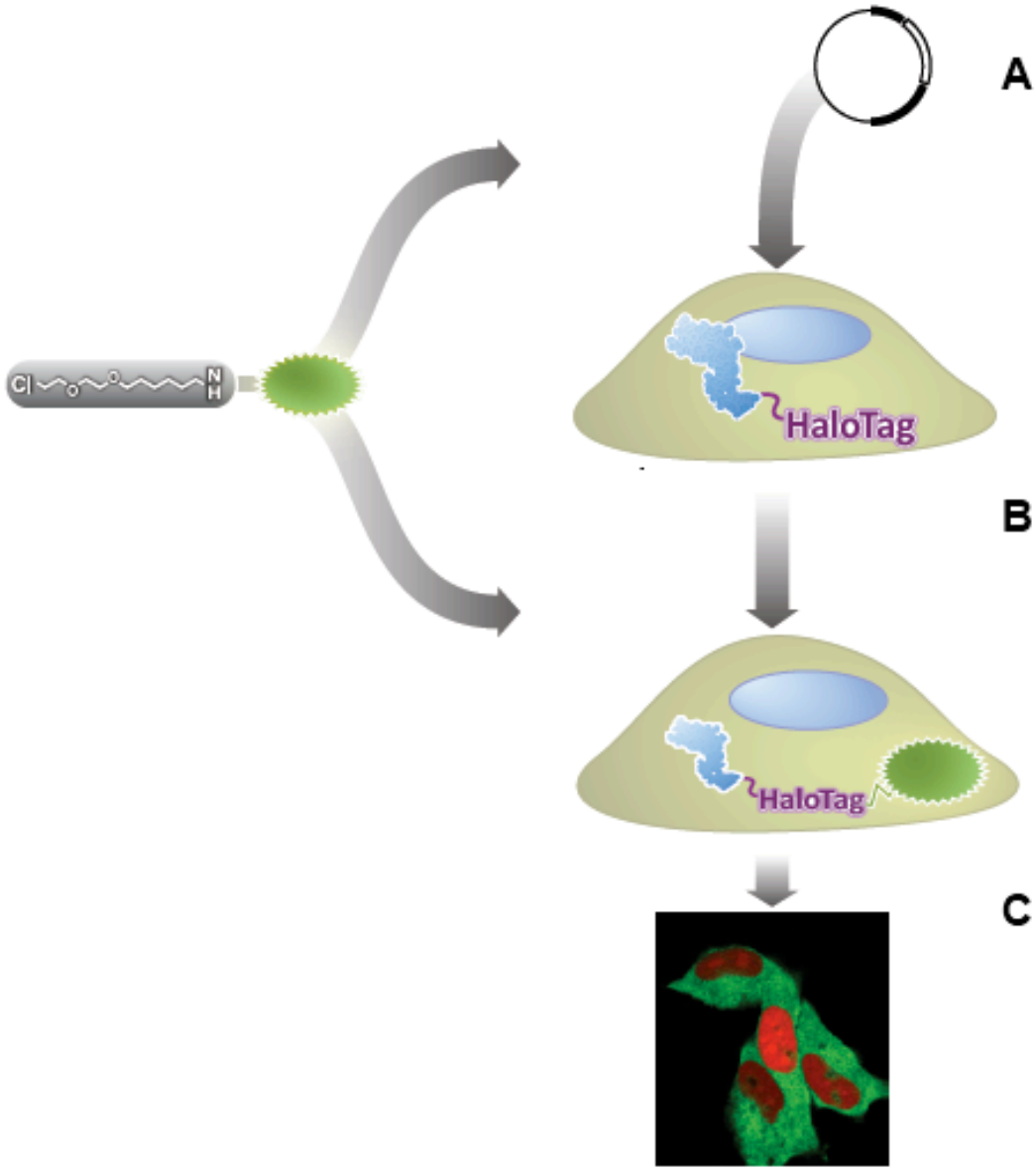

Figure 3. An overview of cellular imaging using Halo Tag conjugation: A) cells are transfected with a vector containing Halo Tag fusion protein; B) the cells expressing Halo Tag protein fused with a protein of interest are incubated with a Halo Tag functional ligand; C) the cells are visualised by confocal microscopy.

The Halo Tag Amino ligand has been conjugated *via* two different ways in order to campare their impact on the conjugates` properties: a EDC/sulfo-NHS coupling reaction involving –COOH groups of the PEG, and a direct conjugation to the PEG containing –NHS reactive groups [26].

A detailed characterization of the conjugates has been performed, using a number of up-to-date techniques. Biological studies including internalization experiments are now in progress and are going to be continued during my post-doc research.

2. Synthesis of monolayer-protected AuNPs

As a basis, gold nanoparticles stabilized by citrate ions have been used. Citrate molecules can be readily exchanged with thiol-containing ligands in a very short period of time, followed by a formation of a self-assembly monolayer (SAM) [27]. For this purpose, citrate nanoparticles have been prepared by a modified Turkevich-Frens method [28,29] and subsequently stabilized and functionalized by a shell of thiolated PEG molecules [30, 31].

2.1. Au-citrate nanoparticles (GNP)

Gold nanoparticles of 16±1.28 nm diameter have been prepared by quickly mixing a boiling solution of $HAuCl_4$ trihydrate(15 mg, 40 μmol) in 150 mL of Milli-Q water with 4.5 mL of warm (60-80 °C) 1 % (wt) aqueous solution of trisodium citrate, followed by reflux for 60 min. The resulted nanoparticle suspension was then allowed to cool down to room temperature and stirred overnight. The nanoparticles were filtered using a 0.45 μm Millipore filter before use, and characterized by UV-vis spectroscopy, TEM and analytical centrifugation (DSC).

2.2. Conjugation of Halo Tag Thiol ligand

2.2.1. Direct conjugation of Halo Tag Thiol (O4) ligand to GNP: GNP@PEG-OH-Halo Tag Thiol (O4) nanoparticles

For direct conjugation, a mixture containing Halo Tag Thiol ligand and thiolated PEG with terminal hydroxyl groups was used (Scheme 1). Due to the presence of a thiol goup, Halo Tag Thiol molecule is able to make a covalent bond with the gold surface contributing to the SAM layer surrounding nanoparticle [32], while PEG-OH layer protects against nonspecific interaction between AuNP surface and biological target.

As prepared GNP were conjugated with PEG-OH and Halo Tag Thiol (O4) ligands *via* citrate exchange method introducing in the ligand shell both 3% and 10 % of the latter ligand. The modification of AuNPs with PEG and Halo Tag Thiol (O4) ligands was carried out as follows. PEG HS-$C_{11}(EG)_4$-OH was dissolved in methanol to give 0.156 M stock solution. Halo Tag Thiol (O4) ligand was dissolved in DMSO to give 0.0152 M stock solution, which was stored at -20 °C. The ligands were pre-mixed in desired proportions in methanol in order to obtain the final volume of 200 µL. The total number of ligands to cover gold particle surface was considered 20500. Subsequently, the methanol-ligand mixture was added quickly under vigorous stirring to 30 mL of 2.58 nM GNP dispersion. The ligands were allowed to attach to the particles overnight, followed by washing by repeated centrifugation at 13500 rpm for 20 min at 10 °C.

The amount of Halo Tag Thiol ligand in the ligand shell was varied from 3% to 10% in order to compare both the properties of the conjugates and their colloidal stability, and their biological behaviour. UV-vis spectra of GNPs before conjugation (Figure 4, a, b; black line) show a SPR band at 522 nm, which shifts to 524 nm after exchange of citrate ions by Halo Tag Thiol molecules. Moreover, the absorbance of the SPR band increases in both cases confirming a change of the local extinction coefficient of the medium surrounding the particle [33]. The results of analytical centrifugation performed on a disc sedimintation centrifuge shown a considerable shift: diameter of citrate nanoparticles obtained by this method is 13.5 nm, while it undergoes a significant change to 12.1 nm and even 11.9 nm with increasing content of Halo Tag Thiol molecule in the ligand shell from 3% to 10%, respectively (Figure 5, a, b).

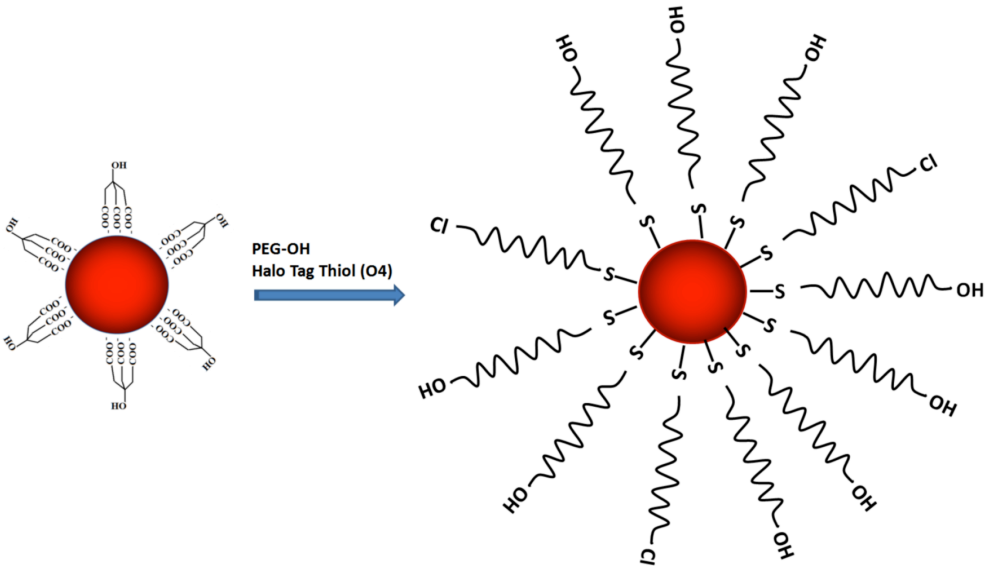

Scheme 1. Representation of direct conjugation of Halo Tag Thiol ligand to citrate-stabilized gold nanoparticles.

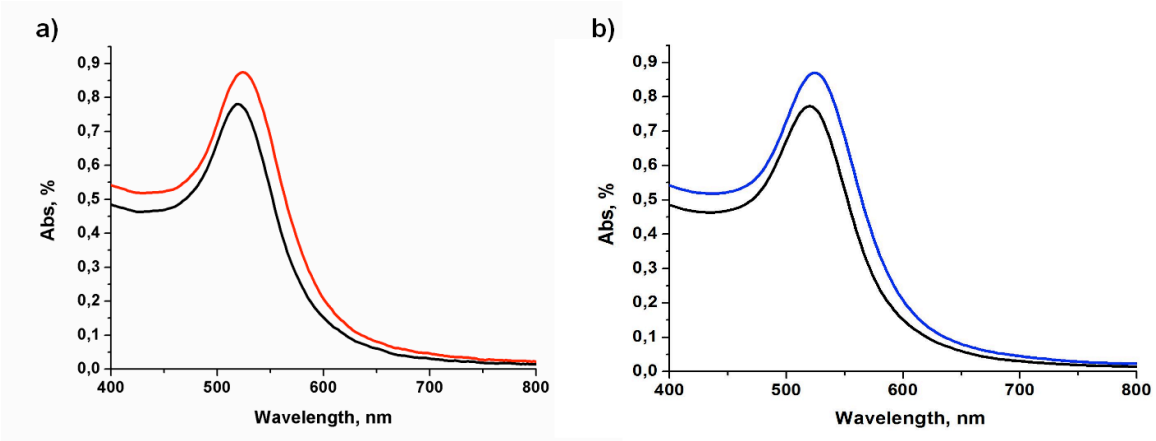

Figure 4. UV-vis spectra of AuNPs: a) GNP-522 nm (black line); GNP@PEG-OH(97%)-Halo Tag Thiol (O4) (3%)- 524 nm (red line); b) GNP-522 nm (black line); b) GNP@PEG-OH(90%)-Halo Tag Thiol (O4) (10%)- 524 nm (red line).

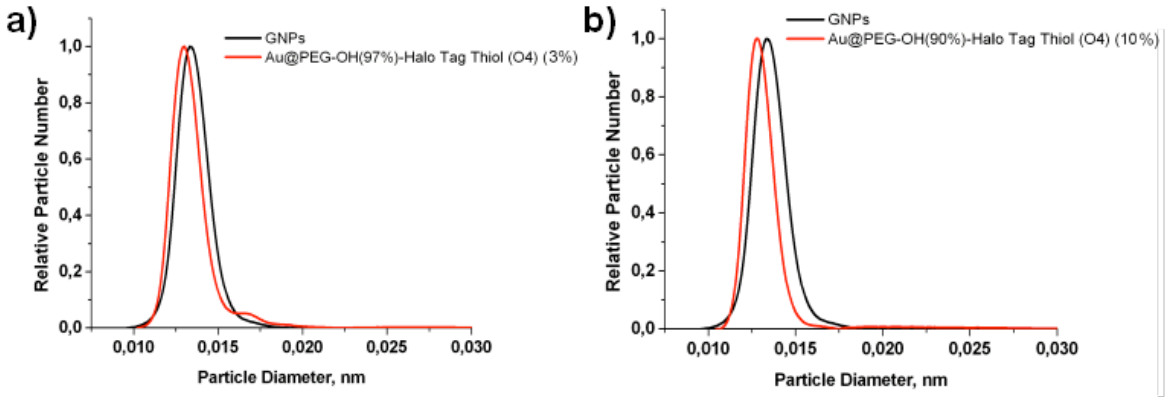

Figure 5. Analytical centrifugation patterns of AuNPs: a) GNPs-13.5 nm (black line); Au@PEG-OH(97%)-Halo Tag Thiol (O4) (3%)-12.1 nm (red line); b) GNP-13.5 nm (black line); b) Au@PEG-OH(90%)-Halo Tag Thiol (O4) (10%)- 11.9 nm (red line).

TEM results illustrated the presence of very monodispersed well separated particles with similar mean diameters of 15.91±1.13 nm (Figure 5) and 15.28±0.83 nm (Figure 6). Interestingly, the particles were able to form a kind of self-assembled 2D structures under natural dewetting process by slow evaporation of nanoparticle-containing solvent on the TEM grid [34].

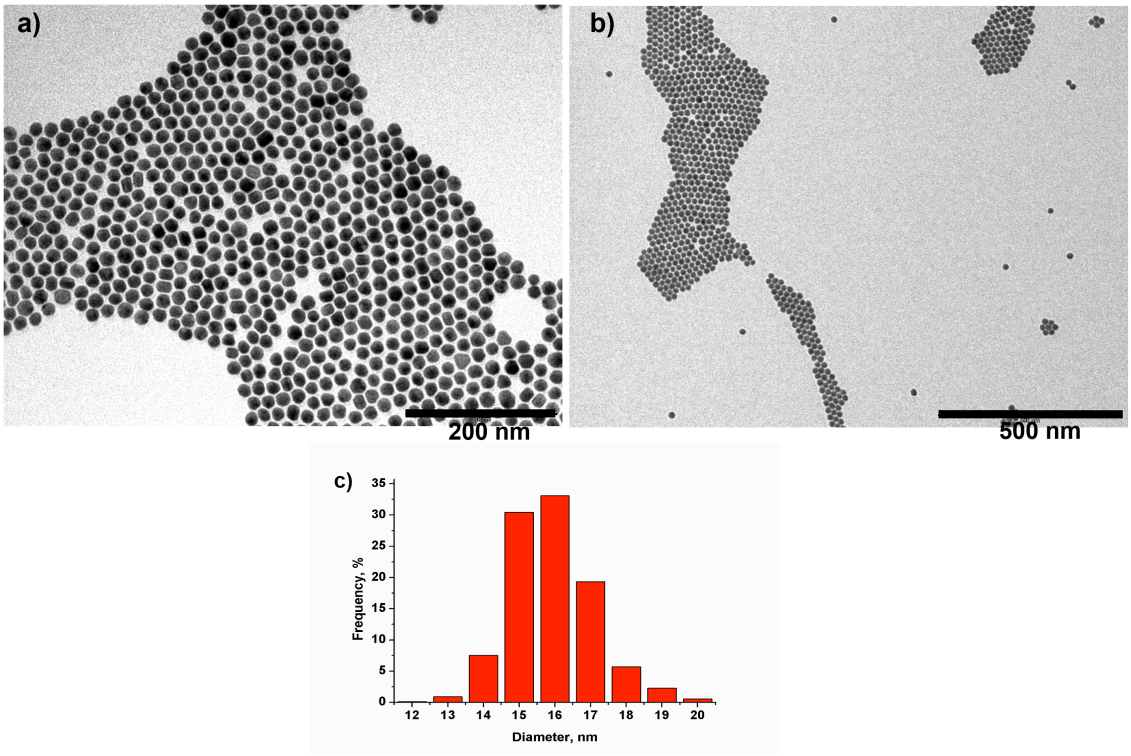

Figure 6a. TEM micrograph of GNP@PEG-OH(97%)- Halo Tag Thiol (O4) (3%): a) scale bar 200 nm; b) scale bar 500 nm; c) size distribution histogram (15.91±1.13 nm mean particle diameter).

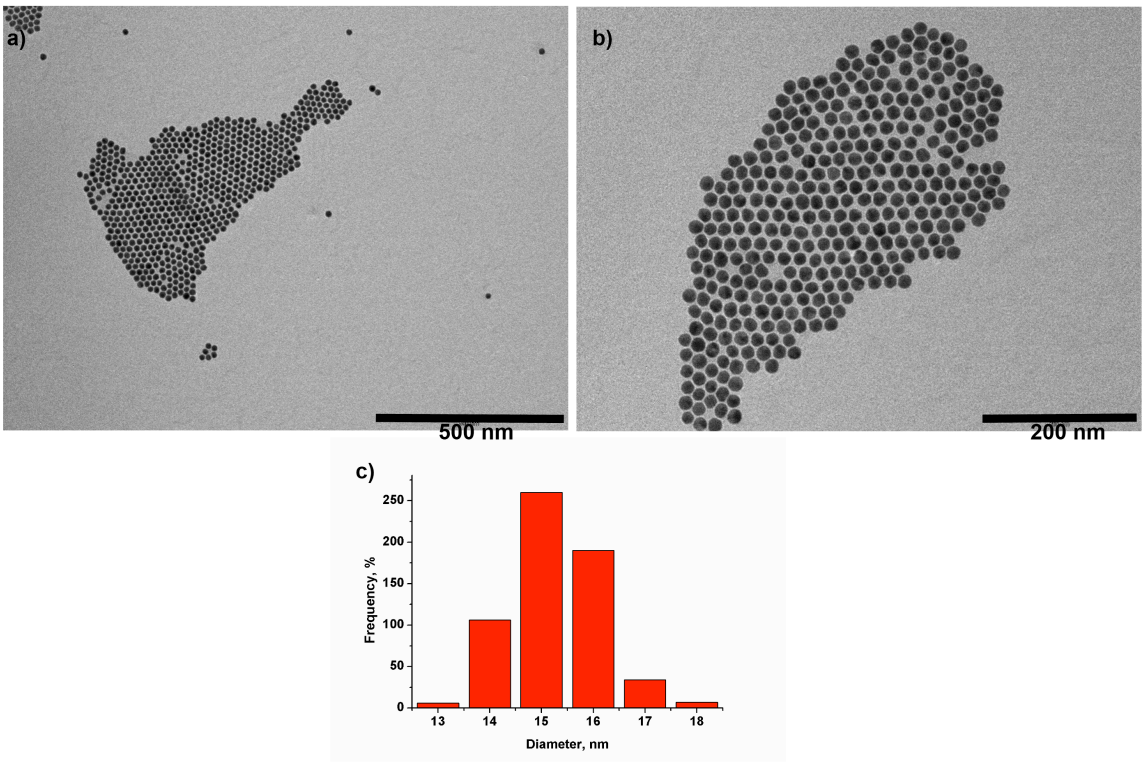

Figure 6b. TEM micrograph of GNP@PEG-OH(90%)-Halo Tag Thiol (O4) (10%): a) scale bar 500 nm; b) scale bar 200 nm; c) size distribution histogram (15.28±0.83 nm mean particle diameter).

To confirm the successful modification of GNPs with PEG and Halo Tag ligands, we measured the zeta-potentials of unmodified and modified particles. The results indicated the zeta-potentials of conjugated particles were significantly different from those of unmodified citrate GNPs: -14.3 and -15.2 mV *versus* -32.7 mV for citrate GNPs. The zeta-potential values considerably increased for functionalized nanoparticles due to the contribution of a great number of “neutral” PEG-OH molecules. However, the chlorine atom of the Halo Tag Thiol ligand is responsible for a negative particle charge. Infact, the zeta-potential of the particles containing 10% of Halo Tag Thiol ligand resulted slightly more negative (Figure 7).

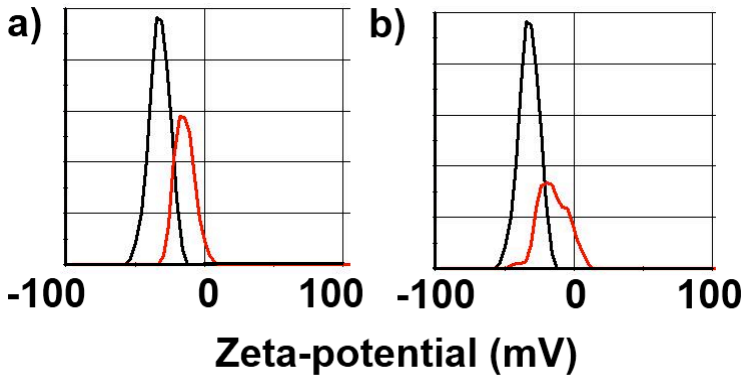

Figure 7. Zeta-potential of gold nanoparticles: black line- GNP, -32.7 mV; red line-Au@PEG-OH-Halo Tag Thiol (O4): a) 3%, -14.3 mV; b) 10%, -15.2 mV.

To be useful for biological applications or for building nanostructures using biological interactions, gold nanoparticles have to be stable over a wide range ionic strength and pH in the absence of an excess of capping ligand [35]. Halo Tag-capped nanoparticles were first separated from the excess of the ligand and citrate by repeated centrifugation and re-dispersion in PBS.

As an empirical measurement of the aggregation process, an aggregation parameter, which measures the variation of the integrated absorbance between 600 and 700 nm, was used. The aggregation parameter AP is defined as follows: $AP=(A-A_0)/A_0$, where A is the integrated absorbance between 600 and 700 nm of the sample at a given moment and A_0 is the integrated absorbance between 600 and 700 nm of the initial, fully dispersed solution of nanoparticles [36]. Figure 8 (a-c) shows the pH-induced aggregation patterns of Halo Tag Thiol-capped nanoparticles, prepared by direct conjugation, with 3% and 10% of bioactive molecule in the ligand shell (black and red line, respectively).

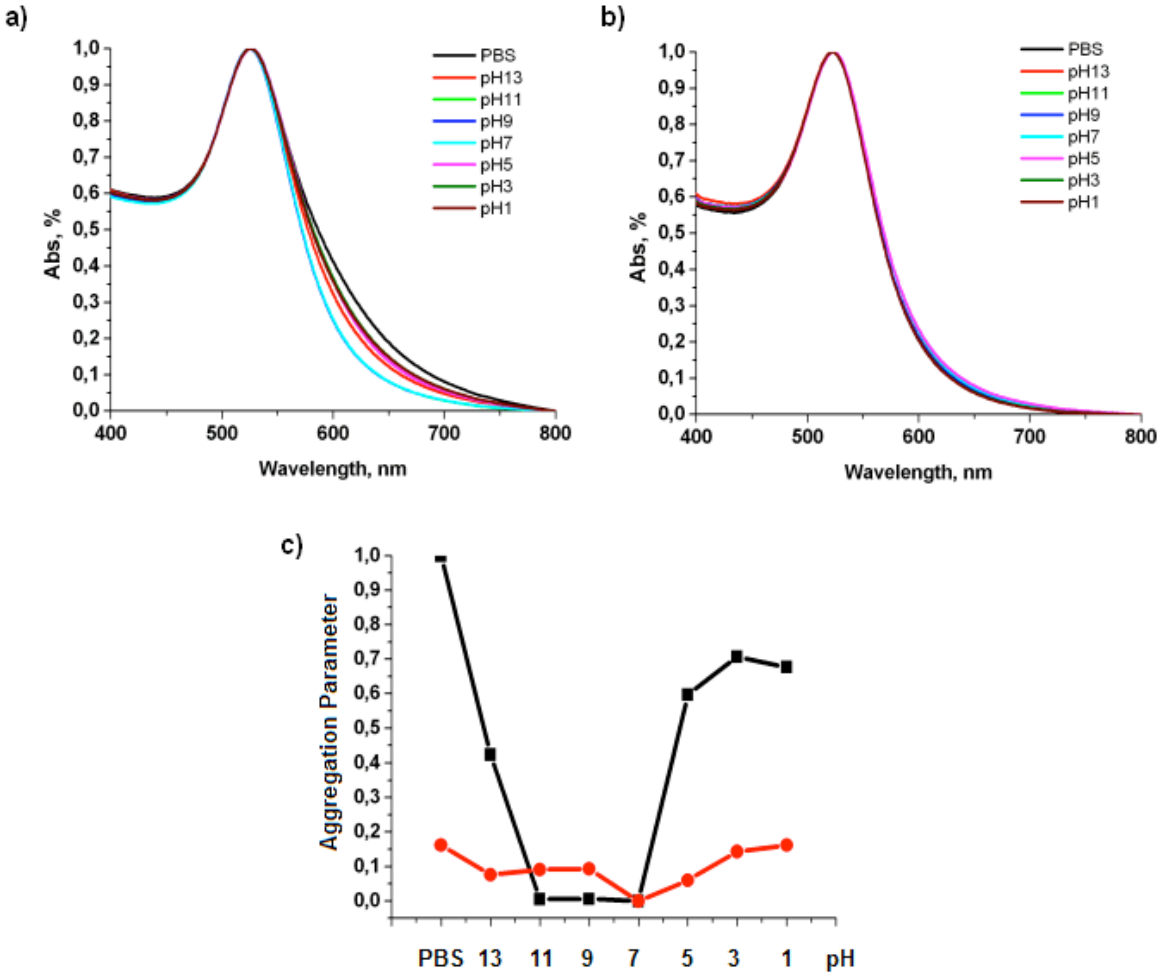

Figure 8. UV-vis spectra of Au@PEG-OH (97%)-Halo Tag Thiol (O4) (3%) (a) and Au@PEG-OH(90%)-Halo Tag Thiol (O4) (10%) (b) in PBS and different pH solutions. The pH values were 1, 3, 5, 7, 9, 11 and 13. (c) Stability against pH-induced aggregation of Au@PEG-OH (97%)-Halo Tag Thiol (O4) (3%) (black line) and Au@PEG-OH(90%)-Halo Tag Thiol (O4) (10%) (red line).

It is clear that the particles with major content of the ligand show a better stability both in PBS and at acidic pH, with aggregation parameter maximum less than 0.2. While PEGylated nanoparticles are subjected to a slight aggregation at acidic pH, probably due to protonation of terminal –OH groups.

The most of the bioassays are performed in the presence of buffers and salts up to the concentration of 300 mM NaCl. To be properly used in cellular uptake studies, the nanoconjugates must be as much as possible stable in presence of salts. Figure 9 represents the results on the stability of the conjugates in high concentrated NaCl solutions. No aggregation of the nanoparticles was detected even in extremely high salt conditions: incubated with NaCl, both particles were stable up to 3M concentration. The same behaviour is observed in this case: the particles containing 10% of Halo Thiol ligand appear more stable with a very low aggregation parameter less than 0.1.

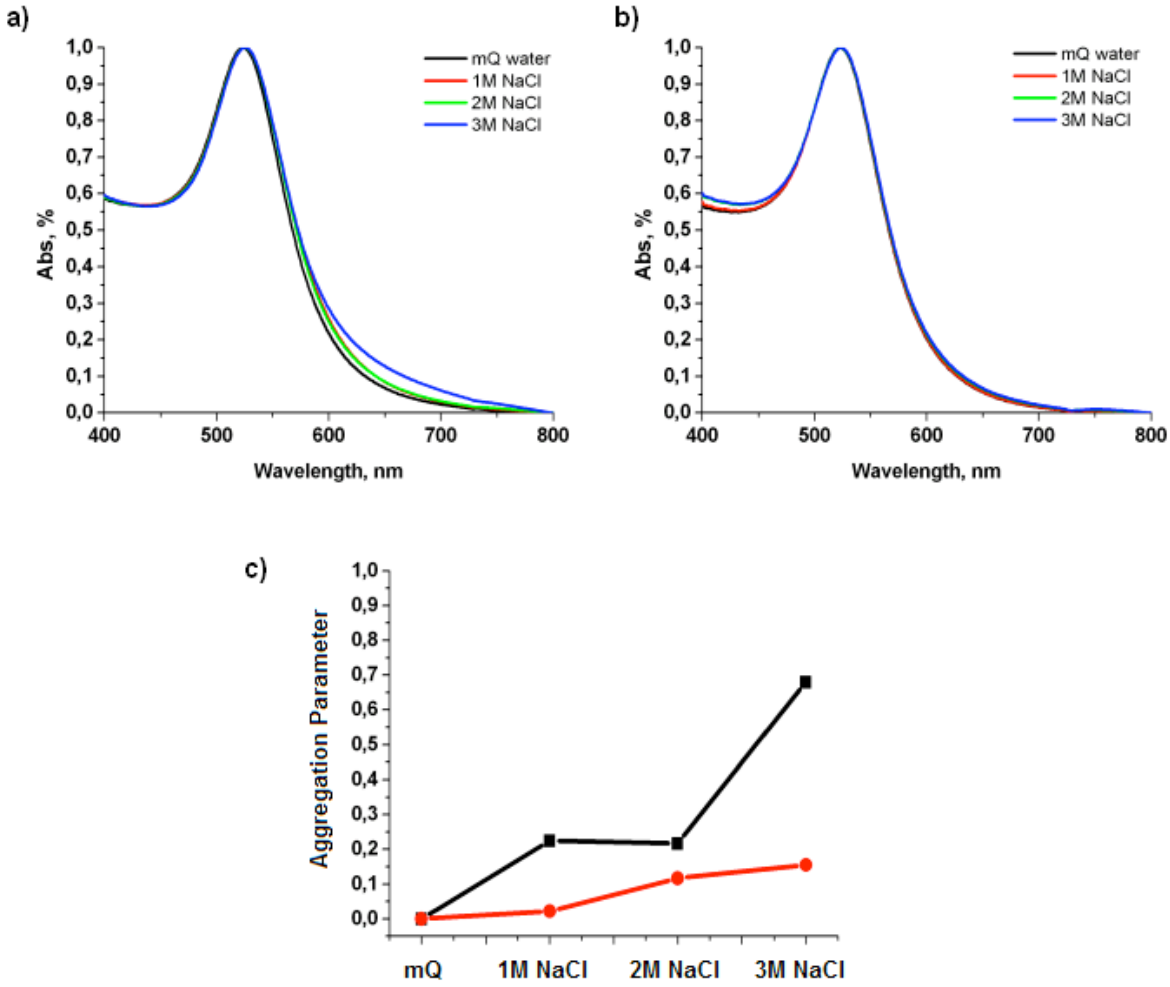

Figure 9. UV-vis spectra of Au@PEG-OH (97%)-Halo Tag Thiol (O4) (3%) (a) and Au@PEG-OH(90%)-Halo Tag Thiol (O4) (10%) (b) in mQ water and different NaCl solutions. The NaCl concentrations were 1M, 2M and 3M. (c) Stability against NaCl-induced aggregation of Au@PEG-OH (97%)-Halo Tag Thiol (O4) (3%) (black line) and Au@PEG-OH(90%)-Halo Tag Thiol (O4) (10%) (red line).

2.2.2. Conjugation of Halo Tag Thiol (O4) ligand via cystamine spacer

An alternative and valuable approach to conjugate Halo Tag molecules requires a deliberate separation of the functionalization process from the passivation: first the particles are covered by a mixture of PEGs with different functional groups aiming to protect the particle, and serves as a loading platform for the bioactive Halo Tag ligands.

To realise this, a siutable linker between the passivation layer and biomolecule should be used. Using a mixture of PEGs, where a hydroxyl PEG-SH used in access is responsible for colloidal stabilization, while a small amount of a carboxyl PEG-SH is introduced for covalent functionalization with cystamine linker. Cystamine is decarboxylated cystine, a small disulfide-containing molecule with primary amines at both ends. Here, cystamine is used as an activating reagent for disulfide exchange reaction [37-39]. The cystamine-modified nanoparticles then are mixed with the Halo Tag Thiol ligand, where the latter cleaves the disulfide of cystamine-modified particles, releasing 2-mercaptoehylamine and forming a disulfide crosslink (Scheme 2). This method is supposed to improve the accessibility of the Halo Tag ligand and, subsequently, of the chlorine atom to be recognized by the Halo Tag protein.

In practice, as prepared citrate GNP were conjugated with PEG-OH and Halo Tag Thiol (O4) ligands via citrate exchange method introducing in the ligand shell both 5% and 10 % of the latter ligand. First, GNP were covered by PEG-OH and PEG-COOH molecules, loading in the passivation layer both 5% and 10% of –COOH groups. In brief, the modification of GNP with PEG ligands was carried out as follows.

PEG HS-$C_{11}(EG)_4$-OH and PEG HS-$C_{11}(EG)_6$-CH_2-COOH were dissolved in methanol to give 0.101 M and 0.00148 M stock solutions, respectively. The ligands were pre-mixed in desired proportions in methanol in order to obtain the final volume of 200 µL. The total number of PEG to cover gold particle surface was considered 20500. Subsequently, the methanol PEG mixture was added quickly under vigorous stirring to 30 mL of 3.1 nM GNP dispersion. The ligands were allowed to attach to the particles overnight, followed by washing by repeated centrifugation at 13500 rpm for 20 min at 10 °C. Purified PEGylated nanoparticles were resuspended in 12 mL of PBS to give 7.5 nM (5% PEG-COOH) and 8.14 nM (10% PEG-COOH) concentration. Cystamine dihydrochloride was dissolved in PBS to give 4.8 mM stock solution. EDC was dissolved in Milli-Q water to give a 6mM stock solution which was kept freezed at -20 °C. An aliquot of cystamine solution to obtain a 20-fold molar excess over the amount of –COOH groups present was added: 32 µL and 69.5 µL corresponding to 5% and 10% of –COOH groups, respectively. Subsequently, an aliquot of EDC solution (128 µL for 5% -COOH and 278 µL for 10%-COOH) in order to obtain a 5-fold molar excess over the amount of cystamine present was added. The nanoparticles were allowed to react for 2 hours at room temperature. Afterwards, the excess of cystamine and EDC was eliminated by repeated centrifugation at 13500 rpm for 20 min at 10 °C. The purified nanoparticles were resuspended in Milli-Q water to give final concentrations of 7.96 nM (5%) and 8.07 nM (10%). As prepared gold nanoparticle dispersion was loaded between 12 protein lo-bind eppendorf tubes (1.0 mL each). Finally, an aliquot of Halo Tag Thiol (O4) ligand (1 µL for 5% -COOH and 2.2 µL for 10%-COOH) in order to obtain a 2-fold molar excess over the amount

of activated –COOH groups present was added. The reaction was allowed to proceed overnight. Excess Halo Tag Thiol ligand was removed by repeated centrifugation and resuspension in PBS.

A red-shift from 520 to 522 nm occured when citrate ions stabilising GNPs were substituted by PEG-OH and PEG-COOH molecules. An increase of SPR band absorbance was indicative of a change of the environment surrounding the particles – the density of PEG molecules is different from that of citrate. Importantly, the particles remained stable and no change in SPR band was found after repeated centrifufigation and final re-dispersion in PBS for further coupling. After cystamine conjugation, a further shift of 2 nm occured for the particles containig 10% PEG-COOH.

Finally, when functionalized by Halo Tag Thiol ligand attached to the cystamine spacer, the SPR band mooves from 522 to 524 nm in both cases, indicating a successful coupling reaction.

Analytical centrifugation data show a considerable shift of 0.7 nm (from 12.4 nm to 11.7 nm) when the GNPs are covered by the mixture of PEG and 5% of cystamine. While increasing the content of cystamine linker to 10%, the shift becomes larger (0.8 nm) indicating the presence of a greater number of cystamine molecules sticking out. When functionalized by Halo Tag Thiol, the ligand shell becomes thicker resulting in a subsequent shift of 0.1 nm (Figure 12). These data are in accordance with those obtained for the GNPs functionalized by direct conjugation of the Halo Tag Thiol ligand.

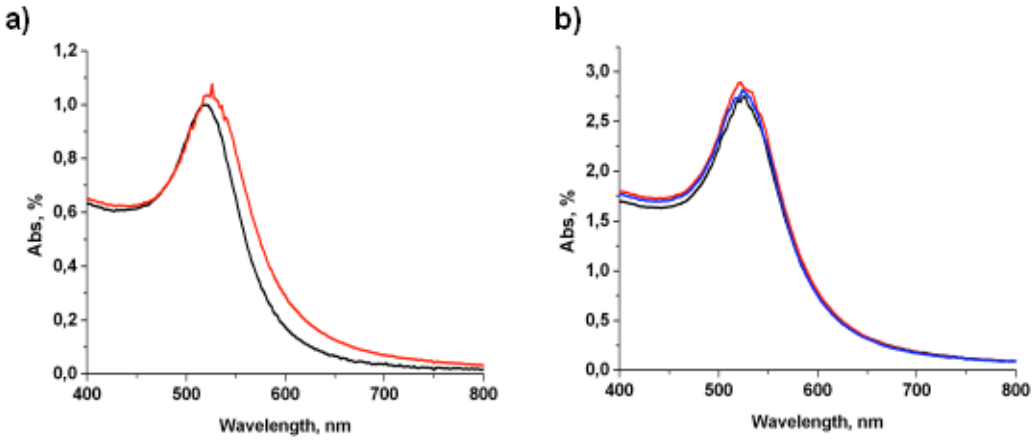

Figure 10. UV-vis spectra of AuNPs: a) GNP-520 nm (black line); GNP@PEG-OH(95%)-PEG-COOH(5%)- 522 nm (red line); b) GNP@PEG-OH(95%)-PEG-COOH(5%) redispersed in PBS- 522 nm (black line); GNP@PEG-OH(95%)-PEG-COOH-cystamine(5%)- 522 nm (red line); GNP@PEG-OH(95%)-PEG-COOH-cystamine-Halo Tag Thiol (O4)(5%)-524 nm (blue line).

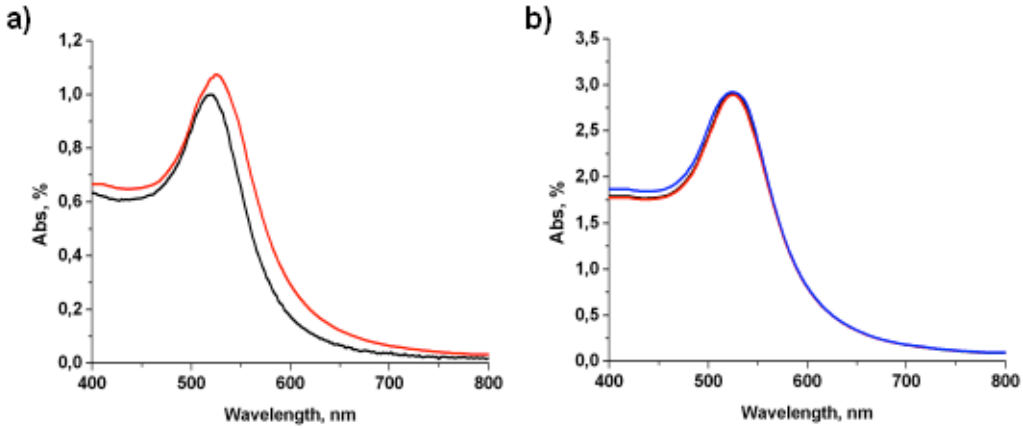

Figure 11. UV-vis spectra of AuNPs: a) GNP-520 nm (black line); GNP@PEG-OH(90%)-PEG-COOH(10%)- 522 nm (red line); b) GNP@PEG-OH(90%)-PEG-COOH(10%) redispersed in PBS- 522 nm (black line); GNP@PEG-OH(90%)-PEG-COOH-cystamine(10%)- 524 nm (red line); GNP@PEG-OH(90%)-PEG-COOH-cystamine-Halo Tag Thiol (O4)(10%)- 524 nm (blue line).

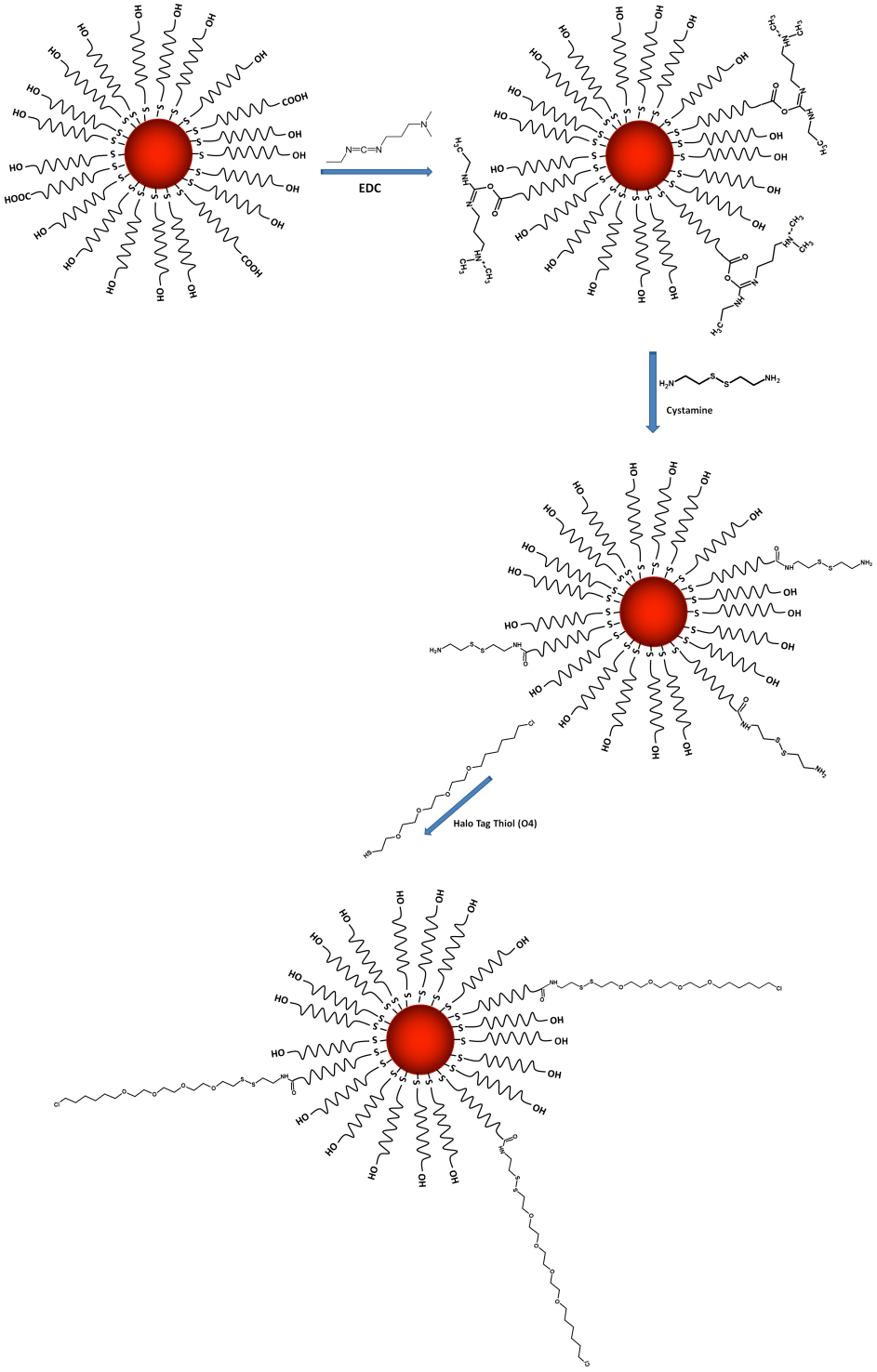

Scheme 2. Representation of Halo Tag Thiol conjugation to citrate-stabilized gold nanoparticles via PEG –SH passivation and functionalization using cystamine linker.

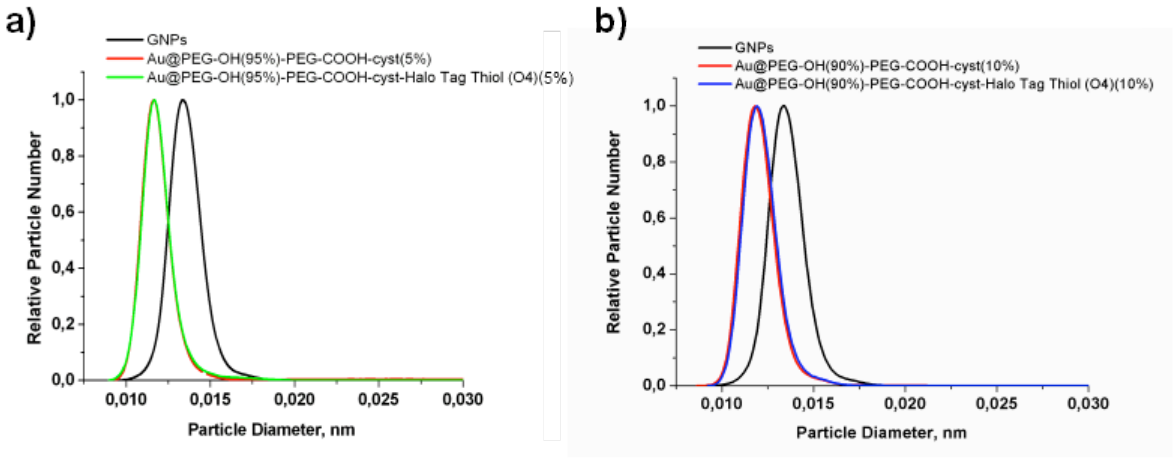

Figure 12. Analytical centrifugation patterns of AuNPs: a) GNPs-12.4 nm (black line); Au@PEG-OH(95%)-PEG-COOH-cyst (5%)-11.7 nm (red line); Au@PEG-OH(95%)-PEG-COOH-cyst-Halo Tag Thiol (O4) (5%)-11.6 nm (green line); b) GNP-12.4 nm (black line); Au@PEG-OH(90%)-PEG-COOH-cyst (10%)- 11.6 nm (red line); Au@PEG-OH(90%)-PEG-COOH-cyst-Halo Tag Thiol (O4) (10%)-11.5 nm (green line).

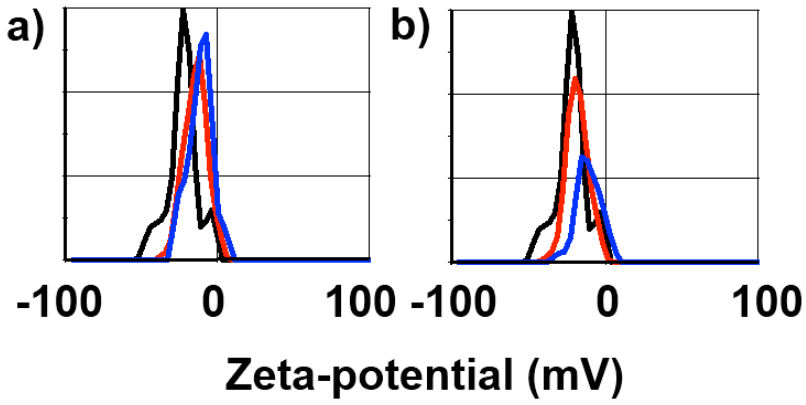

Figure 13. Zeta-potential of gold nanoparticles: black line- GNP, -22.5 mV; a) red line-Au@PEG-OH (95%)-PEG-COOH-cystamine (5%), -14.2 mV; blue line-Au@PEG-OH (95%)-PEG-COOH-cystamine-Halo Tag Thiol (O4) (5%), -11.2 mV; b) red line-Au@PEG-OH (90%)-PEG-COOH-cystamine (10%), -18.7 mV; blue line-Au@PEG-OH (90%)-PEG-COOH-cystamine-Halo Tag Thiol (O4) (10%), -11.4 mV.

Like nanoparticles prepared *via* direct Halo Tag Thiol conjugation, those containing cystamine linker result to have a negative zeta-potential. The particles containing 95% of PEG molecules in the ligand shell are less negative (-14.2 mV) in comparison with their analogues containing 90% of PEG (-18.7 mV), that is explained by the “neutral nature” of the PEG-OH used. The zeta-potential moves in more positive region after conjugation of Halo Tag Thiol to the cystamine, becoming -11.2 mV and -11.4 mV, respectively (Figure 13), as chlorine groups are now present on the particle surface.

TEM results indicate the as-prepared particles to have a spherical shape and a narrow distribution with mean diameters of 16.59±1.25 and 16.19±1.2 nm for the conjugates containig 5%- and 10%-Halo Tag Thiol, respectively (Figures 14, 15). The particles are found to be able to form a lattice-like structures *via* self-assembly on the carbon coated copper grid. It seems that the assembly of the particles takes place only when deposited on a surface, as no secondary SPR band at longer wavelengths is detected by UV-vis spectroscopy.

Theorically, hydrogen atoms of PEG-OH molecule may electrostatically interact with chlorine of Halo Tag Thiol ligand, leading to a self-assembly. However, at the same time, the stabilisation capacity of PEG is high enougth to keep the assembled clasters stable. As shown in Figure 13, at a lower Halo Tag Thiol concentration (5%), the particles are unevenly distributed and form patch-like structures with depletion particles. While at a higher Halo Tag Thiol concentration (10%), the nanoparticles seem to be more evenly distributed (Figure 15) [40].

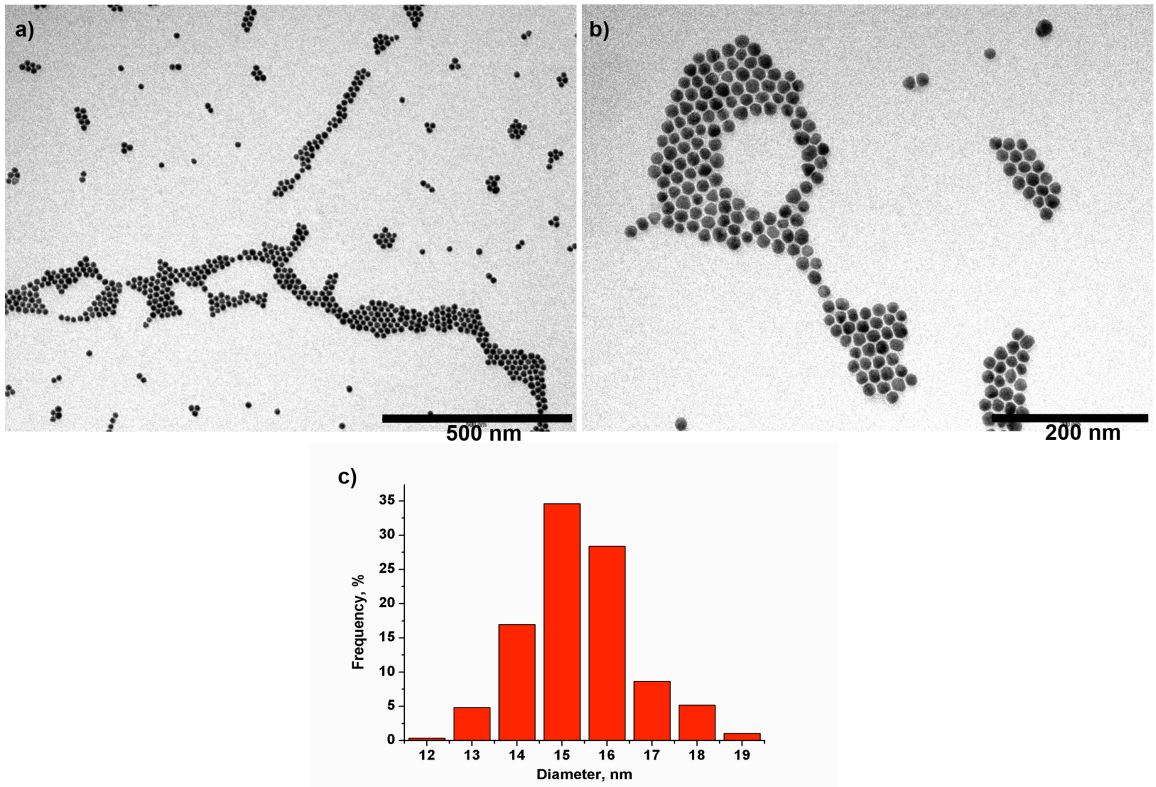

Figure 14. Figure X. TEM micrograph of GNP@PEG-OH(95%)-PEG-COOH-Cyst-Halo Tag Thiol (O4) (5%): a) scale bar 500 nm; b) scale bar 200 nm; c) size distribution histogram (16.59±1.25 nm mean diameter).

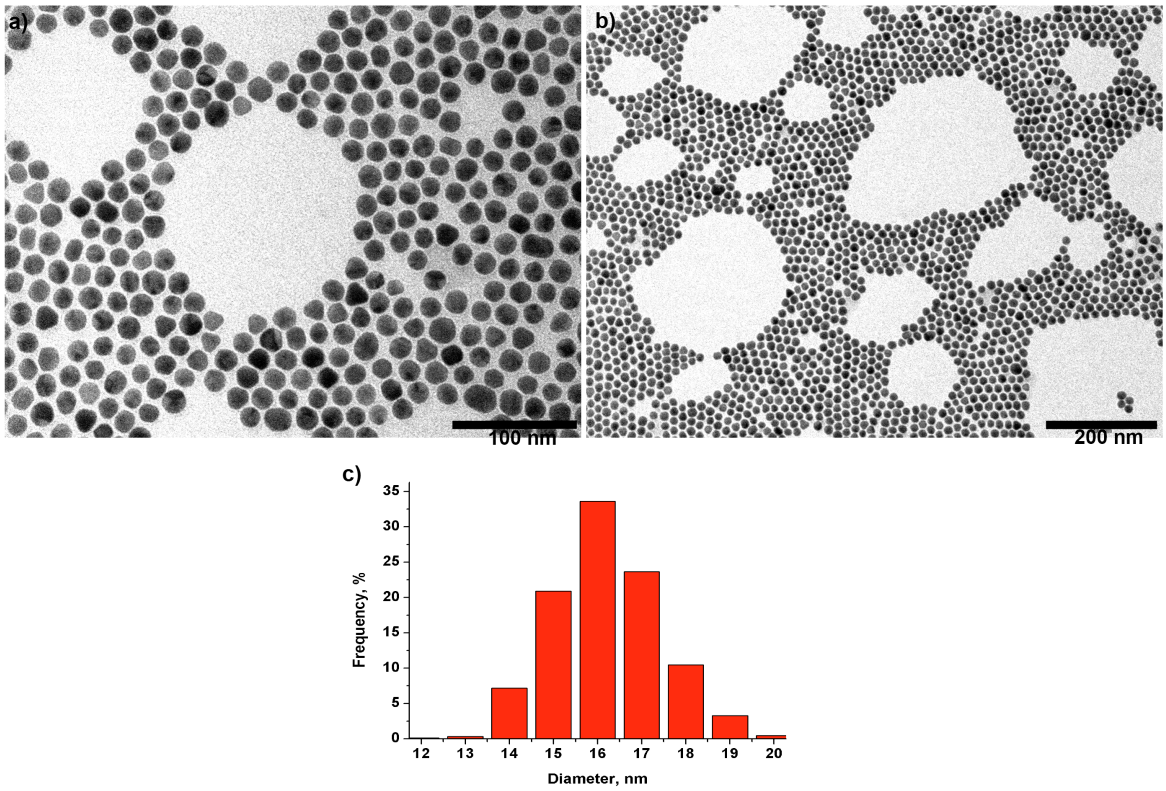

Figure 15. Figure X. TEM micrograph of GNP@PEG-OH(90%)-PEG-COOH-Cyst-Halo Tag Thiol (O4) (10%): a) scale bar 100 nm; b) scale bar 200 nm; c) size distribution histogram (16.19±1.2 nm mean diameter).

Stability experiments were carried out incubating both cystamine-modified PEGylate nanoparticles and Halo Thiol-conjugates. The cystamine-containig PEGylated particles appeared to be stable both in PBS and at the basic and neutral pH (Figure 16). Aggregation parameter values vary from 0 to 0.23 for the particles containing 5% cystamine. Those containing 10% of cystamine seem to be less stable in highly acidic pH (pH 1) showing aggregation parameter value around 0.55 (Figure 17). Nevertheless, both particles demonstrate no pH-induced aggregation and colour change even at extreme pH values.

The conjugation of Halo Thiol ligand allowes to improve pH-induced aggregation stability, as the aggregation parameter values significantly decreases in whole pH interval concerned. Salt-induced aggregation resistance was estimated incubating Halo Thiol-conjugated nanoparticles in 1-3M NaCl solutions, and comparing aggregation parameter values with those obtained for nanoparticles re-dispersed in mQ water.

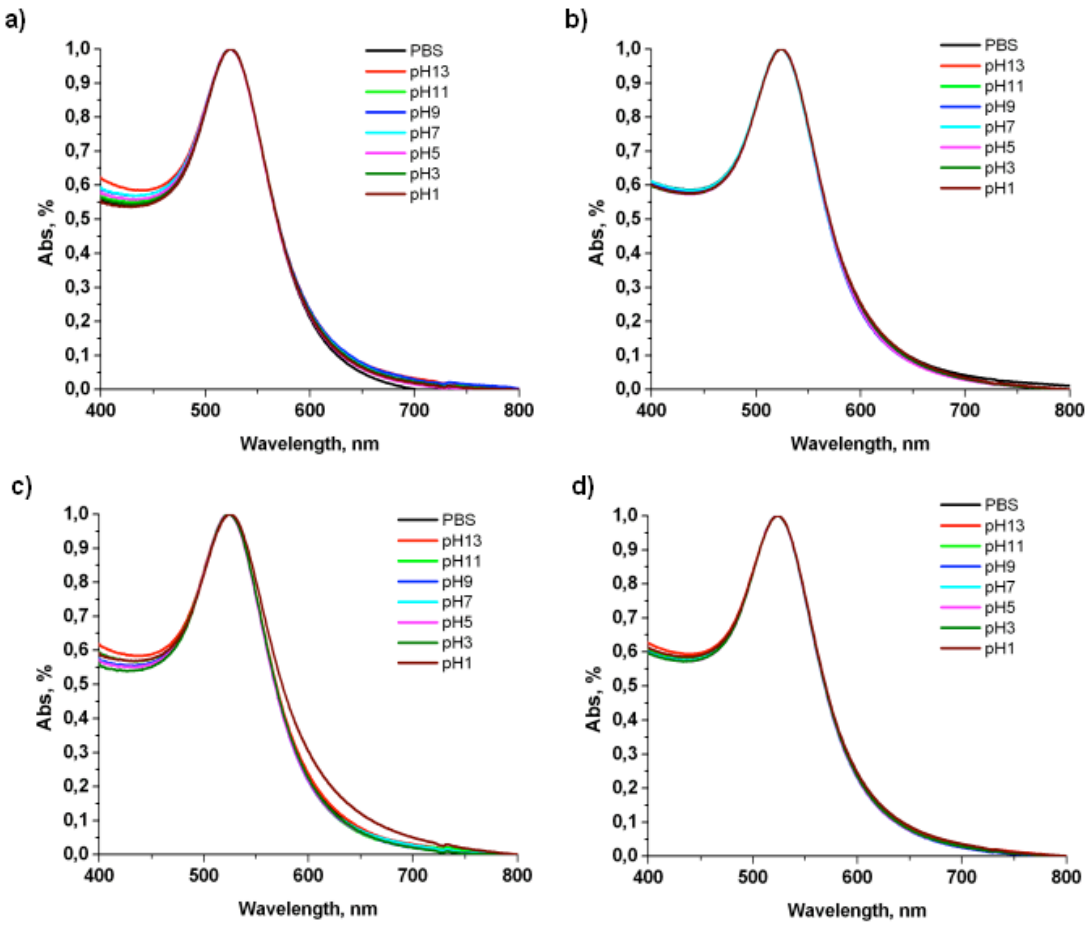

Figure 16. UV-vis spectra of Au@PEG-OH (95%)-cystamine (5%) (a), Au@PEG-OH(95%)-cyst-Halo Tag Thiol (O4) (5%) (b), Au@PEG-OH (90%)-cystamine (10%) (c), Au@PEG-OH(90%)-cyst-Halo Tag Thiol (O4) (10%) (d) in PBS and different pH solutions. The pH values were 1, 3, 5, 7, 9, 11 and 13.

We were interested in testing only Halo Thiol-conjugated nanoparticles, since these were going to be used in internalization experiments with cells, and compare their stability depending on the amount of Halo Thiol legand used. Figure 18 shows UV-vis spectra of the particles containing 5% (a) and 10% (b) of Halo Tag Thiol molecule in the ligand shell. No change of the SPR band profile is detected when the nanoparticles are exposed to the high salt concentrations indicating an excellent colloidal stability even in extreme conditions. However, the particles containig major amount (10%) of Halo Tag Thiol ligand possess a better stability, being the aggregation parameter a little lower (Figure 18, red line).

In conclusion, a comparison of the two conjugation methods indicates that gold nanoparticles synthesised *via* cystamine linker show better colloidal stability both against pH- and NaCl-induced aggregation. Moreover, the cystamine-containing nanoparticles loaded with 10% of Halo Tag Thiol ligand demonstrate the lowest aggregation parameter, and, thus, are the most stable among the studied samples (Figure 19). In order to understand the efficacy of the both conjugation methods form biological piont of view, internalization experiments with Halo Tag protein transfected cells are needed, providing more data on the exposition of the chlorine atom to be specifically recognized by the protein.

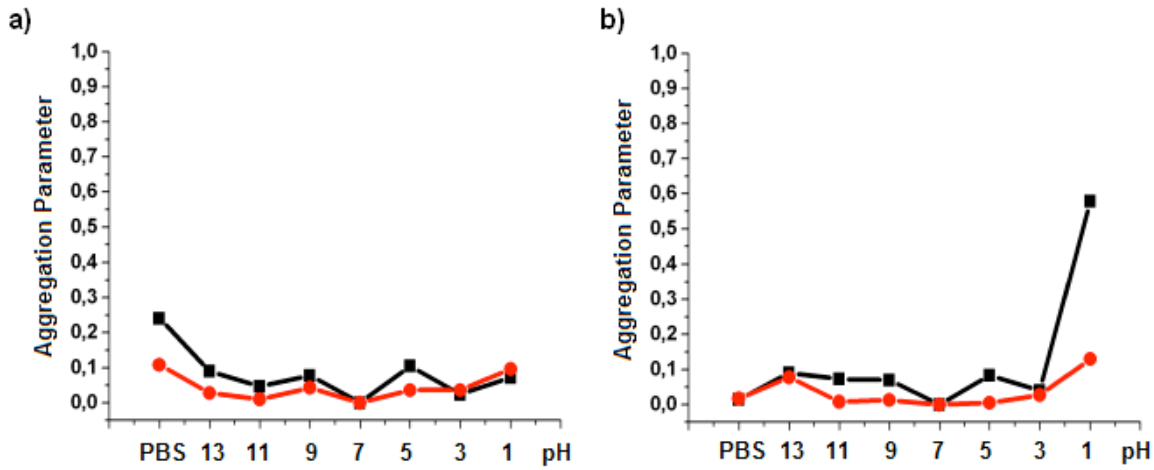

Figure 17. Stability against pH-induced aggregation of Au@PEG-OH (95%)-cystamine (5%) (a) (black line), Au@PEG-OH(95%)-cyst-Halo Tag Thiol (O4) (5%) (a) (red line), Au@PEG-OH (90%)-cystamine (10%) (b) (black line), and Au@PEG-OH(90%)-cyst-Halo Tag Thiol (O4) (10%) (b) (red line).

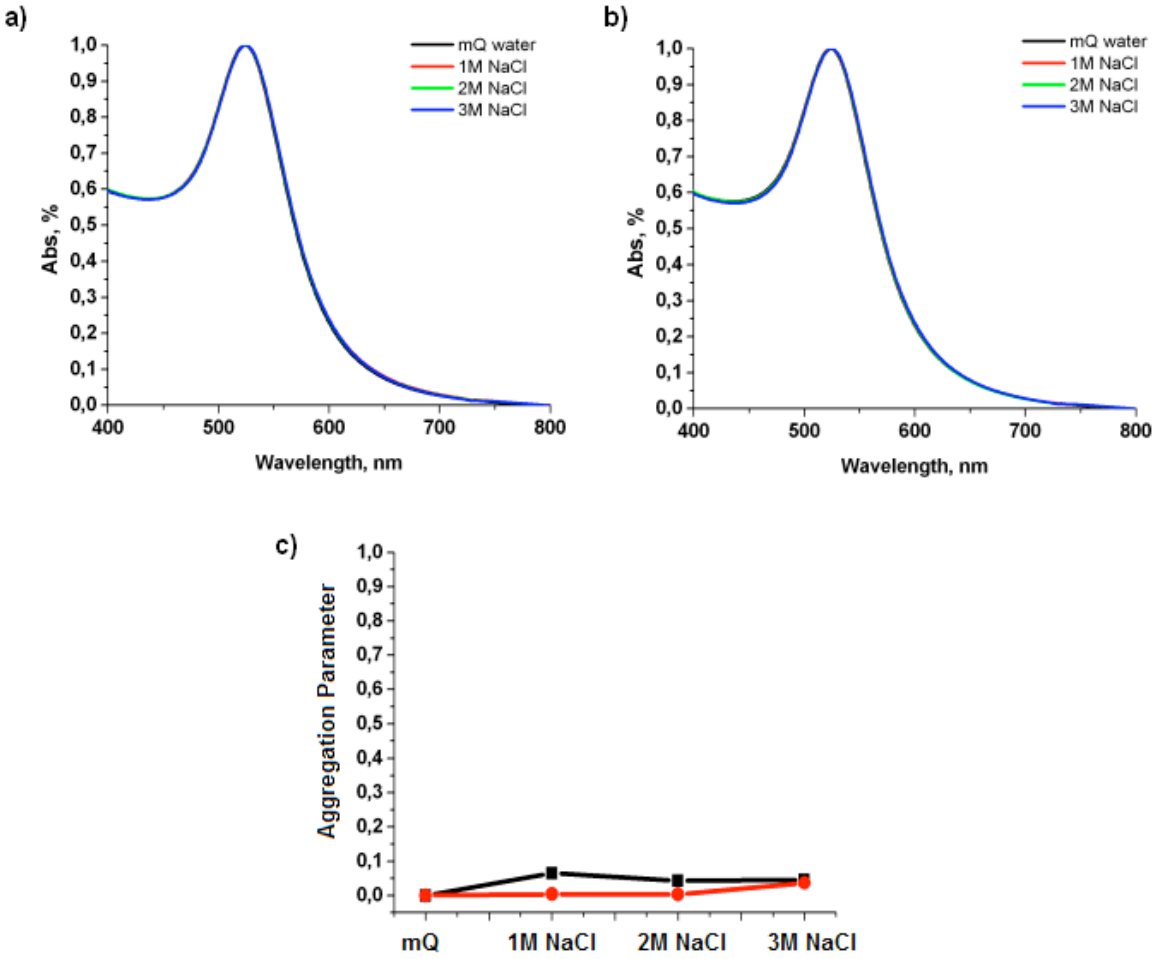

.

Figure 18. UV-vis spectra of Au@PEG-OH (95%)-cyst-Halo Tag Thiol (O4) (5%) (a) and Au@PEG-OH(90%)-cyst-Halo Tag Thiol (O4) (10%) (b) in mQ water and different NaCl solutions. The NaCl concentrations were 1M, 2M and 3M. (c) Stability against NaCl-induced aggregation of Au@PEG-OH (95%)-cyst-Halo Tag Thiol (O4) (5%) (black line) and Au@PEG-OH(90%)-cyst-Halo Tag Thiol (O4) (10%) (red line).

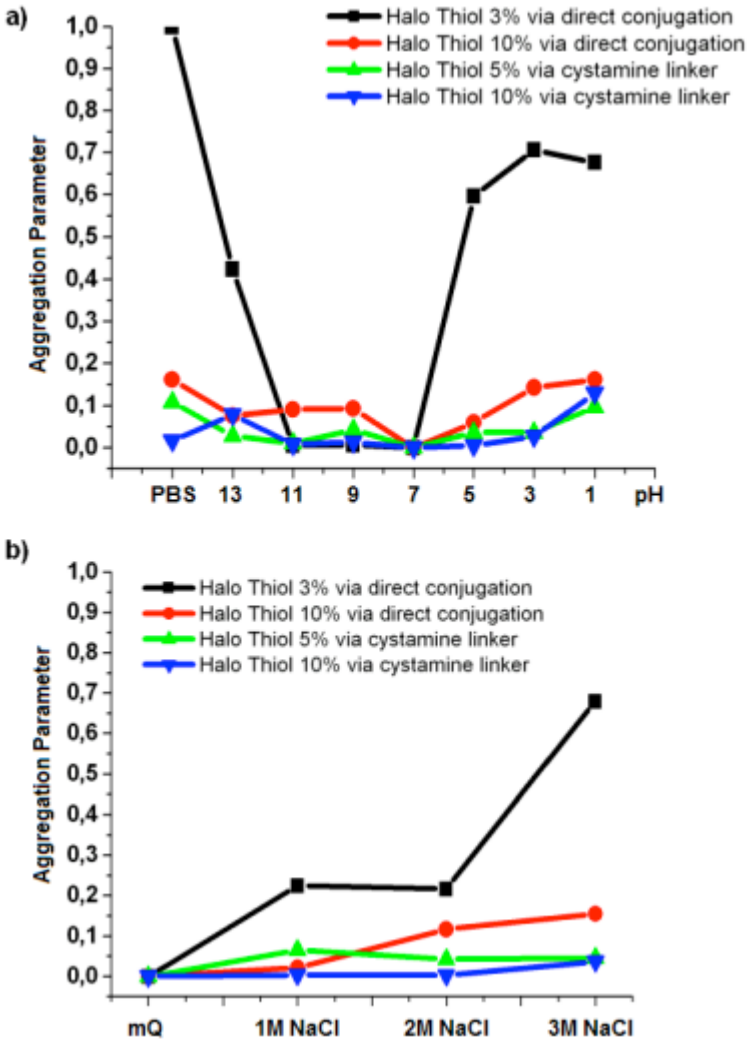

Figure 19. Comparison of the stability against (a) pH-induced aggregation of Au@PEG-OH(97%)-Halo Tag Thiol (O4)(3%) (black line), Au@PEG-OH(90%)-Halo Tag Thiol (O4)(10%) (red line), Au@PEG-OH(95%)-cyst-Halo Tag Thiol (O4)(5%) (blue line), and Au@PEG-OH(90%)-cyst-Halo Tag Thiol (O4)(10%) (green line); (b) Stability against NaCl-induced aggregation of Au@PEG-OH(97%)-Halo Tag Thiol (O4)(3%) (black line), Au@PEG-OH(90%)-Halo Tag Thiol (O4)(10%) (red line), Au@PEG-OH(95%)-cyst-Halo Tag Thiol (O4)(5%) (blue line), and Au@PEG-OH(90%)-cyst-Halo Tag Thiol (O4)(10%) (green line).

2.3. Conjugation of Halo Tag Amino (O4) ligand

The approach applied to conjugate amino-containing Halo Tag ligand to the particles involves the using of a zero-length cross-linking agent, mediating the conjugation of two molecules by forming a bond containing no additional atoms. Carbodiimides are used to mediate the formation of amide linkage between carboxylates and amines [41-43]. They are probably the most popular type of zero-length crosslinker in use, being efficient in forming conjugates between two protein molecules, between a peptide and a protein, between an oligonucleotide and a protein, between a biomolecule and a particle, or any combination of these with small molecules. EDC (or EDAC, 1-ethyl-3-)3-dimethylaminopropyl)carbodiimide hydrochloride) is the most frequently used crosslinking agent in order to conjugate biological substances containing carboxylates and amines. Its application in particle conjugation procedures along with sulfo-NHS (N-hydroxysulfosuccinimide) is nearly universal and commonly used nowadays. EDC is water-soluble, which allows for its direct addition to a reaction without prior organic solvent dissolution.

Both the reagent itself and the isourea formed as the by-product of the crosslinking reaction are water-soluble and may be removed easily by dialysis or centrifugation. Most references to the use of EDC describe the optimal reaction medium to be at a pH from 4.7 to 6.0 [44]. However, the carbodiimide reaction occurs effectively up to at least pH 7.5 without significant loss of yield. Given the reactivity of EDC, a more stable active intermediate can be formed, using sulfo-NHS (*N*-hydroxysulfosuccinimide).

Formed sulfo-NHS esters are hydrophilic reactive groups that coulpe rapidly with amines on target molecules [44]. In the presence of amine nucleophiles that can attack at the carbonyl group of the ester, the sulfo-NHS group rapidly leaves, creating a stable amide linkage with the amine. Thus, amino-containing Halo Tag ligand is subsequently added to the active intermediate and a stable peptidic bond between -COOH group of PEG molecule and -NH_2-group of Halo Tag is formed.

Rao *et al.* used this strategy to conjugate a bioluminescent protein genetically fused with Halo Tag protein *via* its N-terminus to carboxilated quantum dots [4]. They shown this method to be straightforward enougth, since covalent bond formation between the protein and targeting ligand was successfully occured just mixing them under physiological conditions. In another research work, Rao and co-workers genetically fused the Halo Tag protein to a cell membrane anchoring domain to present Halo Tag protein extracellularlly for the quantum dots labelling. By live cell fluorescent imaging they confirmed that the labelling was specific and took place at the cell surface [4].

2.3.1. Conjugation of Halo Tag Amino (O4) ligand by EDC/sulfo-NHS coupling reaction

As prepared citrate GNPs were conjugated with PEG-OH and Halo Tag Amino (O4) ligands *via* citrate exchange method introducing in the ligand shell both 5% and 10 % of the latter ligand. First, GNPs were covered by PEG-OH and PEG-COOH molecules, loading in the passivation layer both 5% and 10% of –COOH groups.

The modification of the GNPs with PEG ligands was carried out as follows. PEG HS-$C_{11}(EG)_4$-OH and PEG HS-$C_{11}(EG)_6$-CH_2-COOH were dissolved in methanol to give 0.101 M and 0.00148 M stock solutions, respectively. The ligands were pre-mixed in methanol in desired proportions in order to obtain the final volume of 200 µL. The total number of PEG to cover gold particle surface was considered 20500. Subsequently, the methanol PEG mixture was added quickly under vigorous stirring to 30 mL of 3 nM GNP dispersion. The ligands were allowed to attach to the particles overnight, followed by washing by repeated centrifugation at 13500 rpm for 20 min at 10 °C. Purified PEGylated nanoparticles were resuspended in 10 mL of PBS to give 6.88 nM (5% PEG-COOH) and 7.49 nM (10% PEG-COOH) concentration. To activate the –COOH groups on the particle surface for covalent conjugation, 5 µL of both freshly prepared EDC (6 mM) and 5 sulfo-NHS solutions (6 mM) were added to the nanoparticles' dispersion and mixed vigorously at 25 °C for 15 min [ref 45]. Excess EDC and sulfo-NHS were separated from the activated nanoparticles by three rounds of centrifugation at 13500 rpm for 20 min at 10°C and resuspension in PBS. The purified activated particles were finally resuspended in 1 mL (5%-COOH) and 1.3 mL (10%-COOH) of PBS. Subsequently, the particles were reacted with the Halo Tag Amino ligand (0.0014 mM, 5 µL and 14.2 µL for 5%- and 10%-COOH containing particles, respectively) at 25°C overnight. Excess Halo Tag Amino ligand was removed by repeated centrifugation and resuspension in PBS. A schematic representation of the conjugation steps is shown in Scheme 3.

The starting citrate GNPs show a characteristic SPR band at 520 nm, which significantly shifts to longer wavelengths at 526 nm after passivation by PEG mixture

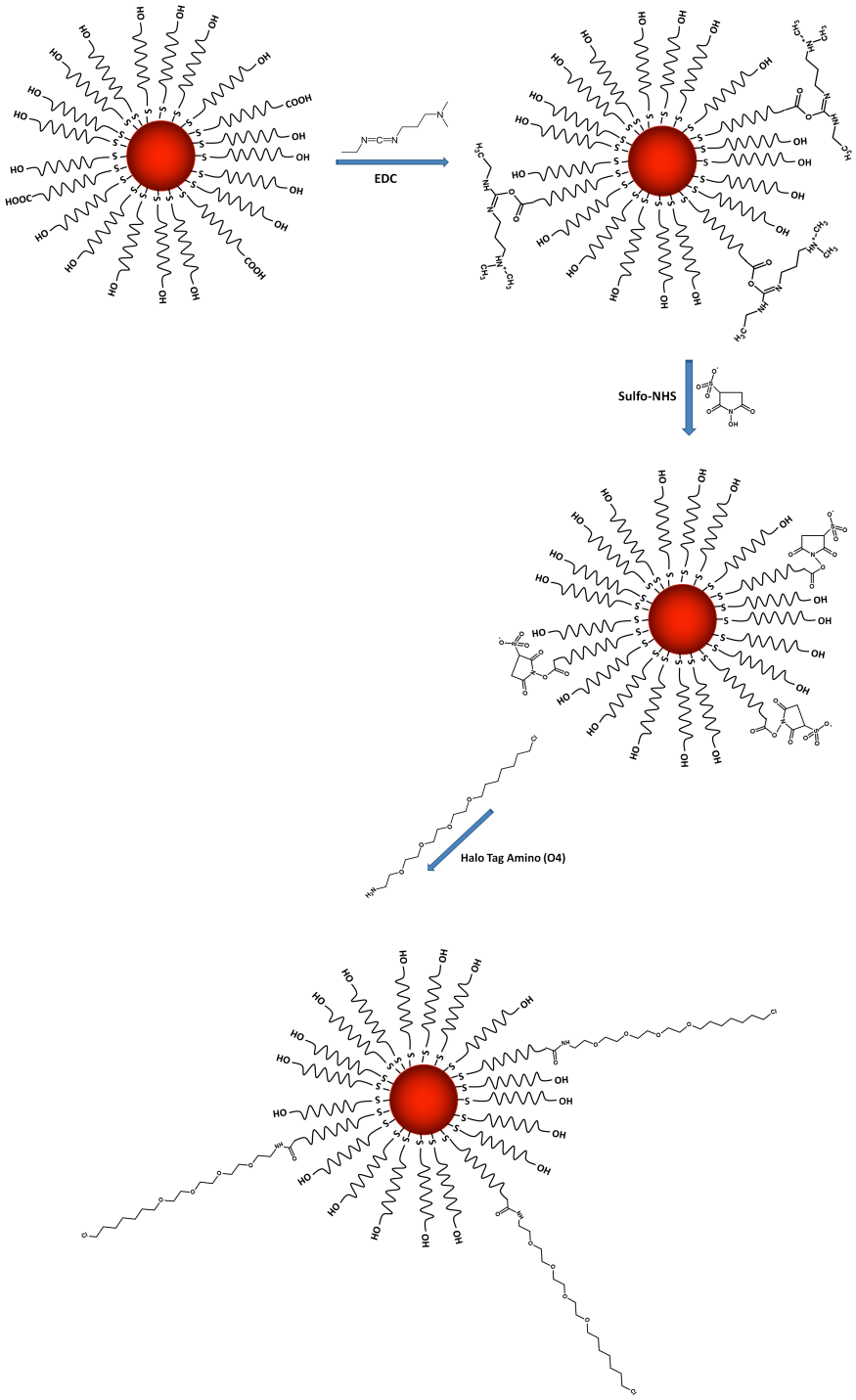

Scheme 3. Representation of Halo Tag Amino conjugation to citrate-stabilized gold nanoparticles via PEG –SH passivation and functionalization using EDC/sulfo-NHS coupling reaction.

(Figure 20, 21). When the particles are washed and redispersed in PBS the SPR band moves at 528 nm, probably, because of concentration of the dispersion used for further coupling. When conjugated with Halo Tag Amino ligand, a little blue-shift of the SPR band takes place, however, its intensity is maintained, indicating good resistance to the coupling reaction. Figure 22a shows the results of analytical centrifugation analysis. A large shift takes place after exchange between citrate ions and PEG molecules: initial value of 12.4 nm now becomes 11.5 nm. Further shift is hardly detectable, however, the peak becomes more narrow after coupling reaction, indicating a narrower particle distribution and better stability (Figure 22b).

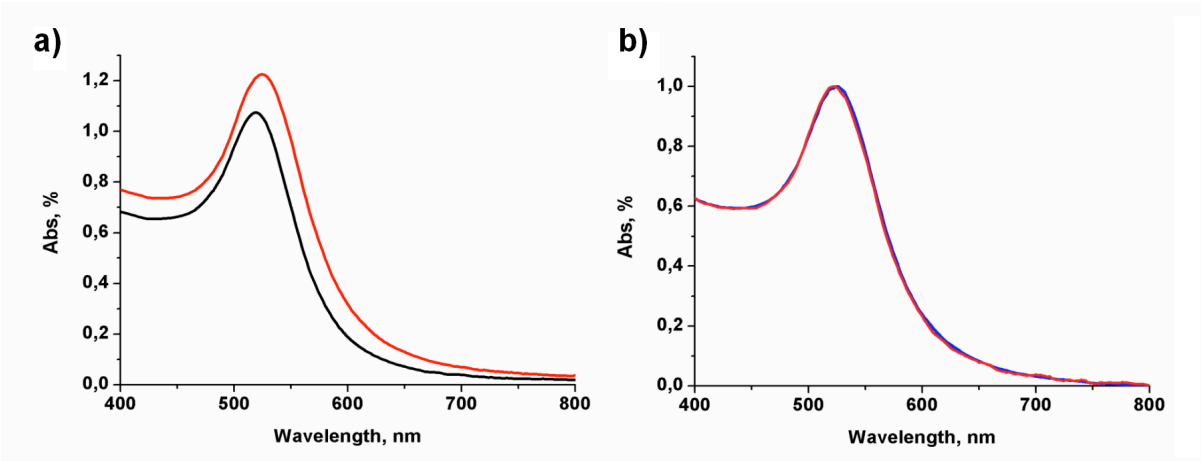

Figure 20. UV-vis spectra of AuNPs: a) GNP-520 nm (black line); GNP@PEG-OH(95%)-PEG-COOH(5%)- 526 nm (red line); b) GNP@PEG-OH(95%)-PEG-COOH(5%) in PBS-528 nm (blue line); GNP@PEG-OH(95%)-PEG-COOH-Halo Tag Amino (O4) (5%)-526 nm (magenta line).

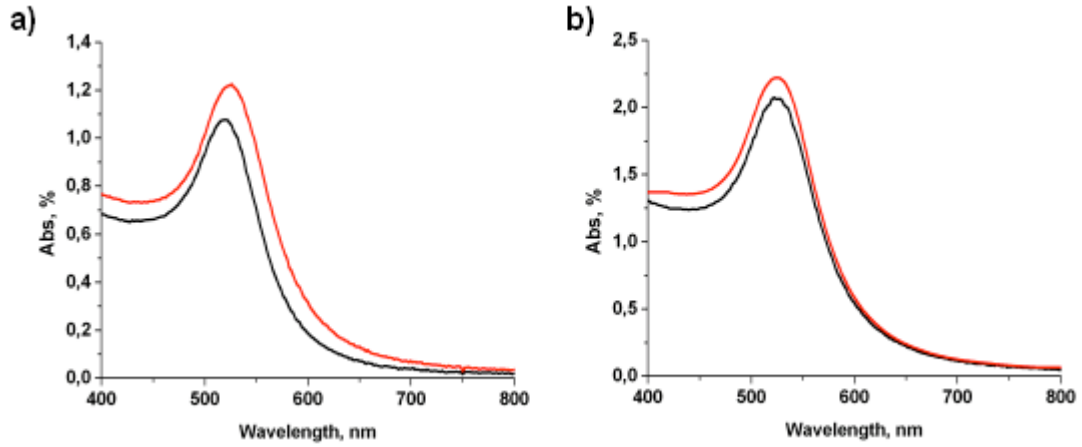

Figure 21. UV-vis spectra of AuNPs: a) GNP-520 nm (black line); GNP@PEG-OH(90%)-PEG-COOH(10%)- 526 nm (red line); b) GNP@PEG-OH(95%)-PEG-COOH(5%) in PBS-528 nm (black line); GNP@PEG-OH(95%)-PEG-COOH-Halo Tag Amino (O4) (5%)-526 nm (red line).

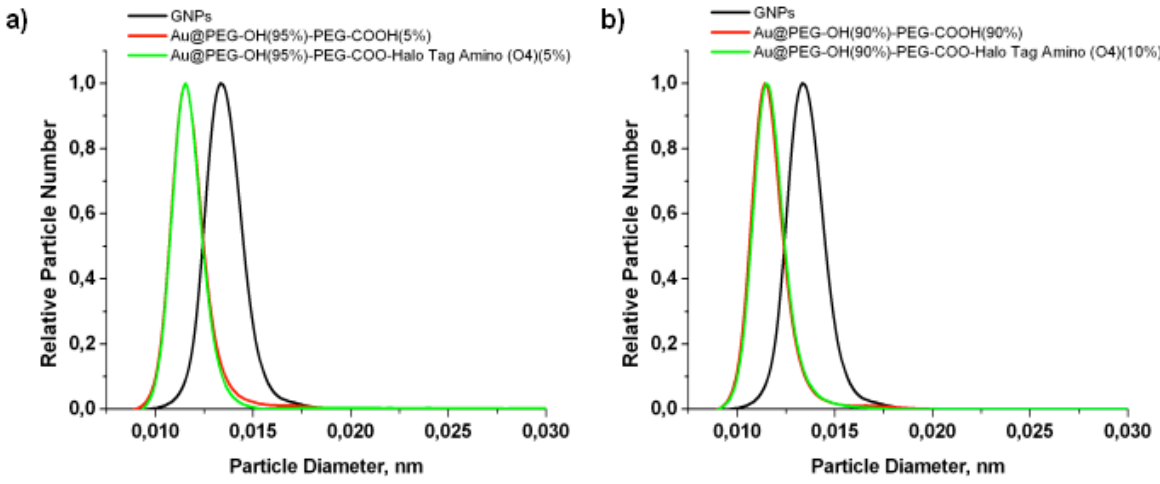

Figure 22. Analytical centrifugation patterns of AuNPs: a) GNPs-12.4 nm (black line); Au@PEG-OH(95%)-PEG-COOH(5%)-11.5 nm (red line); Au@PEG-OH(95%)-PEG-COO-Halo Tag Thiol (O4)(5%)-11.5 nm (green line); b) GNP-12.4 nm (black line); Au@PEG-OH(90%)-PEG-COOH(10%)- 11.5 nm (red line); Au@PEG-OH(90%)-PEG-COO-Halo Tag Thiol(O4)(10%)-11.5 nm (green line).

Zeta-potential studies confirmed the nanoparticles to be negatively charged with zeta-potential value changing after every conjugation step: citrate GNPs show the value of -22.5 mV, which becomes less negative after exchange reaction between citrate ions and PEG molecules, due to domination of “neutral” PEG-OH in the ligand shell. Infact, particles containing 95% PEG-OH show less negative zeta-potential (-11.3 mV) comparing to those containing 90% PEG-OH (-16.9 mV) (Figure 23, red line). After coupling reaction, Halo Amino-conjugated nanoparticles have a more negative zeta-potential of -15.7 mV and -22.2 mV for 5%- and 10%-loading, respectively (Figure 23, blue line). This confirms the successful coupling reaction and presence of a negatively charged molecules in the ligand shell [46-47].

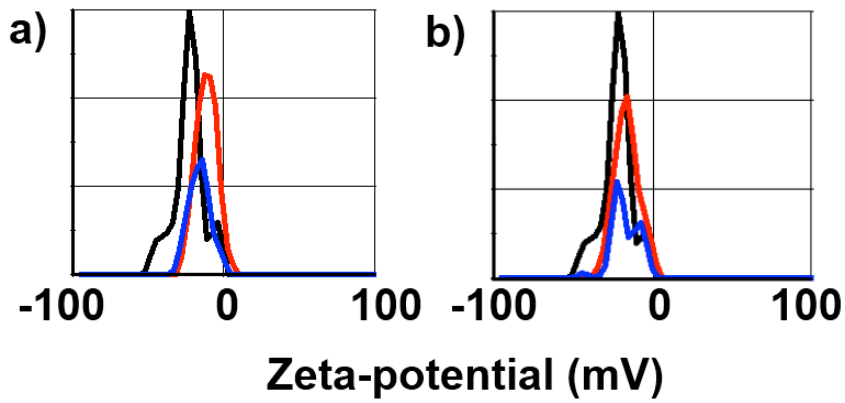

Figure 23. Zeta-potential of gold nanoparticles: black line- GNP; red line-Au@PEG-OH-PEG-COOH, and blue line-Au@PEG-OH-PEG-COOH-Halo Tag Amino (O4): a) 5%, b)10%.

TEM results are shown in Figures 24, 25. The particles slightly differ in diameter, being of 16.12±1.25 and 14.77±1.26 nm for 5%- and 10%-Halo Tag Amino content, respectively. The disagreement in the mean diameter is due to the using of two different batches of starting citrate GNP. The disposition of nanoparticles looks different from the previously discussed conjugates prepared by different methods (Figure 7, 15). In particular, the nanoparticles loaded with 5% Halo Tag Amino ligand are evenly distributed on the copper grid, creating a mass of long wires side by side. On the other hand, 10%-loaded nanoparticles show a different picture, forming short and long clastered wires.

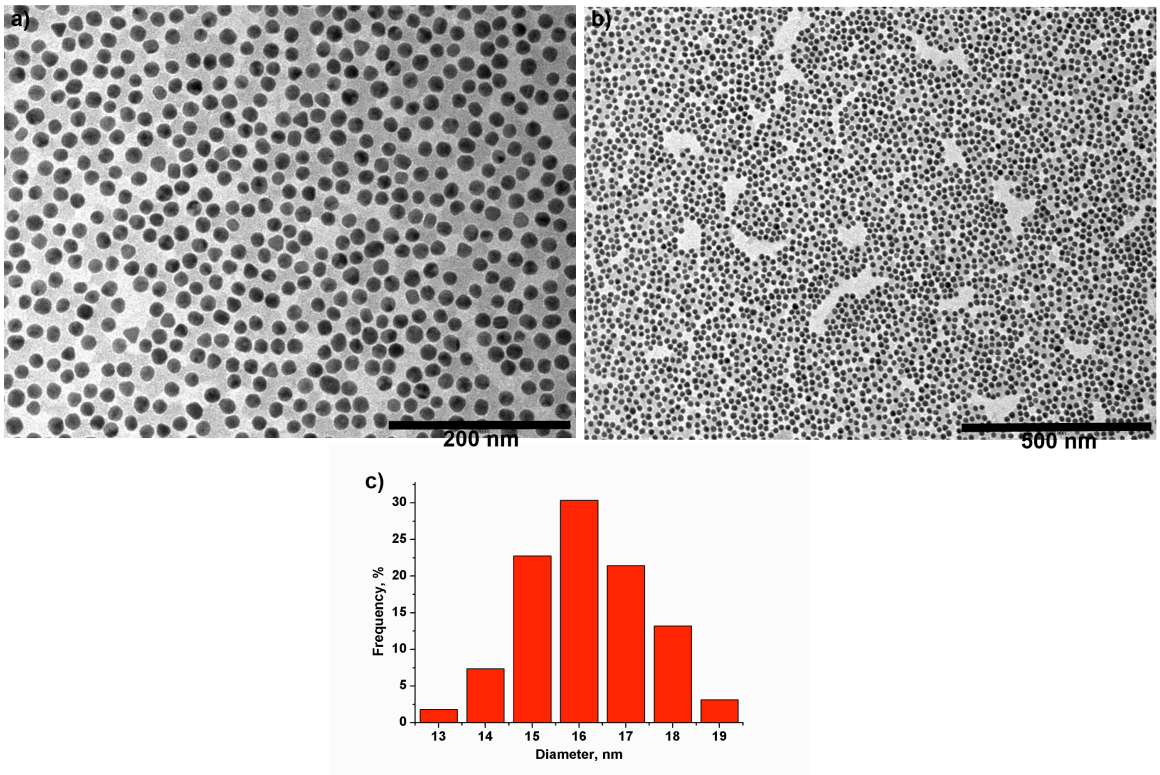

Figure 24. Figure X. TEM micrograph of GNP@PEG-OH(95%)-PEG-COOH-Halo Tag Amino (O4) (5%): a) scale bar 200 nm; b) scale bar 500 nm; c) size distribution histogram (16.12±1.25 nm mean diameter).

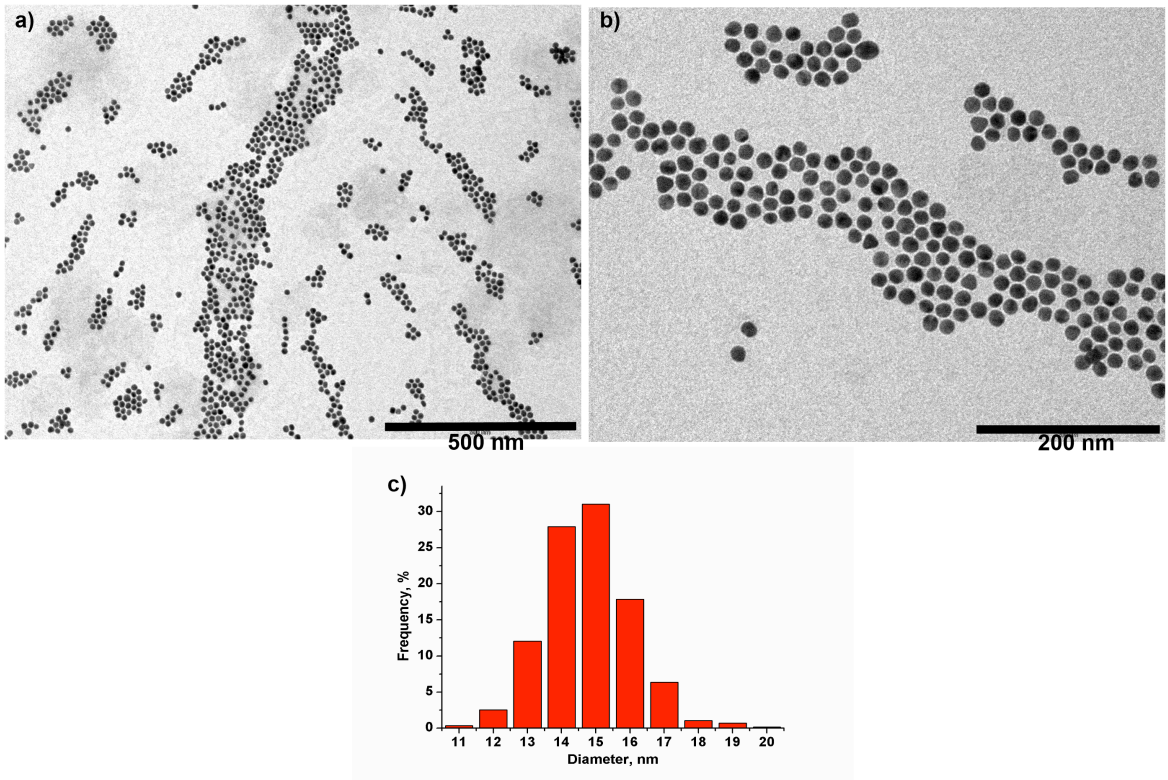

Figure 25. Figure X. TEM micrograph of GNP@PEG-OH(90%)-PEG-COOH-Halo Tag Amino (O4) (10%): a) scale bar 500 nm; b) scale bar 200 nm; c) size distribution histogram (14.77±1.26 nm mean diameter).

Both PEGylated and Halo Tag Amino-conjugated nanoparticles maintain the stability in PBS and against pH-induced aggregation in basic, acidic and neutral medium. UV-vis spectra are reported in Figure 26 and indicate a preservation of the SPR band shape and position even at extreme pH. Aggregation parameter refered to a value of the area (600-700 nm) of the nanoparticles incubated in neutral pH 7 has a linear trend, characterizing a good stability. Independently of Halo Tag Amio loading, the stability of both systems improves comparing with PEGylated nanoparticles (Figure 27).

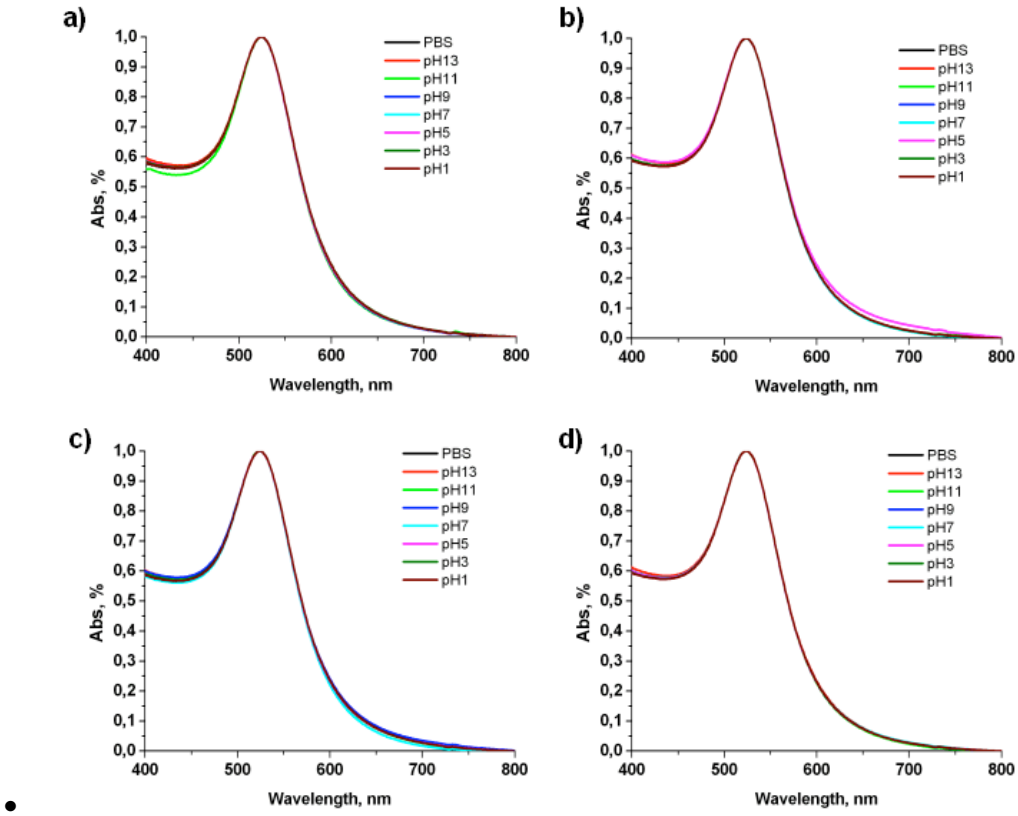

Figure 26. UV-vis spectra of Au@PEG-OH (95%)-PEG-COOH (5%) (a), Au@PEG-OH (95%)-PEG-COOH-Halo Tag Amino (O4) (5%) (b), Au@PEG-OH (90%)-PEG-COOH (10%) (c), Au@PEG-OH (90%)-PEG-COOH-Halo Tag Amino (O4) (10%) (d) in PBS and different pH solutions. The pH values were 1, 3, 5, 7, 9, 11 and 13.

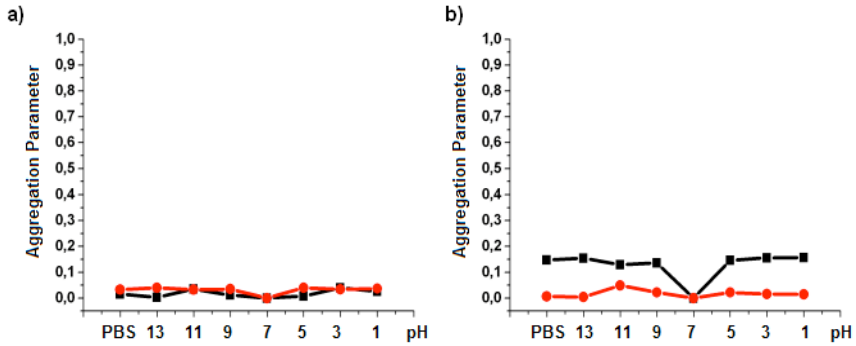

Figure 27. Stability against pH-induced aggregation of (a) Au@PEG-OH (95%)-PEG-COOH (5%) (black line), Au@PEG-OH (95%)-PEG-COOH-Halo Tag Amino (O4) (5%) (red line), and (b) Au@PEG-OH (90%)-PEG-COOH (10%) (black line), Au@PEG-OH (90%)-PEG-COOH-Halo Tag Amino (O4) (10%) (red line).

A similar trend is observed when the nanoparticles are incubated with the solutions containig different salt concentration. The SPR band does not change the shape and position, as well as the colour of the dispersions remains unchanged. Like in other cases, major loading of the ligand (10%) improves stability against NaCl-induced aggregation (Figure 28).

Mixed alkanethiols layers, typically with a ratio of 10-30% of carboxyl-functionalized molecules *vs.* nonfunctionalized ones, have been successfully used to avoid aggregation of small nanoparticles such as quantum dots upon carbodiimide-based protein coupling [48].

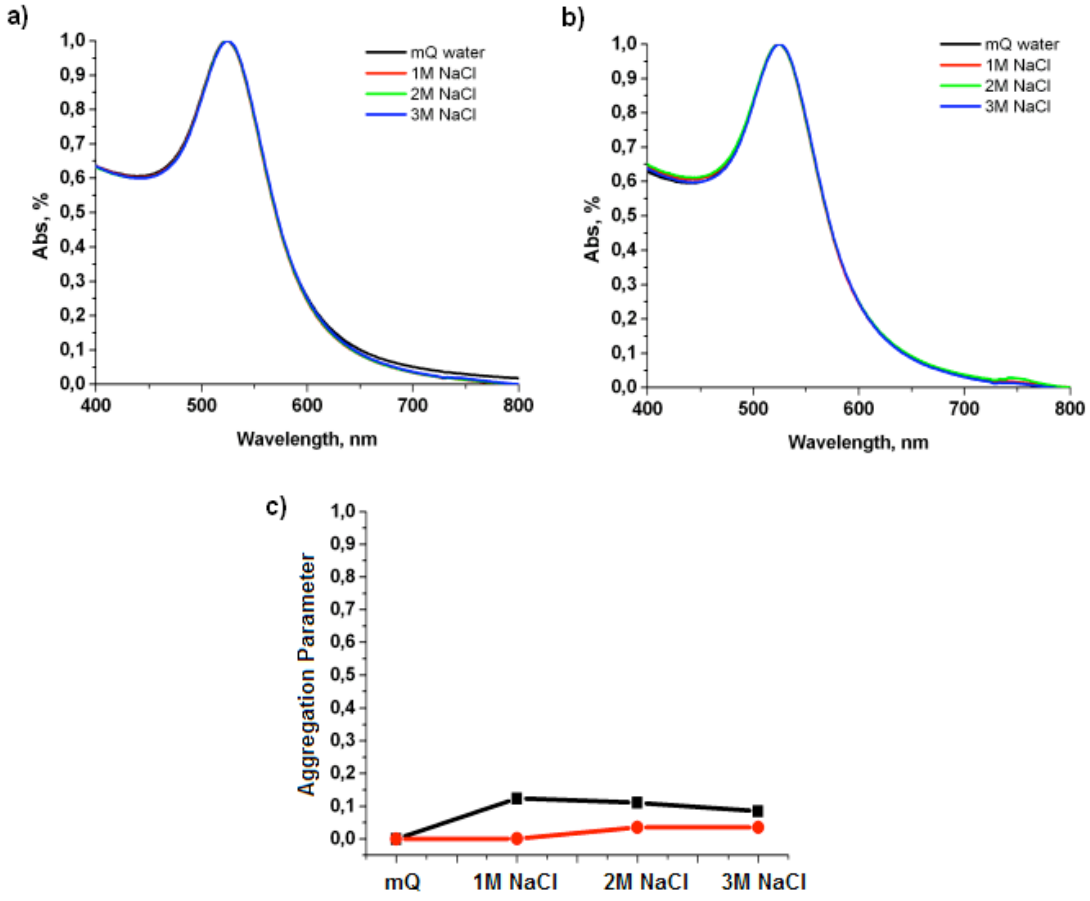

Figure 28. UV-vis spectra of Au@PEG-OH(95%)-PEG-COO-Halo Tag Amino (O4) (5%) (a) and Au@PEG-OH(90%)- PEG-COO-Halo Tag Amino (O4)(10%) (b) in mQ water and different NaCl solutions. The NaCl concentrations were 1M, 2M and 3M. (c) Stability against NaCl-induced aggregation of Au@PEG-OH(95%)-PEG-COO-Halo Tag Amino (O4) (5%) (black line) and Au@PEG-OH(90%)- PEG-COO-Halo Tag Amino (O4)(10%) (red line).

2.3.2. Direct conjugation of Halo Tag Amino (O4) ligand to the PEG-NHS containing layer

Another way to conjugate Halo Tag Amino ligand with PEG shell is to use a PEG containig functional NHS group. In this case, no EDC/sulfo-NHS coupling reaction is needed being PEG molecule already activated and ready to be conjugated. The conjugates were prepared as follows (Scheme 4).

As prepared citrate GNPs were conjugated with PEG-COOH and Halo Tag Amino (O4) ligands introducing in the ligand shell 5%, 10% and 15 % of the latter ligand. First, GNPs were covered by PEG-COOH and PEG-COONHS molecules *via* citrate exchange method, using the above amounts of –COONHS groups. The modification of the GNP with PEG ligands was carried out as follows. PEG HS-$C_{11}(EG)_4$-COOH and PEG HS-$C_{11}(EG)_6$-OCH_2-COONHS were dissolved in methanol to give 0.101 M and 0.023 M stock solutions, respectively. The ligands were pre-mixed in methanol in desired proportions in order to obtain the final volume of 200 µL. The total number of PEG to cover gold particle surface was considered 20500. Subsequently, the methanol PEG mixture was added quickly under vigorous stirring to 20 mL of 2.58 nM GNPs dispersion. The ligands were allowed to attach to the particles overnight, followed by washing by repeated centrifugation at 14000 rpm for 12 min at 10 °C. The purified PEGylated nanoparticles were resuspended in 8 mL, 3 mL and 3 mL of PBS to give 3.7 nM, 5.11 nM and 4.02 nM particle concentration for 5%, 10% and 15% -COONHS content, respectively. These particles do not need to be activated, originally having –COONHS groups.

Thus, the resuspended particles were reacted with the Halo Tag Amino ligand (0.000143 mM, 212 µL, 219 µL and 259 µL for 5%-, 10%-, and 15%-COONHS containing particles, respectively) at 25°C overnight. Excess Halo Tag Amino ligand was removed by repeated centrifugation and resuspension in PBS.

UV-vis spectra of GNPs before conjugation, covered by PEG molecules and after coupling reaction with different amounts of Halo Tag Amino ligand are reported in Figures 29-31. When GNPs are passivated by PEG molecules, independently of the ratio between the components in the “passivation” mixture, SPR band shifts of 4 nm towards longer wavelengths and its intensity rises in absorbance, indicating the exchange between citrate and PEG molecules and formation of a monolayer. After redispersion of washed and concentrated PEGylated particles in PBS, the SPR band is unchanged, giving a first indication of a good colloidal stability.

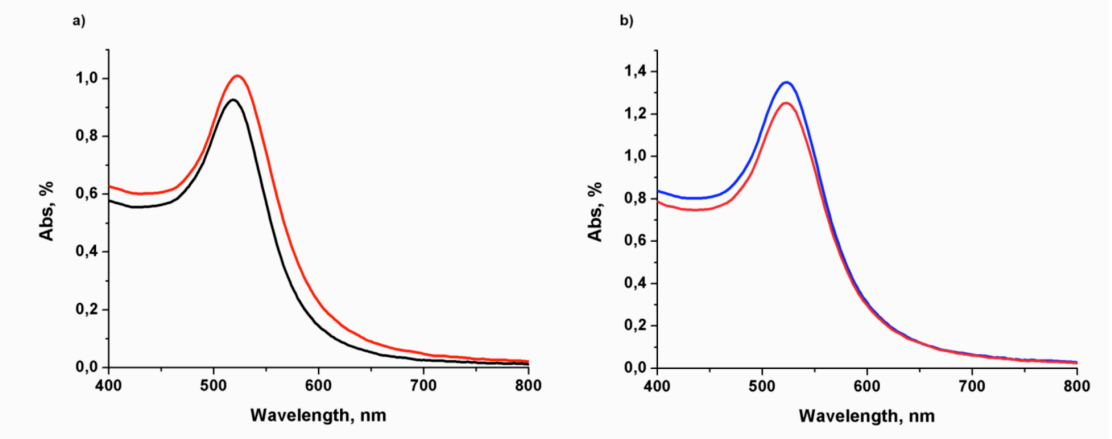

Figure 29. UV-vis spectra of AuNPs: a) GNP-518 nm (black line); GNP@PEG-COOH(95%)-PEG-COONHS(5%)- 522 nm (red line); b) GNP@PEG-COOH(95%)-PEG-COONHS(5%) in PBS-522 nm (blue line); GNP@PEG-COOH(95%)-PEG-CO-NH-Halo(5%)-524 nm (magenta line).

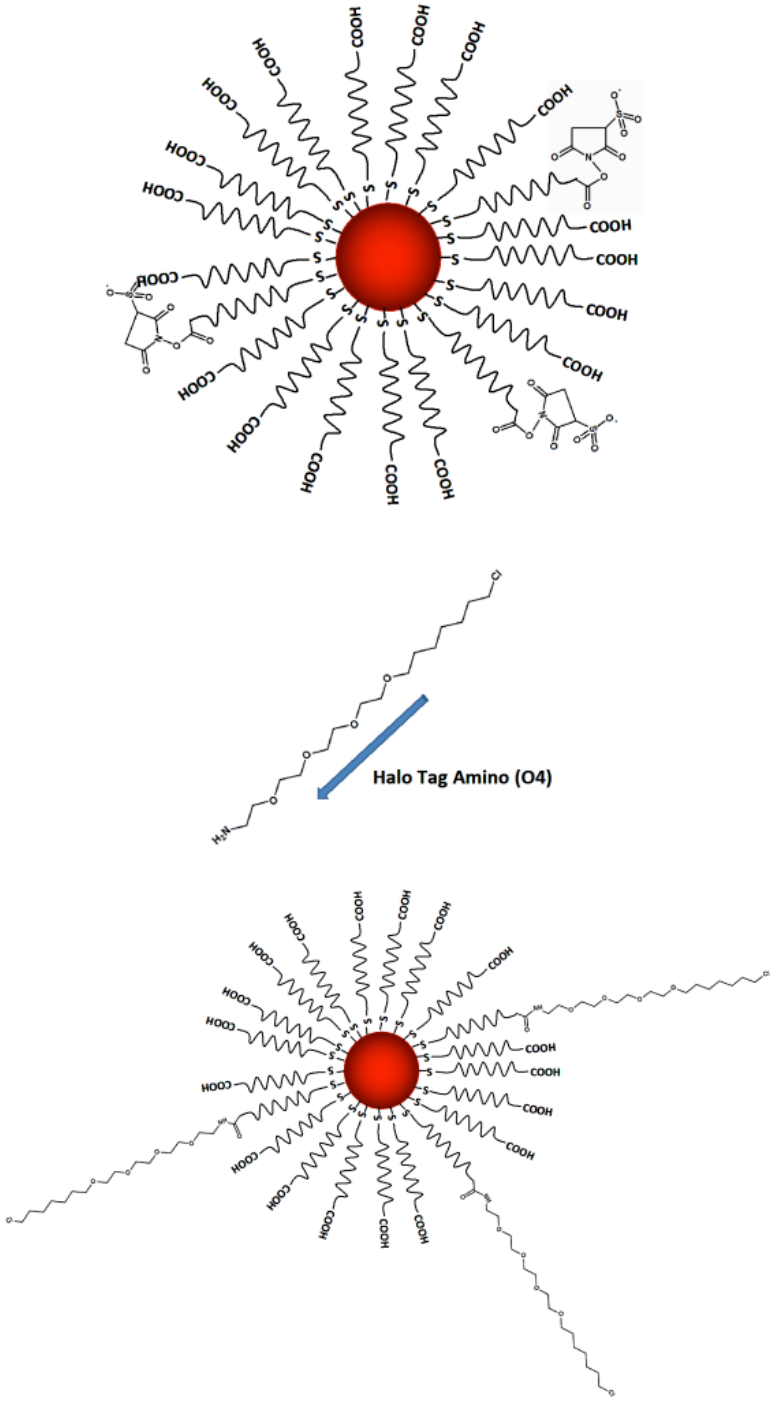

Scheme 4. Representation of Halo Tag Amino conjugation to citrate-stabilized gold nanoparticles via HS-PEG–COOH and NHS-containing PEG-SH passivation.

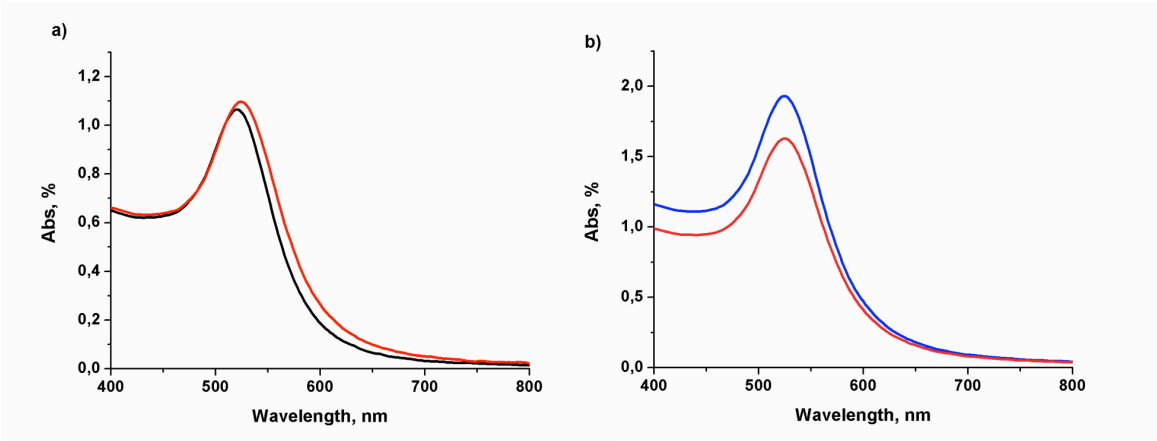

Figure 30. UV-vis spectra of AuNPs: a) GNP-520 nm (black line); GNP@PEG-COOH(90%)-PEG-COONHS(10%)- 524 nm (red line); b) GNP@PEG-COOH(90%)-PEG-COONHS(10%) in PBS-524 nm (blue line); GNP@PEG-COOH(90%)-PEG-CO-NH-Halo(10%)-524 nm (magenta line).

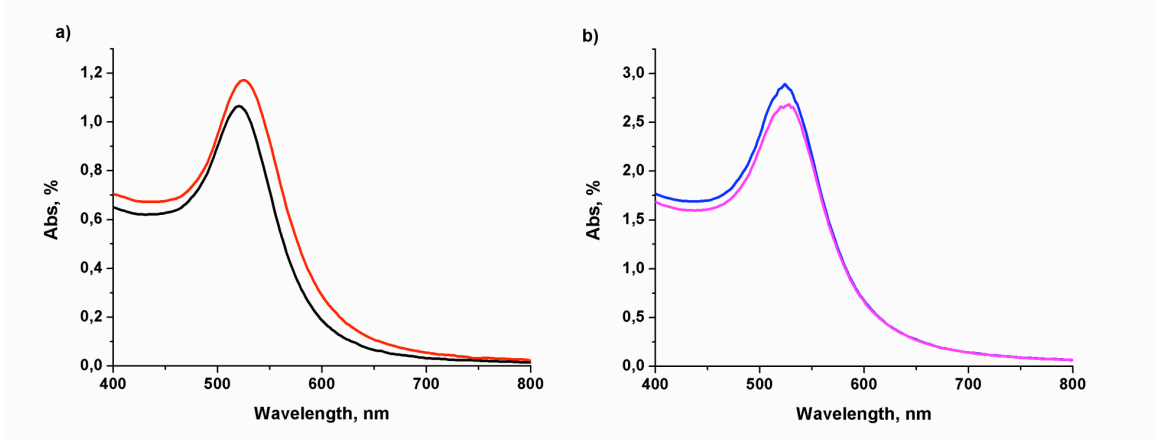

Figure 31. UV-vis spectra of AuNPs: a) GNP-520 nm (black line); GNP@PEG-COOH(85%)-PEG-COONHS(15%)- 524 nm (red line); b) GNP@PEG-COOH(85%)-PEG-COONHS(15%) in PBS-524 nm (blue line); GNP@PEG-COOH(85%)-PEG-CO-NH-Halo(15%)-524 nm (magenta line).

While Halo Amino-conjugated nanoparticles show a slight (2 nm) shift of the SPR band to 524 nm and a decrease in intensity, confirming the changes in the ligand shell.

Analytical centrifugation results are shown in Figure 32. A large shift of the particle diameter values takes place when GNPs are covered by PEG layer: diameter of citrate GNPs of 13.4 nm changes to give 12.1 nm for the particles with a 5% amount of active NHS groups, while for the particles containing 10 and 15% of PEG-NHS the shift is even larger being 11.9 nm.This confirms UV-vis preliminary results on the successful ligand exchange between citrate ions and PEG. A further shift from 11.9 to 11.7 nm can be clearly observed when the particles are conjugated with 15% Halo Tag Amino ligand, while in the case of minor ligand amounts the shift is hardly seen due to the increase of ligand shell diameter (Figure 32, c).

Zeta-potential results shown the change of the values after each functionalization step: initial zeta-potential value of -32.7 mV corresponding to citrate GNPs becomes less negative after passivation by PEG mixture because of the contribution of sulfo-NHS neutral groups, while it turnes to be more negative after conjugation with Halo Tag Amino ligand, due to the negative chlorine terminal groups (Figure 33).

TEM images of final conjugated nanoparticles are reported in Figures 34-36.The mean particle diameter obtained by TEM is around 17 nm and has a narrow distribution. Like in the case of the particles conjugated with Halo Tag Amino ligand *via* EDC/sulfo-NHS, the as-prepared particles are able to form chain-like structures via self-assembly. It is likely due to the presence of a large amount of carboxylic groups in the PEG shell, which can form intermolecular hydrogen bonds. However, a more detailed study of all the systems is needed to better understand the origin of

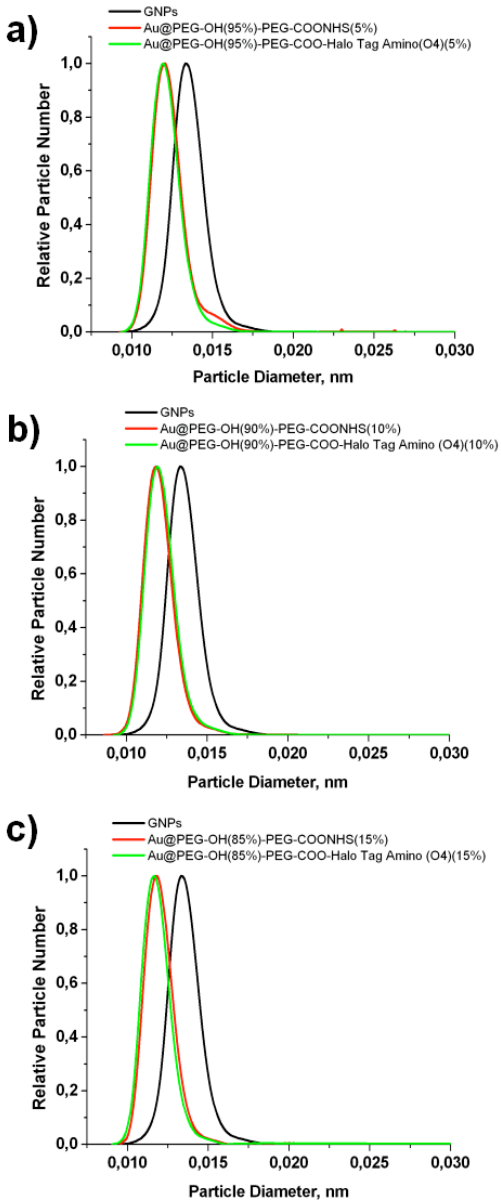

Figure 32. Analytical centrifugation patterns of AuNPs: a) GNPs-13.4 nm (black line); Au@PEG-COOH(95%)-PEG-COONHS (5%)-12.1 nm (red line); Au@PEG-COOH(95%)-PEG-COO-Halo Tag Amino (O4) (5%)-12.1 nm (green line); b) GNP-13.4 nm (black line); Au@PEG-COOH(90%)-PEG-COONHS (10%)- 11.9 nm (red line); Au@PEG-COOH(90%)-PEG-COO-Halo Tag Amino (O4) (10%)-11.9 nm (green line), c) GNP-13.4 nm (black line); Au@PEG-COOH(85%)-PEG-COONHS (15%)- 11.9 nm (red line); Au@PEG-COOH(85%)-PEG-COO-Halo Tag Amino (O4) (15%)-11.7 nm (green line).

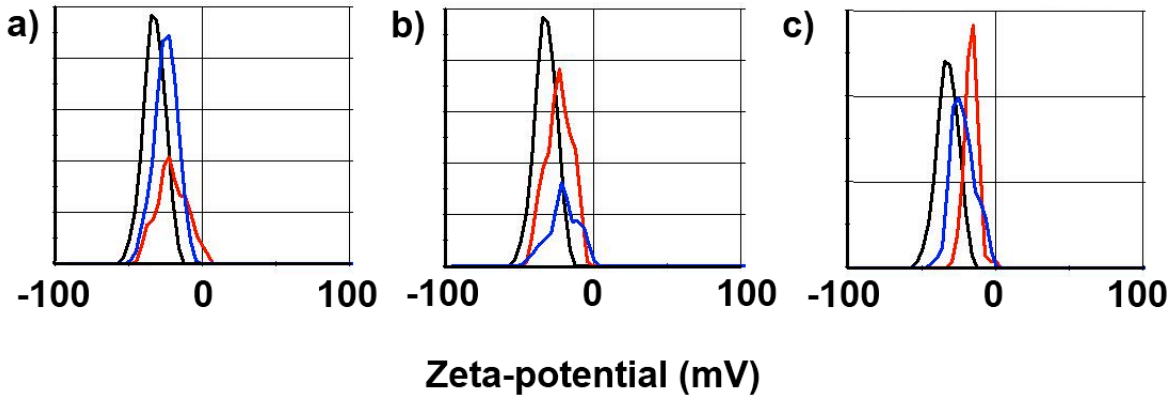

Figure 33. Zeta-potential of gold nanoparticles: black line- GNP, -32.7 mV; a) red line-Au@PEG-COOH (95%)-PEG-COONHS (5%), -20.7 mV; blue line-Au@PEG-COOH (95%)-PEG-COO-Halo Tag Amino (O4) (5%), -24.8 mV; b) red line-Au@PEG-COOH (90%)-PEG-COONHS (10%), -23.6 mV; blue line-Au@PEG-COOH (90%)-PEG-COO-Halo Tag Amino (O4) (10%), -24.5 mV; c) red line-Au@PEG-COOH (85%)-PEG-COONHS (15%), -16.7 mV; blue line-Au@PEG-COOH (85%)-PEG-COO-Halo Tag Amino (O4) (15%), -22.1 mV.

these assembly fenomena and, probably, find them a future application.

The stability of both PEGylated and Halo Amino-conjugated particles against pH- and NaCl-aggregation was examined in the above range of pH (1-13) and salt concentrations (1-3 M). The results slightly differ from those obtained for other kinds of particles. Figure 37 represents a set of UV-vis spectra showing the change in the SPR band both of PEGylated GNP and those conjugated using sulfo-NHS containing PEG incorporated in the ligand shell. These results clearly indicate that in the pH range 13-5 the particles form a well dispersed suspension in water exhibiting a characteristic SPR band at 524 nm. We did not observe any change in the spectra or suspension colour in the whole pH range. However, on further decreasing of pH to 3,

a large shift of the SPR band along with a colour change from red to violet took place. At pH<3 the spectra did not change further and became almost saturated without any shifting of SPR band.

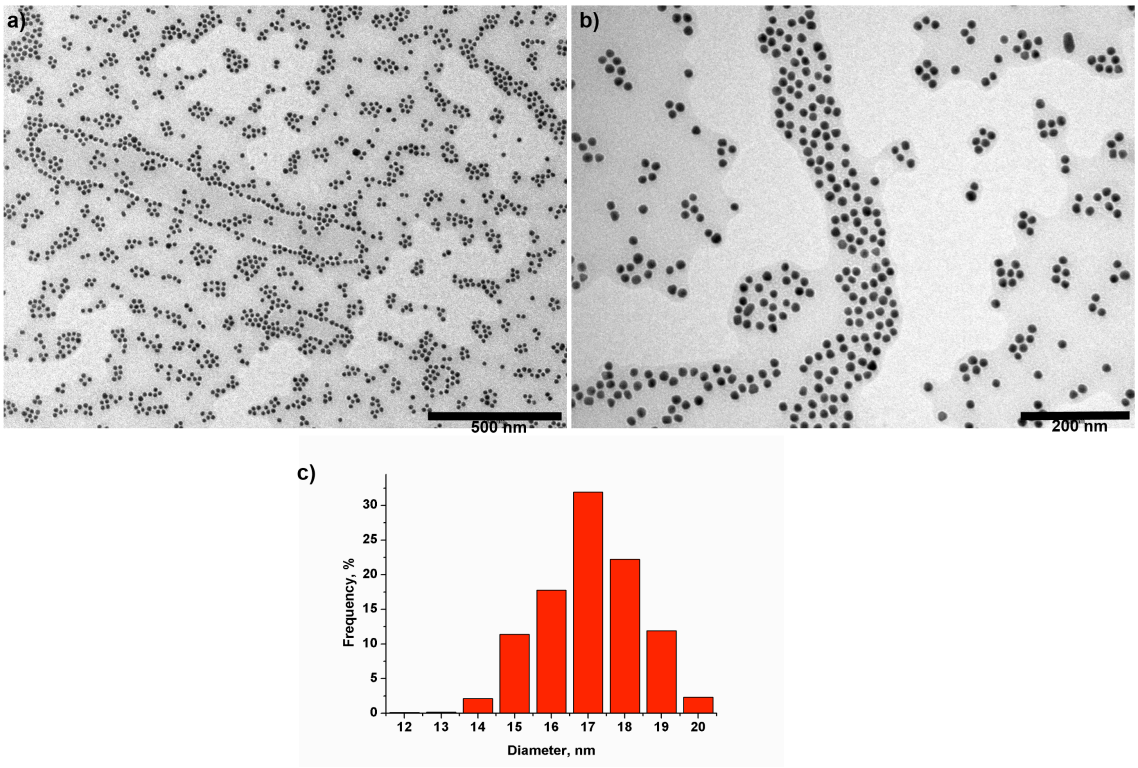

Figure 34. TEM micrograph of GNP@PEG-COOH(95%)-PEG-COONHS-Halo Tag Amino (O4) (5%): a) scale bar 500 nm; b) scale bar 200 nm; c) size distribution histogram (17.17±1.02 nm mean diameter).

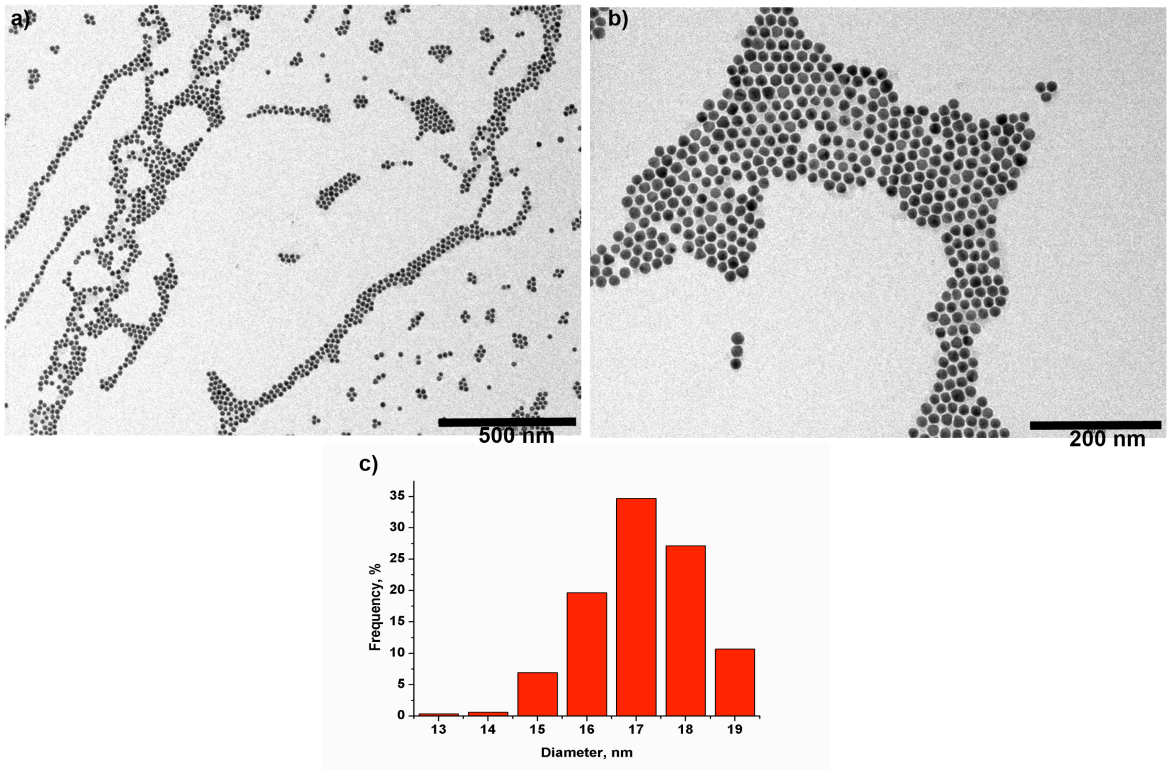

Figure 35. TEM micrograph of GNP@PEG-COOH(90%)-PEG-COONHS-Halo Tag Amino (O4) (10%): a) scale bar 500 nm; b) scale bar 200 nm; c) size distribution histogram (16.96±1.28 nm mean diameter).

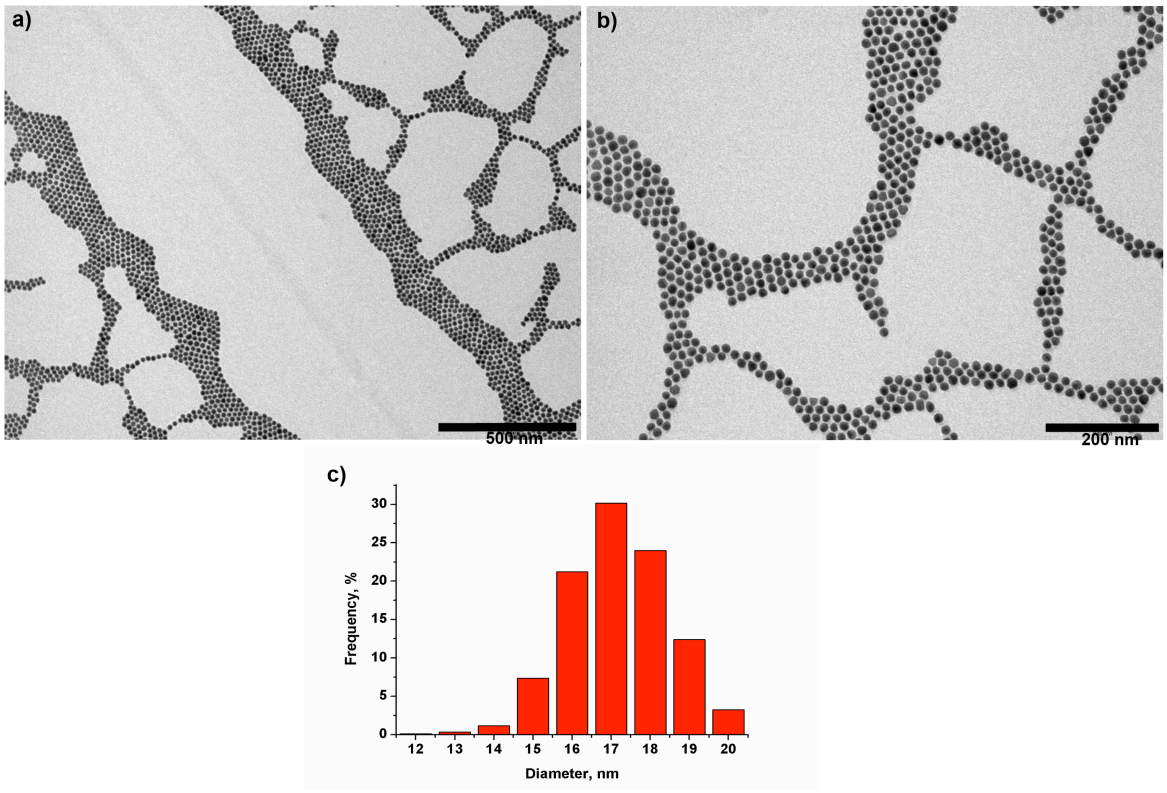

Figure 36. TEM micrograph of GNP@PEG-COOH(85%)-PEG-COONHS-Halo Tag Amino (O4) (15%): a) scale bar 500 nm; b) scale bar 200 nm; c) size distribution histogram (16.96±1.28 nm mean diameter).

These observations can be explained as follows. In general, pK_a values of carboxylic acids vary slightly depending on the chemical environment. The –COOH groups are completely acidified below their pK_a value and usually form an intermolecular H-bonds as shown in Scheme 5 [49]. The H-bonding between two –COOH groups of surface-bound PEG molecules brings the nanoparticles into close proximity to form an assembled structure and results in the development of another SPR band in a higher-wavelength region as a result of the coupling of interparticle plasmon resonance of GNPs.

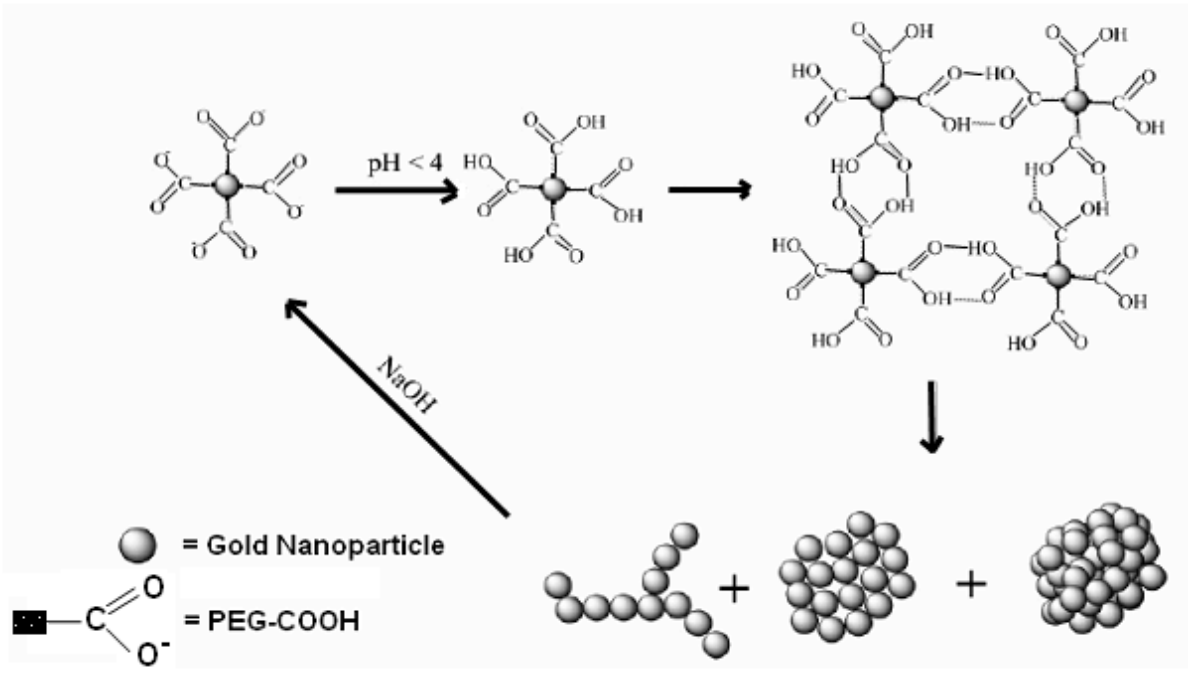

Scheme 5. An overview of reversible pH-induced aggregation of gold nanoparticles covered by PEG-COOH: protonation of $-COO^-$ groups under pH<4; intermolecular H-bonding; nanoparticle aggregates formation and reversible disaggregation under basic conditions.

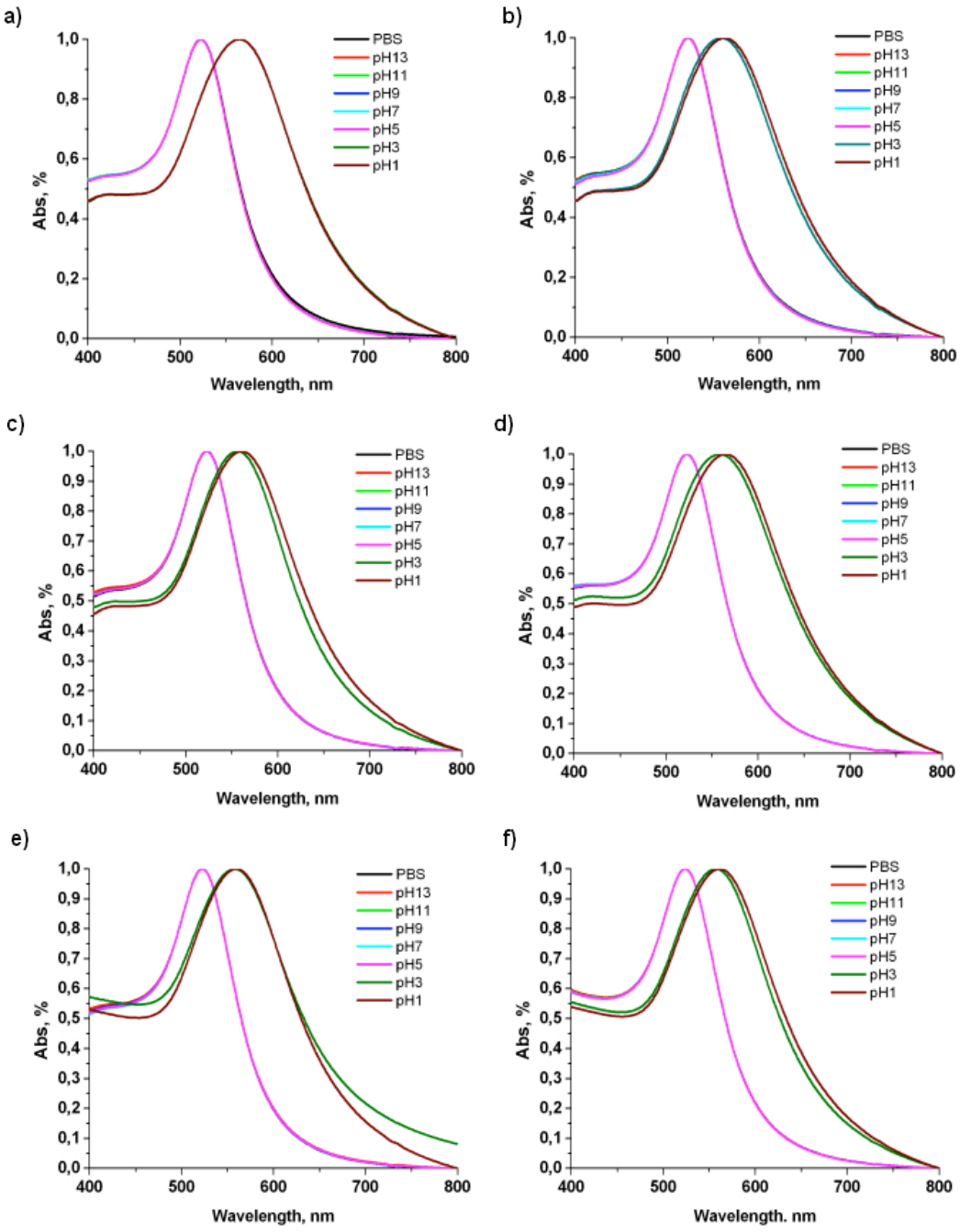

Figure 37. UV-vis spectra of Au@PEG-COOH (95%)-PEG-NHS (5%) (a), Au@PEG-COOH (95%)-PEG-NHS-Halo Tag Amino (O4) (5%) (b), Au@PEG-COOH (90%)-PEG-NHS (10%) (c), Au@PEG-COOH (90%)-PEG-NHS-Halo Tag Amino (O4) (10%) (d), Au@PEG-COOH (85%)-PEG-NHS (15%) (e) and u@PEG-COOH (85%)-PEG-NHS-Halo Tag Amino (O4) (15%) (f) in PBS and different pH solutions. The pH values were 1, 3, 5, 7, 9, 11 and 13.

In order to understand if the assembly process was reversible, 0.1M NaOH solution was added to the assembly medium in order to increase the pH to 10, resulting in a colour change from violet to initial red, indicating a disassembly process (Figure 38). It is clear that the assembly process is driven by hydrogen-bonding interactions, as no red shift of SPR band was observed in the case of Halo Tag Thiol conjugation where the –COOH groups were lacking.

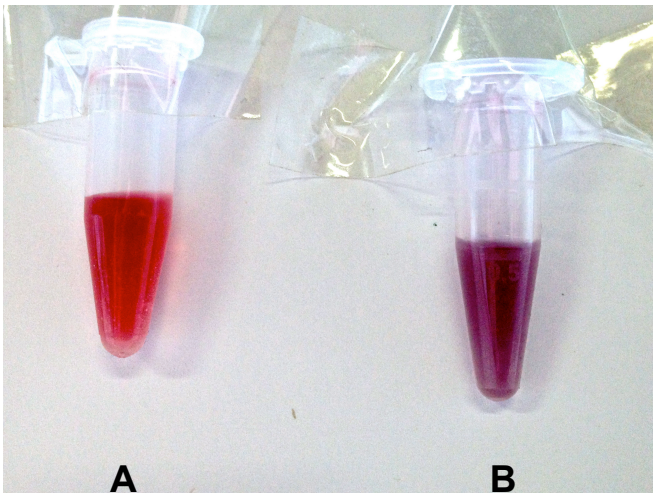

Figure 38. Reversible aggregation of AuNPs: A) After addition of NaOH solution, AuNPs turn back red; B) aggregated AuNPs.

Figure 39 describes the change of aggregation parameter calculated from UV-vis spectra as function of pH. The patterns are very similar in the basic and neutral pH, indicating that Halo Tag Amino conjugation does not improve the stability of nanoparticles respect to PEGylated ones nor influences the stability against pH-induced aggregation.

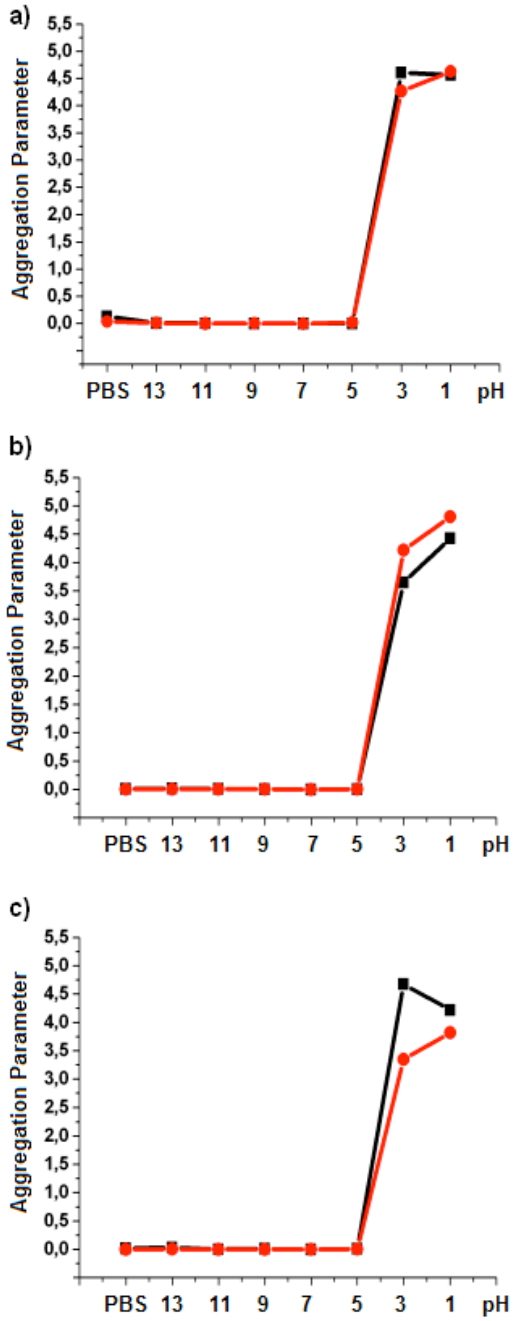

Figure 39. Stability against pH-induced aggregation of (a) Au@PEG-COOH (95%)-PEG-NHS (5%) (black line) and Halo Tag Amino (O4)-conjugated (5%) (red line), (b) Au@PEG-COOH (90%)-PEG-NHS (10%) (black line) and Halo Tag Amino (O4)-conjugated (10%) (red line), and (c) Au@PEG-COOH (85%)-PEG-NHS (15%) (black line) and Halo Tag Amino (O4)-conjugated (15%) (red line).

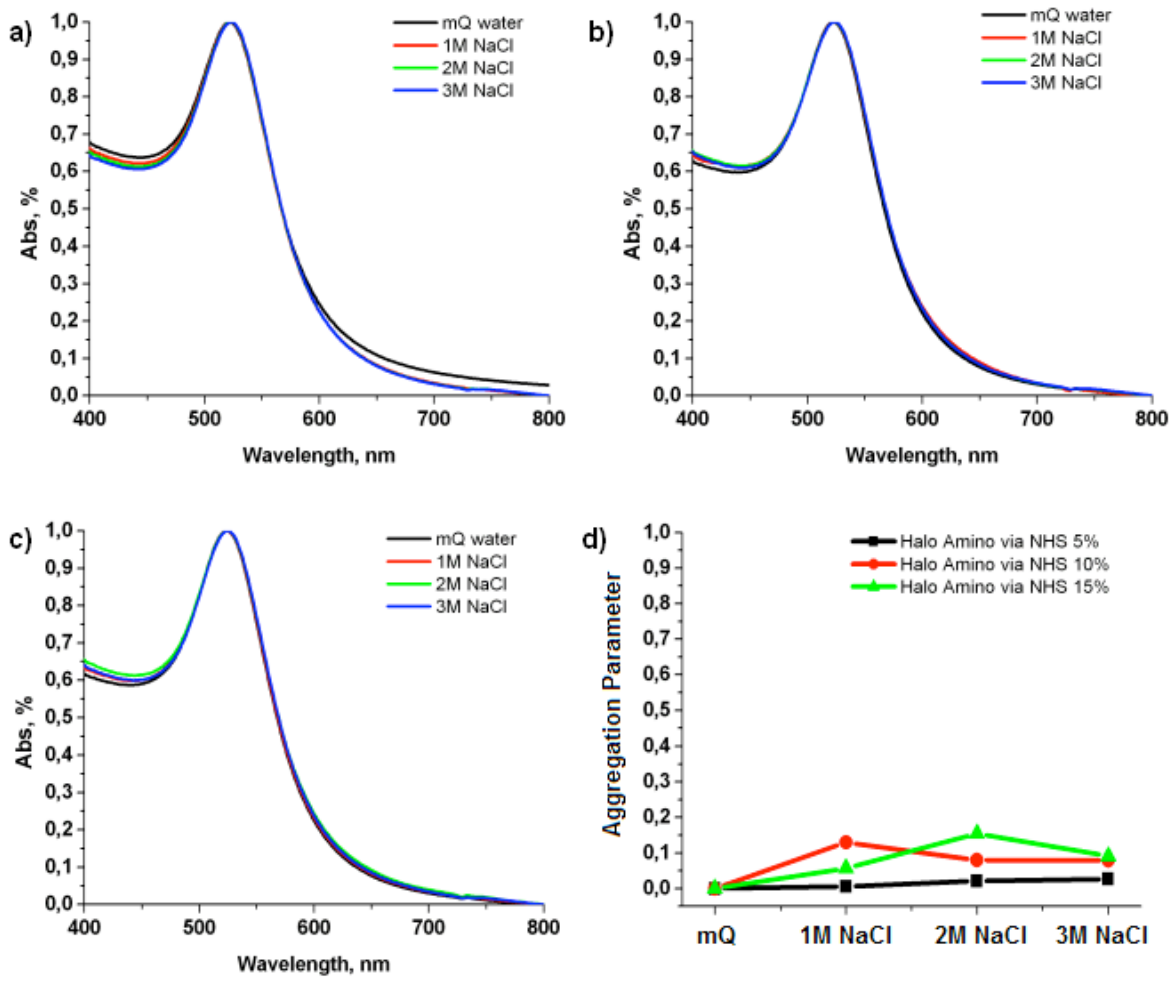

Figure 40. UV-vis spectra of Au@PEG-COOH (95%)-PEG-NHS-Halo Tag Amino (O4) (5%) (a), Au@PEG-COOH (90%)-PEG-NHS-Halo Tag Amino (O4) (10%) (b) and Au@PEG-COOH (85%)-PEG-NHS-Halo Tag Amino (O4) (15%) (c) in mQ water and different NaCl solutions. The NaCl concentrations were 1M, 2M and 3M. (d) Stability against NaCl-induced aggregation of Au@PEG-COOH (95%)-PEG-NHS-Halo Tag Amino (O4) (5%) (black line), Au@PEG-COOH (90%)-PEG-NHS-Halo Tag Amino (O4) (10%) (red line) and Au@PEG-COOH (85%)-PEG-NHS-Halo Tag Amino (O4) (15%) (green line).

On the contrary, the stability against NaCl-induced aggregation slightly decreases with increasing loading of Halo Tag Amino ligand on the particle surface (Figure 40, c).

In conclusion, aggregation parameter patterns for all the systems based on Halo Tag Amino ligand and obtained by two different conjugation techniques are reported in Figure 41. It is clearly seen that conjugation via EDC/sulfo-NHS coupling reaction with 10% loading of Halo Tag Amino ligand gives the best results in terms of stability even in extreme conditions like very acidic or basic pH, or high salt concentrations.

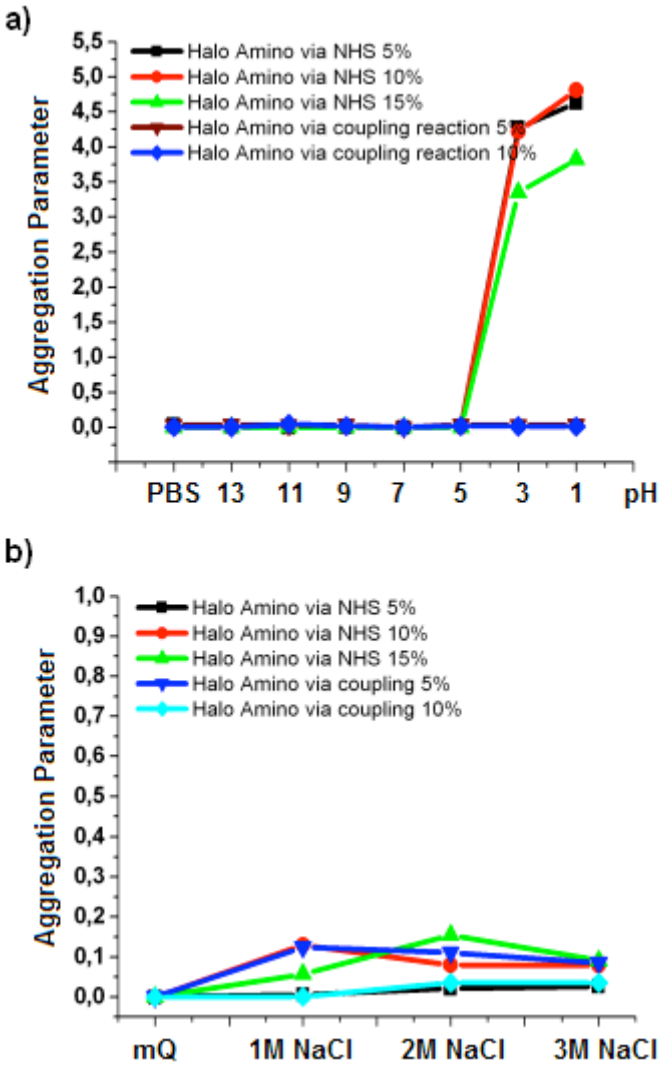

Figure 41. Comparison of the stability against (a) pH-induced aggregation of Au@PEG-COOH(95%)-PEG-NHS-Halo Tag Amino(5%) (black line), Au@PEG-COOH(90%)- PEG-NHS-Halo Tag Amino(10%) (red line), Au@PEG-COOH(85%)-PEG-NHS-Halo Tag Amino(15%) (green line), Au@PEG-OH(95%)-PEG-COO-Halo Tag Amino(5%) (brown line), and Au@PEG-OH(90%)-PEG-COO-Halo Tag Amino(10%) (blue line); (b) Stability against NaCl-induced aggregation of Au@PEG-COOH(95%)-PEG-NHS-Halo Tag Amino(5%) (black line), Au@PEG-COOH(90%)- PEG-NHS-Halo Tag Amino(10%) (red line), Au@PEG-COOH(85%)-PEG-NHS-Halo Tag Amino(15%) (green line), Au@PEG-OH(95%)-PEG-COO-Halo Tag Amino(5%) (blue line), and Au@PEG-OH(90%)-PEG-COO-Halo Tag Amino(10%) (cyan line).

3. Concluding remarks

Bioconjugation technology has affected nearly every discipline in the life sciences. The appication of the available crosslinking reactions and reagents for creating novel conjugates with peculiar activities has facilitated a significant number biological assays, the *in vivo* and *in vitro* targeting of molecules and cells, and the modulation of specific biological processes. To successfully design a nanoconjugate that will meet the requirements to be used in biological experiments, one should keep in mind a number of factors: a molecule with certain biological activity should be used for functionalization of nanoparticles which readily interacts with a biological target, such as antibody, receptor, or specifiv protein; a proper coupling approach should be used in order to obtain the active site of the molecule well exposed from the ligand shell for interaction with the target; and, finally, the nanoconjugate must be stable in phisiological solutions, containing high salt concentrations and PBS, as well in a wide pH-range to be succesfully used in biologhical experiments.

In this Chapter, we have focused our attention on the design, synthesis and characterization of gold nanoparticles functionalized with both amino- and thiol-containing Halo Tag ligands. A number of bioconjugation techniques have been illustrated and the characteristics of the conjugates have been compared in order to select a system meeting the requirements for a successful application in biological experiments. The nanoparticles have been characterized by TEM, UV-vis, analytical centrifugation and zeta-potential measurements. Their stability have been tested both in a wide pH range (pH 1-13) and in extreme salt concentrations (1-3 M NaCl).

Being based on the stability results, we can conclude that the conjugates synthesized *via* EDC/sulfo-NHS coupling reaction using Halo Tag Amino ligand have shown the best stability compared to the other candidates both against pH- and salt-induced aggregation. Further biological experiments will be carried out in order to compare the conjugates' behaviour in the living cells and study internalization mechanism which will drive the nanoparticles in different cellular compartments where Halo Tag fusion protein will be expressed for specific biorecognition.

4. References

1. K.A Giuliamo, and D.L. Taylor. *Trends Biotechnol.* 1998, **16**, 135–140.
2. A. Chapman-Smith, and J.E. Cronan. *Trends Biochem. Sci.,* 1999, **24**, 359–63.
3. G. V. Los, L. P. Encell, M. G. McDougall, D. D. Hartzell, N. Karassina, C. Zimprich, M. G. Wood, R. Learish, R. Friedman Ohana, M. Urh, D. Simpson, J. Mendez, K. Zimmerman, P. Otto, G. Vidugiris, J. Zhu, A. Darzins, D. H. Klaubert, R. F. Bulleit, and K. V. Wood. • *ACS Chemical Biology,* 2008*,* **3** (6), 373-382.
4. a) Y. Zhang, M.-K. So, A. M. Loening, H. Yao, S. S. Gambhir, and J. Rao. *Angew. Chem. Int. Ed*. 2006, **45**, 4936 –4940; b) M. K So, H. Yao, and J. Rao. *Biochemical and Biophysical Research Communications,* 2008*,* **374**, 419–423.
5. W. Russ Algar, D. E. Prasuhn, M. H. Stewart, T. L. Jennings, J. B. Blanco-Canosa, P. E. Dawson, and I. L. Medintz. *Bioconjugate Chem.* 2011, **22**, 825–858.
6. D. H.Tsai, F. W. DelRio, R. I. MacCuspie, T. J.Cho, M. R. Zachariah, and V. A. Hachley. *Langmuir,* 2010, **26**, 10325−10333.
7. H. Lee, S. H. Choi, and T. G. Park. *Macromolecules*, 2006, **39**, 23−25.
8. C. M. Ruan, W. Wang, and B. H. Gu. *Anal. Chim. Acta*, 2006, **567**, 114−120.
9. S. X. Zhang, N. Wang, H. J. Yu, Y. M. Niu, and C. Q. Sun. *Bioeletrochemistry*, 2005, **67**, 15−22.
10. S. Roux, B. Garcia, J. L. Bridot, M. Salome, C. Marquette, L. Lemelle, P. Gillet, L. Blum, P. Perriat, and O. Tillement. Langmuir, 2005, **21**, 2526−2536.
11. B. C. Mei, K. Susumu, I. L. Medintz, J. B. Delehanty, T. J. Mountziaris, and H. J. Mattoussi. Mater. Chem. 2008, **18**, 4949−4958.

12. F. Chai, C. G. Wang, T. T. Wang, L. Li, and Z. M. Su, *ACS Appl. Mater. Interfaces,* 2010, **2**, 1466−1470.

13. P. Ghosh, G. Han, M. De, C. K. Kim, and V. M. Rotello, *Adv. Drug Delivery Rev.* 2008, **60**, 1307−1315.

14. E. D. Kaufman, J. Belyea, M. C. Johnson, Z. M. Nicholson, J. L. Richs, P. K. Shah, M. Bayless, T. Pettersson, Z. Feldotö, E. Blomberg, P. Claesson, and S. Franzen. *Langmuir,* 2007, **23**, 6053−6062.

15. F. Q. Hu, Y. L. Ran, Z. A. Zhou, and M. Y. Gao. *Nanotechnology,* 2006, **17**, 2972−2977.

16. H. W. Huang, X. Y. Liu, T. Hu, and P. K. Chu, *Biosens. Bioelectron.* 2010, **25**, 2078−2083.

17. M. H. Stewart, K. Susumu, B. C. Mei, I. L.Medintz, J. B. Delehanty, J. B. Blanco-Canosa, P. E. Dawson, and H. Mattoussi. *J. Am. Chem. Soc.* 2010, **132**, 9804−9813.

18. J. Gao, X. Huang, H. Liu, F. Zan, and J. Ren. *Langmuir,* 2012, **28**, 4464−4471.

19. N. O. Fischer, C. M. McIntosh, J. M. Simard, and V. M. Rotello. *Proc. Natl. Acad. Sci. U.S.A.* 2002, **99**, 5018–5023.

20. N. L. Rosi, D. A. Giljohann, C. S. Thaxton, A. K. R. Lytton-Jean, M. S. Han, and C. A. Mirkin. *Science,* 2006, **312**, 1027–1030.

21. J. J. Storhoff, R. Elghanian, R. C. Mucic, C. A. Mirkin, and R. L. Letsinger. *J. Am. Chem.* Soc. 1998, **120**, 1959–1964.

22. L. Maus, J. P. Spatz, and R. Fiammengo. Langmuir, 2009, **25** (14), 7910–7917.

23. M. Colombo, S. Mazzucchelli, V. Collico, S. Avvakumova, L. Pandolfi, F. Corsi, F. Porta, and D. Prosperi. Angewandte Chemie International Edition, 2012, **37** (51), 9272–9275.
24. G. Scarì, F. Porta, U. Fascio, S. Avvakumova, V. Dal Santo, M. De Simone, M. Saviano, M. Leone, A. Del Gatto, C. Pedone, and L. Zaccaro. *Bioconjugate Chem.* 2012, **23** (3), 340–349.
25. J. D. Swartz, C. P. Gulka, F. R. Haselton, and D. W. Wright. *Langmuir*, 2011, **27** (24), 15330–15339.
26. D. Bartczak, and A. G. Kanaras. *Langmuir,* 2011, **27**, 10119-10123.
27. A. A. Volkert, V. Subramaniam, M. R. Ivanov, A. M. Goodman, and A. J. Haes. *ACS Nano,* 2011, **5** (6), 4570-4580.
28. J.Turkevich, P. C. Stevenson, and J.Hillier. *Disc. Faraday Soc.* 1951**, 11**, 55-75.
29. G.Frens. *Nature Phys. Sci.* 1973**, 241**, 20-22.
30. A. S. Karakoti, S. Das, S. Thevuthasan, and S. Seal. *Angew. Chem. Int. Ed.* 2011, **50**, 1980 – 1994.
31. E. Pensa, E. Cortès, G. Cortney, P. Carro, C. Vericat, M. H. Fonticelli, G. Benitez, A. A. Rubert, and R. C. Salvarezza. *Acc. Chem. Res.*, 2012, **45** (8), 1183–1192.
32. M. C. Daniel, I. B. Tsvetkova, Z. T. Quinkert, A. Murali, M. De, V. M. Rotello, C. C. Kao and B. Dragnea. *ACS Nano*, 2010, **4** (7), 3853–3860.
33. X. Huang, and M. A. El-Sayed. *Journal of Advanced Research*, 2010, **1**, 13–28.
34. C. F. Chen, S. D. Tzeng, H. Y. Chen, K. J. Lin, and S. Gwo. *J. Am. Chem. Soc.*, 2008, **130**, 824-826.

35. R. Levy, N. T. K. Thanh, R. C. Doty, I. Hussain, R. J. Nichols, D. J. Schiffrin, M. Brust, and D. G. Fernig. *J. Am. Chem. Soc.* 2004, **126**, 10076-10084.

36. I. Olmedo, E. Araya, F. Sanz, E. Medina, J. Arbiol, P. Toledo, A. Álvarez-Lueje, E. Giralt, and M. J. Kogan. *Bioconjugate Chem.*, 2008, **19** (6), 1154–1163.

37. K. Nwe , D. E. Milenic , G. L. Ray , Y. S. Kim , and M. W. Brechbiel. *Mol. Pharmaceutics*, 2012, **9** (3), 374–381.

38. M. A. Burlingame, C. T. M. B. Tom, and A. R. Renslo. *ACS Comb. Sci.*, 2011, **13** (3), 205–208.

39. A. W. York, C. W. Scales, F. Huang, and C. McCormick. *Biomacromolecules*, 2007, **8** (8), 2337–2341.

40. N. V. Seetala, S. Kang, Z. Jia, D. E. Nikles, and J. W. Harrell. *Microsc Microanal,* 2007, **13**, 662-663.

41. S. Huang, W. Y. Gaofei Hu , and L. Wang, *J. Phys. Chem. C*, Article ASAP, **DOI:** 10.1021/jp305211d.

42. K. Jia, J. L. Bijeon, P. M. Adam, and R. E. Ionescu, *Anal. Chem.*, 2012, 84 (18), 8020–8027.

43. J. Conde, A. Ambrosone, V. Sanz, Y. Hernandez, V. Marchesano, F. Tian, H. Child, C. C. Berry, M. R. Ibarra, P. V. Baptista, C. Tortiglione, and J. M. de la Fuente, *ACS Nano*, Article ASAP **DOI:** 10.1021/nn3030223.

44. G. T. Hermanson, Bioconjugate techniques, Second edition, Academic press, 2008.

45. X. Qian, X.-H. Peng, D. O. Ansari, Q. Yin-Goen, G. Z. Chen, D. M. Shin, L. Yang, A. N. Young, M. D. Wang, and S. Nie. *Nature Biotechnology,* **2008***,* 26 (1), 83-90.

46. A. S. Karakoti, S. Das, S. Thevuthasan, S. Seal. *Angew. Chem. Int. Ed.,* 2011*,* **50** (9), 1980–1994**.**

47. K. Knop, R. Hoogenboom, D. Fischer, and U. S. Schubert. *Angew. Chem. Int. Ed.* 2010, **49**, 6288 – 6308.

48. T. Liu, and B. Thierry. *Langmuir*, Just Accepted, **DOI:** 10.1021/la301390u.

49. S. Si, and T. K. Mandal. *Langmuir,* **2007,** *23,* 190-195.

Appendix:

Concentration fraction patterns as function of pH:

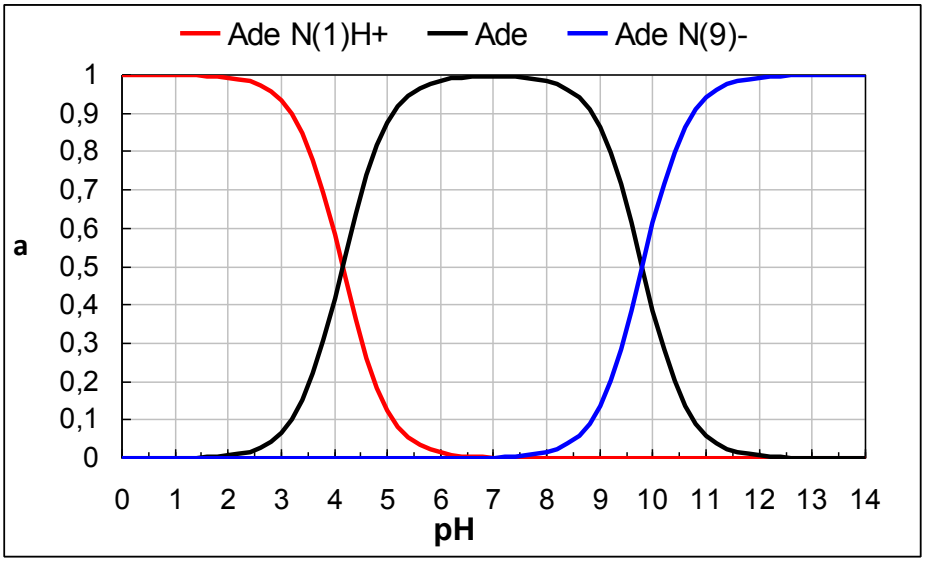

Figure A1. Concentration fraction α patterns as function of pH, where Ade N(1)H^+ is adenine protonated at N(1) atom, Ade-neutral form, and Ade $N(9)^-$-deprotonated at N(9) atom.

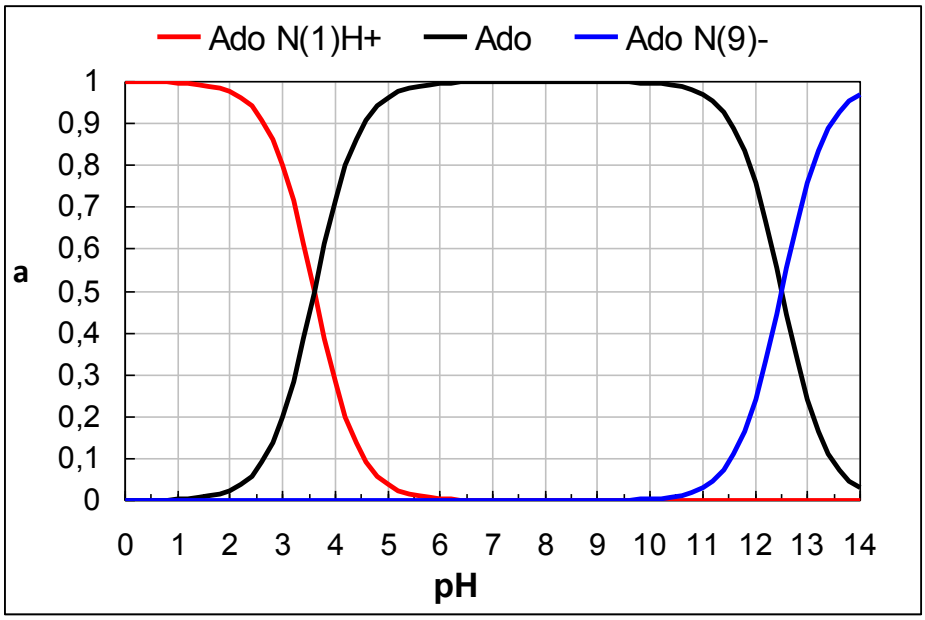

Figure A2. Concentration fraction α patterns as function of pH, where Ado N(1)H^+ is adenosine protonated at N(1) atom, Ado-neutral form, and Ado $N(9)^-$-deprotonated at N(9) atom.

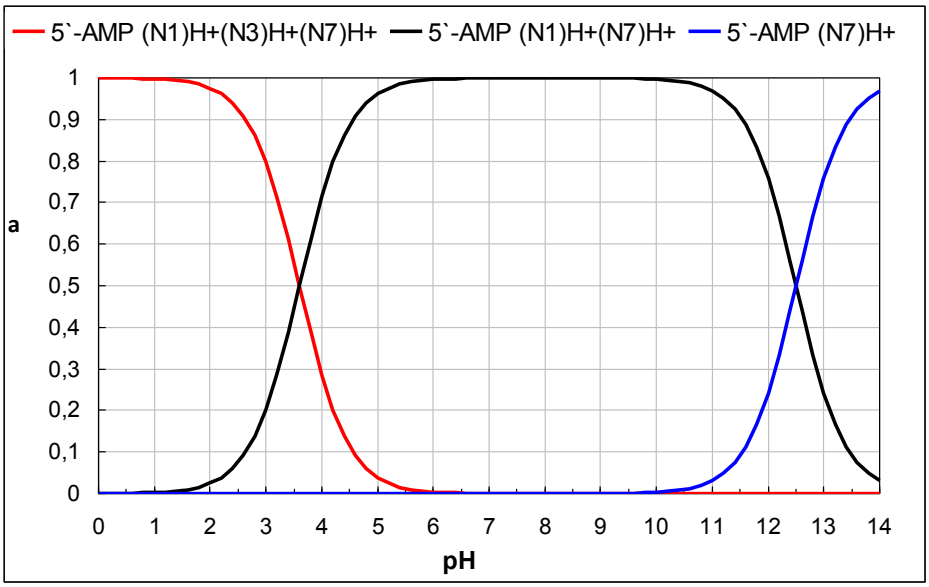

Figure A3. Concentration fraction α patterns as function of pH, where 5'-AMP $N(1)H^+$ $N(3)H^+$ $N(7)H^+$ is adenosine 5'-monophosphate protonated at N(1), N(3) and N(7) atoms, 5'-AMP $N(1)H^+$ $N(7)H^+$ - protonated at N(1) ans N(7) atoms, and 5'-AMP $N(7)H^+$ - protonated at N(7) atom.

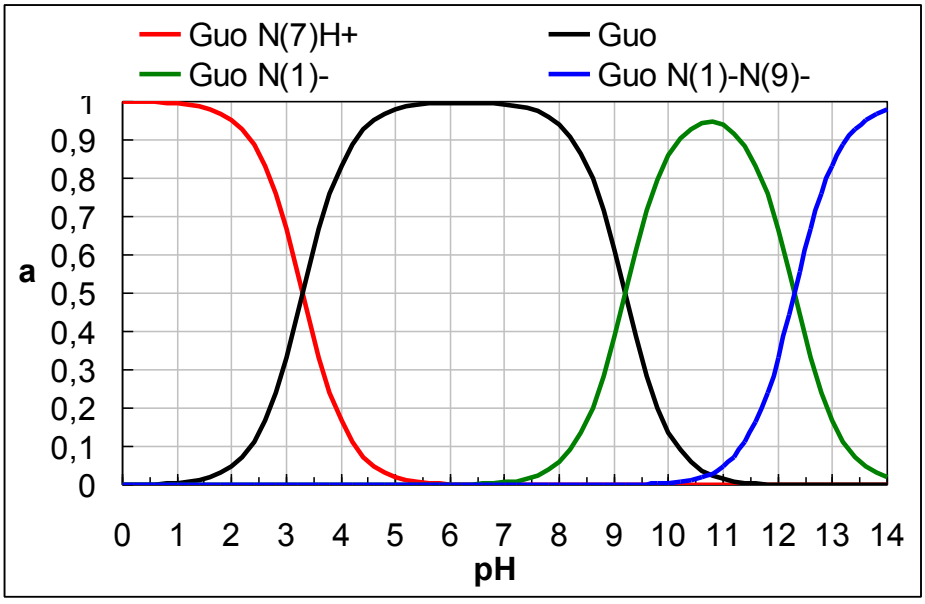

Figure A4. Concentration fractions α patterns as function of pH, where Guo $N(7)^+$ is guanine protonated at N(7) atom, Guo-neutral form, Guo N(1)—deprotonated at N(1) atom and Guo N(1)-N(9)—deptotonated both at N(1) and N(9) atoms.

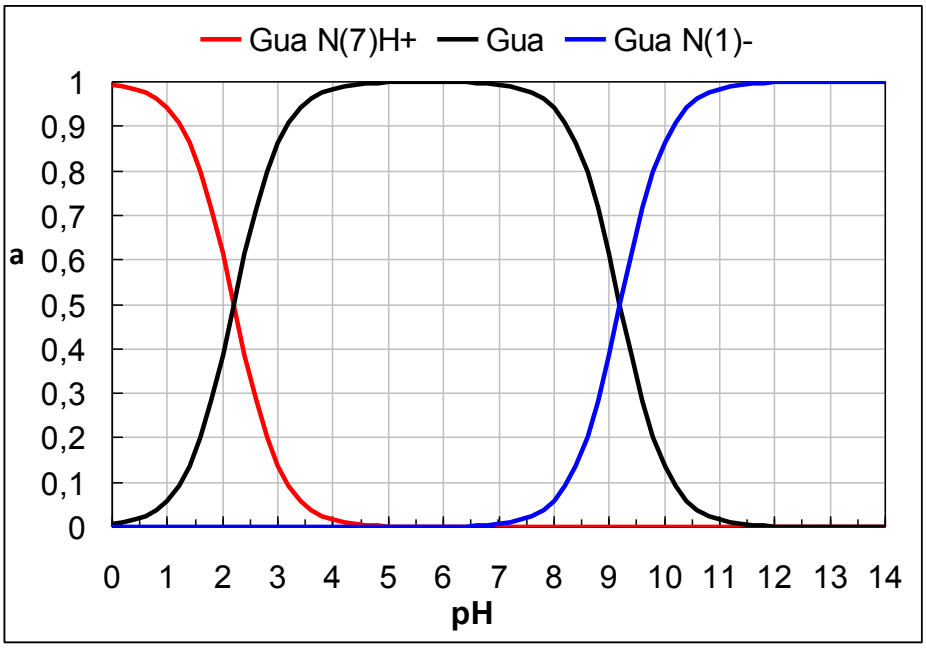

Figure A5. Concentration fractions α patterns as function of pH, where Gua N(7)$^+$ is guanosine protonated at N(7) atom, Gua-neutral form, Gua N(1)—deprotonated at N(1) atom.

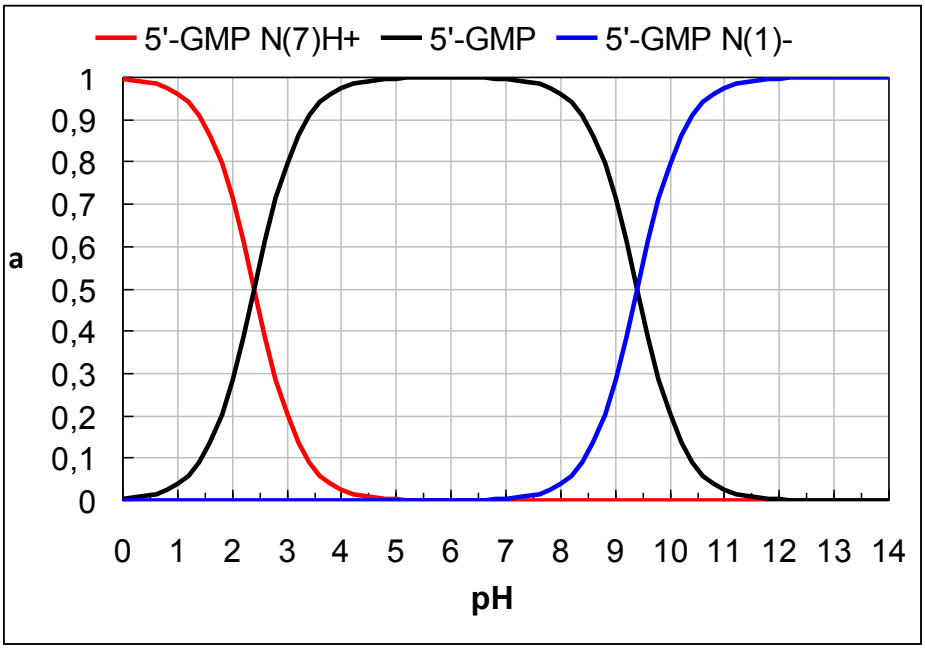

Figure A6. Concentration fractions α patterns as function of pH, where 5'-GMP N(7)H$^+$ is guanosine 5'-monophosphate protonated at N(7) atom, 5'-GMP -neutral form, 5'-GMP N(1)— deprotonated at N(1) atom.

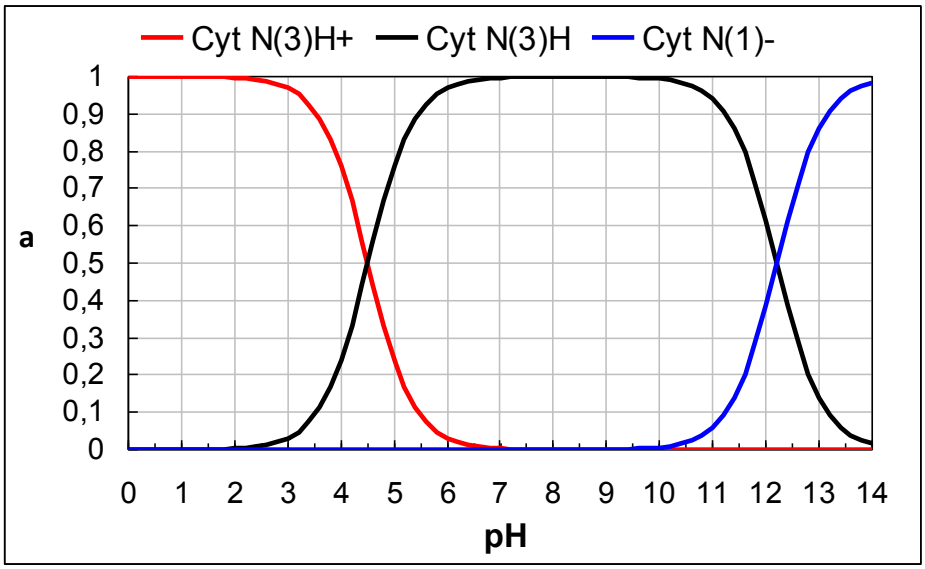

Figure A7. Concentration fractions α patterns as function of pH, where Cyt N(3)H^+ is cytosine protonated at N(3) atom, Cyt-neutral form, and Cyt $N(1)^-$ -deprotonated at N(1) atom.

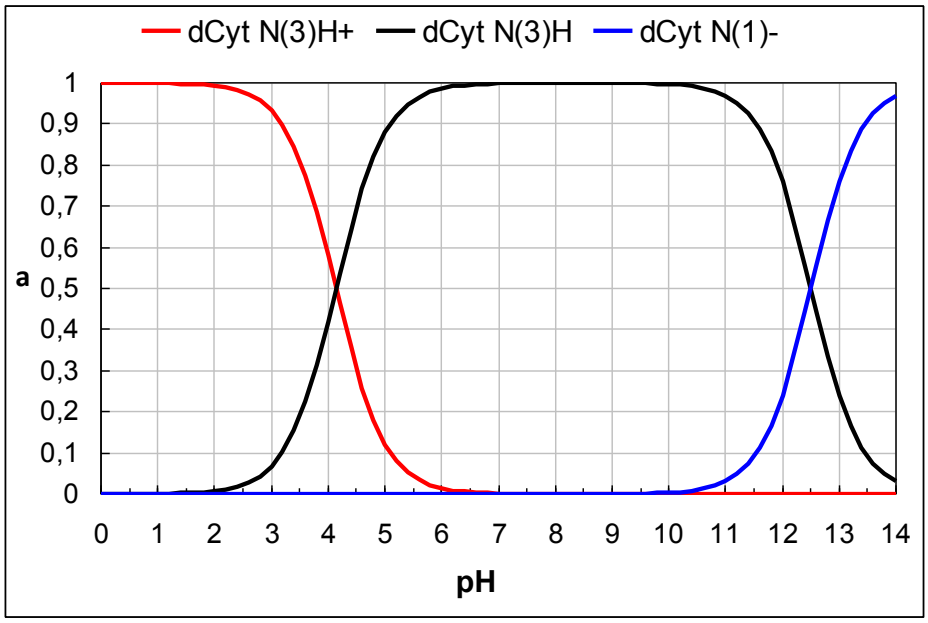

Figure A8. Concentration fractions α patterns as function of pH, where dCyt N(3)H^+ is cytidine protonated at N(3) atom, Cyt-neutral form, and Cyt $N(1)^-$ -deprotonated at N(1) atom.

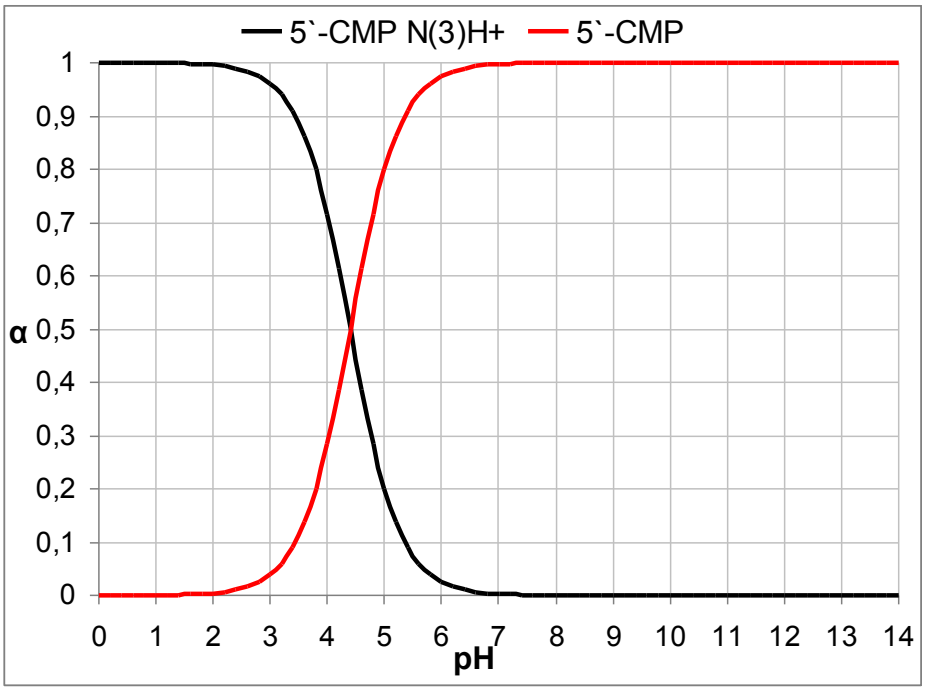

Figure A8. Concentration fractions α patterns as function of pH, where 5'-CMP N(3)H^+ is cytidine 5'-monophosphate protonated at N(3) atom and 5'-CMP -neutral form.

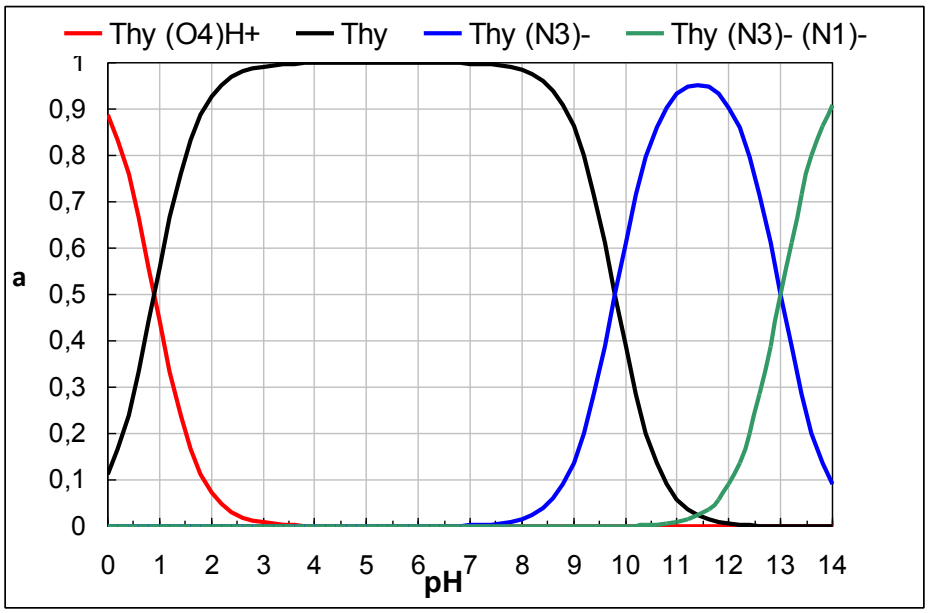

Figure A9. Concentration fractions α patterns as function of pH, where Thy (O4) H^+ is thymine protonated at O(4) atom, Thy – neutral form, Thy $(N3)^-$ -deprotonated at N(3) atom, and Thy $(N3)^-$ $N(1)^-$ -deprotonated at N(3) and N(1) atoms.

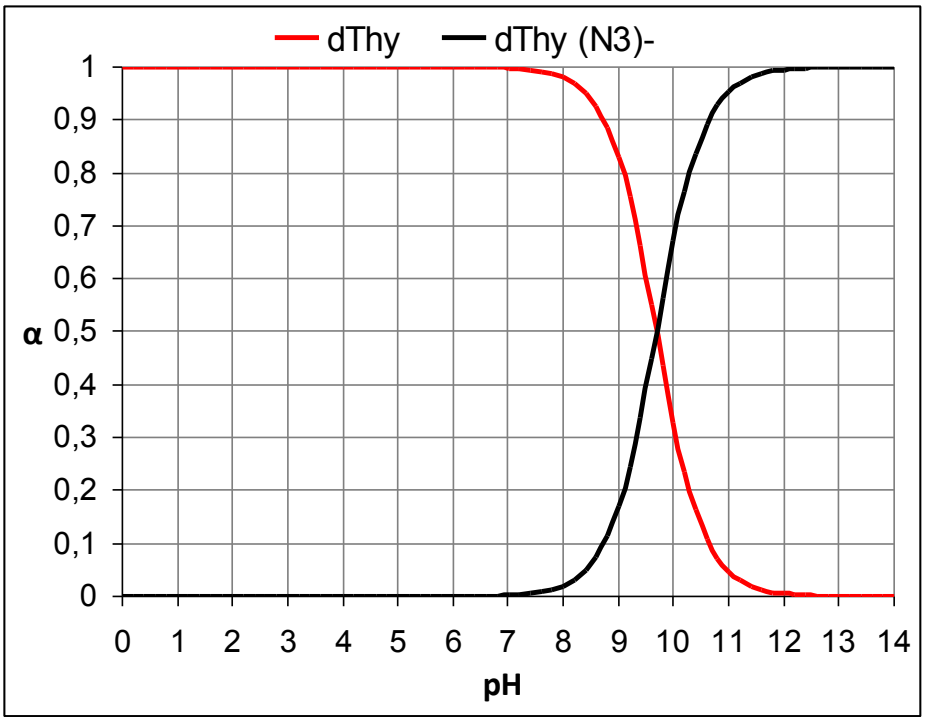

Figure A10. Concentration fractions α patterns as function of pH, where dThy – neutral form, and dThy (N3)$^-$ -deprotonated at N(3) atom.

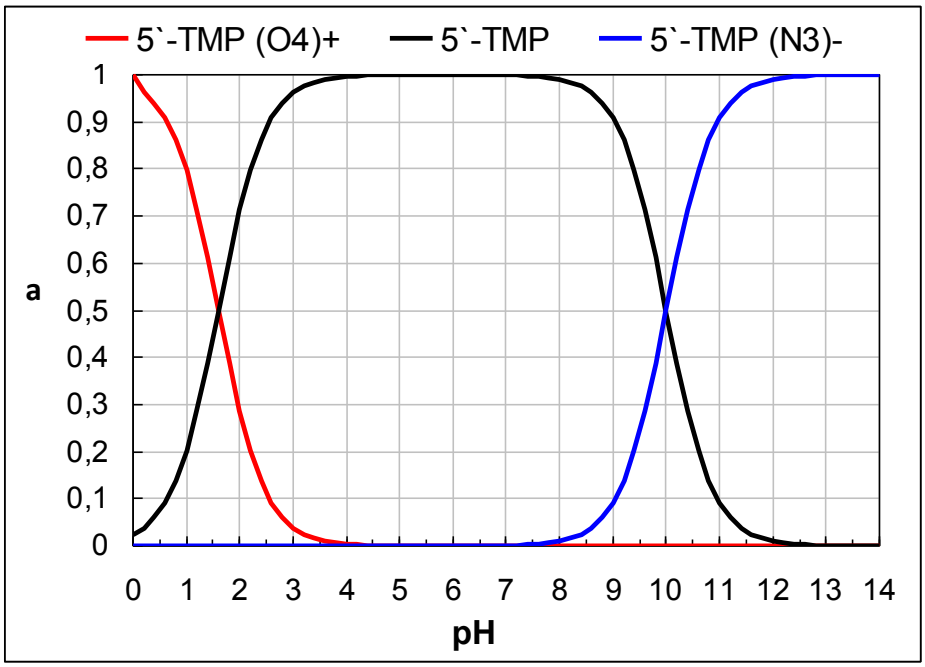

Figure A11. Concentration fractions α patterns as function of pH, where 5'-TMP (O4)H+ is thymidine 5'-monophosphate protonated at O(4) atom, 5'-TMP – neutral form, and 5'-TMP (N3)$^-$ - deprotonated at N(3) atom.

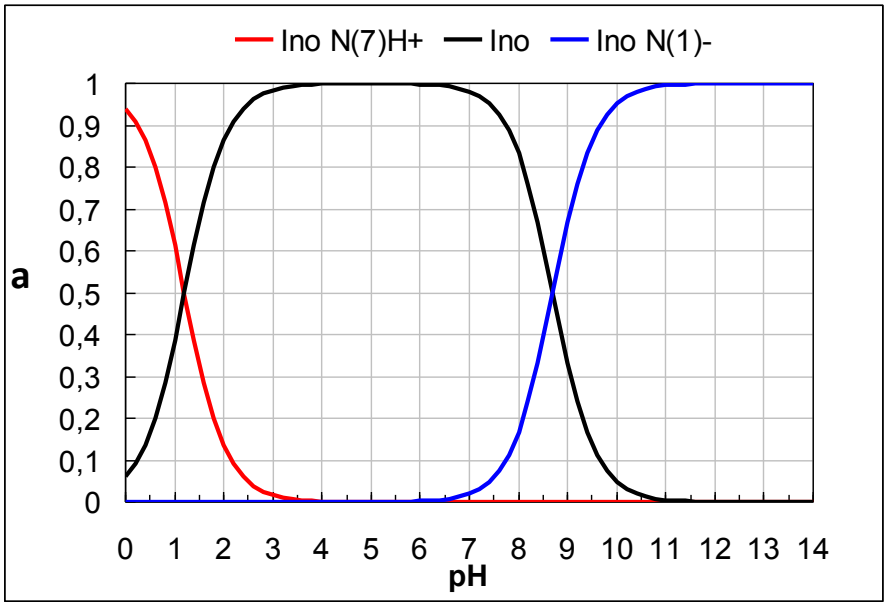

Figure A12. Concentration fractions α patterns as function of pH, where Ino N(7)H^+ is inosine protonated at N(7) atom, Ino -neutral form, Ino N(1)—deprotonated at N(1) atom.

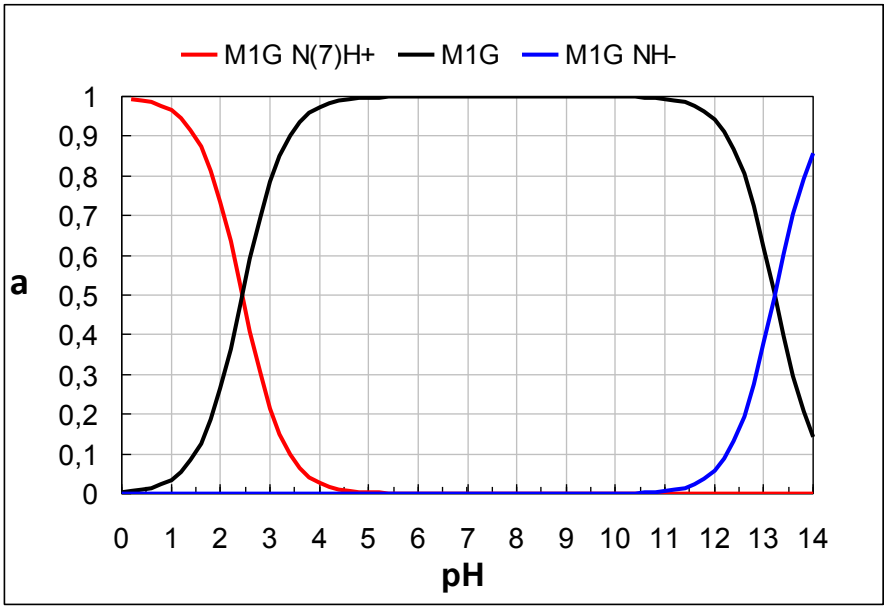

Figure A13. Concentration fractions α patterns as function of pH, where M^1G N(7)H^+ is 1-methylguanosine protonated at N(7) atom, M^1G -neutral form, M^1G NH—deprotonated at NH_2 group.

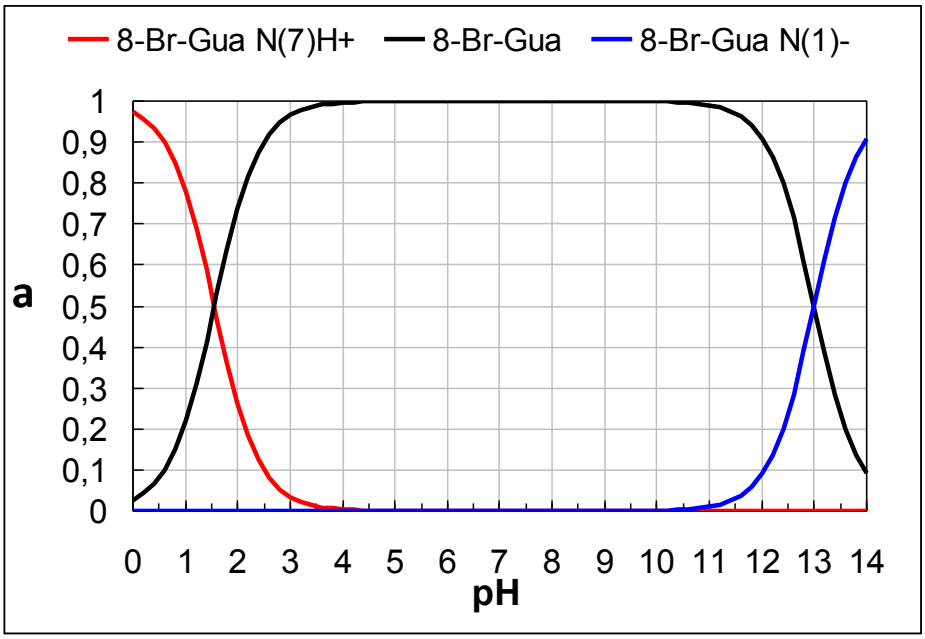

Figure A14. Concentration fractions α patterns as function of pH, where 8-Br-Gua N(7)H^+ is 8-bromoguanosine protonated at N(7) atom, 8-Br-Gua -neutral form, 8-Br-Gua N(1)— deprotonated at N(1) atom.

2. Chemical shift values from ^1H and ^{31}P NMR:

Table 1. ^1H NMR chemical shifts of free ligands at pH 7, pH 3.5 and after interaction with Au NPs.

	Ino pH 7		Ino pH 3.5		Au-Ino	
H2	s	8.26	s	8.24	s	8.42-8.19
H8	s	8.15	s	8.12	s	
H1’	d	6.02	d	6.00	d	6.20-6.07
H2`	Burried under H_20 signal					
H3’	dd	4.36	dd	4.36	dd	4.41
H4’	dd	4.21	dd	4.20	dd	4.25

H5’	dd dd	3.84 3.79	dd dd	3.85 3.77	dd dd	3.96 3.81
	Guo pH 7		**Guo pH 3.5**		**Au-Guo**	
H8	s	7.65	s	7.98	s	8.28
	Gua pH 7		**Gua pH 3.5**		**Au-Gua**	
H8	s	7.95	s	7.96	s	5.59
H1’	d	5.85	d	5.86	d	5.59
H2`	Burried under H_20 signal					
H3’	dd	4.34	dd	4.35	dd	4.40|
H4’	q	4.17	q	4.17	q	4.01
H5’	d d	3.82 3.76	d d	3.82 3.76	dd	3.82 3.65
	5’-GMP pH 7		**5’-GMP pH 3.5**		**Au-5`-GMP**	
H8	s	8.13	s	8.09	s	8.58
H1’	d	5.86	d	5.85	d	5.86
H2`	Burried under H_20 signal					
H3’	dd	4.43	dd	4.42	dd	4.42
H4’	q	4.25	q	4.25	q	4.32
H5’	dd	3.93	dd	3.96	dd	4.11
P	S	3.96	s	2.87	s	0.34
	M^1G pH 7		**M^1G pH 3.5**		**Au- M^1G**	
H8	S	7.92	s	7.93	s	7.99
H1’	D	5.85	d	5.84	d	5.88
H2`	Burreid under H_20 signal					

H3’	dd	4.35	dd	4.35	dd	4.39
H4’	q	4.17	q	4.17	q	4.24
H5’	d d	3.82 3.76	d d	3.81 3.77	d d	3.84 3.82
CH3	s	3.41	s	3.40	s	3.46
	8-Br-Gua pH		**8-Br-Guo pH 3.5**		**Au-8-Br-Guo**	
H1`	s	5.81	s	5.93	s	---
H2`	dd	4.91	dd	5.01	dd	---
H3`	dd	4.28	dd	4.43	dd	4.15
H4`	q	4.17	q	4.15	q	3.95
H5`	d d	3.82 3.75	d d	3.83 3.78	d d	3.73 3.68

Table 2. ^{1}H NMR chemical shifts of free adenine (Ade), adenosine (Ado) and adenosine 5’-monophosphate (5’-AMP) at pH 7, pH 3.5 and after interaction with Au NPs.

	Ade pH 7		**Ade pH 3.5**		**Au-Ade**	
H2	s	8.04	s	8.21	s	8.14
H8	s	7.89	s	8.16	s	8.10
	Ado pH 7		**Ado pH 3.5**		**Au-Ado**	
H2	s	8.23	s	8.28	s	7.94
H8	s	8.13	s	8.17	s	7.68
H1’	d	5.85	d	6.0	d	5.55
H2`		4.69		4.36		4.35

H3’	dd	4.21	dd	4.22	dd	3.95
H4’	q	4.16	q	4.17	q	3.95
H5’	d d	3.83 3.74	d d	3.86 3.77	dd	3.61
	5’-AMP pH 7		**5’-AMP pH 3.5**		**Au-5`-AMP**	
H2	s	8.53	s	8.46	s	8.41
H8	s	8.14	s	8.05	s	8.07
H1’	d	6.06	d	6.01	d	6.03
H2`	Burried under H_20 signal					
H3’	dd	4.45	dd	4.43	dd	4.31-3.89
H4’	q	4.30	q	4.29	q	
H5’	dd	3.95	dd	3.96	dd	
P	s	3.95	s	3.60	s	0.23

Table 3. ^{1}H NMR chemical shifts of free thymine (Thy), thymidine (dThy) and thymidine 5’-monophosphate (5’-TMP) at pH 7, pH 3.5 and after interaction with Au NPs.

	Thy pH 7		**Thy pH 3.5**		**Au-Thy**	
H6	s	7.31	s	7.30	s	7.31
CH3	s	1.79	s	1.80	s	1.81
	dThy pH 7		**dThy pH 3.5**		**Au-dThy**	
H6	s	7.59	s	7.59	s	7.60
CH3	s	1.83	s	1.83	s	1.86
H1’	d	6.22	d	6.22	d	6.25

H2`	t	2.31	t	2.31	t	2.34
H3’	d	4.41	d	4.41	d	4.43
H4’	dd	3.96	dd	3.96	dd	3.98
H5’	ddd	3.74	ddd	3.74	ddd	3.76
	5’-TMP pH 7		**5’-TMP pH 3.5**		**Au-5`-TMP**	
H6	s	7.76	s	7.71	s	8.41
CH3	s	1.87	s	1.86	s	1.83
H1’	d	6.28	d	6.30	d	6.31
H2`	m	2.31	m	2.31	m	2.33
H3’	m	4.52	m	4.52	m	4.53
H4’	m	4.08	m	4.12	m	4.14
H5’	m	3.89	m	4.01	m	4.03
P	s	3.79	s	3.79	s	0.27

Table 3. ^{1}H NMR chemical shifts of free cytosine (Cyt), cytidine (dCyt) and cytidine 5’-monophosphate (5’-CMP) at pH 7, pH 3.5 and after interaction with Au NPs.

	Cyt pH 7		**Cyt pH 3.5**		**Au-Cyt**	
H6	d	7.53	d	7.47	d	8.2-7.4
H5	d	5.83	d	5.93	d	5.40
	dCyt pH 7		**dCyt pH 3.5**		**Au-dCyt**	
H6	d	7.77	d	7.79	s	8.13
H5	d	5.97	d	5.99	d	6.25
H1’	d	5.83	d	5.83	d	---
H2`	m	4.23	m	4.24	m	4.5-3.5

H3’	m	4.13	m	4.13	m	
H4’	dd	4.06	dd	4.06	dd	
H5’	ddd	3.86 3.73	ddd	3.86 3.74	ddd	
	5’-CMP pH 7		**5’-CMP pH 3.5**		**Au-5`-CMP**	
H6	d	8.16	d	7.98	d	8.17
H5	d	6.22	d	6.06	s	6.24
H1’	d	5.89	d	5.94	d	5.90
H2`	m	4.27	m	4.28	m	4.3-3.75
H3’	m	4.20	m	4.23	m	
H4’	m	4.15	m	4.05	m	
H5’	m	4.03	m	3.97	m	
P	s	3.79	s	1.85	s	0.25

3. FTIR data: the secon derivative patterns and main vibrational modes:

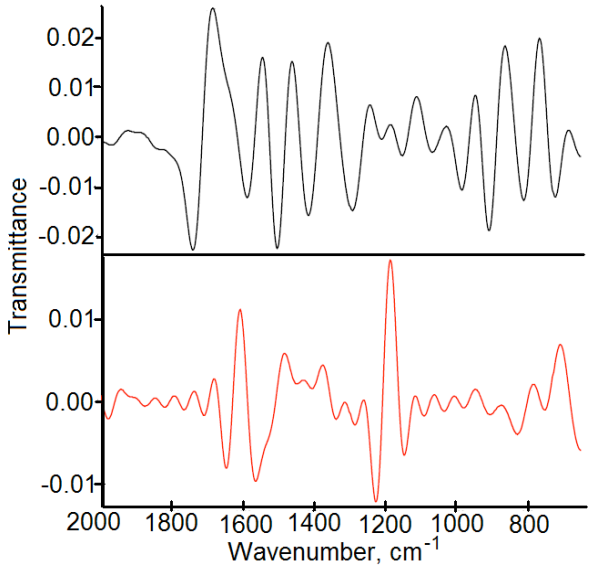

Modes	Guanine	Au-Guanine
v (NH2)asym	3321 (s)	3202 (s)
v (NH2)sym	3103 (s)	
v (CH)	2990 (m) 2897 (m)	---
v (C=O)	1653 (vs)	1608 (w)
δ (NH2)	1545 (w)	1485 (vw)
v (C-N)	1360 (m)	1374 (w)
Ring breathing	765 (s)	710 (s)

Figure A3.1. The second derivative spectra of guanine (black line) and Au-guanine NPs (red line).

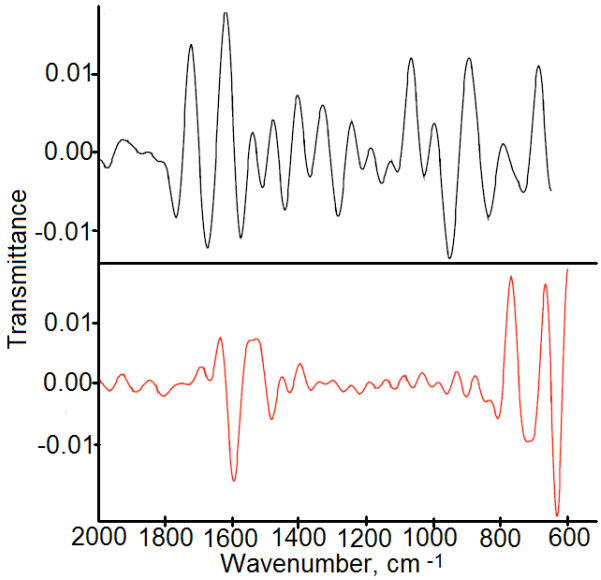

Modes	Guo	Au-Guo
v (NH2)asym	3315 (m)	----
v (N(1)-H)	3200 (s)	2923 (vw)
v (C=O)	1723 (w)	1693 (s) 1637 (s)
δ (NH2)	1621 (s)	1550 (s) 1526 (s)
v (C(2)-NH2)	1405 1331 (m)	1453 1399 (m)
Ribose vibr.	894 (s)	769 (w)
Ring breath.	686 (s)	665 (s)

Figure A3.2. The second derivative spectra of guanosine (black line) and Au-guanosine NPs (red line).

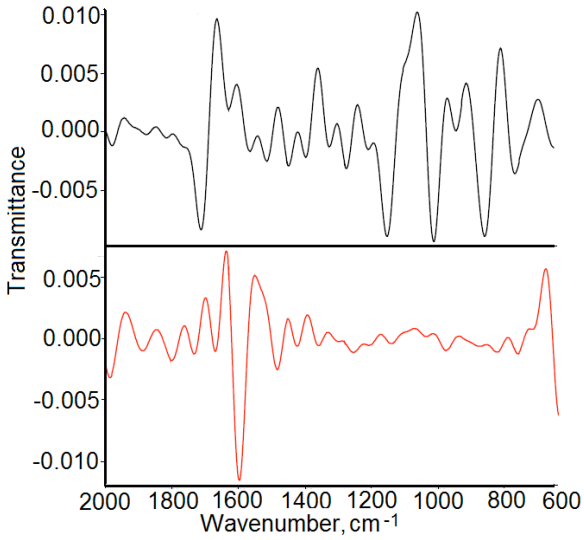

Modes	5`-GMP	Au-5`-GMP
ν (OH)	3443 (vs)	3448 3334 (vw)
ν (NH2)sym	3283 (m)	3224 (v)
ν (N(1)-H)	3117 (m)	3129 (s)
ν (N(1)-H) b	2934 (vw)	2924 (s)
ν (C=O)	1669 1606 (s)	1698 1637 (s)
δ (NH2)	1543 (s)	1518 (vw)
ν (C(2)-NH2)	1362 (m)	1450 (w)
ν (P=O) sym	1071 (vs)	1087 (m)
Ribose vibr.	814 (s)	791 (w)
Ring breath.	699 (s)	674 (m)

Figure A3.3. The second derivative spectra of guanosine 5'-monophosphate (black line) and Au-guanosine 5'-monophosphate NPs (red line)

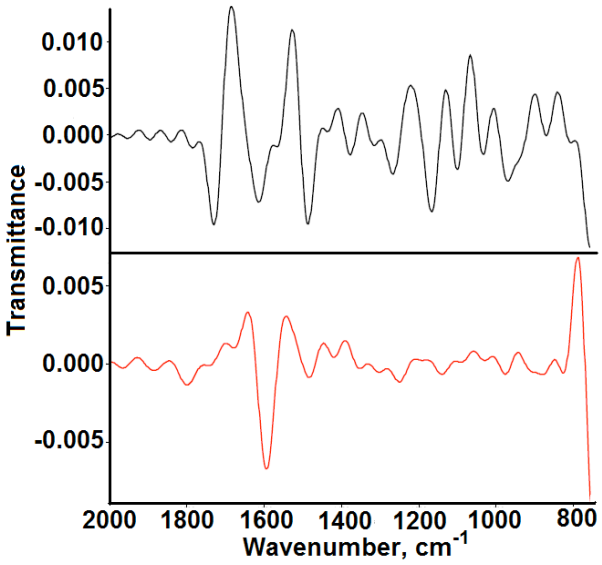

Modes	M^1G	Au-M^1G
v (OH)	3439 (w)	---
v (NH2)asym	3351 (w)	---
v (NH2)sym	3248 (s)	3214 (s)
v (N(1)-H) bound	2938 (w)	2929 (w)
v (C=O)	1686 (s)	1644 (m)
δ (NH2)	1528 (s)	1545 (vw)
Ribose vibr.	899 842 (m)	789 (m)
Ring breath.	668 (vs)	670 (vs)

Figure A3.4. The second derivative spectra of 1-methylguanosine (black line) and Au-1-methylguanosine NPs (red line).

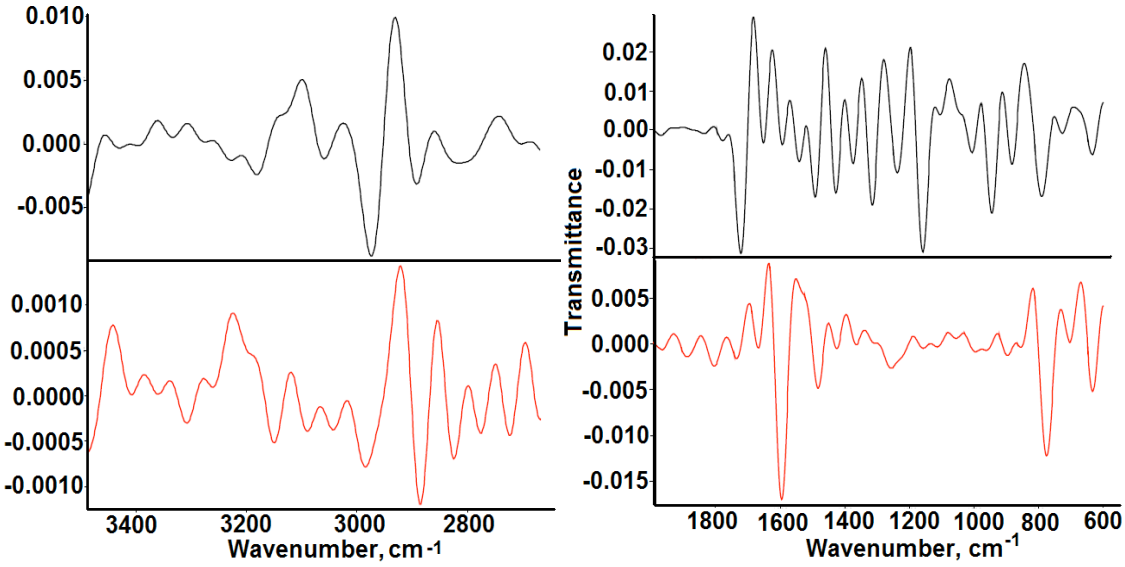

Modes	8-Br-Gua	Au-8-Br-Gua
ν (NH2)	3100 (vs)	3444-3120 (s)
ν (NH) bound	2931 (m)	2922 (vw)
ν (C=O)	1683 1623 (vs)	1696 1636 (m)
δ (NH)	1569 1519 (m)	1518 (vs)
ν (C-N)	1459 1346 (s)	1450 1394 (s)
Ribose vibr.	845 752 (s)	819 731 (vw)
Ring breath.	681 (s)	667 (m)

Figure A3.5. The second derivative spectra of 8-bromoguanosine (black line) and Au-8-bromoguanosine NPs (red line).

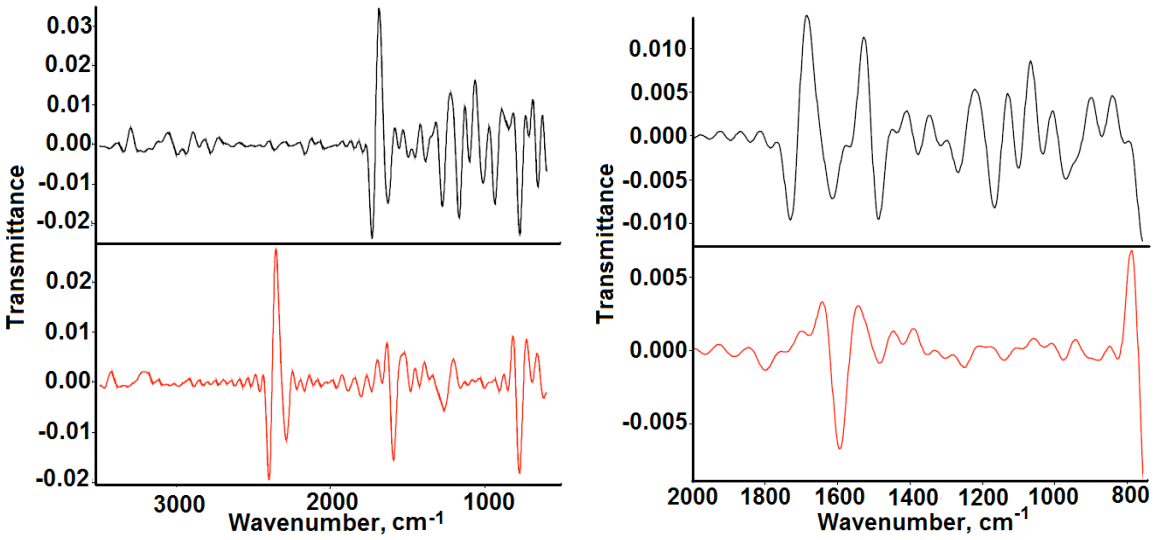

Modes	Ino	Au-Ino
ν (OH)	---	3425 (m)
ν (NH)	3297 (m)	3217 (vs)
ν (C=O)	1687 (vs)	1698 1636 (m)
δ (NH)	1588 1530 (m)	1507 (vs)
ν (C-N)	1420 (m)	1453 (vs)
Ribose vibr.	890 816 (m)	878 818 (vw)
Ring breath.	692 629 (vs)	662 (vs)

Figure A3.6. The second derivative spectra of inosine (black line) and Au-8-inosine NPs (red line).

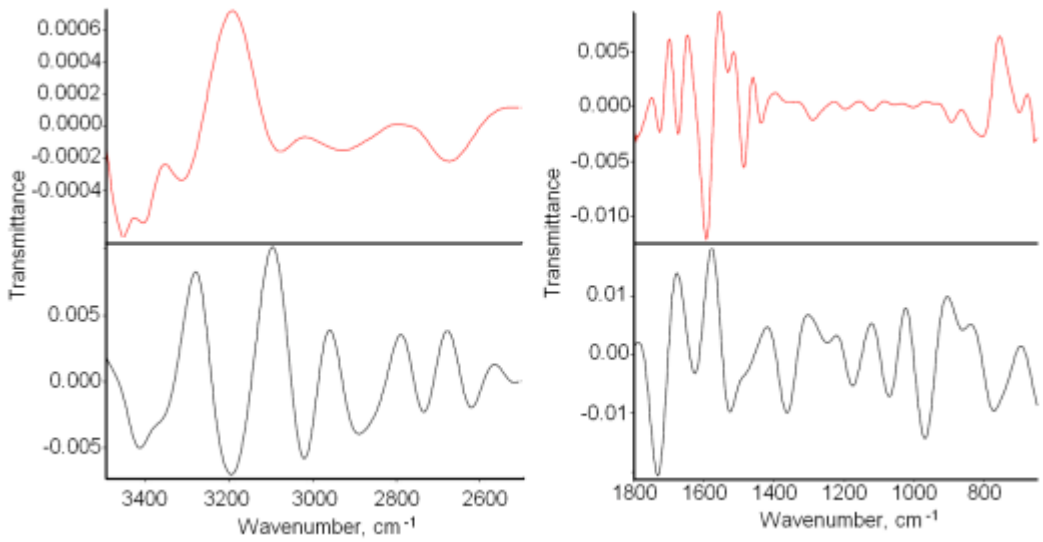

Modes	Ade	Au-Ade
ν (NH)	3273 (m)	3202 (vs)
ν (CH)	3092 (vs) 2969 (m)	---
δ (NH)scis	1663 (s)	1697 (s) 1645(s)
Ring breath.	698 (w)	680 (w)

Figure A3.7. The second derivative spectra of adenine (black line) and Au-adenine NPs (red line).

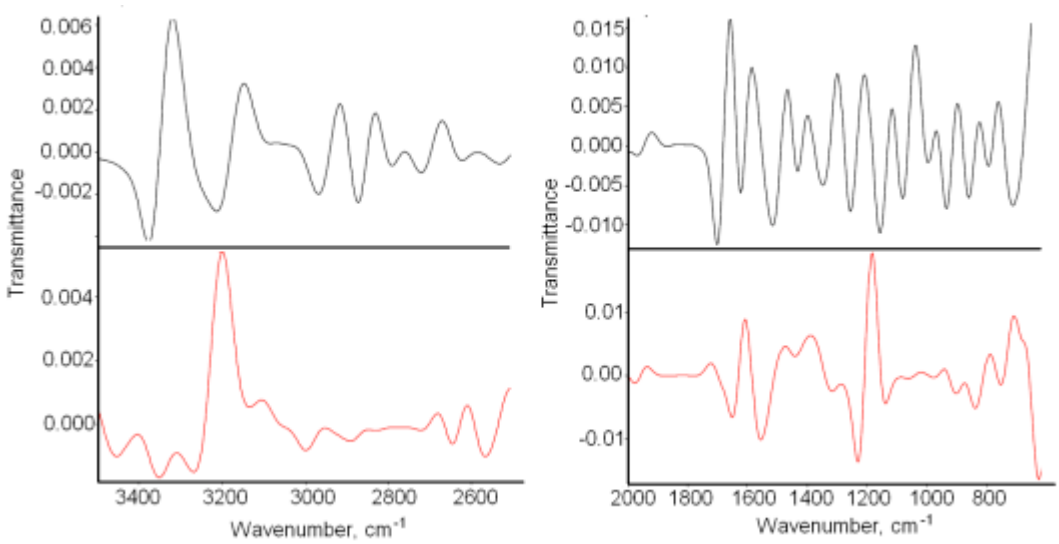

Modes	Ado	Au-Ado
ν (NH)	3147 (s)	3201 (vs)
δ (NH)scis	1644 (s) 1590 (s)	1608 (w)
ν (C-N)	1209 (m)	1184 (vs)
Ribose vibr.	---	788 (vs)
Ring breath.	759 (m)	708 (vs)

Figure A3.8. The second derivative spectra of adenosine (black line) and Au-adenosine NPs (red line).

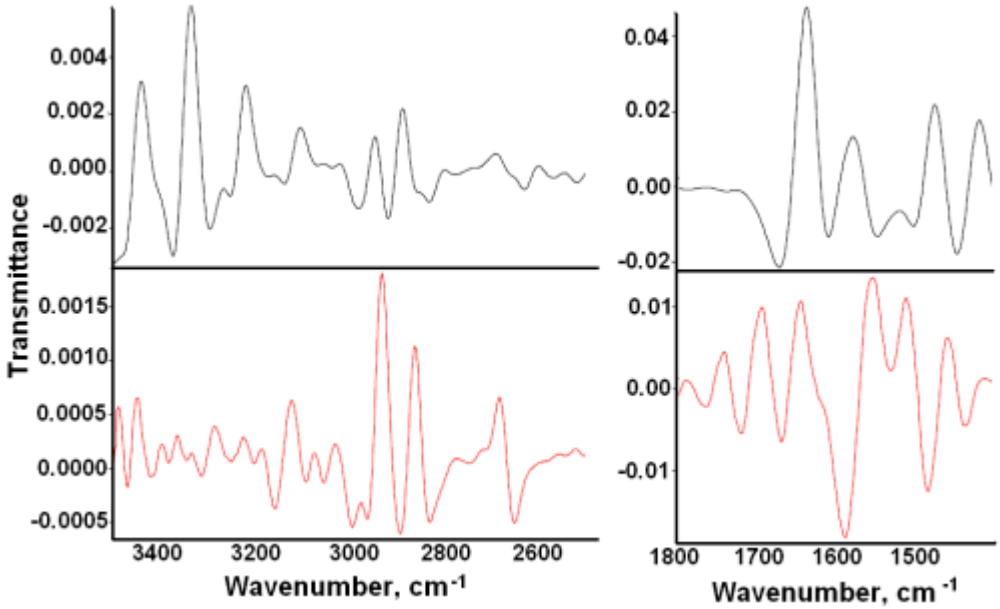
Transmittance
0.004
0.002
0.000
-0.002
0.0015
0.0010
0.0005
0.0000
-0.0005
3400
3200
3000
2800
2600
Wavenumber, cm-1
0.04
0.02
0.00
-0.02
0.01
0.00
-0.01
1800
1700
1600
1500
Wavenumber, cm-1

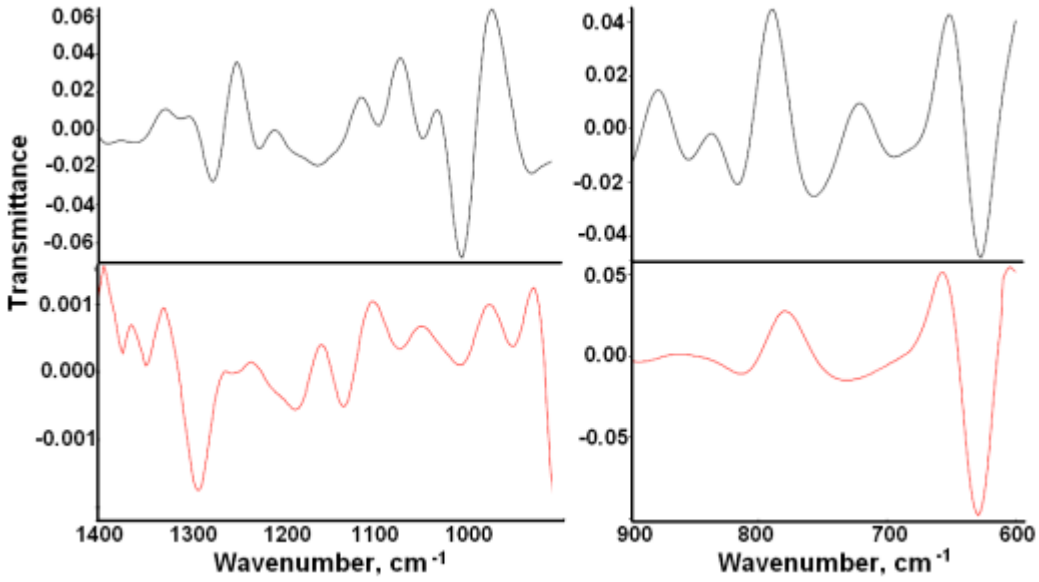
Transmittance
0.06
0.04
0.02
0.00
-0.02
-0.04
-0.06
0.001
0.000
-0.001
1400
1300
1200
1100
1000
Wavenumber, cm-1
0.04
0.02
0.00
-0.02
-0.04
0.05
0.00
-0.05
900
800
700
600
Wavenumber, cm-1

Modes	5'-AMP	Au-5'-AMP
v (OH)	3433 (vw)	3443 (v)
v (NH)	3213 (w) 3096 (w)	---
v (CH)	2953 (v)	2924 (vw)
δ (NH)scis	1640 (s)	1645 (m)
v (P=O)	1074 (s)	1097 (vw) 1028 (vw)
Ring breath.	790 (m)	770 (s)

Figure A3.9. The second derivative spectra of adenosine 5'-monophosphate (black line) and Au-adenosine 5'-monophosphate NPs (red line).

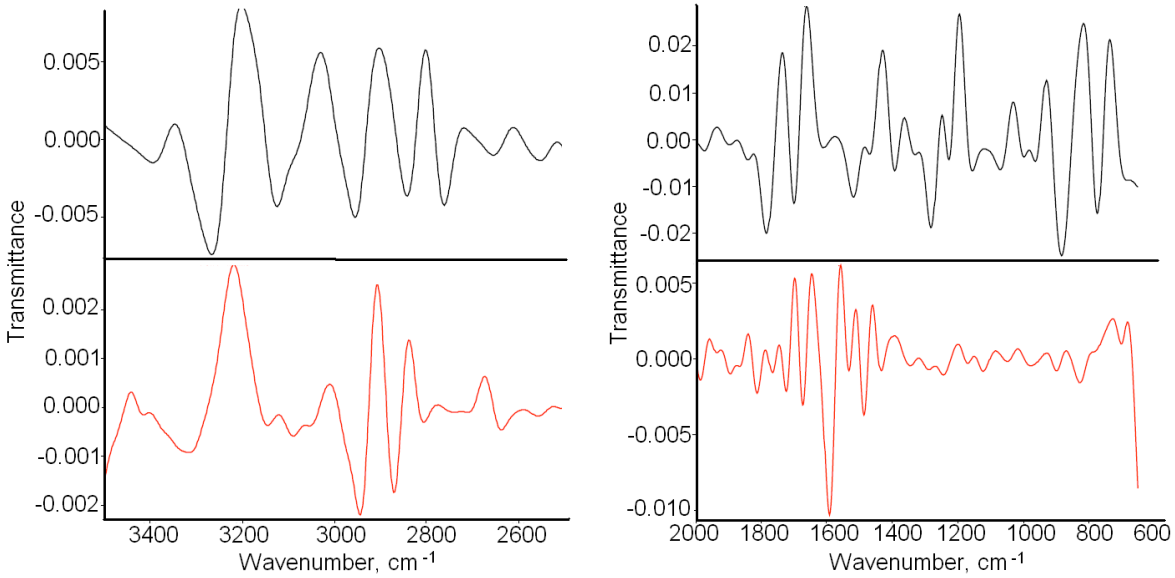

Modes	5'-AMP	Au-5'-AMP
v (NH)	3201 (w)	3217 (s)
v (CH)	3030 (s)	3008 (vw)
v (CH3)	2902 (s)	2907 (vw)
v (C=O)	1736 (vs)	1697 (s)
δ (NH)scis	1431 (s)	1512 (s)
		1415 (s)
δ (CH)oop	735 (vs)	726 (s)

Figure A3.10. The second derivative spectra of thymine (black line) and Au-thymine NPs (red line).

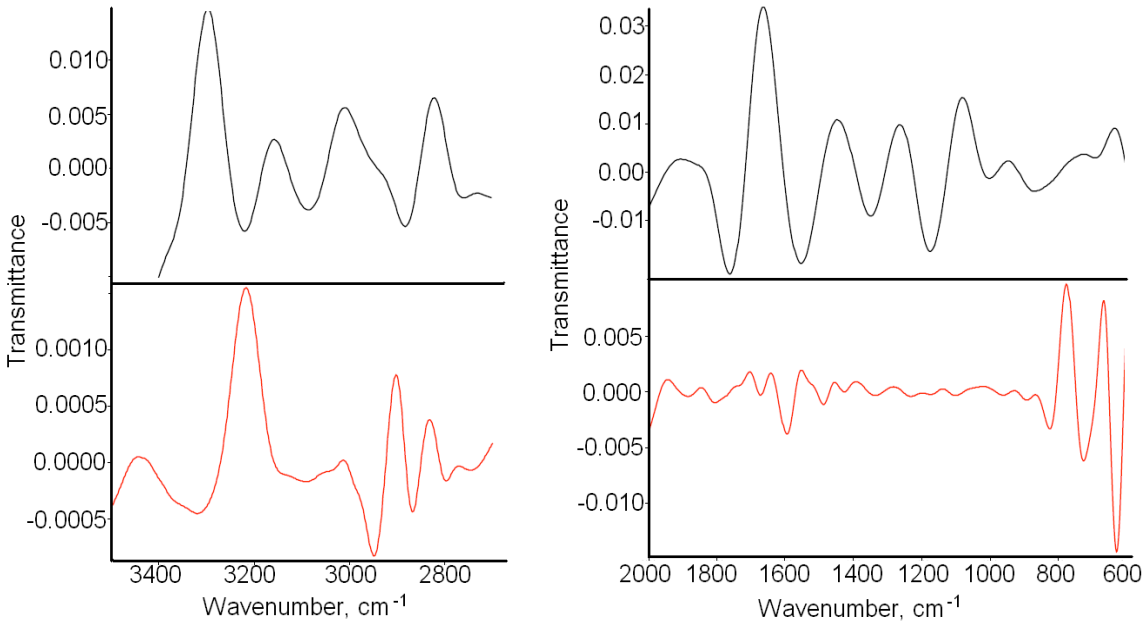

Modes	5'-AMP	Au-5'-AMP
v (NH)	3296 (s)	3216 (s)
v (C=O)	1664	1704 (w)
v (C=C)	(s)	1640 (w)
δ (CH)oop	731 (w)	774 (vs)

Figure A3.11. The second derivative spectra of thymidine (black line) and Au-thymidine NPs (red line).

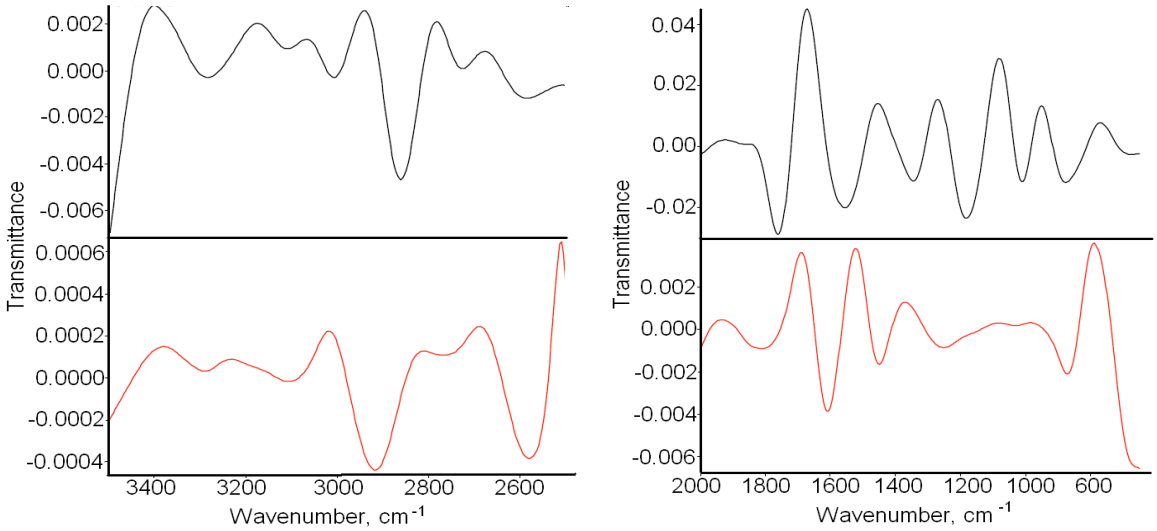

Modes	5'-AMP	Au-5'-AMP
v (OH)	3402 (vw)	3379 (vw)
v (NH)	3175 (vw)	3231
v (CH)	2941 (v)	3018 (vw)
N (C=O)	1671 (s)	1688 (s)
δ (NH)scis	1453 (m)	1522 (s)
v (P=O)	1080 (s)	1084 (vw)
Ribose vibr.	949 (s)	983 (vw)
δ (CH) oop	771 (s)	791 (vs)

Figure A3.11. The second derivative spectra of thymidine 5'-monophosphate (black line) and Au-thymidine 5'-monophosphate NPs (red line).

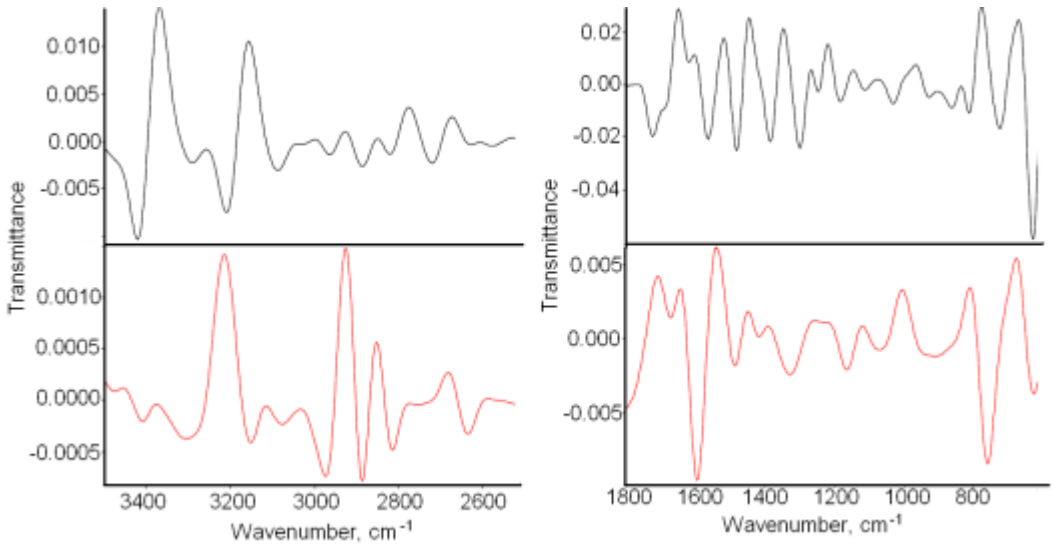

Modes	5'-AMP	Au-5'-AMP
ν (NH)	3368 (vs) 3157 (vs)	3215
ν (CH)	2927 (m)	2927 (vw) 2851
ν (C=O)	1647 (vs)	1710 1645 (s)
ν (C-N)	1520 (s) 1441 (vs)	1541 (vs) 1449 (m)
Ring breath.	773 (vs)	811 (w)
δ (CH) oop	673 (m)	675 (m)

Figure A3.12. The second derivative spectra of cytosine (black line) and Au-cytosine NPs (red line).

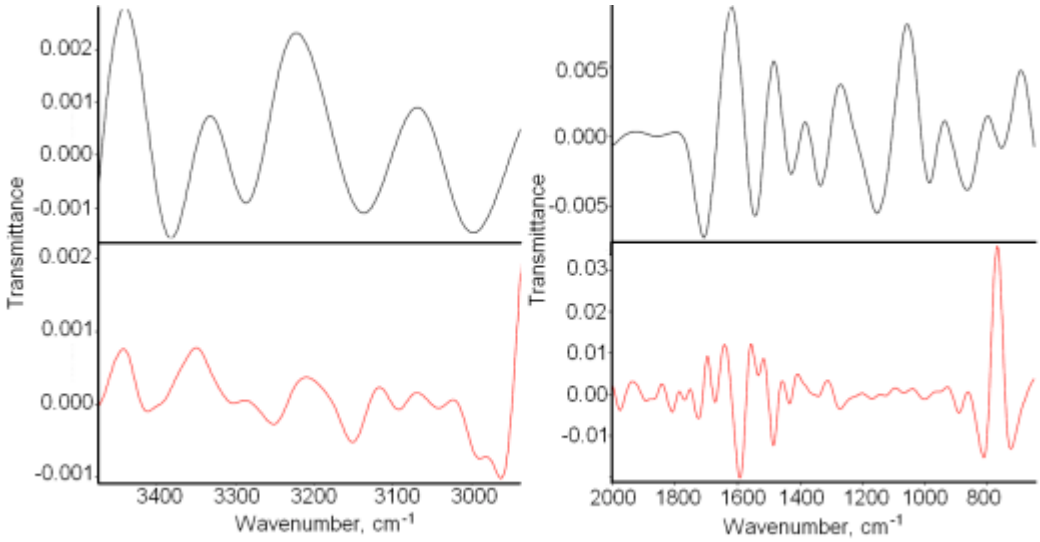

Modes	5'-AMP	Au-5'-AMP
v (OH)	3443 (w)	3442 (vw)
v (NH)	3337 (vs) 3220 (vs)	3350 3209 (vw)
v (CH)	3072 (w) 2909 (m)	2926 (vw) 2854
v (C=O)	1618 (s)	1696 (ms) 1642 (s)
Ring breath.	799 (w)	769 (vs)

Figure A3.13. The second derivative spectra of cytidine (black line) and Au-cytidine NPs (red line).

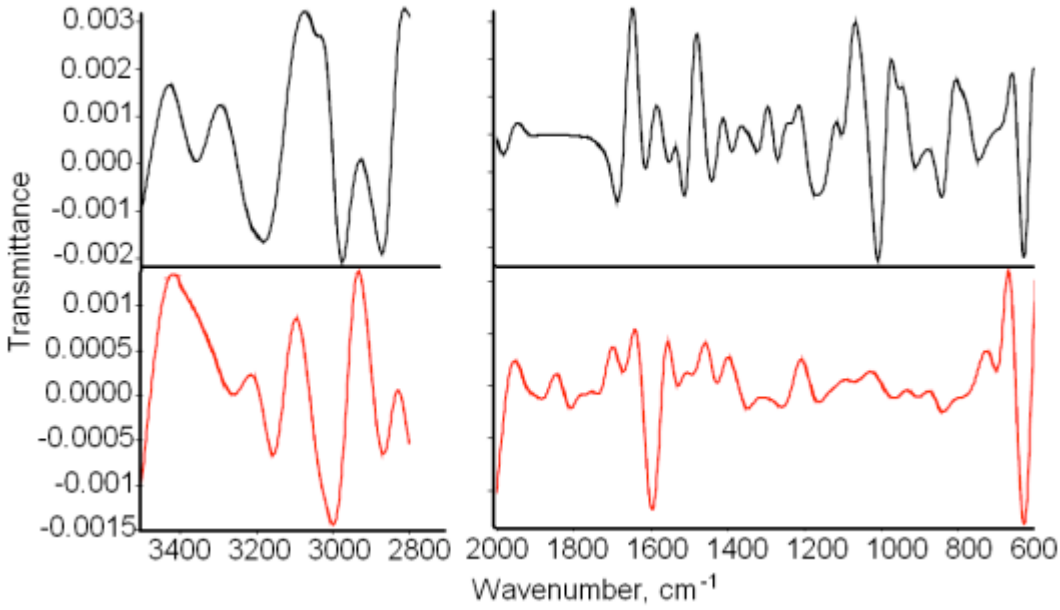

Modes	5'-AMP	Au-5'-AMP
ν (OH)	3427 (vw)	3415 (vs)
ν (NH)	3292 (vw)	3212
ν (CH)	3072 (vs) 3028 2926 (m)	3095 (vw) 2932 (m)
ν (C=O)	1646 (m)	1702 (m) 1641 (m)
δ (NH)scis	1584 (w)	1554 (b)
ν (P=O)	1066 (vs)	1094 (vw) 1026 (vw)
Ring breath.	799 (s)	729 (vs)
δ (CH) oop	664 (s)	672 (vs)

Figure A3.14. The second derivative spectra of cytidine 5'-monophosphate (black line) and Au-cytidine 5'-monophosphate NPs (red line).

4. Biological experiments

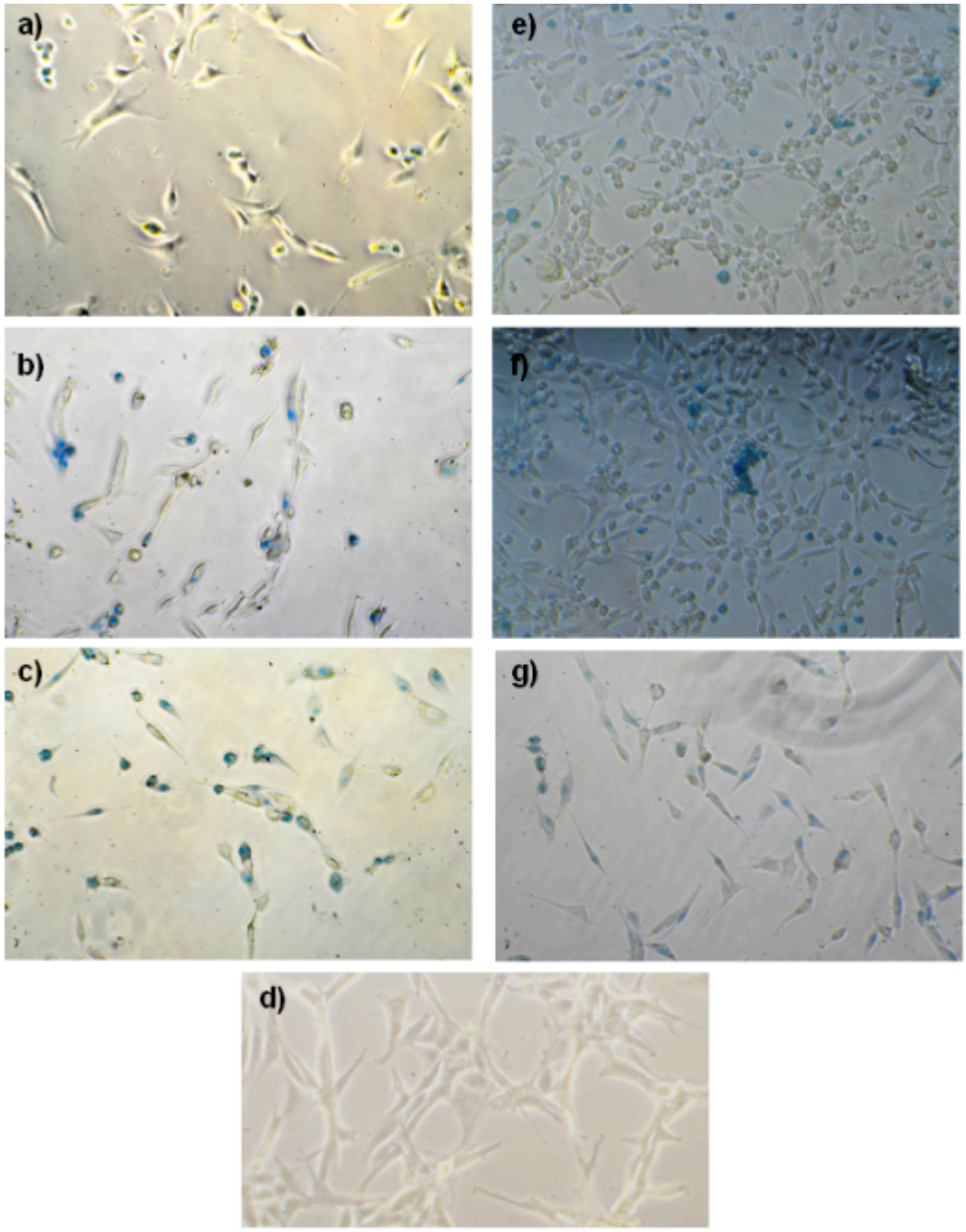

Figure A4.1. Light microscopy image of U87 cells incubated with a) Au-thymine, b) Au-thymidine, c) Au-thymidine 5'-monophosphate, d) Au-citrate, e) Au-cytosine, f) Au-cytidine and g) Au-cytidine 5'-monophosphate NPs.

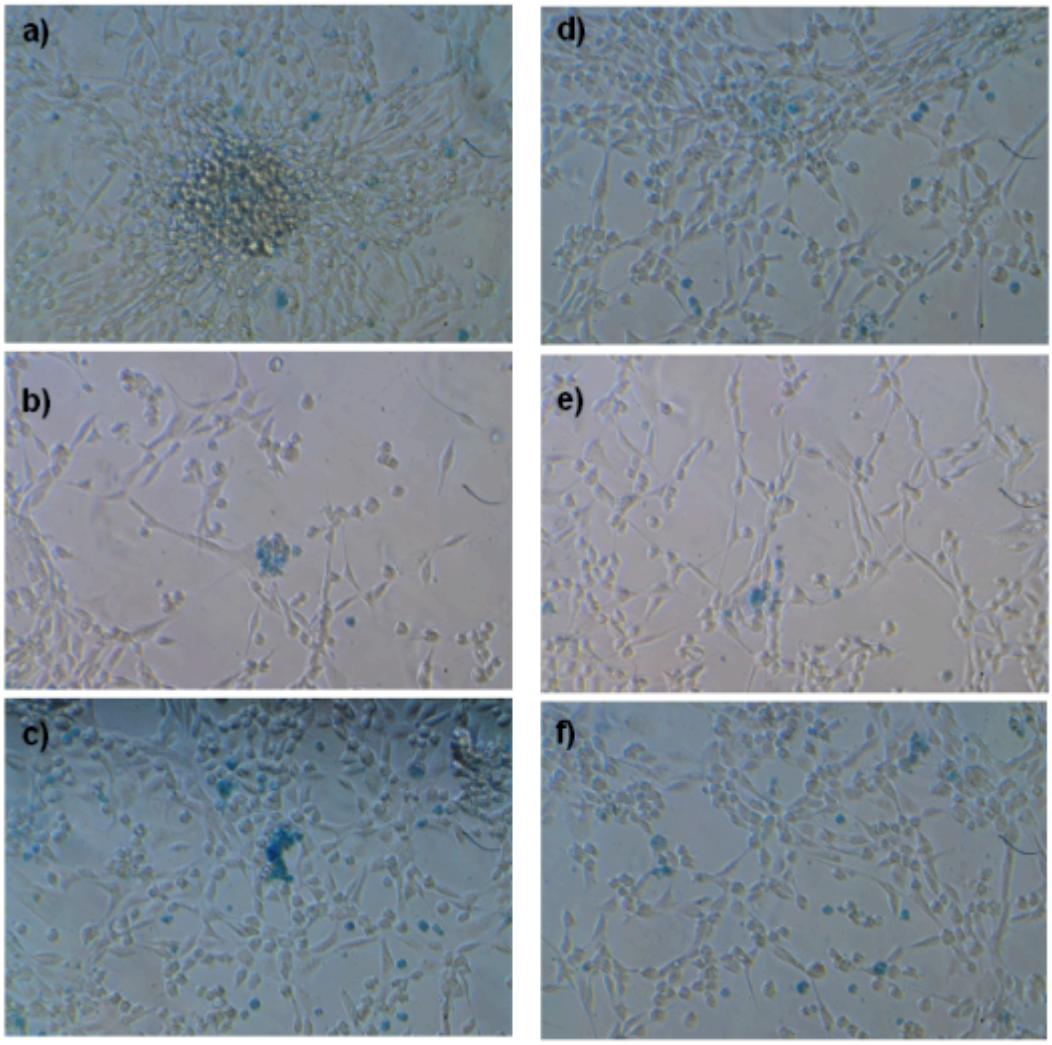

Figure A4.2. Light microscopy image of U87 cells incubated with a) Au-guanine, b) Au-guanosine, c) Au-guanosine 5'-monophosphate, d) Au-adenine, e) Au-adenosine and f) Au-adenosine 5'-monophosphate NPs.

Dott.ssa Svetlana Avvakumova

Scuola di Dottorato in Chimica Industriale

XXV Ciclo

Università degli Studi di Milano

Tutor: Prof Francesca Porta

Co.tutor: Dr Giorgio Scarì

Coordinator: Prof. Domenique Robertò

Introduction

The aim of my PhD research project has been the study of gold nanoparticles (AuNPs) functionalized by different biologically active molecules and their applications in biological systems. Biological studies on cells have been accomplished in collaboration with Dr. Giorgio Scarì from the Department of Biology of Milan University.

During the first two years, my research was focused on the following topics:

- Synthesis and characterization of AuNPs stabilized by nucleic acid components, such as nucleobases (adenine, guanine, thymine and cytosine), corresponding nucleosides and mononucleotides.
- Spectroscopic study of the binding between nucleic acid components and gold surface;
- Cytotoxicity and cellular uptake studies of the conjugates into human glioblastoma cancer cells;
- Synthesis and characterisation of AuNPs functionalized by an RGD-containing peptide for integrin receptor targeting.

The 3rd year of my PhD studies I partly spent working in Prof. Mathias Brust's lab at The University of Liverpool. My research was dedicated to design, synthesis and characterisation of AuNPs conjugated with Halo Tag specific ligands for Halo Tag protein targeting.

AuNPs modified by nucleic acid components: synthesis, spectroscopic study and potential application in biology

The interaction of DNA with gold nanoparticles has found diverse applications in the recent advancements of nanobiotechnology, including diagnostics involving DNA detection employing such techniques as surface plasmon resonance spectroscopy, electrochemical, colorimetric detection, as well as electronics, sensors, drug delivery, chips, imaging, etc [1-19]. In this PhD project, purine and pyrimidine bases, along with corresponding nucleosides and nucleotides are used as stabilizing agents for AuNPs. Moreover, several guanosine derivatives (1-methylguanosine, 8-bromoguanosine and inosine) are used to better understand the binding between the molecules and gold surface.

Small water-soluble AuNPs are prepared following “one-pot” approach, where a gold salt aqueous solution is reduced by sodium borohydride in the presence of stabilizing ligands. The molar ratios between the components are varied in the preliminary experiments in order to find out the reaction conditions at which the resulting AuNPs possess a number of characteristics, such as small particle size and stability. The reaction progress is continuously followed by UV-vis spectroscopy, tracing both shape and position of SPR band along with the colour of resulting colloidal solutions as an indication of stability and certain particle size. As-prepared AuNPs are characterized by TEM, dynamic light scattering (DLS) and zeta-potential techniques. TEM results indicate the diameter of the particles to vary from 6 to 35 nm: the largest nanoparticles of 35 nm were obtained using adenosine 5`-monophosphate as capping agent, while the smallest ones of 6 nm were produced both with guanosine 5`-monophosphate and cytidine and corresponding nucleotide,

which indicates a dependence of the size from the ligand nature and its amount per nanoparticles. DLS studies show an increase of particle diameter comparing to that obtained by TEM (of 3-6 nm), being a good indication of a successful particle modification and presence of a “shell” around the particle. Moreover, it shows the presence of fractions with larger mean diameters (34-95 nm), arising from the formation of small particle agglomerates, however, without bringing about any nanoparticle aggregation.

Electrokinetic studies show that all the nanoconjugates are negatively charged showing negative zeta-potential values. Notably, the particles capped by nucleobases and nucleosides show similar zeta-potential values around -20-23 mV, indicating that sugar does not greatly contribute to the particle charge. On the other hand, the particles capped by nucleotides show very negative values close to -50 mV, indicating a contribution of the phosphate moiety in the stabilization of the AuNPs. Zeta-potential values have been compared to a value of “bare” nanoparticles (+11.04 mV), supporting the results of DLS and a successful modification of the nanoparticles.

Ionization state does have a great impact both on the spectroscopic characteristics of a molecule and on its binding to a surface. In order to understand in which form (neutral or protonated) the molecules exist in the solution under given conditions, we calculated the values of concentration fractions (α) as function of pH, using the acidity constant logarithms, *pKa*. We have found that the majority of the molecules exist both in mono-protonated and neutral state. Only adenosine 5’-monophosphate exists in bi- and tri-protonated state: both at N1, N3, N7 atoms and N1, N7 atoms, respectively. On the other hand, thymine, thymidine and

corresponding nucleotide are mostly nonprotonated (neutral) at given conditions. The same is for guanosine derivatives, which exist mostly in neutral form.

Some structural investigations on the interactions between the nucleobases and gold nanoparticle have been already performed by infrared techniques [20-22]. However, the data on NMR studies are still lacking in the literature. Since NMR spectroscopy have been widely used to study metal complexes with nucleobases or other nucleic acid components, we apply this coordinative metallorganic approach to explain the interaction of the compounds under investigation with gold surface, comparing ^{1}H NMR spectra of free compounds, with ^{1}H NMR spectra of capped AuNPs [23, 24]. In theory, the gold core can interact with the ligands in many ways: *via* phosphate oxygen atoms, sugar oxygen atoms, and (N, C, O) atoms of the heterocyclic base; or combinations thereof [23].

Based on the interpretation of NMR and FTIR results, we conclude that most of “guanine family” compounds interact with the particles *via* N7 atom and C=O group, in their neutral form, as the H8 signal shifts in ^{1}H NMR and the C=O band significantly changes in FTIR spectra, in comparison with free compounds. On the other hand, 8-bromoguanosine differs in its binding, while inosine gives more than one product in the colloidal system, as indicated by the complexity of NMR spectrum. Moreover, guanosine and 8-bromoguanosine derivatives seem to be able to form weak hydrogen bonds between N1-H group and gold surface (or other molecules, creating a multilayered corona)), having observed changes of stretching and bending NH bands after interaction with gold.

The substitution on C8 atom leads to a different constrain depending on bulky substituent and different pathways of reaction can be possible for the building up of

Au-purine NPs, as demonstrated for Au-8-bromoguanosine NPs. Novel results on the conformational changes of ribose puckering highlight that it can occur when purine derivatives interact with AuNPs. The need of conformational changes is strictly related to the electronic properties of guanine ring after contact with gold surface throughout N7 and C=O. Moreover, the phosphate group of guanosine nucleotide is strongly involved in a polar interaction with gold surface, being monoprotonated, HO(O)PO-R)(O^-) due to the pH of colloids.

Thymine and thymidine weakly bind to the gold surface involving C=O4 and N3-H groups, with the latter able to form non-conventional hydrogen bonds with gold surface. Thymidine 5`-monophosphate seems to show a stronger interaction due to the presence of a phosphate group, which may participate in electrostatic stabilization of AuNPs. On the other hand, adenine, adenosine and adenosine 5'-monophosphate seem to interact with AuNPs *via* NH_2 group of adenine ring, involving N7 lone pair of electrons. The ribose moiety is affected by the interaction, giving rise to significant changes in NMR spectra, while the phosphate moiety may interact with gold surface electrostatically, providing the particle stabilization. Finally, "cytosine family" compounds interact with AuNPs involving N3 atom of cytosine moiety, with the ribose moiety to be strongly perturbed under interaction. Likewise other nucleotides, the phosphate group of cytidine 5'-monophosphate is involved in the interaction, showing a large chemical shift in ^{31}P NMR spectrum.

Besides structural studies on AuNPs, we have also performed the cytotoxicity and cellular uptake experiments in order to evaluate their potential application in biology. All the experiments have been performed using U87 human glyoblastoma cell line, used as an *in vitro* model of human glioblastoma cells to investigate the

cytotoxic effect of chemotherapeutic drugs towards cancer cells. The cell mortality has been studied by trypan blue exclusion test by determining the number of viable cells present in the cell suspension, basing on the principle that live cells possess intact cell membrane that exclude certain dyes, whereas dead cells do not [25]. After one hour of incubation, the nanoparticles modified with nucleobases caused 12-18% cell death, while nucleobases and nucleotides conjugates shown 8-23% of cell mortality. It is known that the kind of surface coating may play an important role in the cytotoxicity of AuNPs.

The cellular uptake studies of several gold conjugates have been performed both by confocal microscopy and TEM. All the tested conjugates are taken up by the cells: the nanoparticles are distributed in different cellular compartments, and some of them even can be found inside the nucleus. The cellular uptake of Au-thymidine 5'-monophosphate NPs has been studied by TEM. After one hour of incubation, the nanoparticles are found approaching cellular membrane and clustered together in cellular compartment that appear to be an endosome. Moreover, the nanoparticles are observed free in the cytoplasm, which may indicate their ability to escape endosomal pathway. In fact, the nanoparticles are also found roaming into different cellular compartments, and, in particular, crossing nuclear membrane and even into the nucleus. The Au-thymidine 5'-monophosphate NPs seem to fulfil the necessary conditions to enter the nucleus, being small enough (10 nm) to be able to penetrate nuclear membrane, and be probably taken up by the cells *via* passive uptake. This mechanism is still unclear and needs a more detailed study, by variation of cellular uptake conditions and using different cell lines.

AuNPs functionalized by RGD-containing peptide for integrin targeting

Integrins are a family of proteins that facilitate cellular adhesion and migration on extracellular matrix proteins in the intercellular spaces and basement membranes, and regulate cellular entry and withdraw from the cell cycle [26]. Integrin $\alpha_V\beta_3$ is expressed at low levels on epithelial cells and mature endothelial cells, but is overexpressed on the activated endothelial cells of tumor neovasculature, including osteosarcomas, neuroblastomas, glioblastomas, melanomas, lung carcinomas, and breast cancer [27].

Most integrins recognize their respective extracellular matrix proteins through short peptide sequences such as Arg-Gly-Asp (RGD) [28]. RGD-containing peptides compete in the binding of proteins to cell surface $\alpha_V\beta_3$, preventing cellular adhesion to the extracellular matrix, thwarting cell metastasis, and inducing apoptosis [29].

In this PhD research, both cyclic RGD-$(GC)_2$ and linear $(GC)_2$ peptides are used. The RGD-$(GC)_2$ peptide is a chimeric molecule of 12 amino acids containing two parts: an RGD-sequence and a $(GC)_2$-motif for integrin targeting and nanoparticle stabilization, respectively. The RGD-containing part was derived from the c(RGDfK) peptide, an $\alpha_v\beta_3$ antagonist, where the lysine residue was replaced by glutamic acid to allow the conjugation to the $(GC)_2$-motif by its γ-carboxylic group.

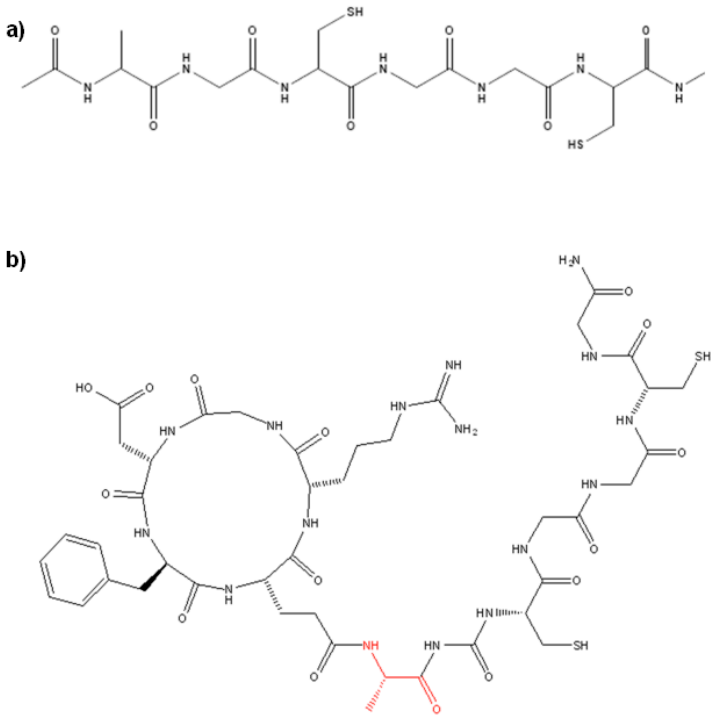

Figure 1. a) $(GC)_2$ peptide; b) RGD-$(GC)_2$ peptide.

The $(GC)_2$ portion contains a sequence of glycines and cysteines needed for the binding to the gold surface via Au-S covalent bond and providing nanoparticle stabilization against aggregation, allowing a parallel disposition towards gold surface. The peptides were synthesized by Dr. Laura Zaccaro's group at the Institute of Biostructures and Bioimages (Naples). A standard Fmoc solid-phase strategy was applied. The products were purified by preparative RP-HPLC and the collected fractions containing the peptides were lyophilized.

AuNPs were prepared using "one-pot" sodium borohydride reduction method in the presence of RGD-$(GC)_2$ and $(GC)_2$ peptides to give small nanoparticles of 10.2 nm and 13.9 nm, respectively. The conjugation of AuNPs with peptides was confirmed by ^{1}H NMR and ATR-FTIR spectroscopy, the stability of the conjugates was verified using both UV-vis spectroscopy and Zeta-potential studies, while their

morphology analysed by TEM. Varying the molar ratios between the reagents (Au:peptide:sodium borohydride), the conditions corresponding to the most stable nanoconjugates have been matched: the 1:0.005:2 and 1:0.001:2 ratios for $(GC)_2$ and (RGD)-$(GC)_2$ peptides, showing 514 and 529 nm SPR band, respectively.

Zeta-potential studies show the AuNPs to be negatively charged with zeta-potential values of -27.27 mV and -40.59 mV for Au-RGD-$(GC)_2$ and Au-$(GC)_2$, respectively. The difference between the zeta-potential values can be due to a different local environment surrounding a single nanoparticle, and can depend on: surface concentration of the peptides on the particle, possible ionic dissociations or zwitterionic forms of the peptides, disposition of the peptide molecules on the particle surface, interactions of the two organic chains with water, and, most importantly, ionic strengths of the solutions [30].

In order to have an idea of coverage density on the nanoparticle surface, the number of peptide molecules per particle was determined by TGA analysis. The weight losses of 1.609% and 1.058% were recorded in the 120-450°C heating range, and assigned to the combustion of the peptides bound to the particle surface. The number of peptide molecules residing on each gold particle was calculated, using a simple equation described by De Palma and co-workers [31], giving the numbers of 94 and 298 molecules for RGD-$(GC)_2$ and $(GC)_2$ peptides, respectively.

In order to verify the binding of the peptides to nanoparticle surface and investigate the interactions in the ligand shell of the conjugates, ATR-FTIR and NMR spectroscopy have been performed. From the perusal of the spectroscopic data the following conclusions about the conjugation of the peptides to the gold particle are drawn: a strong interaction of the $(GC)_2$ part with gold surface *via* the sulphur atom of

cysteine residues results in a strong perturbation of CO and NH groups and disappearance of Cys β-CH_2 proton signal. On the contrary, the rigid RGD ring seems to be almost unaffected upon interaction with gold: from NMR spectra only a minor structural rearrangement of the peptide-cyclic portion can be detected; in the FTIR spectrum, amide I and amide II bands show the patterns different from those found in the Au-$(GC)_2$ spectrum, likely, because of the amide I band to be forbidden by surface selection rules causing its low intensity. Summing up, the interaction between $(GC)_2$ or RGD-$(GC)_2$ and AuNPs mainly consists in the formation of S-Au bonds between the cysteine residues of $(CG)_2$ part and gold surface, leaving the RGD moiety almost unaffected and free for the interaction with integrin receptor.

For cellular uptake studies, peptide conjugated nanoparticles are added to cultures of U87 cells, a human glioblastoma cell line, and the cellular uptake is compared after different incubation times, using confocal microscopy. Importantly, the extent of cellular uptake in each case seems vastly different: a large amount of Au-RGD-$(GC)_2$ conjugates is found to be present into cellular body even after 5 min of incubation, while Au-$(GC)_2$ particles are hardly taken up by the cells even after 30 min of incubation.

The quantitative analysis of cellular uptake is evaluated by measuring the pixel brightness of the confocal images taking into consideration the cellular areas nearly equal to 780 μm^2. As expected, the amount of Au-RGD-$(GC)_2$ particles taken up by the cells is growing along with incubation time, giving the pixel brightness of 0.87 and 13.3 after 5 and 30 min of incubation, respectively. On the contrary, the cells incubated with the particles conjugated with peptide lacking RGD-moiety, show the pixel brightness near to the zero.

TEM results support confocal microscopy data: the nanoparticles functionalized by $(GC)_2$ peptide are approaching the cellular membrane after 1 h of incubation, however, are not able to cross it and be taken up by the cells, whereas Au-RGD-$(GC)_2$ NPs are found while crossing cellular membrane and enclosed into the endosomes. The results suggest an internalization mechanism *via* integrin-receptor mediated endocytosis [19]. Of extreme interest is that the RGD-conjugated nanoparticles are also found crossing nuclear pore complex, accumulated inside the nucleus and even into the nucleolus. The presence of nanoparticles free in the cytoplasm does suggest endosomal escape mechanism to take place, allowing the nanoparticles to get free to be ready to interact with nuclear pore complex. Even though RGD-peptide has not ever been recognized as nuclear localization signal (NLS) peptide, it appears to be able to perform this functionality. Undoubtedly, the internalization mechanism and nanoparticle fate still need to be explored in details, performing more specific experiments, as the ability to direct the "cargo" nanoparticles into the nucleus has been a task of a great interest so far.

Design and synthesis of AuNPs conjugated with Halo Tag specific ligands for cellular targeting

The goal of this project was to design and synthesize gold nanoparticles conjugated with Halo Tag functional ligands, in order to obtain bioactive conjugates with a number of properties, such as stability in a wide pH range and physiological media, certain size and functionality. These particles should be able to be recognised by Halo Tag protein expressed in different cellular compartments of interest.

A new modern approach, called Halo Tag technology, is being widely applied

for cellular imaging, protein quantification and interaction analysis. It is designed for rapid, side-specific labelling of proteins in living cells and *in vitro,* and based on the efficient formation of a covalent bond between the Halo Tag protein and synthetic ligands (Figure 2). The Halo Tag protein is a catalytically inactive, genetically modified derivative of a hydrolase protein [32]. This protein is used to generate N- or C-terminal fusions that can be efficiently expressed in a variety of cell types. The Halo Tag ligands are small chemical tags, containing two crucial components: a common Halo Tag reactive linker that initiates formation of the covalent bond (chlorine) and a functional reporter such as a thiol or amino-group. The rate of the ligand-protein binding is remarkably fast and the covalent bond formed is highly specific and irreversible.

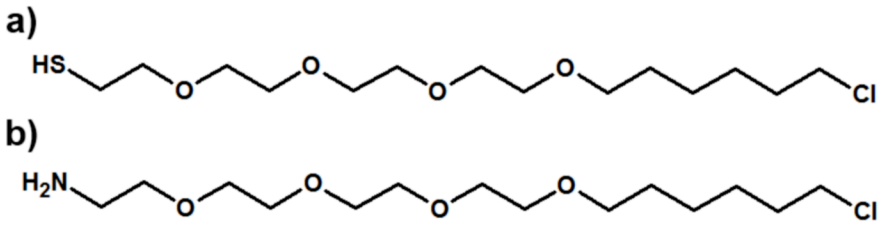

Figure 2. Halo Tag ligand building blocks: a) Halo Tag Thiol (O4); b) Halo Tag Amino (O4).

Normally, nanoparticle bioconjugates are prepared *via* formation of new chemical bonds between functional groups associated with a nanoparticle and a biomolecule or small molecule of interest. For creating a continuous passivation layer around AuNPs thiol compounds have been widely used, allowing efficiently improve their stability and dispersity in aqueous solution. In this project several bifunctional PEGs (-SH/NH_2-, or –SH/ -COOH, or –SH/-OH) have been used for nanoparticle

stabilization. Thiol groups can bind covalently to the surface of AuNPs *via* an Au−S bond, while reactive groups can be readily coupled with Halo Tag reactive sites.

As a basis, gold nanoparticles stabilized by citrate ions have been used. For this purpose, citrate nanoparticles have been prepared by a modified Turkevich-Frens method [33, 34] and subsequently stabilized and functionalized by a shell of thiolated PEG molecules [35, 36].

The Halo Tag Thiol ligand has been used both for direct conjugation to the citrate nanoparticles and conjugation *via* a spacer separating a PEG layer and Halo Tag ligand. The spacer allows to expose the active chlorine atom from the particle surface to be coupled to the Halo Tag protein in the cells. The Halo Tag Amino ligand has been conjugated *via* two different ways with the aim to compare their impact on the conjugates` properties: an EDC/sulfo-NHS coupling reaction involving –COOH groups of the PEG, and a direct conjugation to the PEG containing –NHS reactive groups [37]. As-prepared nanoparticles were purified by repeated centrifugation in order to eliminate the excess of the ligands. The clear nanoconjugates were characterized by UV-vis, analytical centrifugation, TEM, and Zeta-potential studies. Moreover, stability against salt- and pH-induced aggregation was compared. As an empirical measurement of the aggregation process, an aggregation parameter, which measures the variation of the integrated absorbance between 600 and 700 nm, was used.

For direct conjugation, a mixture containing Halo Tag Thiol ligand and thiolated PEG with terminal -OH groups was used. Both 3% and 10 % of the Halo Tag molecules were introduced into the shell. The successful conjugation was confirmed by a shift of SPR band from 522 to 524 nm and an increase in intensity.

Analytical centrifugation shows a large shift as well: diameter of citrate NPs obtained by this method is 13.5 nm, while it undergoes a significant change to 12.1 nm and even 11.9 nm with increasing content of Halo Tag Thiol molecule in the ligand shell from 3% to 10%, respectively. TEM results illustrated the presence of very monodispersed well separated particles with similar mean diameters of 15.91±1.13 nm and 15.28±0.83 nm. Interestingly, the particles were able to form a kind of self-assembled 2D structures under natural dewetting process by slow evaporation of nanoparticle-containing solvent on the TEM grid [38]. The zeta-potentials of conjugated particles were significantly different from those of unmodified citrate GNPs: -14.3 and -15.2 mV *versus* -32.7 mV for citrate GNPs, supporting the occurred conjugation. Stability studies show that the particles with major content of the ligand have a better stability both in PBS and at acidic pH, with aggregation parameter maximum less than 0.2. While PEGylated nanoparticles are subjected to a slight aggregation at acidic pH, probably due to protonation of terminal –OH groups. On the other hand, no aggregation of the nanoparticles was detected even in extremely high salt conditions: incubated with NaCl, both particles were stable up to 3M concentration. The same behaviour is observed in this case: the particles containing 10% of Halo Thiol ligand appear more stable with a very low aggregation parameter less than 0.1.

An alternative and valuable approach to conjugate Halo Tag Thiol molecule is to use the cystamine linker. To realise this, a mixture of PEGs (-SH/-OH and –SH/-COOH), with 5% and 10% of the latter PEG, is used. Cystamine is decarboxylated cystine, a small disulfide-containing molecule with primary amines at both ends. Here, cystamine is used as an activating reagent for disulfide exchange reaction [39-

41]. The cystamine-modified nanoparticles then are mixed with the Halo Tag Thiol ligand, where the latter cleaves the disulfide of cystamine-modified particles, releasing 2-mercaptoehylamine and forming a disulfide crosslink. A red-shift from 520 to 522 nm occurred when citrate GNPs were substituted by PEG-OH and PEG-COOH molecules. After cystamine conjugation, a further shift of 2 nm occurred for the particles containing 10% PEG-COOH. Finally, when functionalized by Halo Tag Thiol ligand attached to the cystamine spacer, the SPR band moves from 522 to 524 nm in both cases, indicating a successful coupling reaction. Analytical centrifugation data show a considerable shift of 0.7 nm (from 12.4 nm to 11.7 nm) when the GNPs are covered by the mixture of PEG and 5% of cystamine. While increasing the content of cystamine linker to 10%, the shift becomes larger (0.8 nm), and a subsequent shift of 0.1 nm is occurred when functionalized by Halo Tag Thiol. Like nanoparticles prepared *via* direct Halo Tag Thiol conjugation, those containing cystamine linker result to have a negative zeta-potential, which changes after each conjugation step. TEM shows a similar behaviour of the as-prepared NPs with those directly conjugated, with particle diameters to be 16.59±1.25 and 16.19±1.2 nm for the conjugates containing 5%- and 10%-Halo Tag Thiol, respectively. Stability experiments were carried out incubating both cystamine-modified PEGylated nanoparticles and Halo Thiol-conjugates.

The cystamine-containing PEGylated particles appeared to be stable both in PBS and at the basic and neutral pH. The conjugation of Halo Thiol ligand allows improving pH-induced aggregation stability, as the aggregation parameter values significantly decreases in whole pH interval concerned. Concerning salt-induced aggregation, no change of the SPR band profile is detected when the nanoparticles

are exposed to the high salt concentrations indicating an excellent colloidal stability even in extreme conditions. However, the particles containing major amount (10%) of Halo Tag Thiol ligand possess a better stability, being the aggregation parameter a little lower.

The approach applied to conjugate amino-containing Halo Tag ligand to the particles involves the using of a zero-length cross-linking agent, mediating the conjugation of two molecules by forming a bond containing no additional atoms. EDC (or EDAC, 1-ethyl-3-)3-dimethylaminopropyl)carbodiimide hydrochloride) along with sulfo-NHS (N-hydroxysulfosuccinimide) are the most frequently used crosslinking agents in order to conjugate biological substances containing carboxylates and amines [42-44].

First, GNPs were covered by PEG-OH and PEG-COOH, loading in the passivation layer both 5% and 10% of –COOH groups. Afterwards, Halo Tag Amino (O4) ligand was coupled to the –COOH functionality. The starting citrate NPs show a characteristic SPR band at 520 nm, which significantly shifts to longer wavelengths at 526 nm after passivation by PEG mixture. When conjugated with Halo Tag Amino ligand, a further blue-shift of the SPR band takes place, however, its intensity is maintained, indicating good resistance to the coupling reaction. A large shift of analytical centrifugation spectra takes place after exchange between citrate ions and PEG: initial value of 12.4 nm now becomes 11.5 nm. Further shift is hardly detectable; however, the peak becomes narrower after coupling reaction, indicating a narrower particle distribution and better stability.

Zeta-potential studies confirmed the nanoparticles to be negatively charged with zeta-potential value changing after every conjugation step. TEM indicates the

disposition of the nanoparticles to look different from the previously discussed conjugates prepared by different methods. In particular, the nanoparticles loaded with 5% Halo Tag Amino ligand are evenly distributed on the copper grid, creating a mass of long wires side by side. On the other hand, 10%-loaded nanoparticles show a different picture, forming short and long clustered wires. Finally, both PEGylated and Halo Tag Amino-conjugated nanoparticles maintain the stability in PBS and against pH-induced aggregation in basic, acidic and neutral medium.

Another way to conjugate Halo Tag Amino ligand with PEG shell is to use a PEG containing functional NHS group. In this case, no EDC/sulfo-NHS coupling reaction is needed being PEG molecule already activated and ready to be conjugated. For this purpose, citrate NPs were covered by PEG-COOH and PEG-COONHS molecules *via* citrate exchange method, using 5%, 10% and 15 % of the latter ligand, followed by the coupling with Halo Tag Amino molecule. As indicated by UV-vis, when citrate NPs are passivated by PEG, independently of the ratio between the components in the “passivation” mixture, SPR band shifts of 4 nm towards longer wavelengths and its intensity rises in absorbance. While Halo Amino-conjugated nanoparticles show a slight (2 nm) further shift to 524 nm and a decrease in intensity, confirming the changes in the ligand shell. Analytical centrifugation results show a large shift from 13.4 nm to 12.1 nm when citrate NPs are covered by PEG layer containing 5% of active NHS-groups, while for the particles containing 10 and 15% of PEG-NHS the shift is even larger being 11.9 nm. A further shift from 11.9 to 11.7 nm can be clearly observed when the particles are conjugated with 15% Halo Tag Amino ligand, while in the case of minor ligand amounts the shift is hardly seen due to the increase of ligand shell diameter.

Zeta-potential results have shown the change of the values after each functionalization step: initial zeta-potential value of -32.7 mV corresponding to citrate GNPs becomes less negative after passivation by PEG mixture because of the contribution of sulfo-NHS neutral groups, while it turns to be more negative after conjugation with Halo Tag Amino ligand, due to the negative chlorine terminal groups. TEM indicates that like in the case of the particles conjugated with Halo Tag Amino ligand *via* EDC/sulfo-NHS, the as-prepared particles are able to form chain-like structures via self-assembly. It is likely due to the presence of a large amount of carboxylic groups in the PEG shell, which can form intermolecular hydrogen bonds. The results of stability studies slightly differ from those obtained for other kinds of particles: in the 13-5 pH range the particles form a well dispersed suspension in water exhibiting a characteristic SPR band at 524 nm. However, on further decreasing of pH to 3, a large shift of the SPR band along with a colour change from red to violet take place. At pH<3 the spectra do not change further and become almost saturated without any shifting of SPR band. These observations can be explained as follows: the H-bonding between two –COOH groups of surface-bound PEG molecules brings the nanoparticles into close proximity to form an assembled structure and results in the development of another SPR band in a higher-wavelength region as a result of the coupling of interparticle plasmon resonance of GNPs [45].

In order to understand if the assembly process is reversible, 0.1M NaOH solution is added to the assembly medium in order to increase the pH to 10, resulting in a colour change from violet to initial red, indicating a disassembly process. It is clear that the assembly process is driven by hydrogen-bonding interactions, as no red shift of SPR band was observed in the case of Halo Tag Thiol conjugation where

the –COOH groups were lacking. Regarding salt-induced aggregation, Halo Tag Amino conjugation does not improve the stability of nanoparticles respect to PEGylated ones nor influences the stability against pH-induced aggregation. On the contrary, the stability against NaCl-induced aggregation slightly decreases with increasing loading of Halo Tag Amino ligand on the particle surface.

In conclusion, several bioconjugation techniques have been illustrated and the characteristics of the conjugates have been compared in order to select a system meeting the requirements for successful application in biological experiments. Being based on the stability results, we can conclude that the conjugates synthesized *via* EDC/sulfo-NHS coupling reaction using Halo Tag Amino ligand have shown the best stability compared to the other candidates both against pH- and salt-induced aggregation. Further biological experiments are being carried out in order to compare the conjugates' behaviour in the living cells and study internalization mechanism which will drive the nanoparticles in different cellular compartments where Halo Tag fusion protein will be expressed for specific biorecognition.

References:

1. X. Xie, W. Xu, and X. Liu. *Acc. Chem. Res.*, 2012, ***45*** (9), 1511–1520.
2. R. Wan, Y. Mo, L. Feng, S. Chien, D. J. Tollerud, and Q. Zhang. *Chem. Res. Toxicol.*, 2012, **25** (7), 1402–1411.
3. Y. Zhang, Q. Yuan, T. Chen, X. Zhang, Y. Chen, and W. Tan. *Anal. Chem.*, 2012, **84** (4), 1956–1962.
4. C. H Lalander, Y. Zheng, S. Dhuey, S. Cabrini, and U. Bach. *ACS Nano*, 2010, **4** (10), 6153–6161.
5. Z. Wang, J. Zhang, J. M. Ekman, P. J. A. Kenis, and Y. Lu. *Nano Lett.*, 2010, **10** (5), 1886–1891.
6. D. Li, S. Song, and C. Fan. *Acc. Chem. Res.*, 2010, **43** (5), 631–641.
7. D. G. Thompson, A. Enright, K. Faulds, W. E. Smith, and D. Graham. *Anal. Chem.*, 2008, **80** (8), 2805–2810.
8. P. J. Endres, T. Paunesku, S. Vogt, T. J. Meade, and G. E. Woloschak. *J. Am. Chem. Soc.*, 2007, **129** (51), 15760–15761.
9. G. Braun, S. Joon Lee, M. Dante, T.-Q. Nguyen, M. Moskovits, and N. Reich. *J. Am. Chem. Soc.*, 2007, **129** (20), 6378–6379.
10. Y. Chen, W. Cheng. *Wiley Interd. Rev.: Nanomedicine and Nanobiotechnology.* 2012, **4** (6), 587-604.
11. L. Song, V. H.B. Ho, C. Chen, Z. Yang, D. Liu, R. Chen, and D. Zhou. *Adv. Health. Mat.* **DOI**: 10.1002/adhm.201200112.

12. A. Elbakry, E.-C. Wurster, A. Zaky, R. Liebl, E. Schindler, P. Bauer-Kreisel, T. Blunk, R. Rachel, A. Goepferich, M. Breunig. *Small*, **DOI**: 10.1002/smll.201201112.

13. R. P. Johnson, J. A. Richardson, T. Brown, and P. N. Bartlett. *J. Am. Chem. Soc.*, 2012, **134** (34), 14099–14107.

14. S. Zhang, J. Xia, and X. Li. *Anal. Chem.*, 2008, **80** (22), 8382–8388.

15. L. Authier, C. Grossiord, P. Brossier, and B. Limoges. *Anal. Chem.*, 2001, **73** (18), 4450–4456.

16. A. Charrier, N. Candoni, and F. Thibaudau. *J. Phys. Chem. B*, **2006**, **110** (26), 12896–12900.

17. J.-H. Oh, and J.-S. Lee. *Anal. Chem.*, 2011, **83** (19), 7364–7370.

18. C. M. Alexander, J. C. Dabrowiak, and M. M. Maye. *Bioconjugate Chem.*, 2012, **23** (10), 2061–2070.

19. D.-Q. Tang, D.-J. Zhang, D.-Y. Tang, and H. Ai. *Electroanalysis*, 2006, **18** (22), 2194-2201.

20. E. S. Kryachko, F. Remacle. *Nano Lett.* 2005, **5**, 735-739.

21. M. Ostblom, B. Liedberg, L. M. Demers, and C. A. Mirkin. *J. Phys. Chem. B,* 2005**, 109***,* 15150-15160.

22. B. Pergolese, A. Bonifacio, and A. Bigotto. *Phys . Chem. Chem. Phys*. 2005, **7** , 3610–3613.

23. B.Lippert. *Coordination Chemistry Reviews,* 2000, **200–202**, 487–516.

24. D. Yang, S. G. E. Van Boom, J. Reedijk, J. H. Van Boom, and A. H. Wang. *J. Biochemistry,* 1995, **34**, 12912- 12920.

25. S. A. Altman, L. Randers, and G. Rao. *Biotechnology Progress,* 1993*,* **9** (6), 671–674.

26. L. Shuang, *Bioconjugate Chem.,* 2009, **12** (20), 2199-2213.

27. R. K. Goswami, K. M. Bajjuri, J. S. Forsyth, S. Das, W. Hassenpflug, Z.-Z. Huang, R. A. Lerner, B. Felding-Habermann, and S. C. Sinha, *Bioconjugate Chem*., 2011, **22**, 1535–1544.

28. N. Graf, D. R. Bielenberg, N. Kolishetti, C. Muus, J. Banyard, O. C. Farokhzad, and S. J. Lippard, *ACS Nano*, 2012, **5** (6), 4530-4539.

29. S. Mukhopadhyay, C. M. Barnes, A. Haskel, S. M. Short, K. R. Barnes, and S. J. Lippard, *Bioconjugate Chem.*, 2008, **19**, 39-49.

30. G. Scarì, F. Porta, U. Fascio, S. Avvakumova, V. Dal Santo, M. De Simone, M. Saviano, M. Leone, A. Del Gatto, C. Pedone, and L. Zaccaro. *Bioconjugate Chem.*, 2012, **23** (3), 340–349.

31. R. De Palma, S. Peeters, M. J. Van Bael, H. Van den Rul, K. Bonroy, W. Laureyn, J.Mullens, G. Borghs, and G. Maes, *Chem Mater.,* 2007*,* **19**, 1821-1831.

32. G. V. Los, L. P. Encell, M. G. McDougall, D. D. Hartzell, N. Karassina, C. Zimprich, M. G. Wood, R. Learish, R. Friedman Ohana, M. Urh, D. Simpson, J. Mendez, K. Zimmerman, P. Otto, G. Vidugiris, J. Zhu, A. Darzins, D. H. Klaubert, R. F. Bulleit, and K. V. Wood. • *ACS Chemical Biology,* 2008*,* **3** (6), 373-382.

33. J.Turkevich, P. C. Stevenson, and J.Hillier. *Disc. Faraday Soc.* 1951**, 11**, 55-75.

34. G.Frens. *Nature Phys. Sci.* 1973**, 241**, 20-22.

35. A. S. Karakoti, S. Das, S. Thevuthasan, and S. Seal. *Angew. Chem. Int. Ed.* 2011, **50**, 1980 – 1994.

36. E. Pensa, E. Cortès, G. Cortney, P. Carro, C. Vericat, M. H. Fonticelli, G. Benitez, A. A. Rubert, and R. C. Salvarezza. *Acc. Chem. Res.*, 2012, **45** (8), 1183–1192.

37. D. Bartczak, and A. G. Kanaras. *Langmuir,* 2011, **27**, 10119-10123.

38. C. F. Chen, S. D. Tzeng, H. Y. Chen, K. J. Lin, and S. Gwo. *J. Am. Chem. Soc.*, 2008, **130**, 824-826.

39. K. Nwe , D. E. Milenic , G. L. Ray , Y. S. Kim , and M. W. Brechbiel. *Mol. Pharmaceutics*, 2012, **9** (3), 374–381.

40. M. A. Burlingame, C. T. M. B. Tom, and A. R. Renslo. *ACS Comb. Sci.*, 2011, **13** (3), 205–208.

41. A. W. York, C. W. Scales, F. Huang, and C. McCormick. *Biomacromolecules*, 2007, **8** (8), 2337–2341.

42. S. Huang, W. Y. Gaofei Hu , and L. Wang, *J. Phys. Chem. C*, Article ASAP, **DOI:** 10.1021/jp305211d.

43. K. Jia, J. L. Bijeon, P. M. Adam, and R. E. Ionescu, *Anal. Chem.*, 2012, 84 (18), 8020–8027.

44. J. Conde, A. Ambrosone, V. Sanz, Y. Hernandez, V. Marchesano, F. Tian, H. Child, C. C. Berry, M. R. Ibarra, P. V. Baptista, C. Tortiglione, and J. M. de la Fuente, *ACS Nano*, Article ASAP **DOI:** 10.1021/nn3030223.

45. S. Si, and T. K. Mandal. *Langmuir,* **2007,** *23,* 190-195.

List of Publications:

1. Svetlana Avvakumova, Paolo Verderio, Giovanna Speranza and Francesca Porta, Gold nanoparticles modified by guanine and its derivatives: study of conformational changes. *Submitted to Physical Chemistry C.*
2. Miriam Colombo, Serena Mazzucchelli, Veronica Collico, Svetlana Avvakumova, Laura Pandolfi, Fabio Corsi, Francesca Porta and Davide Prosperi, Protein-assisted one-pot synthesis and biofunctionalization of monodisperse gold nanoparticles for selective targeting of cancer cells, *Angewandte Chemie International Edition*, **2012**, 37 (51), 9272–9275.
3. Giorgio Scarì, Francesca Porta, Umberto Fascio, Svetlana Avvakumova, Vladimiro Dal Santo,Mariarosaria De Simone, Michele Saviano, Marilisa Leone, Annarita Del Gatto, Carlo Pedone and Laura Zaccaro. Gold nanoparticles capped by a GC-containing peptide functionalised with a RGD motif for integrin targeting. *Bioconjugate Chem.*, **2012**, 23 (3), 340–349.
4. Svetlana Avvakumova, Giorgio Scari and Francesca Porta. Au-thymine, thymidine and thymidine 5'-monophosphate nanoparticles: chemical characterisation and cellular uptake studies into U87 cancer cells. *RSC Adv.*, **2012**, 2, 3658-3661.
5. Svetlana Avvakumova, Vladimiro dal Santo, Giorgio Scari, and Francesca Porta. An analytical study of a large set of purine and pyrimidine compounds capped to gold nanoparticles. In preparation for *ChemPhysChem*.

List of Communications:

1. F. Porta, S. Avvakumova, G. Scarì. Gold nanoparticles stabilised by GGC peptide terminated with a RDG motif. *The 3rd International Congress of European Association for Chemical and Molecular Sciences,* Nuremberg, 2010.
2. S. Avvakumova, F. Porta, G. Scarì. Gold nanoparticles stabilised by nucleobases, nucleosides and nucleotides. *The 3rd International Congress of European Association for Chemical and Molecular Sciences,* Nuremberg, Germany, 2010.
3. M. De Simone, S. Avvakumova, A. Del Gatto, M. Saviano, C. Pedone, F. Porta, L. Zaccaro. Biomedical nanotechnology: preparation and characterisation of new functionalised gold nanoparticles. *12th edition of the Naples Workshop on Bioactive Peptides, a joint meeting together with the 2nd Italy-Korea Symposium on Antimicrobial Peptides,* Napoli, 2010.
4. M. De Simone, S. Avvakumova, A. Del Gatto, M. Saviano, C. Pedone, F. Porta, L. Zaccaro. Biomedical nanotechnology: preparation and characterisation of new functionalised gold nanoparticles. *The 31st European Peptide Symposium,* Copenhagjen, 2010.
5. S. Avvakumova, F. Porta, G. Scarì, A. Del Gatto, L. Zaccaro. Synthesis, characterization and application of gold nanoparticles capped by RGD fuctionalised peptides. I*nternational Meeting on Developments in Materials, Processes and Applications of Emerging Technologies (MPA),* Alvor, Portugal, 2011.